RATIONAL DESIGN OF DIGITALLY MANUFACTURED CERAMIC MICRO-REACTORS FOR GAS-PHASE CHEMICAL KINETIC MEASUREMENTS

by

JATINDER SAMPATHKUMAR

B.E., B.M.S College of Engineering, 2014

M.S., University of Colorado, 2021

A thesis submitted to the
Faculty of the Graduate School of the
University of Colorado in partial fulfillment
of the requirement for the degree of
Doctor of Philosophy
Paul M. Rady Department of Mechanical Engineering
2023

Committee:
Dr. Nicole Labbe, Chair
Dr. Gregory Whiting
Dr. Gregory Rieker
Dr. John Daily
Dr. Barney Ellison

Sampathkumar, Jatinder (Ph.D., Mechanical Engineering)

Rational Design of Digitally Manufactured Ceramic Micro-reactors for Gas Phase Chemical Kinetic Measurements

Thesis directed by Assistant Professor Nicole J. Labbe and Associate Professor Gregory Whiting

Increasing global concern over energy security and the continued ecological impact of using fossil fuels has pushed the development of sustainable energy alternatives – making research into renewable fuels essential. Identifying and implementing environmentally viable fuel sources requires understanding the combustion process and hence the chemistry of these biofuels. Low residence time flow reactors (≤100 μs), when combined with photoionization mass spectrometry (PIMS) and Matrix Fourier Transform Infrared FTIR spectroscopy, have the capability to probe the elementary pyrolytic reaction mechanism for various fuels directly. When combined with advanced computational methods, these results produce reliable and scalable models that can predict combustion behavior.

First, an explanation of this hybrid experimental and theoretical approach is presented, followed by its application to evaluating the pyrolysis chemistry of three isomers of methylcyclohexene. The nuanced capabilities of this approach are highlighted in the ability of this technique to explain subtle differences in the combustion behavior of these isomers through the results obtained from these evaluations. A similar study is carried out to elucidate the reduced sooting observed when oxygen-containing polyoxymethylene ethers (POM-E) are blended with diesel. The combined approach is used to identify trends in the decomposition of these molecules as a function of increasing the number of oxymethylene units $(\text{-O-CH2-})_n$ and altering the terminal alkyl group. The radicals formed because of these secondary decompositions are critical to suppressing soot formation and are among these molecules' first high-level quantum calculations.

Second, an analysis of the micro-reactor, a key component in previously described experimental techniques, is presented. A qualitative examination of flow inside these reactors (straight tubes approximately 1mm inner diameter and 3cm in length made of SiC) suggests pressure and velocity significantly change along the length of the reactor. This presents a challenge in determining actual flow conditions within the reactor, making it complicated to establish conditions at which pyrolytic chemistry occurs. Computational and experimental testing has been used to optimize a new reactor geometry to control the flow profiles by adding a constriction at one end of the reactor. The nozzle has been shown computationally to stabilize fluid flow within the reactor. A novel digital manufacturing method to fabricate these geometries is detailed, which harnesses the rapid iterability of 3D printing and combines it with the knowledge base for fabricating ceramics conventionally. The capability of this processing technique is extended to other high aspect ratio structures and ceramic types, showcasing its broad applicability. Material characterization studies are presented to compare features of the sintered SiC geometries constructed using this process to typical fabrication methods. The novel reactor geometry is validated through experiments in the PIMS setup, with results showcasing the impact of stabilized pressure, velocity, and increased residence times. The novel design of these micro-reactors will provide researchers with a fundamentally new technique to probe the short residence time pyrolytic reactions of fuels. Combining theory, experiment, model development, and simulation will enable qualitative or even quantitative predictions for many combustion situations of practical relevance. Understanding key elements of this chemistry is an essential step toward the intelligent selection of next-generation alternative fuels.

Dedication

To Dr. Dheeraj Kalladka, thank you for always inspiring me.

Thirukkural (Ancient Tamil language text):

எப்பொருள் யார் யார் வாய்க் கேட்பினும்
அப்பொருள் மெய்ப்பொருள் காண்ப தறிவு.

To discern the truth in everything, by whomsoever spoken, is wisdom.

Sarvajna Pada (16 Century Kannada poetry)*:*

ಸರ್ವಜ್ಞನೆಂಬುವನು ಗರ್ವದಿಂದಾದವನೆ
ಸರ್ವರೊಳು ಒಂದೊಂದು ನುಡಿಗಲಿತು
ವಿದ್ಯೆಯ ಪರ್ವತವೆ ಆದ ಸರ್ವಜ್ಞ

No one possesses knowledge of the universe at birth; it is acquired from those around you.

Acknowledgments

I started graduate school in 2017 with the express intention of finishing a master's in mechanical engineering. The fact that I decided to pursue a doctoral course and have now finished it is a testament to many people who encouraged and supported me. This is my thanks to them.

To my parents, S Sampathkumar and Shashikala, thank you for providing an environment where I could always be curious (even if that came at the cost of breaking things). Appa, you have always shown me the value of being thorough and detail-oriented. Mum, you're never daunted by challenges and face them head-on, a skill I wish I could have applied more in my Ph.D.

To my sister, Jamini Sampathkumar, you have been my touchstone throughout life. Thank you for always supporting me and introducing me to incredible new things. Your integrity and focus are traits I have tried to mimic but fall well short of. To my brother-in-law, Phani Garimella, your ability to stay level-headed and see the big picture inspires me. A big thanks to you and Jamini for making sure the USA felt like home.

To Aradhana Gahlaut, thank you for making the last three years of my Ph.D. feel a lot easier than they were. You've been with me through all the program's important stages and have shown tremendous patience, kindness, and understanding. Celebrating all the highs felt even better and wishing away the lows a lot easier when I could share them with you. Thank you for being a source of strength throughout this time. I can't wait for what's next!

To the rest of my extended family and friends, thank you for always supporting and encouraging me. To Dr. Dheeraj Kalladka, you have and will always remain the yardstick by which I judge myself – thank you for setting the bar high. I would not be a mechanical engineer today if it weren't for P.H. Rama Prabhu; thank you, for showing me the value of always asking how we can do things better. To Stephen Jacob, your patience and attention to detail pushed me to pick up product design and development; there has been no looking back since. To Veda, your ability to break down even the most complex designs into simple working components is incredible – I hope I become half as good an engineer as you. To Balram Prabhu, Manish Manjunatha, Dushyanth Nagraj, Kangkan Saikia, Krishna Vasudevan, Anand Joy, and Samujjwal Baruah – thank you all for being a phone call away and always making even minor progress feel like significant accomplishments. Our friendship is something I will cherish for life.

To my advisor Dr. Nicole Labbe, I'm honored to be the first experimentalist who graduates from the Labbe Lab. It has been an incredible journey. Five years on, I am now even more confident that a Ph.D. working with anyone else would not have been anywhere as rewarding. You are a phenomenal scientist, a great mentor, and a wonderful human being. Thank you for trusting

in my skills and letting me explore how best to accomplish our research goals. Thank you for showing me the value of standing up for myself and not backing down. I'm excited about the future of the Labbe Lab and look forward to having you as someone I can always count on for years to come.

To Dr. Gregory Whiting, thank you for being my sanity check. I have always enjoyed our conversations on all things technology. You have taught me the value of not being daunted by failure and the importance of trying again. I hope to continue to call on you as my mentor in the future.

To Dr. Barney Ellison, thank you for coming in and making every group member feel like their work counted. You always managed to make me feel like I was doing important research. Your zeal for science and curiosity for the world around you are inspirational. I am immensely lucky to have had you as an advisor, mentor, and friend.

A massive shoutout to Nik Ninos at Calix Ceramic Solutions. Nik, you have been a fantastic collaborator. Your willingness to explore the boundaries of ceramics processing and depth of knowledge on all things silicon carbide are aspirational. I am grateful to call you a friend and look forward to collaborating in the future.

I owe a tremendous amount of gratitude to the IIDF shop down the hallway at Cristol Chemistry. To Dr. Donald David and Ken Smith, thank you for humoring all my whacky design ideas and patiently listening to my outlandish plans. If I have managed to build something through my Ph.D., it is thanks to your unwavering support and tremendous skill.

Thank you to the other mentors and teachers that have made me a better scientist, including Dr. John Daily, Dr. Greg Rieker, Dr. Greg Hampson, Dr. Steven George, Dr. Anand Shivapuji, and Dr. S. Srinivas.

To all the members of the Labbe Lab, thank you for making the University and the research lab a welcoming space. Thank you, Cory Rogers, for being my first lab mate and showing me the importance of balancing work and life. I have always admired your kindness and ability to make people feel included. Thank you, Dr. Katie Lockwood, for being a second sibling. Thank you also for not giving up and showing me the value of seeing things through. To Sadie Stutzman, thank you for your infectious optimism and for demonstrating the importance of following your passion. Thank you to Dr. David Couch, for always being patient with my petulant questions and for showing me the importance of approaching a problem through multiple viewpoints. To Rory McClish, we may have been working together only for a year, but it feels like I have known you for much longer – thank you for being a wonderful friend. You always asked me the tough questions and ensured that I thought things through; thank you for making me a better researcher.

Jas Shahanand, your enthusiasm to try new things will hold you in good stead as you become an accomplished researcher. Thank you for always being ready to do the tough assignments. To the rest of the members of the Labbe Lab, thank you for making this research group a fun and rewarding space to work in. Thank you to Austin Hayes, Dr. Jorge Osio-Norgaard, and other BEEM lab members for supporting and guiding me with all things materials and 3D printing. You have all been kind in sharing your time and taught me much. A huge thank you also to former members of the Ellison lab and the Chemistry Stores for always being available.

To Revathi, Vyjayanthi, Karan, Srinath, Kajal, Hari, Shruthi, Sandeep, Abhi, Ashray, Keya, and Shankar- my extended community of friends here at the University; thank you for making Boulder home.

CONTENTS

Chapter 1: Mobility in the Global Energy Context 1

1.1 World energy outlook 1

1.1.1 Emissions 1

1.1.2 Combustion and mobility 2

1.2 Evaluating combustion chemistry 4

1.2.1 Experimental methods 5

1.2.2 Computational methods 7

1.2.3 Pyrolysis and oxidation chemistry 7

1.3 Thesis outline 8

1.4 References 12

Chapter 2: Experimental Methods to Elucidate Combustion Chemistry 15

2.1 Introduction 15

2.1.1 Mass Spectrometry in Combustion 16

2.1.2 Molecular Beam Mass Spectroscopy 16

2.1.3 VUV Ionization Source 18

2.1.4 Micro-reactor 19

2.2 Experimental Methods 21

2.2.1 Pulsed micro-reactor 21

2.2.2 Continuous Flow Reactor 22

2.2.3 Optical Temperature Measurement 23

2.3 Diagnostics 24

2.3.1 Photo Ionization Mass Spectrometry 24

2.3.2 Matrix Isolation Infrared Spectroscopy 29

2.4 Analysis 31

2.5 History of the PIMS and Matrix IR experiments at the University of Colorado 33

2.6 Oxidation reactions using the micro-reactor geometry 37

2.7 References 38

Chapter 3: Computational Modeling of Combustion Phenomena 45

3.1 Introduction 45

3.1.1 Potential Energy Surfaces 50

3.1.2 Rate Constant Calculations 51

3.2 References 52

Chapter 4: Experimental and theoretical evaluation of the links between structural details and the sooting tendency of methylcyclohexene isomers 56

4.1 Introduction 56

4.2 Experimental and computational methods 61

4.2.1 Experimental evaluation of pyrolysis 61
4.2.2 Computational evaluation of pyrolysis 63
4.3 Results: Pyrolysis kinetics of methylcyclohexene isomers 64
4.3.1 1 methyl-1-cyclohexene 65
4.3.2 4 methyl-1-cyclohexene 70
4.3.3 3 methyl-1-cyclohexene 75
4.4 Implications on the sooting tendency of the methylcyclohexene isomers 84
4.5 Conclusions 86
4.6 References 87
Chapter 5: Probing the pyrolysis of Polyoxymethylene Ethers (POM-E) 94
5.1 Polyoxymethylene Ethers (POM-E) as diesel fuel additives 94
5.2 Research into the pyrolysis and oxidation of Polyoxymethylene Ether (POM-E) with diesel 96
5.3 Chemical kinetic investigation of chain length effects of polyoxymethylene ethers (POM-E) during pyrolysis 99
5.3.1 Experimental methods 100
5.3.2 Computational modeling methods 102
5.3.3 Experimental results 103
5.3.4 Computational Results 108
5.4 Chemical kinetic investigation of end-group effects of polyoxymethylene ethers (POM-E) during pyrolysis 124
5.4.1 Experimental methods 125
5.4.2 Computational modeling methods 126
5.4.3 Experimental results 126
5.4.4 Computational results 129
5.5 Exploration of secondary decomposition products of methyl-terminated polyoxymethylene ethers 134
5.5.1 Computational modeling of secondary decomposition 134
5.5.2 Results and discussion 134
5.6 Conclusions 138
5.7 References 139
Chapter 6: Redesigning the micro-reactor 144
6.1 Introduction 144
6.2 Redesigning the Chen Reactor 149
6.3 Parametric evaluation of the redesigned reactor 152
6.3.1 Geometric parametric evaluation 152
6.3.2 Thermodynamic evaluation 155
6.4 Prototype redesigned micro-reactor 156

6.5 References 157

Chapter 7: Fabrication of the novel micro-reactor geometry 159

7.1 Evaluating the ideal nozzle geometry 159

7.2 Shortcomings of traditional manufacturing using silicon carbide 160

7.3 Manufacturing process overview 163

7.3.1 Precursor development 165
7.3.2 Compaction tooling development 166
7.3.3 Pyrolysis and Sintering 176

7.4 Materials Characterization 177

7.4.1 Modulus of Rupture (MOR) evaluation 177
7.4.2 X-Ray Diffraction 178
7.4.3 Micro Computerized tomography (μ-CT) 178
7.4.4 Scanning Electron Microscopy (SEM) 179
7.4.5 Optical Microscopy Imaging 180
7.4.6 Characterization Results and Discussion 180

7.5 Experimental Validation of the nozzle micro-reactor 184

7.6 Multi-Material Capability 187

7.7 Multi-Geometry Capability 187

7.8 Conclusions 188

7.9 References 189

Chapter 8: Exploring the effects of pressure and residence time on unimolecular decomposition reactions in nozzle micro-reactors 194

8.1 Introduction 194

8.2 Computational Fluid Modeling (CFD) Evaluations 197

8.3 Experimental validation of nozzle reactors using photoionization mass spectrometry 205

8.3.1 Anisole 206
8.3.2 Furan 227

8.4 Conclusion 241

8.5 References 242

Chapter 9: Conclusions and future research directions 247

9.1 Thesis summary 247

9.2 Recommendations for future experiments 250

9.2.1 Alternate micro-reactor materials and oxidation experiments 250
9.2.2 X-ray Fluorescence (XRF) Studies 252
9.2.3 Building a low temperature and low-pressure oxidation mechanism for aviation fuels 254

9.3 Acknowledgment and Funding....255
9.3.1 Methylcyclohexene isomers work (Chapter 4) 255
9.3.2 Polyoxymethylene Ether decomposition work (Chapter 5)....256
9.3.3 Nozzle micro-reactor development and fabrication (Chapter 6, 7 and 8) 256
9.3.4 Aircraft flameout analysis and modeling (Chapter 8 and 9) 256
9.4 References....257
Bibliography. ……..259
Appendix……. 287

LIST OF FIGURES

Figure 1.1: Global sources of greenhouse gases with energy contributing over 70% of the total emissions of concern [8] 2

Figure 2.1:Schematic sketch of one-half of a nozzle and the first slit showing the various waves generated by the nozzle flow. The oblique shock has an initial angle of 38°, the maximum angle such a shock can negotiate at Mach 4. This design is intended 18

Figure 2.2: Inner pyrolyzer assembly with pulsed valve. SiC micro-reactor measured at 3 cm length and 1 mm inner diameter. 22

Figure 2.3: Reflectron photoionization time-of-flight mass spectrometer with fixed frequency photons at 118.2 nm 24

Figure 2.4: Generation of 118.2 nm photons (10.487 eV) and ion flight path in the reflectron ... 25

Figure 2.5: Pyrolysis products entrained in Ar exit the μtubular reactor and become trapped on a cryogenic window. 29

Figure 2.6: After deposition on the cold (10 K) window, the outer shroud is rotated 90 for spectroscopic analysis of molecules frozen in Ar. 30

Figure 4.1: The Retro-Diels-Alder stepwise mechanism for each MCHe isomer, as described by Kim et al.[12]. The pathways are initiated through biomolecular reactions where free radicals abstract H-atoms from the fuel. 58

Figure 4.2: Potential energy surface of the unimolecular decomposition of 1MCHe including the bond dissociation pathways and the concerted retro-Diels-Alder (r-DA) route. The energies are calculated at the CCSD(T)/cc-pV∞Z//M06-2X/cc-pVTZ level of theory and reported in kcal/mol relative to the parent molecule. Solid lines (red) are active, and dashed lines (black) are inactive pathways under our experimental conditions (T=300-1500 K, P≅0.1 atm) according to our rate constant calculations. Branching ratio plots of the decomposition rates can be found in Figure 4.3. 65

Figure 4.3: Theoretically calculated rate constants (left) and branching ratios (right) for 1MCHe pyrolysis, including bond fissions and the retro-Diels-Alder reaction. Radical names in the legend are the same used in the PES in Figure 2. The most dominant reaction is the concerted retro-Diels-Alder reaction shown in black. 67

Figure 4.4: Percentage (%) of the total maximum peak signal height as a function of temperature is shown for significant mass values from 1MCHe spectra (IE= 8.67 ± 0.02 eV [35]). *Top:* major species (greater than 20 % flux). *Bottom:* minor species (less than 20 % flux). The presence of dissociative ionization is detected in the 10.487 eV by the presence of m/z 81 at room temperature. PIMS spectra from all three laser intensities used in this work can be found in the Appendix C4. C_{13} peaks of the fuel (m/z 97) and isoprene (m/z 69) were left out of the figure for clarity. 68

Figure 4.5: Potential energy surface of the unimolecular decomposition of 4MCHe,including the bond dissociation pathways and the concerted retro-Diels-Alder route. The energies are calculated at the CCSD(T)/cc-pV∞Z//M06-2X/cc-pVTZ level of theory and reported in kcal/mol relative to the parent molecule Solid lines (red) are active and dashed lines (black) are inactive pathways under our experimental conditions (T=300-1500 K, P≅0.1 atm) according to our rate constant calculations. Branching ratio plots of the decomposition rates can be found in Figure 4.6. 71

Figure 4.6: Theoretically calculated rate constants (left) and branching ratios (right) for 4MCHe pyrolysis, including bond fissions and the retro-Diels-Alder reaction. Radical names in the legend are the same used in the PES in Figure 4.5. The two active reactions are the concerted retro-Diels-Alder reaction (black) and the methyl bond fission (blue). 72

Figure 4.7: Percentage (%) of the total maximum peak signal height as a function of temperature is shown for significant mass values from 4MCHe spectra (IE= 8.91 ± 0.01 eV [35]). *Top:* major species. *Bottom:* minor species. The presence of dissociative ionization is detected in the 10.487 eV by the presence of m/z 81 at room temperature. PIMS spectra from all three laser intensities used in this work can be found in the Appendix C4. C_{13} peaks of the fuel (m/z 97) and 1,3-butadiene (m/z 55) were left out of the figure for clarity. 73

Figure 4.8: Potential energy surface of the unimolecular decomposition of 1MCHe including the bond dissociation pathways and the concerted retro-Diels-Alder (r-DA) route. The energies are calculated at the CCSD(T)/cc-pV∞Z//M06-2X/cc-pVTZ level of theory and reported in kcal/mol relative to the parent molecule. Solid lines (red) are active and dashed lines (black) are inactive pathways under our experimental conditions (T=300-1500 K, P≅0.1 atm) according to our rate constant calculations. Branching ratio plots of the decomposition rates can be found in Figure 4.9. 76

Figure 4.9: Theoretically calculated rate constants (left) and branching ratios (right) for 3MCHe pyrolysis including bond fissions and the retro-Diels-Alder reaction. Radical names in the legend are the same used in the PES in Figure 4.8. The two active reactions are the concerted retro-Diels-Alder reaction (black) and the methyl bond fission (blue). 77

Figure 4.10: Percentage (%) of the total maximum peak signal height as a function of temperature is shown for significant mass values from 3MCHe spectra (IE= 8.89 ± 0.01 eV [35]). *Top:* major species. *Bottom:* minor species. The presence of dissociative ionization is detected in the 10.487 eV by the presence of m/z 81 at room temperature. PIMS spectra from all three laser intensities used in this work can be found in the Appendix C4. C_{13} peaks of the fuel (m/z 97) and 1,3-pentadiene (m/z 69) were left out of the figure for clarity. 78

Figure 4.11: Branching ratio for calculated rates of 2-cyclohexenyl radical unimolecular decomposition at P=0.1 atm with He as the collider. 82

Figure 4.12: Summary and comparison of the main soot precursors producing pathways for each isomer of methylcyclohexene.Species fall into color-coded bins corresponding to the wall temperature at which they are formed: blue: $T_{wall} < 800$ K, yellow: 800 K $\leq T_{wall} \leq$ 1100 K, red: $T_{wall} >$ 1100 K. As discussed, the centerline gas temperature is ~100 K lower than the measured wall temperature of the reactor [26]..... 85

Figure 5.1: PIMS of 0.1% Dimethoxymethane in He in the micro-reactor at 200 SCCM heated from 300 to 1700 K and ionized by 118.2 nm (10.487 eV) photons 104

Figure 5.2: PIMS of 0.1% 2,4,6 Trioxanonane in He in the micro-reactor at 200 SCCM heated from 300 to 1700 K and ionized by 118.2 nm (10.487 eV) photons 106

Figure 5.3: PIMS of 0.1% 2,4,6,8 Tetraoxanonane in He in the micro-reactor at 200 SCCM heated from 300 to 1800 K and ionized by 118.2 nm (10.487 eV) photons 108

Figure 5.4: BDEs (kcal/mol) for three POM-E molecules 112

Figure 5.5: Comparison of BDEs (kcal/mol) for three POM-E molecules..... 113

Figure 5.6: Potential energy surface (PES) of important unimolecular reactions involved during the initial phase of pyrolysis of $CH_3OCH_2OCH_3$ 115

Figure 5.7: Potential energy surface (PES) of important unimolecular reactions involved during the initial phase of pyrolysis of $CH_3OCH_2OCH_2OCH_3$ (n=2)..... 115

Figure 5.8: Potential energy surface (PES) of important unimolecular reactions involved during the initial phase of pyrolysis of $CH_3OCH_2OCH_2OCH_2OCH_3$ (n=3) 116

Figure 5.9: Molecular structures of TS involved in Pathway 3 for all three POM-E molecules (n=1-3) 118

Figure 5.10: Temperature (T) dependent rate constants (k) for reactions involved in Pathway 2 and Pathway 3 at pressure, P =10 atm 119

Figure 5.11: Comparison of QM calculated rate constant in this study with existing literature 120

Figure 5.12: Comparison of QM calculated BRs in this study with existing literature..... 121

Figure 5.13: Branching ratio plots for three different POM-E molecules (n=1-3) at pressure, P=10 atm..... 123

Figure 5.14: Temperature (T) dependent total rate constants (k_total) for three different POM-E molecules (n=1-3) at pressure, P=10 atm. 124

Figure 5.15: PIMS of 0.1% diethoxymethane in He in the micro-reactor at 200 SCCM heated from 300 to 1800 K and ionized by 118.2 nm (10.487 eV) photons..... 127

Figure 5.16: PIMS of 0.1% dipropoxymethane in He in the micro-reactor at 200 SCCM heated from 300 to 1700 K and ionized by 118.2 nm (10.487 eV) photons 129

Figure 5.17: Bond Dissociation Energies of diethoxymethane and dipropoxymethane..... 130

Figure 5.18: Rates of thermal decomposition for diethoxymethane as a function of temperature at 1 atm pressure 131

Figure 5.19: Branching ratio for the primary routes of decomposition of diethoxymethane as a function of temperature at 1 atm. 132

Figure 5.20: Rates of thermal decomposition for dipropoxymethane as a function of temperature at 1 atm..... 133

Figure 5.21: Branching ratio for the primary routes of decomposition of dipropoxymethane as a function of temperature at 1 atm. 133

Figure 5.22: (left) Rate comparison of the significant secondary decomposition routes of $[O](CH_2O)nCH_3$; (right) Branching ratio plot of the different secondary decomposition routes $[O](CH_2O)nCH_3$..... 135

Figure 5.23: Potential Energy Surfaces (PES) for the decomposition of oxygen-containing radical formed by the decomposition of 2,4,6 trioxahpetane (M-2-M) 137

Figure 5.24: Potential Energy Surfaces (PES) for the decomposition of oxygen-containing radical formed by the decomposition of 2,4,6 tetraoxanonane (M-3-M) 137

Figure 6.1: Simulated centerline pressure (left) and temperature (right) profiles for a 280 sccm continuous flow of helium along the length of a 2.5 cm reactor (0.66 mm i.d.) as a function of wall temperature (Tw) [1]. The electrodes for resistive heating are placed at 1 cm and 2.4 cm (adapted from [3])..... 146

Figure 6.2: Simulated centerline velocity profile for a 280 sccm continuous flow of He along the length of a 2.5 cm reactor (0.66 mm i.d.) at Tw = 1500 K [49]. The electrodes for resistive heating are placed at 1 cm and 2.4 cm. (adapted from [3]) 147

Figure 6.3: Redesigned reactor structure diagram (adapted from [4])..... 150

Figure 6.4: Centerline pressure distribution for various choke diameters d.(adapted from [4]) 153

Figure 6.5: Redesigned reactor structure with a single converging section 154

Figure 6.6: Central line Mach number distribution along the reactor length for various choke diameters, d.(adapted from [4]) 154

Figure 6.7: Centerline temperature and Knudsen number distribution along with the reactor of both redesigned micro-reactor and original “Chen nozzle” (adapted from [4]) 156

Figure 6.8: A photo and structure diagram of the novel reactor prototype (adapted from [4]) .. 157

Figure 7.1: The CAD rendering of the redesigned reactor shows a step nozzle (left) and a tapered nozzle (right). 160

Figure 7.2: CAD rendering of a section view of the target reactor geometry featuring internal taper from 1 mm to 0.500 mm 163

Figure 7.3: Process flow for creating microreactor geometry. (A) Creation of a digital tool geometry applying the principles of design for manufacturability and tailored for production using both polymer additive manufacturing (Stereolithography) and metal additive manufacturing (Direct metal laser sintering). (B) A specialized raw material composition custom-made using a spray drying process for compaction. (C) Casting and isostatic pressing are two compaction methods chosen for their compatibility with the final geometry and precursor composition. (D) The component post-compaction is in a 'green state'. (E) Pyrolysis is carried out in a Lindberg M Blue Retort at 650°C. (F) Final component sintering is completed in a Thermal Technology

Furnace Model 1000-3560-FP24 at 2150°C. (G) Component post-processing is completed to finish edge surfaces and verify hole dimensions. 164

Figure 7.4: Casting tooling assembly with components labeled in the order of assembly (A) Stainless steel mandrel produced using DMLS. (B)Primary split casting block made with Watershed XC 11122 using SLA featuring location pips. (C) Secondary casting block made using ABS and SLA. (D) Support jacket made using Watershed XC 11122 and SLA used to stabilize the setup. (E) Watershed XC 11122 lid to seal the assembly and prevent contaminant entry. 169

Figure 7.5: Additively manufactured tooling components to produce isopressing mold bags. (A) Mold mast produced using WaterShed XC 11122 and SLA 3D printing. (B) Mold jacket produced using WaterShed XC 11122 and SLA 3D printing..... 171

Figure 7.6: Isopressing tooling assembly with components labeled in the order of assembly. (A) Stainless steel mandrel produced using DMLS. (B)Iospressing jacket made of polyurethane cast in-house. (C) Support jacket made using WaterShed XC 11122 and printed using SLA. (D) Perforated jacket was made using WaterShed XC 11122 and SLA was used to stabilize the pressure application on the setup. (E) Polyurethane lid to seal the assembly and prevent contaminant entry. 173

Figure 7.7: CAD renderings of the geometry of the mandrel highlighting the changing geometry with the evolution of process capabilities (left: oldest, right: newest) 175

Figure 7.8: Modulus of rupture tests carried out on cast rod samples of different silicon carbide grades. The material used in this process is Calix High Strength 2, and the material used in the tube reactor is Hexoloy. 181

Figure 7.9: X-ray diffraction results for material used to manufacture the tube reactor (in red) and the material used to manufacture the nozzle reactor (blue). 182

Figure 7.10: Composite Micro Contrast Tomography (Micro-CT) showing a section view of the reactor produced using the technique described in this work. (nozzle reactor, left and tube reactor, right)..... 183

Figure 7.11: Scanning Electron Microscope (SEM) images at 1000X showing internal defects in the tube reactor (left) as compared to the reactor (right) produced using the technique described in this work. 183

Figure 7.12: Optical microscope images at 50 X zoom showing the tube reactor (left) and the reactor produced using the process (right) described in this work. 184

Figure 7.13: Cyclohexene decomposition reaction producing ethylene and 1,3 - butadiene 185

Figure 7.14: Ratio of the signal height of butadiene to cyclohexene versus temperature in the nozzle reactor as compared to the tube reactor 186

Figure 7.15: Image showing the tooling component featuring a helical thread produced using direct metal laser sintering with the inset image showing a rendering of the cross-section of the geometry fabricated using this tooling. B.) Silicon carbide SiC, alumina, and Yttria stabilized Zirconia reactor geometries fabricated using the method described in this work. 188

Figure 8.1: Typical pressure dependence of unimolecular reactions [2] 195

Figure 8.2: MESH geometry generated using SpaceClaim in ANSYS to model flow into the reactor geometry. Average mesh sizes at all regions outside of the reactor is 0.15 mm with the reactor mesh size at 0.01 mm 199

Figure 8.3: Comparison of pressure as a function of axial length between four nozzle reactor geometries evaluated P1650 (0.650 mm exit diameter), P1400 (0.400 mm exit diameter), P1300 (0.300 exit diameter) and P1200 (0.200 exit diameter) 201

Figure 8.4: Comparison of pressure as a function of axial length between the nozzle reactor geometry P1200 and the Chen reactor (tube configuration) 202

Figure 8.5: Comparison of velocity as a function of axial length between four nozzle reactor geometries evaluated P1650 (0.650 mm exit diameter), P1400 (0.400 mm exit diameter), P1300 (0.300 exit diameter) and P1200 (0.200 exit diameter) 203

Figure 8.6: Comparison of velocity as a function of axial length between the nozzle reactor geometry P1200 and the Chen reactor (tube configuration) 204

Figure 8.7: Variation of fluid residence time in the nozzle reactor as a function of the exit diameter (P1650 (0.650 mm exit diameter), P1400 (0.400 mm exit diameter), P1300 (0.300 exit diameter) and P1200 (0.200 exit diameter) 205

Figure 8.8: PIMS of 0.1% anisole in He in the Chen micro-reactor at 200 SCCM heated from 300 to 1800 K and ionized by 118.2 nm (10.487 eV) photons 213

Figure 8.9: PIMS of 0.1% anisole in He in the P1650 nozzle micro-reactor at 200 SCCM heated from 300 to 1800 K and ionized by 118.2 nm (10.487 eV) photons 214

Figure 8.10: Normalized signal height for the decomposition of 0.1% anisole as a function of temperature in the Chen reactor (on the left) and the P1650 nozzle reactor (on the right) 215

Figure 8.11: PIMS of 0.05% anisole in He in the Chen micro-reactor at 200 SCCM heated from 300 to 1800 K and ionized by 118.2 nm (10.487 eV) photons 216

Figure 8.12: PIMS of 0.05% anisole in He in the P1650 nozzle micro-reactor at 200 SCCM heated from 300 to 1800 K and ionized by 118.2 nm (10.487 eV) photons 217

Figure 8.13: Normalized signal height for the decomposition of 0.05% anisole as a function of temperature in the Chen reactor (on the left) and the P1650 nozzle reactor (on the right) 218

Figure 8.14: PIMS of 0.025% anisole in He in the Chen micro-reactor at 200 SCCM heated from 300 to 1800 K and ionized by 118.2 nm (10.487 eV) photons 219

Figure 8.15: PIMS of 0.025% anisole in He in the P1650 nozzle micro-reactor at 200 SCCM heated from 300 to 1800 K and ionized by 118.2 nm (10.487 eV) photons 220

Figure 8.16: Normalized signal height for the decomposition of 0.025% anisole as a function of temperature in the Chen reactor (on the left) and the P1650 nozzle reactor (on the right) 221

Figure 8.17: PIMS of 0.025% anisole in He in the P1400 nozzle micro-reactor at 200 SCCM heated from 300 to 1800 K and ionized by 118.2 nm (10.487 eV) photons 222

Figure 8.18: Normalized signal height for the decomposition of 0.025% anisole as a function of temperature in the P1400 nozzle reactor (on the right)..... 223

Figure 8.19: PIMS of 0.1% d3-anisole in He in the Chen micro-reactor at 200 SCCM heated from 300 to 1800 K and ionized by 118.2 nm (10.487 eV) photons 224

Figure 8.20: PIMS of 0.1% d3-anisole in He in the P1650 nozzle micro-reactor at 200 SCCM heated from 300 to 1800 K and ionized by 118.2 nm (10.487 eV) photons..... 225

Figure 8.21: PIMS of 0.1% d8-anisole in He in the Chen micro-reactor at 200 SCCM heated from 300 to 1800 K and ionized by 118.2 nm (10.487 eV) photons 226

Figure 8.22: PIMS of 0.1% d8-anisole in He in the P1650 nozzle micro-reactor at 200 SCCM heated from 300 to 1800 K and ionized by 118.2 nm (10.487 eV) photons..... 227

Figure 8.23: PIMS of 0.025% furan in He in the Chen reactor at 200 SCCM heated from 300 to 1700 K and ionized by 118.2 nm (10.487 eV) photons 236

Figure 8.24: PIMS of 0.025% furan in He in the P1650 nozzle micro-reactor at 200 SCCM heated from 300 to 1700 K and ionized by 118.2 nm (10.487 eV) photons 237

Figure 8.25: PIMS of 0.025% furan in He in the P1400 nozzle micro-reactor at 200 SCCM heated from 300 to 1700 K and ionized by 118.2 nm (10.487 eV) photons 238

Figure 8.26: PIMS of 0.025% furan in He in the P1400 nozzle micro-reactor at 200 SCCM heated from 300 to 1700 K and ionized by 118.2 nm (10.487 eV) photons 239

Figure 8.27: Ratio of products measured at 10.487 eV from the α-carbene (m/z 42, ketene) relative to the β-carbene (propargyl, m/z 39 and propyne, m/z 40) as a function of changing reactor exit diameter (and indirectly pressure) 240

Figure 9.1: Alumina nozzle reactor inside a SiC heating jacket. The upright geometry is shown with two graphite heating disks mounted in a specially designed MACOR collet. 251

Figure 9.2: The experimental geometry for X-ray studies of Kr fluorescent tags in the nozzle micro-reactor 253

LIST OF TABLES

Table 5.1: Barriers (kcal/mol) of important unimolecular reactions involved during the initial phase of pyrolysis of three different POM-E molecules (n=1, 2, 3)……..114

Table 8.1: Summary of the prototype reactor dimensions utilized as part of the micro-reactor validation studies……..198

Chapter 1: Mobility in the Global Energy Context

1.1 World energy outlook

Energy is among the most critical factors influencing economic and industrial development. Today, the combustion of fossil fuels accounts for more than two-thirds of the world's primary energy utilization [1]. Projections for the next two decades assume the continued leading role of fossil fuel-based energy, with a global share of about 30% of primary energy to be utilized in Asia, mainly China and India [1]. The growing global population, the increasing mobility of that population, the rising production and consumption of goods, and the movement of those goods are considerable concerns in future energy strategies. The need for clean, sustainable, and affordable energy sources starkly contrasts the environmental and health issues connected with fossil fuel use. While alternatives to coal, petroleum, and natural gas have been implemented or are being discussed for power generation (e.g., hydroelectricity and nuclear, solar, wind), transportation of people and goods depends on the availability of high-density energy sources, primarily delivered to the market today as liquid fuels derived from petroleum [2].

1.1.1 Emissions

The need to develop an alternative to fossil fuels is not only motivated by its reduced availability and increasing cost. The emissions produced by burning these fuels have been of concern ecologically and environmentally. It has been at the center of multiple health and ecological debates since the 1970s [3]. Figure 1.1 presents the contribution to global greenhouse gases by energy sources. Among the causes of alarm are the effects of nitrogen dioxide (NO_2). This is one of the most observed oxides of nitrogen, which react in the upper atmosphere to form

ozone, causing acid rain. Extensive medical research has shown that even relatively small concentrations of these molecules can lead to catastrophic effects like pulmonary edema [4], [5]. Particulate matter, a mixture of fine solid and liquid contaminants, has been linked to heart-related conditions and cancer [6]. Another pollutant identified as highly damaging is CO_2 [7]. The exact environmental consequences of massive anthropogenic CO_2 emissions are currently uncertain. We do know, however, that CO_2 is a strong infrared absorber. This means that when sunlight hits CO_2, its temperature quickly rises, unlike N_2, which composes over 70% of our atmosphere and is inactive in infrared. These factors and the need to secure global energy availability mandate research into alternative sustainable energy sources essential.

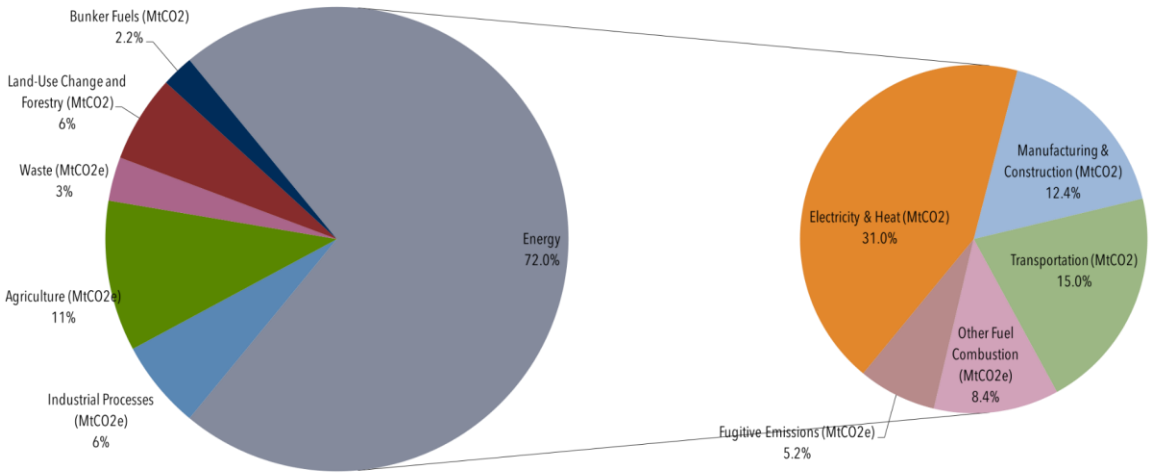

Figure 1.1: Global sources of greenhouse gases with energy contributing over 70% of the total emissions of concern [8]

1.1.2 Combustion and mobility

The scarcity and cost associated with continued dependence on fossil fuels and the ecological and environmental impact have resulted in stringent regulations limiting its use in next-generation vehicles [9]. Since transforming alternative energy sources for mobility and transport is especially difficult, energy-efficient, clean combustion processes remain an essential research

topic. Despite increasing electrification in some areas, the transportation sector is largely powered by combustion. Solar and hydrogen-powered vehicles are carbon-neutral solutions capable of replacing fossil fuel-powered vehicles; however, affordable consumer options are still being developed. The lack of an integrated, easily accessible recharging network has further delayed the widespread adoption of electric vehicles. High-energy-density energy carriers such as today's liquid fuels are advantageous, especially for long-distance and heavy-duty transportation, marine applications, and aviation. Combustion systems for these purposes are harder to replace than in personal vehicles.

Understanding combustion becomes even more important with the focus on optimizing the available fossil fuel reserves and developing technology for compatibility with alternative fuels. A systematic approach to evaluating combustion behavior demands chemical knowledge. Combustion systems can be described, tailored, and improved by considering chemical knowledge. Combining theory, experiment, model development, simulation, and systematic analysis of uncertainties enables qualitative or even quantitative predictions for many combustion situations of practical relevance. The joint optimization of fuel and propulsion systems can exploit the potential of efficient, ultra-low-emission combustion using renewably made fuels or fuel additives. Chemistry knowledge is needed to tailor their combustion properties and understand the influence of their molecular structure on their reaction mechanisms for current and advanced combustion conditions, as well as to determine efficient pathways to make such fuels sustainably and on a large scale. The advances in the development of engine combustion systems, such as homogeneous charge compression ignition (HCCI) [10], [11] or related designs that are compatible with a variety of fuels, have made the use of biofuels as alternative neat fuels or fuel additives possible[12]–[15]. Energy independence, possible decreases in CO_2, soot, unburned hydrocarbon

emissions, and other factors are driving this possibility for transformation. These biomass-related fuel sources are important topics of discussion and research for powering next-generation mobility.

1.2 Evaluating combustion chemistry

Chemistry and combustion are interlinked in multiple ways. The result of a combustion event in terms of the energy and material balance for the delivery of useful work and harmful emissions is heavily dependent on the fuels' molecular structure and thermodynamic conditions [24]. In a standard internal combustion engine (I.C.E.), chemistry is initiated either by compression ignition or spark ignition following a considerable temperature and pressure spike, at which time fuel is ignited. This ignition releases a cascade of highly reactive species called radicals, or chemical species possessing unpaired electrons. Also present in the engine will be short-lived products that are thermally unstable, called metastables, which will rapidly decompose to radicals or more stable species. Radicals initiate the remaining chemistry, reacting with the starting material, oxygen, each other, and other intermediates. The final products are exhausted from the engine within a few milliseconds, and the process immediately restarts. Enormous research efforts have been applied to understand these combustion processes of hydrocarbon fuels. However, most biofuels (like Oxy-Methylene Ethers O.M.E.s) include an oxygen-containing group in addition to the standard hydrogen and carbon found in fossil fuels. Adding this oxygen group changes the fundamental behavior of these molecules within an engine environment altering the rate and likely locations for decomposition [16], [17]. The number and location of the oxygen atoms in the molecule can affect parameters such as sooting, ignition tendency, and performance. With all suggested alternative fuels, fundamental knowledge of their combustion properties is needed, including ignition and extinction characteristics, flame development, combustion speciation, and emissions, most of which may depend sensitively on the fuel's chemical composition and the

molecular nature of its compounds. Further, to address globally relevant emission-specific questions, combustion science and, in particular, chemistry and diagnostics can contribute specific insight into the management and reduction of harmful effluents.

1.2.1 Experimental methods

A quantitative description of these chemical processes is essential to develop efficient, low-emission combustion devices. Experimental observation through diagnostics of laboratory combustion systems is crucial to developing and validating chemical kinetic models. Multiple parameters characterize the combustion state and its development along with the reaction progress, including temperature, pressure, density, velocity, mixing status, species composition, reactivity, heat release, and others, many of which can be experimentally determined. Specifically designed laboratory experiments permit access to information such as ignition delay time, flame speed, flame structure, autoignition and extinction behavior, reactive species identification, their relative or absolute concentrations, and occurrence of specific chemical reactions as a function of boundary conditions and the fuel's molecular structure.[18] Historically, probing the nature and concentration of species has usually been carried out using optical spectroscopy, gas chromatography (G.C.), and/or mass spectrometry (M.S.). Laser diagnostic experiments in particular, have proved vital in the field of combustion to probe the processes of combustion and the products generated by it [19]–[22]. The emphasis here is on non-intrusive measurements of molecular parameters with a good spatial resolution that provides insight into rates and mechanisms of combustion reactions. Micro-reactors find application as the medium in which flash pyrolysis (combustion in the absence of oxygen) of fuels can be carried out. When combined with sensitive diagnostic techniques, these devices can probe the fundamental chemistry of a range of fuels and fuel surrogates. These techniques are designed to probe the products of pyrolysis

produced during a residence time of 100 -125μs. This makes the reactors ideally suited for use in infrared spectroscopy (I.R.) and photoionization mass spectroscopy (PIMS) setups. This system allows for the evaluation of atoms, radical, metastable, and stable species without the products of any secondary reactions affecting the results. The insight gained from such partly idealized systems can serve to develop, advance, and validate transferable combustion chemistry models that bridge fundamental chemical knowledge and practical systems behavior.

1.2.1.1 Materials and manufacturing for experimentation

The requirement of high-fidelity experimental methods and diagnostic strategies has constantly pushed the boundaries of the materials and manufacturing methods involved in these techniques. Computational design and manufacturing methods have increasingly been applied to develop tools that can simulate in-engine processes with greater accuracy. The capability to produce experimental devices featuring intricate shapes at higher speeds and with greater tunability has been key to extending the capabilities of existing diagnostics to more complex systems. Digital manufacturing and 3D printing are examples of relatively new processing methods being applied to combustion devices and experimentation. These fabrication processes allow experimentalists to develop unique instruments customized to answer specific problems encountered in the experimental setup. These techniques can significantly reduce hardware costs, shorten fabrication lead times, increase reliability by reducing the number of components, and improve hardware performance by allowing the fabrication of designs not feasible by conventional means alone. This thesis describes one such novel manufacturing method which can be used to create tailored experimental devices reliably, repeatedly, and with extremely small features (<100 μm) to probe fundamental combustion chemistry.

1.2.2 Computational methods

A complementary focus of combustion research is on developing a predictive understanding of various combustion processes through chemical kinetic modeling [23]. Chemical kinetics is a field that attempts to understand and predict the rates of chemical reactions. The presence of many species and reactions had limited the application of these methods due to numerical calculations being both time and cost-intensive. With the recent advances in computational power, it is now possible to automate most of these calculations to produce comprehensive mechanisms featuring more than tens of thousands of reactions. It is possible to develop comprehensive models of molecule behavior by utilizing these methods and applying experimental results as a real-world check.

1.2.3 Pyrolysis and oxidation chemistry

Complete discernment of a molecule's combustion chemistry can be a formidable challenge, especially if multiple element types and numbers are involved. To help focus resources, studies explore combustion under certain conditions (temperature, pressure, and equivalence ratios), or confine themselves to specific reaction types. Providing insight into a fuel's unimolecular decomposition and oxidation chemistry are two evaluations from which an approximation of the overall combustion behavior of a molecule can be discerned. These two subtypes of reactions require a synergistic approach between experimental measurements and computational modeling to fully develop useful mechanisms.

The ability to observe the first 25-150 microseconds of pyrolysis is critical to obtaining information on how a molecule might decompose inside a hot engine in the absence of oxygen. The extension of experimental techniques to study oxidation reactions is being carried out in parallel with the application of robust computational models. This complementary experimental-

theoretical approach can extend the insight obtained from pyrolysis and oxidation studies to more complex combustion reactions. These methods explore the impact of individual bond strengths and the presence of oxygen in the molecule. Together they can be evaluated to produce an accurate mechanism that can be leveraged to develop sustainable, efficient propulsion technologies.

1.3 Thesis outline

A combined approach of experimental techniques and theoretical calculations is used to evaluate promising fuel additives and characterize existing fuels. Detailed mechanisms to describe these molecules' combustion behavior are developed using these methods. This thesis aims to describe enhancements to the geometry of the microreactor used in laser diagnostics, specifically in the Photoionization Mass Spectrometry (PIMS) apparatus. The updates made to the microreactor geometry augment its accuracy in simulating combustion phenomena when used in conjunction with laser diagnostic experiments. The improvements made to the experimental capabilities required creating a novel manufacturing process. This digital manufacturing method enabled the production of ceramic geometries at a scale and feature detail not previously possible with silicon carbide.

Chapter 2 begins with a review of mass spectroscopy and laser diagnostics in combustion. This is followed by a detailed description of PIMS and Fourier Transform Infrared (FTIR) experimental setups and changes made to the apparatus to be compatible with the new microreactor geometry. The operation of the experimental apparatus in the pulsed and continuous configurations is presented. Integration of an optical temperature measurement system is described. Operation with a fixed wavelength energy source is explained, and a prototype tunable energy source developed at C.U. Boulder is detailed.

Chapter 3 details a brief overview of the computational workflow developed for characterizing the thermal decomposition of different organic molecules. The method combines results from the experimental evaluations described in chapter 2 with numerical models featuring electronic structure theory. The process of producing rate constants which can then be used to build comprehensive chemical kinetic mechanisms, is outlined.

Chapter 4 presents an application of the combined experimental and theoretical workflow described in the previous two chapters to compare the pyrolysis of three isomers of methylcyclohexene (1-methyl-1-cyclohexene, 3-methyl-1-cyclohexene, and 4-methyl-1-cyclohexene). Identifiable differences in the sooting behavior of the three isomers of methylcyclohexene have been observed despite only subtle differences in their molecular structures. Thus, an in-depth understanding of their pyrolysis chemistry can help link specific structural features, like double bond location, to differences in soot precursor formation ability. This presents a unique opportunity to apply the PIMS experimental setup with a fixed and tunable ionization source. Findings from this work showed that the active bond fission routes for 3-methyl-1-cyclohexene present pathways to directly form unsaturated rings such as cyclopentadiene and benzene, both known soot precursors. This ability to directly form these large unsaturated rings helps explain this particular isomer's higher sooting propensity.

Chapter 5 reviews the application of this combinatorial approach to a class of oxygenated molecules - Poly Oxy-Methylene Ethers (POM-E). A selection of POM-E molecules with varying end groups and the number of functional (CH_2-O) groups are assessed. The energies and other calculated properties are used to calculate pressure and temperature-dependent reaction rate constants across various conditions. These reaction rates are assembled along with thermochemistry and transport properties (when applicable) into detailed sub-mechanisms that can

be coupled with existing core mechanisms. The resulting mechanisms are validated against available experimental data to help confirm their predictive ability.

Chapter 6 begins by examining the challenges involved with using the existing microreactor geometry and material. Computational Fluid Dynamics (C.F.D.) calculations which were used to identify modifications are outlined. Theoretical advantages of the new design are described along with details of a prototype reactor manufactured for preliminary evaluation.

Chapter 7 details the novel hybrid digital manufacturing method developed to produce the redesigned microreactor. The synergy produced by combining digital tooling manufacturing and conventional ceramics processing is highlighted by the fabrication of a monolithic silicon carbide microreactor geometry featuring an internal taper. Characterization studies of the new microreactor are presented to highlight the improvements made. The extension of this manufacturing technique to produce a range of reactor geometries is presented along with the ability to create other similar high aspect ratio geometries. The capabilities of the new microreactor for evaluating the thermal decomposition of molecules are showcased with experimental validation using cyclohexene.

Chapter 8 documents validation studies carried out to establish the performance of the nozzle reactor in the PIMS setup. A range of microreactors featuring exit diameters ranging from 0.600 mm to 0.200 mm to understand their impact on pyrolysis chemistry. Molecules were evaluated to understand the effect of raising the internal fluid flow pressure and residence time on the thermal decomposition behavior. The molecules chosen were – anisole, toluene, ethyl benzene, iso-octane, and furan. The results from these evaluations demonstrate either the presence of new decomposition products previously inaccessible in the Chen-style tubular reactor [25] or increased intensities of products being formed at relatively lower temperatures. These results demonstrate

how the presence of a constriction in the micro-reactor environment produces a larger region of sustained pressure and temperature distribution. This affects the rate at which these molecules decompose, resulting in a more realistic approximation of pressure on the thermal decomposition process. In addition to understanding the effect of varying the pressure inside the reactor geometry – experiments were also carried out with alternate reactor materials – alumina and yttria-stabilized zirconia. These experiments were used to understand the effect of wall reactions and material dependence on the pyrolysis reaction.

The beginning of Chapter 9 summarizes the research efforts completed as part of this thesis. This is followed by an overview of ongoing and future avenues of research now accessible thanks to the developments made in experimental, design, manufacturing, and computational capabilities in this work. The ability of the hybrid manufacturing method to produce micro-reactor geometries of alternate ceramics presents the opportunity to study oxidation chemistry combined with laser diagnostics. Application of the SiC nozzle micro-reactor suite to investigate the pressure dependence of ignition chemistry for an extreme case: aircraft turbine flameout and re-light. This project aims to obtain a fundamental understanding of the chemical mechanism for the ignition of jet fuel to assist in the design of novel post-flameout ignition technology by identifying how the chemical pathways for ignition differ at takeoff and flameout conditions. Experimental characterization studies of flow phenomena inside the micro-reactor are proposed in collaboration with the Advanced Photon Source (A.P.S.). A series of experiments involving X-ray fluorescence and X-ray absorption at the A.P.S. is suggested to compare the performance of these new micro-reactors to the standard tube reactor geometry.

1.4 References

[1] IEA (2022), World Energy Outlook 2022, IEA, Paris https://www.iea.org/reports/world-energy-outlook-2022, License: CC BY 4.0 (report); CC BY NC SA 4.0 (Annex A)

[2] IEA (2020), Key World Energy Statistics 2020, IEA, Paris https://www.iea.org/reports/key-world-energy-statistics-2020, License: CC BY 4.0

[3] O. US EPA, "Evolution of the Clean Air Act," May 29, 2015. https://www.epa.gov/clean-air-act-overview/evolution-clean-air-act (accessed Dec. 26, 2021).

[4] G. Freeman and G. B. Haydon, "Emphysema After Low-Level Exposure to NO2," *Arch. Environ. Health Int. J.*, vol. 8, no. 1, pp. 125–128, Jan. 1964, doi: 10.1080/00039896.1964.10663640.

[5] H. E. Stokinger, "Ozone Toxicology," *Arch. Environ. Health Int. J.*, vol. 10, no. 5, pp. 719–731, May 1965, doi: 10.1080/00039896.1965.10664082.

[6] Z. Zhang, W. Yan, Q. Chen, N. Zhou, and Y. Xu, "The relationship between exposure to particulate matter and breast cancer incidence and mortality," *Medicine (Baltimore)*, vol. 98, no. 50, p. e18349, Dec. 2019, doi: 10.1097/MD.0000000000018349.

[7] "Irreversible climate change due to carbon dioxide emissions | PNAS." https://www.pnas.org/content/106/6/1704?sid4fdad7e-23ad-4d54-a3c6-75041ad31328 (accessed Dec. 26, 2021).

[8] Climate Analysis Indicators Tool (CAIT), Climate Data Explorer, World Resources Institute, Washington DC, USA. Data for the Year 2017

[9] PAPO. US EPA, "Regulations for Greenhouse Gas Emissions from Passenger Cars and Trucks," Sep. 09, 2016. https://www.epa.gov/regulations-emissions-vehicles-and-engines/regulations-greenhouse-gas-emissions-passenger-cars-and (accessed Dec. 26, 2021).

[10] S. Onishi, S. H. Jo, K. Shoda, P. D. Jo, and S. Kato, "Active Thermo-Atmosphere Combustion (ATAC) — A New Combustion Process for Internal Combustion Engines," *S.A.E. Trans.*, vol. 88, pp. 1851–1860, 1979.

[11] M. Noguchi, Y. Tanaka, T. Tanaka, and Y. Takeuchi, "A Study on Gasoline Engine Combustion by Observation of Intermediate Reactive Products during Combustion," *S.A.E. Trans.*, vol. 88, pp. 2816–2828, 1979.

[12] L. Wright, B. Boundy, B. Perlack, S. Davis, and B. Saulsbury, "Biomass Energy Data Book, Volume 1," p. 189.

[13] A. Demirbas, “Progress and recent trends in biofuels,” *Prog. Energy Combust. Sci.*, vol. 33, no. 1, pp. 1–18, Feb. 2007, doi: 10.1016/j.pecs.2006.06.001.

[14] R. Luque *et al.*, “Biofuels: a technological perspective,” *Energy Environ. Sci.*, vol. 1, no. 5, p. 542, 2008, doi: 10.1039/b807094f.

[15] A. K. Agarwal, “Biofuels (alcohols and biodiesel) applications as fuels for internal combustion engines,” *Prog. Energy Combust. Sci.*, vol. 33, no. 3, pp. 233–271, Jun. 2007, doi: 10.1016/j.pecs.2006.08.003.

[16] C. K. Westbrook, “Biofuels Combustion,” *Annu. Rev. Phys. Chem.*, vol. 64, no. 1, pp. 201–219, 2013, doi: 10.1146/annurev-physchem-040412-110009.

[17] K. Kohse-Höinghaus *et al.*, “Biofuel Combustion Chemistry: From Ethanol to Biodiesel,” *Angew. Chem. Int. Ed.*, vol. 49, no. 21, pp. 3572–3597, 2010, doi: 10.1002/anie.200905335.

[18] F. Qi, “Combustion chemistry probed by synchrotron V.U.V. photoionization mass spectrometry,” *Proc. Combust. Inst.*, vol. 34, no. 1, pp. 33–63, Jan. 2013, doi: 10.1016/j.proci.2012.09.002.

[19] M. A. Bolshov, Yu. A. Kuritsyn, and Yu. V. Romanovskii, “Tunable diode laser spectroscopy as a technique for combustion diagnostics,” *Spectrochim. Acta Part B At. Spectrosc.*, vol. 106, pp. 45–66, Apr. 2015, doi: 10.1016/j.sab.2015.01.010.

[20] A. Ehn, J. Zhu, X. Li, and J. Kiefer, “Advanced Laser-Based Techniques for Gas-Phase Diagnostics in Combustion and Aerospace Engineering,” *Appl. Spectrosc.*, vol. 71, no. 3, pp. 341–366, Mar. 2017, doi: 10.1177/0003702817690161.

[21] S. S. Penner, C. P. Wang, and M. Y. Bahadori, “Laser diagnostics applied to combustion systems,” *Symp. Int. Combust.*, vol. 20, no. 1, pp. 1149–1176, Jan. 1985, doi: 10.1016/S0082-0784(85)80605-6.

[22] S. H. Chung, “Several applications of laser diagnostics for visualization of combustion phenomena,” *J. Vis.*, vol. 6, no. 2, pp. 95–106, Jun. 2003, doi: 10.1007/BF03181614.

[23] S. J. Klippenstein, “From theoretical reaction dynamics to chemical modeling of combustion,” *Proc. Combust. Inst.*, vol. 36, no. 1, pp. 77–111, Jan. 2017, doi: 10.1016/j.proci.2016.07.100.

[24] K. Kohse-Höinghaus, Combustion in the future: The importance of chemistry, Proceedings of the Combustion Institute, https://doi.org/10.1016/j.proci.2020.06.375

[25] P. Chen, S. D. Colson, W. A. Chupka, and J. A. Berson, “Flash pyrolytic production of rotationally cold free radicals in a supersonic jet. Resonant multiphoton spectrum of the 3p2A2" .rarw. X2A2" origin band of methyl,” J. Phys. Chem., vol. 90, no. 11, pp. 2319–2321, May 1986, doi: 10.1021/j100402a014.

Chapter 2: Experimental Methods to Elucidate Combustion Chemistry

2.1 Introduction

Combustion chemistry is inherently challenging to study, particularly due to the large number of species and reactions involved. High temperatures and fast kinetics add further difficulty in experimentally probing elementary reactions. A detailed understanding of combustion chemistry requires experimental information from the reactive system. Pyrolysis is among the different classes of chemical reactions essential to describe combustion fully. Fuel decomposition under high-temperature conditions and no oxygen is termed pyrolysis or thermal decomposition. The ubiquitous presence of pyrolysis across different fuel types, engine designs, and combustion strategies makes it a vital phenomenon to characterize. There are regimes of engine operation (both terrestrial and airborne) during which it is not possible to have a proportionate amount of fuel and oxidizer - resulting in fuel-rich situations.

Often multiple analytical methods are used in combination to probe fundamental combustion chemistry. Several different experiment types have been developed for studying pyrolysis and combustion chemistry to date, including static reactors[1], [2], flow reactors[3], [4], stirred reactors[5], [6], shock tubes[7], [8], rapid compression machines (RCM) [9], burner stabilized laminar flames [10], heated grid experiments, fluidized beds, and fixed beds. Each device and technique is suited for probing different facets of combustion. Comprehensive reactive species information essential for a deeper understanding of the reaction processes as a function of temperature, pressure, fuel–oxidizer mixture, reaction time, and other system variables are

revealed through mass spectrometry combined with flow reactors[11]. The following sections describe this technique's development, application, and components to study combustion.

2.1.1 Mass Spectrometry in Combustion

Mass spectrometry (MS) is an analytical technique that measures the mass-to-charge ratio of charged particles. It is used to determine the masses of particles for evaluating the elemental composition of a sample or molecule. The application of mass spectrometry as a characterization tool for combustion was pioneered almost 70 years ago by Eltenton [12]. In 1947 mass spectroscopy was applied to study decomposition by coupling a Dempster type mass-spectrometer to a reaction chamber with a specialized sampling method. This unique method later became the basis of molecular beam sampling. In 1951, Kantrowitz et al. [13] used theoretical calculations to demonstrate that a high-intensity molecular beam could be achieved with an appropriately designed apparatus [13]. These findings were then applied to evaluating ammonia[14] by Kistiakowsky and Slichter. Following these pioneering experiments, molecular beam spectroscopy was used to study the flames of basic hydrocarbons[15]– [19]. These initial experiments featured electron impact (EI) ionization as the technique to produce charged particles for detection. This ionization method involved intercepting a beam of molecules with a stream of electrons to produce charged particles that can be characterized.

2.1.2 Molecular Beam Mass Spectroscopy

A key component for high-resolution spectroscopic imaging is the molecular beam. Molecular beams are directed beams of neutral or charged molecules at such low pressures that the effects of molecular collisions are, for most purposes, negligible. Some of the earliest molecular bean experiments were by Dunoyer in 1913 [60], using a series of evacuated glass chambers to produce a beam of sodium. Succeeding this pioneering work were several experiments

made by Stern and Knauer [61], [62], which laid down the fundamental principles of molecular-beam techniques. Precision measurements of molecular, nuclear, and atomic properties began with the introduction of the molecular-beam resonance method by Rabi et al. [63],[64]. Originally applied to the measurement of nuclear magnetic moments, this was soon extended as a more general method for use in radiofrequency spectroscopy. Any molecular-beam setup aims to produce a collimated and uniform stream of particles (which can be both neutral or charged in the case of ions) for interception and characterization by a diagnostic tool. Typical molecular-beam systems (shown in Figure 2.1) consist of a reservoir with high-pressure gas, a small aperture in the reservoir, one or two skimmers to collimate the beam, and a vacuum chamber maintained at low pressures downstream. In supersonic molecular-beam experiments, a noble gas whose translational temperature can be lowered to an extremely small value is used as the carrier gas. This quenches any further reaction before an interception by the ionizing source. Other experiments require setting a temperature profile or limiting detection to a few species, but in molecular beam mass spectroscopy (MBMS) experiments, concentration profiles for molecular, radical, and atomic species and temperatures may be recorded in a free-standing collimated molecular beam.

An extensive review of MBMS for studying the fundamental chemistry of flames was published by Biordi [20] in 1977. Later work by several research groups [22]–[30] applied MBMS to probe combustion chemistry. These initial measurements set a baseline for developing and validating multiple chemical kinetic models. The primary disadvantage to working with electron impact ionization is the tendency to hard-ionize and the energy resolution of the ionizing electrons. This makes resolving isomers and products of similar mass extremely challenging [29]. Early studies of flames using mass spectrometry focused on direct observations of ions. More recent

advances in the free-radical theory of combustion particulate matter have shifted focus to characterizing radicals in molecular beams.

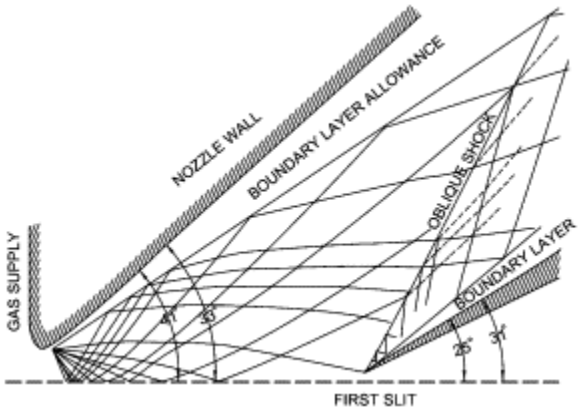

Figure 2.1: Schematic sketch of one-half of a nozzle and the first slit showing the various waves generated by the nozzle flow. The oblique shock has an initial angle of 38°, the maximum angle such a shock can negotiate at Mach 4. This design is intended

2.1.3 VUV Ionization Source

Synchrotron vacuum ultraviolet (SVUV) photoionization combined with MBMS, also called synchrotron VUV photoionization mass spectrometry (SVUV-PIMS), was first applied to low-pressure premixed laminar flame studies at the Advanced Light Source (ALS) [30], [31]. Benefiting from its operability and superior energy resolution, tunable VUV photoionization can minimize fragmentation interference, distinguish isomers, and detect radicals. It is a selective and sensitive ionization method making it ideal for probing molecules with low ionization energy. The application of SVUV-PIMS has achieved great success in combustion diagnostics, providing remarkable detection of combustion intermediates and identification of isomers [11]. Fixed wavelength photon sources also offer many of these advantages but are limited in their ability to resolve isomers.

The inherent challenges associated with a fixed wavelength ionization source can be offset using a complementary spectroscopy technique such as Matrix Fourier Transform Infrared Spectroscopy (Matrix FT-IR) [32]. As all polyatomic molecules possess diagnosable vibrational spectra, this technique can distinguish thermal products with identical mass. A similar molecular beam approach is used in place of instantaneous detection using a high-energy ionization source - characterization is accomplished by evaluating the vibrational frequencies generated by absorbing infrared light.

2.1.4 Micro-reactor

Used in conjunction with photoionization mass spectrometry and Matrix Fourier Transform Infrared Spectroscopy in the Labbe Lab, the micro-reactor acts as a medium for flash pyrolysis. The heated micro-reactor, sometimes referred to as a 'Chen nozzle,' was developed in the lab of Dr. Peter Chen [33]– [35]. These devices were first proposed as a reactor for radical production in 1986. These reactors were subsequently improved by Kohn et al. [35]. In their work, Kohn et al. [35] wanted to create a reactor that 1) would form a supersonic jet to isolate the radicals from any further reaction, 2) have conditions that encourage complete reaction of the radical precursor, and 3) be inexpensive and reusable. The resultant design involved the production of a tube with approximately 1mm internal diameter and around 2cm in length made of materials that could be resistively heated to high temperatures. As such, the original tube made of alumina was modified, including material changes to both SiC, which is commonly used in similar reactors today, and yttria-stabilized zirconia. By making them small in dimension, it is possible to constrain the fluid flow residence times to very short intervals (25–150μs), allowing observation of the earliest kinetic processes. One of the main advantages of micro-reactors is that for a given set of flow conditions, it is possible to thermally decompose samples over short times scales so that only

the initial decomposition is observed. Combined with laser diagnostics, these devices identify all species emerging from the reactor, including atoms, radicals, and metastables, as well as stable species. When operated under dilute conditions, the micro-reactor can isolate unimolecular reaction schemes allowing examination of thermal products formed at the earliest time scales (approximately 100μs). From a fluid dynamics and heat transfer perspective, the experiments conducted in the micro-tubular reactor also come in two distinct forms: pulsed flow and continuous flow in helium and argon.

In recent years, the micro-reactor has been used to study the thermal decomposition of fuels [36] by coupling to a matrix isolation spectroscopy scheme [32]. Initially mainly used as a source of organic radicals [37]–[39] for IR spectroscopic analysis, the value of the reactor as a means to study pyrolysis quickly emerged and since has also been used as a means to study thermal decomposition [40]–[42]. One shortcoming of the micro-reactor setup is that the temperature and pressure inside the reactor are poorly characterized. Although the exterior surface temperature of the reactor can be measured and the upstream pressure monitored, these parameters cannot be solved inside the reactor due to the complex flow conditions and dimensional constraints. For helpful information to be extracted for combustion modeling, the temperature and pressure must be measurable within the reactor so that the products detected can be tied to the prevailing conditions that led to their creation.

Collaboration with other members of the Labbe Group has provided significant progress in directly predicting the temperature and pressure at different points inside the reactor. Using computational fluid dynamics (CFD) simulations of inert carrier gasses like He, Ar, or Ne, it was possible to carry out simulations of these two critical variables (gas temperature and pressure) as a function of wall temperature, pressure differential, and mass flow rate. The findings are

summarized in a 2014 review paper [43] establishing a comprehensive investigation of fluid flow through a heated micro-reactor. The following section describes two experimental laser diagnostic techniques which involve the existing micro-reactor as the primary source of radicals. Details of the experimental integration of micro-reactors with these diagnostic techniques are described next.

2.2 Experimental Methods

2.2.1 Pulsed micro-reactor

One version of the pulsed flow reactor assembly is shown in Figure 2.2. The reactor consists of a resistively heated silicon carbide (SiC) tube. The reactor is heated using interference-fitted carbon disks slotted into molybdenum clips, passing up to 5 A current through the reactor to heat to 1600 K. The heated length is about half to two-thirds the size of the reactor, with the temperature of the outer wall monitored by a tungsten/rhenium Type C thermocouple (Omega, wire pairs W/5% Re and W/26% Re, diameter 0.005 in). Upstream of the reactor is a pulsed valve (Parker General Valve, series 9, 0.25 mm orifice). The valve is controlled with an Iota One pulsed valve controller (the open time of the valve is on the order of hundreds of μs[32]), set to operate at 10 Hz for pulsed He. The temperature of the pulsed valve is monitored with a Type-K thermocouple (Omega, chrome-alumel, 0.01 in diameter). It can also be controlled (Love Controls, series 16A) with a flexible heater (0.75 in by 2 in, Minco). A 1 cm inner diameter alumina cylinder surrounds the SiC reactor to reduce radiative heat losses.

The reactant mixtures for the pulsed experiments range from 0.03%−0.1% in He carrier gas. Liquid precursors with adequate vapor pressure to prepare gaseous mixtures are degassed using a freeze-pump-thaw cycle and used without purification from the manufacturer unless otherwise indicated. The total backing pressure to the pulsed valve is about 1500 Torr He for PIMS experiments. The pressure at the reactor exit for both experiments is maintained at approximately

1−10μTorr. The flow at the reactor exit chokes (reaches the local sonic velocity) and undergoes a supersonic expansion. It is estimated that the free-jet expansion rapidly cools the molecules in the beam to about 40K (rotationally)[32]within a tube diameter, eliminating any additional reactions. The degree of vibrational cooling in the molecular beam is unknown and can affect the photoionization experiments' interpretation.

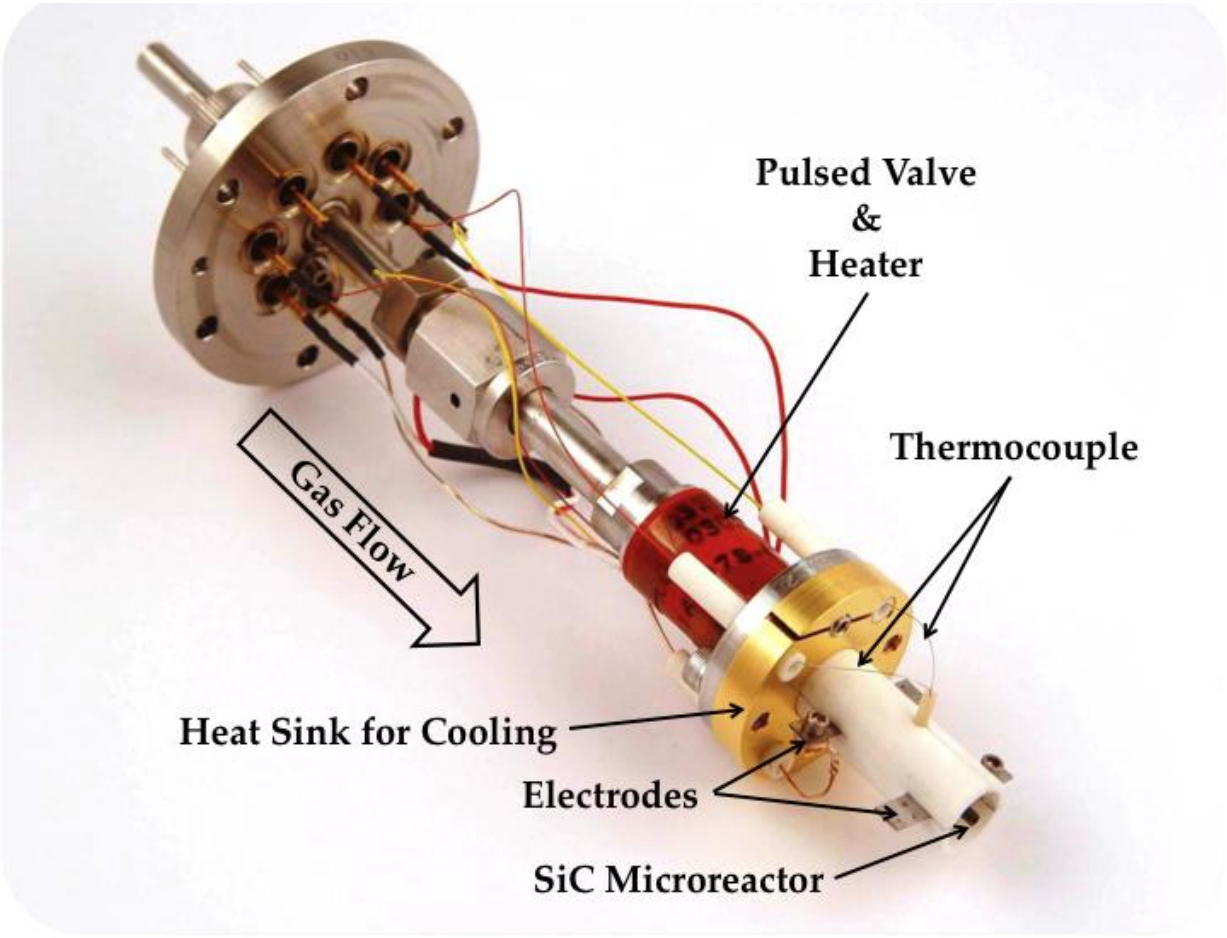

Figure 2.2: Inner pyrolyzer assembly with pulsed valve. SiC micro-reactor measured at 3 cm length and 1 mm inner diameter.

2.2.2 Continuous Flow Reactor

The continuous flow reactor is similar in assembly and orientation to the pulsed flow reactor but differs in the absence of any solenoid-driven pulsing system. It is replaced by an externally mounted commercial mass flow controller (MKS P4B 0-200sccm N_2) set to operate at

a 200sccm helium flow rate. The pressure upstream of the reactor is monitored with an MKS Baratron capacitance manometer and increases approximately linearly with the operating temperature. At room temperature, the upstream pressure is about 100 Torr; with a reactor temperature of 1600 K, the upstream pressure is about 290 Torr. The pressure at the reactor exit is measured with a Micro-Ion gauge (Granville-Phillips) and remains constant at about 10 μTorr. The primary source chamber housing the micro-reactor assembly was modified to integrate a turbo-molecular pump to be compatible with continuous flow operations. The standard ASA flange connecting the source chamber to a 6-inch Varian A195 oil diffusion pump was replaced with a composite ASA-ConFlat (CF) flange of 10-inch diameter for compatibility with a turbo-=molecular pump. The primary pumping system fitted is the Pfeiffer Vacuum TPU 1201 P pump with an Alcatel Type 2033 SD roughing pump. While operating the system at a 200sccm flow rate, the backing pump pressure is measured using a TC vacuum gauge at 500mTorr.

2.2.3 Optical Temperature Measurement

Modifications were made to the temperature measurement system to reduce the time taken to set up the experiment and improve accuracy. An optical temperature measurement system replaced the type C thermocouple described in section 2.2.1. The Micro-Epsilon ThermoIMAGER TIM M-1 camera with a 16mm focusing lens was selected as the imaging tool. This device measures temperature by characterizing the radiation produced by the heated silicon carbide reactor. The camera system has a spectral range between 0.92- 1.1 μm. The system has a thermal resolution of 0.1°C with an accuracy of +/- 2% (<1500°C) and an adjustable emissivity input of 0.1-1.0. The camera integrates via USB-A with a computational interface and continuous temperature measurement through the TIM-Connect software's output. A 3" diameter viewing port was created in the source chamber. This opening was sealed using a ConFlat (CF) flange with a

fused silica optical window. The camera is positioned using a multi-pivot arm and stabilized to produce an 18 cm by 11 cm field of view. The camera can operate across a temperature range of 450-1800 °C with a resolution of 250 micron at a rate of 32 Hz acquisition.

2.3 Diagnostics

Molecules exiting the micro-tubular reactor are probed with two diagnostic techniques: photoionization time-of-flight mass spectrometry or matrix isolation FT-IR absorption spectroscopy. At CU Boulder, the masses of the thermal cracking products are identified by fixed frequency vacuum ultraviolet photons of the 9th harmonic of an Nd: YAG laser. The second set of experiments utilized a pre-production KM Labs Hyperion tunable VUV laser system to identify products emerging from the micro-reactor. An application of this is described in Chapter 4.

2.3.1 Photo Ionization Mass Spectrometry

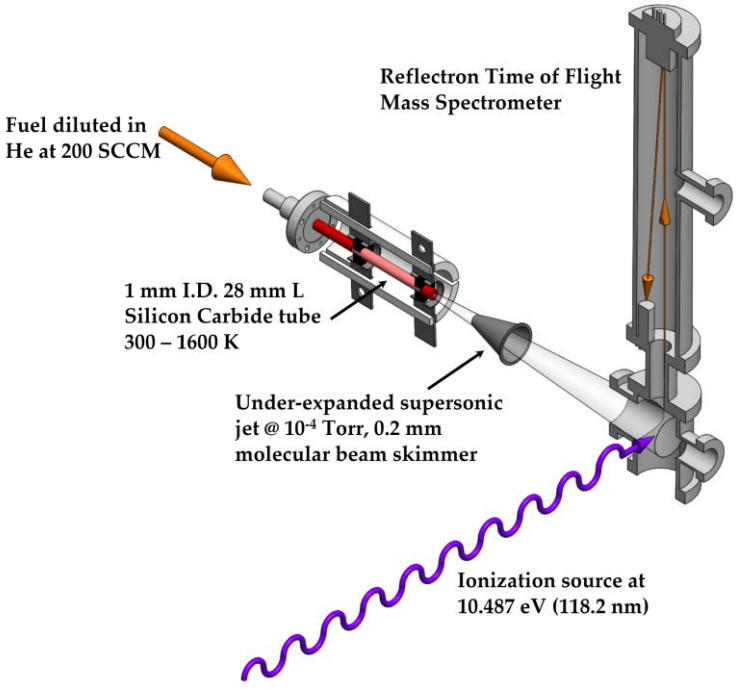

Figure 2.3: Reflectron photoionization time-of-flight mass spectrometer with fixed frequency photons at 118.2 nm

The fixed wavelength ionization source used to characterize the products of pyrolysis is the Spectra-Physics Quanta-Ray Pro 30 Hz pulsed neodymium-doped yttrium aluminum garnet (Nd: YAG) laser (with fundamental wavelength 1064 nm). This system is tripled twice to generate vacuum ultraviolet (VUV) photons at 118.2 nm (10.487 eV), the 9th harmonic of the fundamental. The 118.2 nm light is generated by first tripling the 1064 nm fundamental to 355 nm in a harmonic generator with KD*P (potassium dideuterium phosphate) crystals. The 355 nm light is then focused into a xenon: argon gas cell with a fused silica lens, where a small fraction of the incoming light is tripled to 118.2 nm (estimated at 10 μJ per pulse at 30 Hz [32]. The tripling cell is 30 cm long and has a total cell pressure of about 300 Torr (Xe: Ar ratio 1:10 [44]–[46]). A schematic of the laser alignment and time-of-flight operations is shown in Figure 2.4.

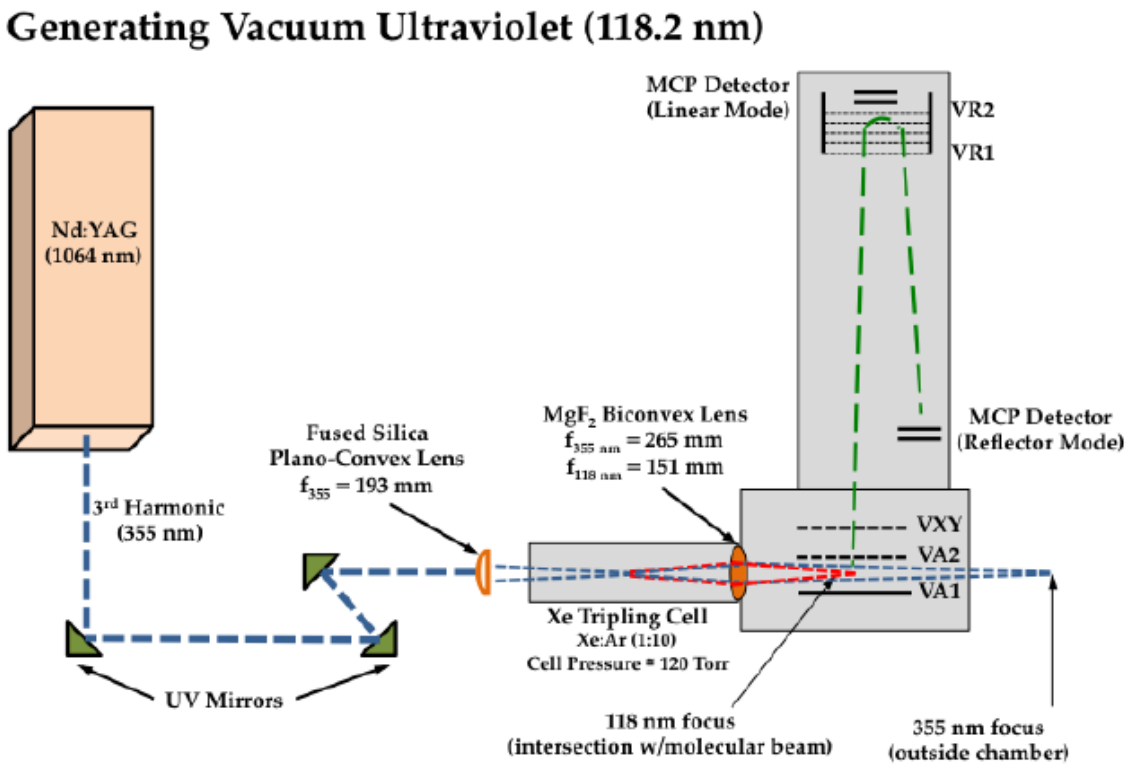

Figure 2.4: Generation of 118.2 nm photons (10.487 eV) and ion flight path in the reflectron

Molecules in the molecular beam with ionization thresholds less than 10.487 eV are ionized and separated for detection in a 100 cm Jordan (Jordan TOF Products, Inc.) reflectron time-of-flight mass spectrometer. The ions are accelerated from the source region by a repeller plate behind the packet of ionized molecules (VA1 = 1403 V) and then drawn through an extraction grid (VA2 = 680V). Ion optics (VXY = 76 V) guide the ion packet into a field-free region of the flight tube where separation occurs based on the mass-to-charge ratio (m/z).

The ions are reflected at the opposite end of the flight tube, reversing their direction of travel (VR1 = 1089 V, VR2 = 1774 V). Assuming all ions created by the 118.2 nm light have a charge of +1, the lighter molecules will travel faster than the heavier molecules and reach the detector first. Ions are detected with a microchannel plate (MCP) detector (dual plate, chevron-type, VD = -1850 to -1900 V), creating an avalanche of electrons. For every ion that hits the detector, approximately 100 electrons are ejected from the plates, thus amplifying the signal [47]. The MCP signal for the fixed-frequency experiments is reported as an analog voltage.

The reflectron-type separation of the ions reduces the kinetic energy distribution of an individual mass within the ion packet, thus improving the spectrometer's resolution. The mass resolution in the spectrometer is limited by the temporal width of the ion packet (which is determined by the pulse width of the ionization source) and the velocity distribution of the ions, determined by where they were formed spatially with respect to the extractor plates (VA1, VA2). The mass resolution (m/Dm) in the Jordan reflectron is about 800.

An alternate ionization source that was applied to carry out photoionization mass spectrometry was the KMLabs Hyperion VUV(TM) pre-production prototype, which uses an ultrafast fiber laser source coupled with highly-cascaded four-wave-mixing harmonic generation in a xenon-filled hollow negative-curvature fiber[48]. Photon generation is started with a prototype

ultrafast ytterbium-doped fiber laser producing 10 μJ, 160 fs pulses at 1035 nm with a repetition rate of 1 MHz. The output is then frequency-doubled to 518 nm using a betabarium borate (BBO) crystal [Eksma Optics], with about 50% efficiency. The fundamental at 1035 nm and the second harmonic at 518 nm pulses are meshed together in time using a delay stage and focused into a negative curvature fiber ((Glo-Photonics PMC-500/700) filled with ~1000 Torr (20 psia) of xenon gas. With 4W of 1035 nm and 3 W of 518 nm light entering the fiber in parallel, about 200 mW of the third harmonic is created using a degenerate four-wave mixing process. This third harmonic light is combined with the fundamental and the second harmonic to create a cascading effect driving more four-wave mixing. After generation, the VUV light passes through a monochromator maintained at a vacuum to select a specific harmonic for the experiment. The VUV generated in the fiber is spectrally separated and focused onto the target gas jet using an in-vacuum folded Wadsworth monochromator. The monochromator consists of a flat custom-coated rejector mirror, a spherical focusing mirror, a flat diffraction grating, and a 1 mm exit slit. The rejector mirror is a 2″ diameter fused silica window mounted near grazing angle, coated to transmit 99% of the 1035 nm, 517 nm, and 345 nm light while reflecting >90% of all shorter wavelengths. The focusing mirror is a 1″ diameter, R = 400 mm spherical MgF2-coated aluminum concave mirror. The diffraction grating is blazed for 120 nm with 600 grooves/mm (33021FL01–100R, Newport Richardson), recoated with MgF2-coated aluminum. No optics are used between the exit slit and the gas jet except for an MgF_2 window to prohibit xenon from flowing from the monochromator into the ionization chamber. This window absorbs about 70% of the 10.8 eV photons and all photons of higher energy. Modifications made to the monochromator setup to obtain alternate harmonics are described in work by Couch et al. [49].

For evaluation of the products of pyrolysis, the following harmonics generated by the setup are used: 7th harmonic (8.4 eV, 6×10^{12} photons/s), 8th harmonic (9.6 eV, 3×10^{12} photons/s), and 9th harmonic (10.8 eV, 4×10^{11} photons/s). These harmonics provided the ideal coverage in terms of ionization energy to evaluate nearly 99% of all organic molecules. The effective repetition rate was reduced for compatibility with the experimental detection system. This is achieved by pulsing the voltages on the ion optics in the ionization chamber. Under ordinary operation, the time between the laser pulse and the ion detection on the MCP is used to calculate the mass of the ion. However, this laser generates pulses at a repetition rate of 1 MHz, while the ion flight times are typically 30 μs. With the repeller and extractor always charged to operational voltage, every signal peak copied every 1 μs would be observed. With 5–10 species present during each pyrolysis experiment, the density of peaks would severely impede interpretation. Instead, the voltage on the repeller is pulsed at a repetition rate of 10 kHz, corresponding to a 100 μs delay between pulses. A commercial high-voltage switch (Behlke HTS 21–03-GSM) with a home-built circuit is used to switch the repeller voltage. Ions take approximately 2 μs to drift out of the extractable region, so each voltage pulse extracts ions produced during the previous 2–3 laser pulses. Thus, this setup only extracts 2–3% of the ions produced (1000,000 Hz/10,000 Hz = 100 VUV pulses per voltage pulse). The time between the voltage pulse and the signal on the MCP is used to calculate the ion's mass; this is independent of the timing of the laser pulses. The precise timing of the brief voltage pulse (2 ns) from the MCP during an ion detection event is recorded by a high-speed digitizer (Acqiris U1084A-001) using the Acqiris PeakTDC software. The mass resolution of this instrument is about $m/\Delta m=750$ (FWHM).

2.3.2 Matrix Isolation Infrared Spectroscopy

As a complement to the PIMS, infrared spectroscopy in an argon matrix provides structural information for the pyrolysis products, differentiating thermal products of identical mass. Additionally, those molecules and radicals whose ionization energy lies beyond the energy of the photons produced by the fixed wavelength light source can also be characterized. The molecular beam formed at the reactor exit impinges on a cold window. The products, now trapped in frozen argon, are detected by FT-IR spectroscopy, as shown in Figure 2.5

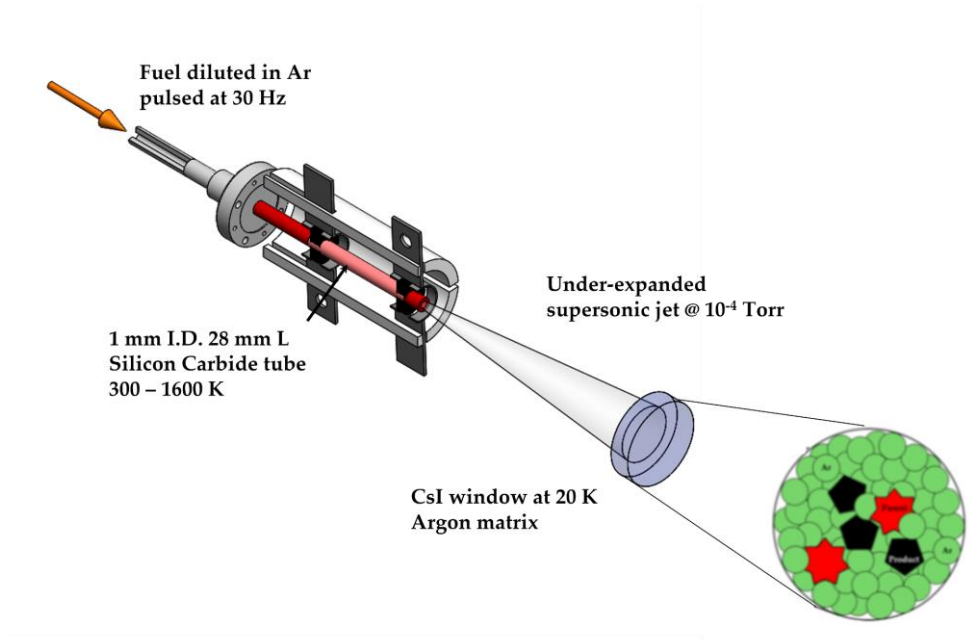

Figure 2.5: Pyrolysis products entrained in Ar exit the μtubular reactor and become trapped on a cryogenic window.

A Varian Turbo V 81 AG, backed by a mechanical pump (Edwards Vacuum Systems), produces the high-vacuum conditions (10^{-6} Torr) necessary for matrix isolation spectroscopy. The flow reactor assembly is mounted to the vacuum shroud of a two-stage closed-cycle helium cryostat (APD Cryogenics, model DE-202, 60 Hz and 2.5W cooling capacity at 20 K; compressor model HC-2D), which cools an infrared transparent cesium iodide (CsI) window to 10 K. Figure

2.6 shows a detailed cross-sectional view of the matrix assembly and the positions for deposition and collection of the FT-IR spectrum. The CsI window is mounted in a metallic holder, which is screwed into the cold finger of the He-cryostat expansion unit. Thermal contact between the finger and the window holder is enhanced by a thin layer of indium. Molecules exiting the reactor are aimed at the cold, IR transparent window (approximately 3 cm away). The deposition of many thin layers of the pulsed reactant gas mixture forms a matrix. A pair of CsI windows on opposing sides of the cryostat shroud allow an infrared beam to pass for spectroscopic detection.

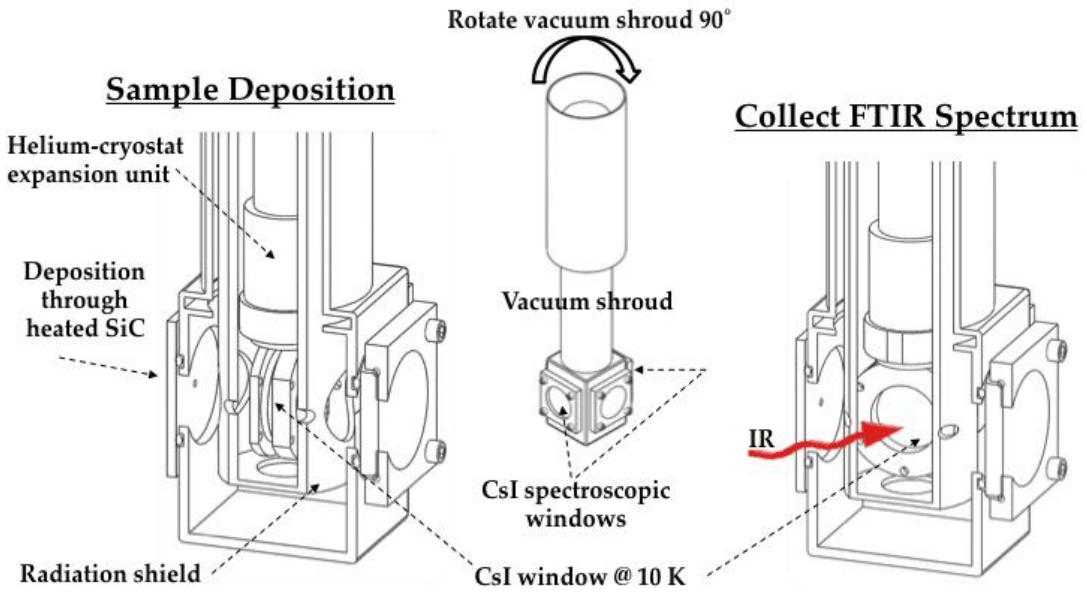

Figure 2.6: After deposition on the cold (10 K) window, the outer shroud is rotated 90 for spectroscopic analysis of molecules frozen in Ar.

Gaseous reactant mixtures are prepared in a glass 1.2 L reservoir upstream of the reactor in concentrations of 0.04−0.1% in approximately 800 Torr Ar. To achieve resolved IR spectra, typical deposition rates through a pulsed valve were 0.8 to 1 Torr min^{-1} from the reservoir (equivalent to 3−3.6 mmol hr^{-1}), depositing between 3 to 6.5 mmol total onto the cold window. Based on the concentration of the reactants in argon, this is equivalent to about 10^{13} radicals per pulse. The vibrational spectra are measured using a Nicolet 6700 infrared spectrometer equipped with a liquid N_2-cooled mercury/cadmium/telluride detector (MCT/A, 4,000−650 cm-1). The

spectrometer is purged with purified dry air, and the spectra are collected with the OMNIC software package on a Windows operating system. A background scan is taken approximately 1 to 2 hours before the sample scan; all spectra averaged 500 scans at 0.25 cm^{-1} resolution.

2.4 Analysis

The composition of the gas mixture can be quantified using the results of photoionization spectroscopy. The ionization of a neutral target produces an ion signal proportional to the target concentration in the area sampled by the photon source. Using Beer's law it is possible to determine the radiation (in photons per second). This is represented in equation 2.1

$$I(\boldsymbol{\nu}) = I_0(\boldsymbol{\nu}) \exp(-n\sigma(\boldsymbol{\nu})z) \tag{2.1}$$

Where n is the density of the target gas, $\sigma(\boldsymbol{\nu})$ is the ionization cross-section and z is the gas sample distance, I is the radiation, and $\boldsymbol{\nu}$ is the frequency.

Since the VUV radiation is ionizing the gas, the resultant ion current j+ is proportional to the difference between the incident $I_0(\boldsymbol{\nu})$ and transmitted radiation $I(\boldsymbol{\nu})$:

$$j+ \propto [I_0(\boldsymbol{\nu}) - I(\boldsymbol{\nu})] = I0(\boldsymbol{\nu}) [1 - \exp(-n\sigma(\boldsymbol{\nu})z)] \tag{2.2}$$

Finally, since it can be assumed that $(-n\sigma(\boldsymbol{\nu})z)$ is a small value, by a Taylor's series approximation, the photoion current j+ is proportional to the product $I_0 n\sigma(\boldsymbol{\nu})z$. Converting this expression from a formulation of Beer's law to photoionization, the ion signal is a function of the number of molecules in the interaction region, the VUV photon flux through the volume, and the photoionization cross-section. However, neither the absolute value of the volume nor the incident

photon flux is known. The volume could be estimated with some uncertainty; however, it can be gathered into an empirical constant which is ultimately obtained by calibration or can factor out when taking ratios. The value of the photon flux is a power measurement using a calibrated energy-dependent photodiode. Therefore, to a first approximation, the photoionization signal S_i^+ due to species i exiting the micro-reactor can be written as:

$$S_i^+ = C n_i \phi(E) \sigma_i(E) \tag{2.3}$$

Where n_i is the number density of a particular species in the interaction volume, $\phi(E)$ is the photon flux at a given photon energy, and $\sigma_i(E)$ is the molecule's photoionization cross-section at the given photon energy. Here the signal S_i^+ refers to the total ion counts summed over the desired mass peak and normalized on the sampling time or the number of scans. Equation (2.3) ignores the fact that, because of differential diffusion, mass differences, and other factors, molecules of differing mass and collision cross-sections will be detected with different efficiency. This effect is considered by defining a mass discrimination factor Di that is empirically determined by calibration[50]. Incorporating the mass discrimination factor and evaluating the number density of the neutral target, one finds:

$$ni = Si + /CDi\phi(E)\sigma i(E) \tag{2.4}$$

Where the constant C contains all the geometry-dependent factors that remain unchanged with differing masses, this value could be obtained by absolute calibration.

However, while it will be challenging to use Eq. (2.4) to measure the absolute concentration of a species, it should be straightforward to measure the ratio of two different species, i and j:

$$n_i/n_j = (S_i +/S_i+)(CD_j\phi(E)\sigma_j(E)/CD_i\phi(E)\sigma_i(E)) \quad (2.5)$$

To measure the ratios via (2.6) requires knowledge of the photoionization cross-sections $\sigma(E)$, the measured photon flux $\phi(E)$, and an estimate of the mass discrimination factors D_i.

2.5 History of the PIMS and Matrix IR experiments at the University of Colorado

The first forays into using the micro-reactor in the pulsed setting coupled with a matrix FTIR setup was in 2003 to study the pyrolysis of allyl radicals (CH_2CHCH_2) and methyl-peroxyl radicals (CH_2OO) by Xu Zhang and G. B. Ellison[32]. A challenge to working with the matrix IR setup lies in discerning the first pyrolytic decomposition products. This is alleviated by using it to complement photoionization mass spectroscopy, where spectra from the pyrolysis process can be visualized nearly instantaneously. Using these two techniques and evaluating multiple precursors, it was possible to evaluate the thermal decomposition of these two radicals.

Another application of these techniques was to understand the impact of furans in polycyclic aromatic hydrocarbons (PAH) formation during biomass gasification. This research was carried out by Vasiliou et al. [51] and included exploring the decomposition of furans under different temperature conditions using the straight tube micro-reactor. The products observed were validated against results obtained using corresponding electronic structure theory calculations. The primary products obtained through thermal decomposition are (CO + CH_3CCH) and (HCCH + CH_2CO) at around 1350 K. Propargyl radicals were also observed when the micro-reactor is heated

at around 1550 K. These studies were pivotal in also demonstrating that the pyrolysis process is pressure dependent. This was confirmed by the additional reactions identified using different micro-reactor configurations.

Vasiliou and Ellison et al. [52] then applied both Matrix FTIR and PIMS experiments to characterize the decomposition of acetaldehyde . The decomposition of this molecule over a range of temperatures and at short residence times had already been well documented, and multiple products had been identified. These studies validated the primary products of decomposition and also confirmed that the isotopomers of acetaldehyde CH_3CDO, CD_3CHO, and CD_3CDO were similar to CH_3CHO. The results obtained here produced a detailed scheme for the pyrolysis of acetaldehyde, including an analysis of other byproducts. This research effort provided correction factors to the previously developed Rice-Herzfeld method[53].

To evaluate the properties of gasoline substitutes 2-methylfuran (2MF) and 2,5-dimethylfuran (DMF), furan was studied as a surrogate molecule[54]. Experiments with furan were run using the PIMS setup, and two distinct decomposition products alpha-carbene and beta-carbene were identified. To quantify the concentration of each product, the number density method described in section 2.4 was applied. It was confirmed that almost 80% of furan decomposed to form beta-carbene, forming the basis for more extensive research in engine testbeds.

With the results obtained from the previous evaluation, 2-methoxyfuran was analyzed in both the PIMS and FTIR setup[55]. These studies revealed secondary bimolecular reactions between 2-methoxyfuran and 2-furanyloxy and methyl radicals generate other organic byproducts. These include $CH_2=CHCHO$, $CH_3CH=CHCHO$, and $CH_3COCH=CH_2$. An analysis of the concentration of these products revealed only 1-3% of the parent molecule was consumed in these secondary reactions. These specific insights showcase the combined capability of these

experiments to discern both the first products of decomposition and also the extent of secondary reactions.

In 2017, Porterfield et al. [56] applied these setups to assess the thermal cracking of fatty acid methyl esters. These molecules have been identified as possessing similar combustion properties to traditional fuels. Silicon carbide tube micro-reactors in PIMS and FTIR were used to observe the decomposition of methyl acetate and methyl butanoate from 300K to 1600K. Primary products of decomposition include methanol and ketene at 1000K. As the temperature was raised to 1300K other products were identified including formaldehyde, methyl, and carbon monoxide. Methyl butanoate was shown to form similar products with the first decomposition reactions occurring at 800K. These results were instrumental in developing a generalized scheme for the decomposition of esters with the formula RCH_2-$COOCH_3$. The primary product of decomposition of relevance to engine operation involved the elimination of methanol to produce ketone.

Rogers et al. [57] applied the PIMS experiment in combination with electronic structure theory calculations to study the decomposition of propionic acid. This molecule has been identified as an important combustion intermediate during the combustion of oxygenates such as ethyl esters. By applying a tunable VUV source, (the pre-production version of the KM Labs Hyperion VUV Laser), isomer resolution was made possible. This helped narrow down the decomposition of propionic acid to methyl ketene and water. Two possible routes were discerned - either through forming a dystonic ion or directly well-skipping to methyl ketene. The Matrix FTIR experiment was also utilized to confirm that there was no decarboxylation of propionic acid under these conditions. These results and computational evaluations were utilized to produce updated rates and branching ratios for the decomposition of propionic acid.

Multiple other research facilities have also applied the micro-reactor with laser diagnostic methods to discern the first products of thermal decomposition. These include work at the National Renewable Energy Laboratory (NREL)[58] where similar diagnostics were applied to understand the decomposition of 2-phenethyl phenyl ether (PPE) and phenyl ethyl ether (PEE). These studies presented that the C-O bond breakage was the primary pathway to forming combustion-relevant radicals. In contrast, the cleavage of C-C bonds was shown to be inoperative across the temperature spectrum. Another example of the application of the micro-reactor was in research efforts to understand the pyrolysis behavior of methyl tert butyl ether (MTBE)[59]. These efforts were focused on measuring the mole fractions of different radicals produced across engine-relevant temperatures.

The extensive work carried out at the University of Colorado Boulder and the broader combustion and physical chemistry community, in general, is a testament to the capabilities of the micro-reactor in combination with powerful laser diagnostics. Together they have been instrumental in providing scientists and engineers with the knowledge of the very first products of decomposition. Results have been vital in extending these experimental capabilities to understand the relationship between the structure and function of individual fuel molecules.

Characterizing the fluid behavior within these devices is an important aspect of further extending these micro-reactors capabilities to develop next-generation fuels. The thermodynamic properties of the fluid inside the micro-reactors, such as temperature, pressure, and velocity distributions, significantly impact experimental results. The first effort to accomplish this was made by Guan et al. in 2013 [43]. This research effort applied computational fluid dynamics (CFD) to simulate decomposing large molecules within the reactor. They applied Navier-Stokes equations to solve for the thermodynamic properties of several tubular micro-reactors in the PIMS

configuration. Centerline profiles and radial profiles were obtained by varying wall temperature and mass flow rate. Accurate thermodynamic data is critical to producing precise information on reaction kinetics. Here, cyclohexene decomposition and methoxy furan pyrolysis were selected as examples to demonstrate how their reaction rates and mole fractions change with reactors.

The results from this work highlighted the thermodynamic behavior of the tube micro-reactor. Because of its geometric configuration and the prevailing operating conditions, fluid within the micro-reactor travels from a region of high pressure to a low-pressure outlet. This causes a dramatic drop in pressure with a corresponding ramp in pressure across the length of the reactor. Providing a stabilized pressure environment and controlling the residence times becomes increasingly difficult under these circumstances, both vital to producing valuable chemical kinetic inputs. The efforts to remedy this deficiency by applying CFD simulations to develop a new reactor geometry and fabricating this novel geometry using a digital manufacturing technique are described in Chapters 6 and 7.

2.6 Oxidation reactions using the micro-reactor geometry

The previous experiments have concentrated on probing the pyrolysis of different fuel and fuel surrogate molecules. Another critical reaction type that is relevant to modeling combustion behavior is oxidation reactions. This will require evaluating the interaction between the fuel molecule with an oxidizer. While reactions with more than one fuel molecule have been carried out previously in the form of abstraction reactions, experiments with an oxidizer have not been performed with this setup. The current reactor material, silicon carbide, is ideally suited to operate in high-temperature, chemically active environments and is incompatible with oxygen. Under conditions of high temperature and in the presence of molecular oxygen (or air), silicon carbide oxidizes to form silicon dioxide. The formation of silicon dioxide degrades the reactor's

capabilities, leading to sustained heating and fracturing challenges at temperatures beyond 1200K. This has limited the current experiments with the micro-reactor to only the pyrolysis type. The simulation of combustion reactions involving alternate fuels will require a new reactor material. This alternate material must be able to operate in an oxidizing atmosphere and retain its chemical identity while being compatible with existing heating strategies and thermal shock requirements. Chapter 7 details efforts toward identifying and processing alternate reactor materials using the digital manufacturing process developed to create silicon carbide geometries. Experimental evaluations to validate this new material and reactor geometry are proposed in Chapter 8.

2.7 References

[1] R. R. Baker, R. R. Baldwin, C. J. Everett, and R. W. Walker, "The addition of neopentane to slowly reacting mixtures of hydrogen and oxygen at 480°C—I: Formation of primary products from neopentane," *Combust. Flame*, vol. 25, pp. 285–300, Aug. 1975, doi: 10.1016/0010-2180(75)90100-5.

[2] R. R. Baldwin and R. F. Simmons, "Inhibition of the First Limit of the Hydrogen–Oxygen Reaction by Ethane," *Nature*, vol. 175, no. 4451, pp. 346–347, Feb. 1955, doi: 10.1038/175346b0.

[3] F. L. Dryer, "High Temperature Oxidation of Carbon Monoxide and Methane in a Turbulent Flow Reactor," PRINCETON UNIV NJ DEPT OF AEROSPACE AND MECHANICAL SCIENCES, Mar. 1972. Accessed: Dec. 26, 2021. [Online]. Available: https://apps.dtic.mil/sti/citations/AD0746284

[4] T. B. Hunter, H. Wang, T. A. Litzinger, and M. Frenklach, "The oxidation of methane at elevated pressures: Experiments and modeling," *Combust. Flame*, vol. 97, no. 2, pp. 201–224, May 1994, doi: 10.1016/0010-2180(94)90005-1.

[5] P. Dagaut *et al.*, "A jet-stirred reactor for kinetic studies of homogeneous gas-phase reactions at pressures up to ten atmospheres ($\approx$1 MPa)," *J. Phys. [E]*, vol. 19, no. 3, pp. 207–209, Mar. 1986, doi: 10.1088/0022-3735/19/3/009.

[6] B. F. Gray and P. G. Felton, "Low-temperature oxidation in a stirred-flow reactor—I.

Propane," *Combust. Flame*, vol. 23, no. 3, pp. 295–304, Dec. 1974, doi: 10.1016/0010-2180(74)90111-4.

[7] H. K. Ciezki and G. Adomeit, "Shock-tube investigation of self-ignition of n-heptane-air mixtures under engine relevant conditions," *Combust. Flame*, vol. 93, no. 4, pp. 421–433, Jun. 1993, doi: 10.1016/0010-2180(93)90142-P.

[8] E. L. Petersen, "Interpreting Endwall and Sidewall Measurements in Shock-Tube Ignition Studies," *Combust. Sci. Technol.*, vol. 181, no. 9, pp. 1123–1144, Sep. 2009, doi: 10.1080/00102200902973323.

[9] G.Mittal, and Chih-Jen Sung. "A Rapid Compression Machine for Chemical Kinetics Studies at Elevated Pressures and Temperatures." Combustion Science and Technology, vol. 179, no. 3, Mar. 2007, pp. 497–530, https://doi.org/10.1080/00102200600671898.

[10] A. E. Karataş and Ö. L. Gülder, "Soot formation in high pressure laminar diffusion flames," *Prog. Energy Combust. Sci.*, vol. 38, no. 6, pp. 818–845, Dec. 2012, doi: 10.1016/j.pecs.2012.04.003.

[11] K. Kohse-Höinghaus, "Combustion in the future: The importance of chemistry," *Proc. Combust. Inst. Int. Symp. Combust.*, Sep. 2020, doi: 10.1016/j.proci.2020.06.375.

[12] G. C. Eltenton, "The Study of Reaction Intermediates by Means of a Mass Spectrometer Part I. Apparatus and Method," *J. Chem. Phys.*, vol. 15, no. 7, pp. 455–481, Jul. 1947, doi: 10.1063/1.1746565.

[13] A. Kantrowitz and J. Grey, "A High Intensity Source for the Molecular Beam. Part I. Theoretical," *Rev. Sci. Instrum.*, vol. 22, no. 5, pp. 328–332, May 1951, doi: 10.1063/1.1745921.

[14] G. B. Kistiakowsky and W. P. Slichter, "A High Intensity Source for the Molecular Beam. Part II. Experimental," *Rev. Sci. Instrum.*, vol. 22, no. 5, pp. 333–337, May 1951, doi: 10.1063/1.1745922.

[15] S. N. Foner and R. L. Hudson, "The Detection of Atoms and Free Radicals in Flames by Mass Spectrometric Techniques," *J. Chem. Phys.*, vol. 21, no. 8, pp. 1374–1382, Aug. 1953, doi: 10.1063/1.1699226.

[16] R. Friedman and J. A. Cyphers, "Flame Structure Studies. III. Gas Sampling in a Low-Pressure Propane-Air Flame," *J. Chem. Phys.*, vol. 23, no. 10, pp. 1875–1880, Oct. 1955, doi: 10.1063/1.1740596.

[17] R. M. Fristrom, "The structure of laminar flames," *Symp. Int. Combust.*, vol. 6, no. 1, pp. 96–110, Jan. 1957, doi: 10.1016/S0082-0784(57)80016-2.

[18] E. A. Bunt, "Mass analysis of flames and flue gases," *Symp. Int. Combust.*, vol. 7, no. 1, pp. 325–331, Jan. 1958, doi: 10.1016/S0082-0784(58)80060-0.

[19] C. P. Lazzara, J. C. Biordi, and J. F. Papp, "Concentration profiles for radical species in a methane-oxygen-argon flame," *Combust. Flame*, vol. 21, no. 3, pp. 371–382, Dec. 1973, doi: 10.1016/S0010-2180(73)80060-4.

[20] J. C. Biordi, "Molecular beam mass spectrometry for studying the fundamental chemistry of flames,"" *Prog. Energy Combust. Sci.*, vol. 3, no. 3, pp. 151–173, Jan. 1977, doi: 10.1016/0360-1285(77)90002-8.

[21] U. Bonne, K. H. Homann, and H. Gg. Wagner, ""Carbon formation in premixed flames," *Symp. Int. Combust.*, vol. 10, no. 1, pp. 503–512, Jan. 1965, doi: 10.1016/S0082-0784(65)80197-7.

[22] P. Weilmünster, A. Keller, and K.-H. Homann, "Large molecules, radicals, ions, and small soot particles in fuel-rich hydrocarbon flames: Part I: positive ions of polycyclic aromatic hydrocarbons(PAH) in low-pressure premixed flames of acetylene and oxygen," *Combust. Flame*, vol. 116, no. 1, pp. 62–83, Jan. 1999, doi: 10.1016/S0010-2180(98)00049-2.

[23] V. Detilleux and J. Vandooren, "Molecular Beam Mass Spectrometry Analysis of Pah Production Pathways in $C_6H_6/O_2/Ar$ and $C_6H_6/C_2H_2/O_2/Ar$ Flames," *Combust. Sci. Technol.*, vol. 180, no. 7, pp. 1347–1369, May 2008, doi: 10.1080/00102200802043284.

[24] J. Vandooren, J. Peeters, and P. J. V. Tiggelen, "Rate constant of the elementary reaction of carbon monoxide with hydroxyl radical," *Symp. Int. Combust.*, vol. 15, no. 1, pp. 745–753, Jan. 1975, doi: 10.1016/S0082-0784(75)80343-2.

[25] A. Lamprecht, B. Atakan, and K. Kohse-Höinghaus, "Fuel-rich flame chemistry in low-pressure cyclopentene flames," *Proc. Combust. Inst.*, vol. 28, no. 2, pp. 1817–1824, Jan. 2000, doi: 10.1016/S0082-0784(00)80584-6.

[26] T. S. Kasper, P. Oßwald, M. Kamphus, and K. Kohse-Höinghaus, "Ethanol flame structure investigated by molecular beam mass spectrometry," *Combust. Flame*, vol. 150, no. 3, pp. 220–231, Aug. 2007, doi: 10.1016/j.combustflame.2006.12.022.

[27] A. Bhargava and P. R. Westmoreland, "Measured Flame Structure and Kinetics in a Fuel-Rich Ethylene Flame 11This report was prepared as an account of work sponsored by the

United States Government. Neither the United States nor the Department of Energy, nor any of their employees, nor any of their contractors, subcontractors, or their employees, makes any warranty, express or applied, or assumes any legal liability or responsibility for the accuracy, completeness, or usefulness of any information, apparatus, product, or process disclosed or represents that its use would not infringe privately owned rights.," *Combust. Flame*, vol. 113, no. 3, pp. 333–347, May 1998, doi: 10.1016/S0010-2180(97)00208-3.

[28] J. A. Cole, J. D. Bittner, J. P. Longwell, and J. B. Howard, "Formation mechanisms of aromatic compounds in aliphatic flames," *Combust. Flame*, vol. 56, no. 1, pp. 51–70, Apr. 1984, doi: 10.1016/0010-2180(84)90005-1.

[29] F. Qi, "Combustion chemistry probed by synchrotron VUV photoionization mass spectrometry," *Proc. Combust. Inst.*, vol. 34, no. 1, pp. 33–63, Jan. 2013, doi: 10.1016/j.proci.2012.09.002.

[30] T. A. Cool *et al.*, "Selective detection of isomers with photoionization mass spectrometry for studies of hydrocarbon flame chemistry," *J. Chem. Phys.*, vol. 119, no. 16, pp. 8356–8365, Oct. 2003, doi: 10.1063/1.1611173.

[31] T. A. Cool *et al.*, "Photoionization mass spectrometer for studies of flame chemistry with a synchrotron light source," *Rev. Sci. Instrum.*, vol. 76, no. 9, p. 094102, Sep. 2005, doi: 10.1063/1.2010307.

[32] X. Zhang *et al.*, "Intense, hyperthermal source of organic radicals for matrix-isolation spectroscopy," *Rev. Sci. Instrum.*, vol. 74, no. 6, pp. 3077–3086, Jun. 2003, doi: 10.1063/1.1574397.

[33] P. Chen, J. B. Pallix, W. A. Chupka, and S. D. Colson, "Resonant multiphoton ionization spectrum and electronic structure of CH radical. New states and assignments above 50 000 cm^{-1}," *J. Chem. Phys.*, vol. 86, no. 2, pp. 516–520, Jan. 1987, doi: 10.1063/1.452303.

[34] P. Chen, S. D. Colson, W. A. Chupka, and J. A. Berson, "Flash pyrolytic production of rotationally cold free radicals in a supersonic jet. Resonant multiphoton spectrum of the 3p2A2" .rarw. X2A2" origin band of methyl," *J. Phys. Chem.*, vol. 90, no. 11, pp. 2319–2321, May 1986, doi: 10.1021/j100402a014.

[35] D. W. Kohn, H. Clauberg, and P. Chen, "Flash pyrolysis nozzle for generation of radicals in a supersonic jet expansion," *Rev. Sci. Instrum.*, vol. 63, no. 8, pp. 4003–4005, Aug. 1992, doi: 10.1063/1.1143254.

[36] A. L. Brown, D. C. Dayton, M. R. Nimlos, and J. W. Daily, “Design and Characterization of an Entrained Flow Reactor for the Study of Biomass Pyrolysis Chemistry at High Heating Rates,” *Energy Fuels*, vol. 15, no. 5, pp. 1276–1285, Sep. 2001, doi: 10.1021/ef010083k.

[37] Friderichsen, Anders V., et al. “The Infrared Spectrum of the Matrix-Isolated Phenyl Radical.” Journal of the American Chemical Society, vol. 123, no. 9, 7 Feb. 2001, pp. 1977–1988, https://doi.org/10.1021/ja0024338. Accessed 8 Apr. 2023.

[38] S. N, P. A. Arnold, B. K. Carpenter, M. R. Nimlos, D. C. Dayton, and G. B. Ellison, “Polarized Infrared Absorption Spectra of Matrix-Isolated Allyl Radicals.” 2001.

[39] Jochnowitz, Evan B., et al. “Propargyl Radical: Ab Initio Anharmonic Modes and the Polarized Infrared Absorption Spectra of Matrix-Isolated HCCCH2.” The Journal of Physical Chemistry A, vol. 109, no. 17, 8 Apr. 2005, pp. 3812–3821, https://doi.org/10.1021/jp040719j. Accessed 8 Apr. 2023.

[40] A. M. Scheer, C. Mukarakate, D. J. Robichaud, G. B. Ellison, and M. R. Nimlos, "Radical Chemistry in the Thermal Decomposition of Anisole and Deuterated Anisoles: An Investigation of Aromatic Growth," *J. Phys. Chem. A*, vol. 114, no. 34, pp. 9043–9056, Sep. 2010, doi: 10.1021/jp102046p.

[41] Zhang, Xu, et al. “Unimolecular Thermal Fragmentation Of ortho-Benzyne.” The Journal of Chemical Physics, vol. 126, no. 4, 28 Jan. 2007, p. 044312, https://doi.org/10.1063/1.2409927. Accessed 5 Nov. 2019.

[42] Vasiliou, AnGayle, et al. “The Products of the Thermal Decomposition of CH3CHO.” The Journal of Chemical Physics, vol. 135, no. 1, 7 July 2011, p. 014306, https://doi.org/10.1063/1.3604005. Accessed 8 Apr. 2023.

[43] Q. Guan, K. N. Urness, T. K. Ormond, D. E. David, G. Barney Ellison, and J. W. Daily, “The properties of a micro-reactor for the study of the unimolecular decomposition of large molecules,” *Int. Rev. Phys. Chem.*, vol. 33, no. 4, pp. 447–487, Oct. 2014, doi: 10.1080/0144235X.2014.967951.

[44] A. H. Kung, J. F. Young, and S. E. Harris, “Generation of 1182-Å radiation in phase-matched mixtures of inert gases,” *Appl. Phys. Lett.*, vol. 22, no. 6, pp. 301–302, Mar. 1973, doi: 10.1063/1.1654647.

[45] A. H. Kung, J. F. Young, and S. E. Harris, “Erratum: Generation of 1182-Å radiation in phase-matched mixtures of inert gases,” p. 2.

[46] Briles, Travis C.,“Production, Deceleration, and Detection of OH Radicals - Thesis.” 2008

[47] J. L. Wiza, “Microchannel Plate Detectors,” *Nucl Instrum Methods*, vol. 162, pp. 60–1, 1979.

[48] J. Ramirez *et al.*, “1 MHz Ultrafast High Order Cascaded VUV Generation in Negative Curvature Hollow Fibers,” in *Conference on Lasers and Electro-Optics*, San Jose, California, 2019, p. JM3E.4. doi: 10.1364/CLEO_AT.2019.JM3E.4.

[49] D. E. Couch *et al.*, “Ultrafast 1 MHz vacuum-ultraviolet source via highly cascaded harmonic generation in negative-curvature hollow-core fibers,” *Optica*, vol. 7, no. 7, p. 832, Jul. 2020, doi: 10.1364/OPTICA.395688.

[50] Terrill A. Cool, et al. “Photoionization Cross Sections for Reaction Intermediates in Hydrocarbon Combustion.” International Journal of Mass Spectrometry, vol. 247, no. 1-3, Dec. 2005, pp. 18–27, https://doi.org/10.1016/j.ijms.2005.08.018. Accessed 20 Feb. 2021.

[51] “Thermal Decomposition of Furan Generates Propargyl Radicals | The Journal of Physical Chemistry A.” https://pubs.acs.org/doi/abs/10.1021/jp903401h (accessed Dec. 30, 2021).

[52] A. K. Vasiliou *et al.*, “Thermal decomposition of CH3CHO studied by matrix infrared spectroscopy and photoionization mass spectroscopy,” *J. Chem. Phys.*, vol. 137, no. 16, p. 164308, Oct. 2012, doi: 10.1063/1.4759050.

[53] Laidler, K. J., and M. T. H. Liu. “The Mechanism of the Acetaldehyde Pyrolysis.” Proceedings of the Royal Society of London. Series A. Mathematical and Physical Sciences, vol. 297, no. 1450, 7 Mar. 1967, pp. 365–375, https://doi.org/10.1098/rspa.1967.0073.

[54] K. N. Urness *et al.*, “Pyrolysis of furan in a microreactor,” *J. Chem. Phys.*, vol. 139, no. 12, p. 124305, Sep. 2013, doi: 10.1063/1.4821600.

[55] K. N. Urness *et al.*, “Pyrolysis Pathways of the Furanic Ether 2-Methoxyfuran,” *J. Phys. Chem. A*, vol. 119, no. 39, pp. 9962–9977, Oct. 2015, doi: 10.1021/acs.jpca.5b06779.

[56] J. P. Porterfield *et al.*, “Thermal Decomposition of Potential Ester Biofuels. Part I: Methyl Acetate and Methyl Butanoate,” *J. Phys. Chem. A*, vol. 121, no. 24, pp. 4658–4677, Jun. 2017, doi: 10.1021/acs.jpca.7b02639.

[57] C. O. Rogers, K. S. Lockwood, Q. L. D. Nguyen, and N. J. Labbe, “Diol isomer revealed as a source of methyl ketene from propionic acid unimolecular decomposition,” *Int. J. Chem. Kinet.*, vol. 53, no. 12, pp. 1272–1284, 2021, doi: 10.1002/kin.21532.

[58] M. W. Jarvis *et al.*, “Direct Detection of Products from the Pyrolysis of 2-Phenethyl Phenyl Ether,” *J. Phys. Chem. A*, vol. 115, no. 4, pp. 428–438, Feb. 2011, doi: 10.1021/jp1076356.

[59] Zhang, Taichang, et al. “Pyrolysis of Methyl Tert-Butyl Ether (MTBE). 1. Experimental Study with Molecular-Beam Mass Spectrometry and Tunable Synchrotron VUV Photoionization.” The Journal of Physical Chemistry A, vol. 112, no. 42, 30 Sept. 2008, pp. 10487–10494, https://doi.org/10.1021/jp803622w. Accessed 14 May 2022.

[60] Dunoyer, L. "Comptes rendus acad." *Sc. Paris* 152 (1911): 594.

[61] F. Knauer and O. Stern, “Zur Methode der Molekularstrahlen. II,” *Z. Fr Phys.*, vol. 39, no. 10–11, pp. 764–779, Oct. 1926, doi: 10.1007/BF01451747.

[62] O. Stern, “Zur Methode der Molekularstrahlen. I,” *Z. Fr Phys.*, vol. 39, no. 10–11, pp. 751–779, Oct. 1926, doi: 10.1007/BF01451747.

[63] I. I. Rabi, J. R. Zacharias, S. Millman, and P. Kusch, “A New Method of Measuring Nuclear Magnetic Moment,” *Phys. Rev.*, vol. 53, no. 4, pp. 318–318, Feb. 1938, doi: 10.1103/PhysRev.53.318.

[64] J. M. B. Kellogg, I. I. Rabi, N. F. Ramsey, and J. R. Zacharias, “An Electrical Quadrupole Moment of the Deuteron,” *Phys. Rev.*, vol. 55, no. 3, pp. 318–319, Feb. 1939, doi: 10.1103/PhysRev.55.318.

Chapter 3: Computational Modeling of Combustion Phenomena

3.1 Introduction

Experimental techniques and their advances have been an important part of the developments made in understanding combustion phenomena [1]. Experiments have enabled measurements ranging from molecular interactions to observing complex multiphase combustion systems. Multiple factors characterize the combustion state and its progress from fuel to exhaust particles, including temperature, pressure, density, velocity, and mixing. Beyond these fundamental parameters, further characteristics of the combustion system may include the formation of droplets, sprays, and particles, phase changes, heat transfer, flame–wall interactions, heterogeneous reactions, and after-treatment performance. Different experimental techniques have been developed to probe each of these phases and parameters to develop models to simulate the sub-processes of combustion. Fundamental molecular-level experiments are used to identify reactant species, quantify molecular reaction rates, and the occurrence of specific chemical reactions in relation to boundary conditions. Techniques such as laser diagnostics can provide real-time information on the pressure, temperature, and species concentration in reactive systems and practical engines [2]–[4]. Mass spectrometry is another method used to isolate specific species and probe their behavior in engine-like conditions using reactors and flames [5]–[7]. When coupled with powerful ionization sources, these techniques enable the detection of elemental constituents of combustion and as part of emissions. These observations can be scaled from measurements of individual reaction rate coefficients to advanced propulsion systems [2], [3]. The insight gained

from such partly idealized systems can help develop, advance, and validate chemical models that act as a conduit between fundamental chemical knowledge and more practical systems behavior.

At the other end of the spectrum, alternate diagnostic techniques such as turbulence imaging, fluorescence, and absorption techniques permit the capture of temporal and spatial variations [8] of the fuel mixture in the engine system. Experiments that are closer in practical application to engines have been integral in evaluating the performance of additives and fuels at scale. Specifically designed laboratory experiments like Rapid Compression Machines (RCM) [9], and Advanced Fuel Ignition Delay Analyzer (AFIDA) [10]t provide access to information such as the ignition delay time, flame speed, flame structure, tendency to auto-ignite and extinction behavior. Full-size engine evaluations provide the most realistic measurements of different fuels under varying engine conditions. These evaluations are useful for making user-relevant measurements such as efficiency and power [11], [12]. However, they are incapable of elaborating on the impacts of nuanced interactions between different components in the engine system. This limitation extends to laser diagnostics and mass spectrometry, where experimental shortcomings curtail the type, number, and complexity of species that can be evaluated. Even in the flame environment, transport and heat transfer uncertainties might obscure the influence of reactions of particular interest for a complete combustion process analysis. Comprehensive reaction information essential for a deeper understanding of the reaction process as a function of temperature, pressure, fuel mixture and reaction time is often unavailable from each of these different techniques individually. Understanding combustion processes and the concurrent development of combustion models require information over a wide range of temperatures and pressures. It is, therefore, important to consider multiple reaction environments with their specific

target conditions and advantages for studying a given question since they may show different sensitivity to certain species and specific reaction pathways.

Designing experiments to provide insight into a range of parameters can be costly and time-consuming. The inability of each of the techniques described previously to probe more than a few combustions variables has led to an increased reliance on computational modeling to predict the global behavior of molecules based on a small number of observable characteristics [13]. This increased focus on chemical modeling arises from the ever-improving fidelity, the utility of modeling efforts, and the continuing expansion in computational capabilities. Simulations of internal combustion engines require applying chemical models to convert the fuel into combustion products with numerical treatments of the fluid dynamics of reacting flows. Many recent efforts to meet the demands of improved fuel economy and reduced emissions focus on low-temperature combustion schemes [14], [15], where the chemical aspects of the simulations are essential. Similarly, the push to consider alternative fuels to reduce net CO_2 emissions and improve our energy security requires a detailed understanding of the connection between engine performance and fuel structure, with fuel chemistry being an integral part of this connection [16]. Chemical models for combustion are also of continuing importance for stationary combustors with oxy-fuel [17] and mild combustion [18] schemes continuing to be developed and ever higher pressures being considered [19], [20] again in response to efficiency and pollutant formation concerns.

Historically, engine simulations have, by necessity, employed minimal representations of either the chemistry or the fluid dynamics. Continuing advances in computational algorithms and hardware allow simulations that employ more physically realistic treatments of both aspects of the problem [21], [22]. As a result, such simulations are beginning to be used as engine design tools [23]. Continued improvements in the predictive accuracy of such simulations should greatly

enhance their utility in reducing the number of expensive and time-consuming prototypes that need to be built.

Chemical models for combustion are used to describe not only the conversion of the fuel into oxidation products but also the formation of various pollutants such as NO_x, soot, and unburned hydrocarbons. Thus, comprehensive chemical models nowadays consist of thermochemical and transport properties for hundreds to thousands of species, together with rate coefficients for the thousands to tens of thousands of reactions that connect these species within the combustion environment. The most extensive mechanisms focus on surrogate fuels' low-temperature chemistry. In contrast, the smaller mechanisms tend to be either reduced versions of these large mechanisms for utility in complex fluid dynamics simulations or mechanisms that focus on the chemistry of small foundational fuels such as hydrogen, methane, syngas, and natural gas.

The fidelity of the full simulations naturally depends on the accuracy of the parameters that make up the chemical model. Theoretical chemical reaction kinetics has long been critical in developing quantitative models for the underlying elementary reaction rate coefficients [24]–[26]. Historically, theory has focused on interpreting and extrapolating data from experimentally accessible conditions to those relevant to combustion. The overarching goal of combustion chemical modeling is to provide a model that faithfully reproduces the chemical transformations that occur during the conversion of the fuel into products and pollutants for all relevant conditions of temperature, pressure, stoichiometry, and dilution. With computational advancements, the accuracy of high-level computational chemistry studies now often rivals that of experiments. As a result, theoretical predictions are routinely incorporated into chemical kinetic mechanisms.

Early studies predicting chemical phenomena often relied on experiments and empirical rules while limited to specific conditions based on experimental capabilities [27]. Early theoretical

methods allowed for further extension of these experimentally predicted rates for small molecules to a wider range of conditions outside experimental capabilities, but applications of which were limited by computing power and resources. Computational power and capability have advanced rapidly since the start of the 21st century, and the development of more accurate and detailed chemical kinetic mechanisms has progressed alongside it [28], [29]. Before the year 2000, some of the largest kinetic mechanisms contained less than 500 species and 1000 reactions, whereas now increased computing power has allowed for larger mechanisms containing thousands of species and tens of thousands of reactions [30]. These mechanisms utilize electronic structure theory calculations to describe the interaction between individual atoms and molecules. These high-level quantum calculations are used to understand the thermochemistry of each species involved. Estimating methods may be used to determine the thermochemical properties where these quantum calculations cannot be applied due to complexity or computational cost. These molecular-level interactions are then scaled up to produce complete mechanisms. Various experiments have been developed over the years to help elucidate important aspects of fuel combustion, each type providing different insights and data sets at varying conditions. In general, experiments provide a way to measure combustion properties and behavior directly. Experiments provide datasets that can be used to narrow the scope of computational evaluation reducing the time and computational cost involved in modeling combustion phenomena. Efforts to automate the computational process has provided another avenue for application of results from experiments as training datasets. As these mechanisms continue to become more comprehensive, they have been recognized as a cost-effective way to predict parameters over a wide range of conditions including those outside of experimental capabilities.

An example of the synergy that can be achieved between experimental measurement and computational modeling is presented in Chapter 4 and Chapter 5. Micro-reactor experiments are used in conjunction with chemical kinetic mechanism development to predict the decomposition behavior of various fuels and fuel additives. These molecules are evaluated using Time of Flight (TOF) Mass Spectrometry (MS), and wherever relevant, the results from these experiments are used to refine the chemical kinetic model.

A detailed description of the theoretical methodology used to calculate energetics and reaction rate constants has been explained elsewhere [4], but a brief description is provided in the next section.

3.1.1 Potential Energy Surfaces

Preliminary potential energy surfaces (PES) of the primary fuel molecule and subsequent radicals showing the relative energies of each chemical species and the energetic barriers to reaction (transition states (TS)) connecting these species are generated using KinBot[31], a code that automatically identifies relevant stationary points and reactions on a surface. KinBot jobs were run at the b3lyp/6-311++g* level of theory. An energy barrier threshold of 120 kcal/mol above the reactant well was used for each PES to reduce the computational cost of the calculations performed by KinBot. This combination of method and basis set is identified as a happy medium between accuracy and computational cost. Simple bond fissions and reactions featuring a transition state below the lowest bond fission (+5 kcal/mol) were considered for further manual computational exploration.

The rovibrational properties of the stationary points of the relevant pathways identified with KinBot were calculated at the M06–2X/cc-pVTZ level of theory using Gaussian16[32]. At

the same level of theory, 1-D hindered rotor scans were performed for each rotatable bond to capture better the internal motion's influence on the rate constants. Additionally, the scans help confirm the lowest energy conformers of the stationary points were found. More accurate energy estimates of the static points were achieved via single-point energy calculations at the CCSD(T)/cc-pVnZ level of theory (where n=D, T). These energies were extrapolated to an infinite basis set using the formulation found in[33], [34]. To confirm the suitable single-reference methods used in this work, the T1diagnostic was calculated for each stationary point. Final energies are reported at the CCSD(T)/cc-pV∞Z//M06-2X/cc-pVTZ level of theory.

3.1.2 Rate Constant Calculations

Optimized geometries, frequencies, energies, and rotor scans are inputs used to calculate pressure and temperature-dependent rate constants. The master equation system solver (MESS) code [35] developed at Argonne National Laboratories was used to calculate reaction rate constants due to its ability to handle "multiple-well" interactions effectively. When experimental data was not available to tune parameters, a value of $<\Delta Ed> = 200$ cm-1(T/298 K)0.85 was assumed for the collider N2, which helps model a molecule's ability to transfer energy with pressure-related collisions. For all transition state barriers, Eckart tunneling corrections were included. The PhaseSpaceTheory keyword was used to model the barrierless reactions of with the interaction potential assumed to follow a standard Cr-6 model. The exponential prefactor C was varied until the high-pressure rate of the recombination of the radicals had a value of approximately 1.5 x 10-11 cm3/molecules-s based on previous work[36], [37]. The final rates were calculated and converted to the standard PLOG format accepted by CHEMKIN-Pro. Only reactions that had non-zero branching ratios under these P and T conditions were included in the updated mechanism.

3.2 References

[1] K. Kohse-Höinghaus, "Combustion in the future: The importance of chemistry," *Proc. Combust. Inst. Int. Symp. Combust.*, Sep. 2020, doi: 10.1016/j.proci.2020.06.375.

[2] R. K. Hanson, "Applications of quantitative laser sensors to kinetics, propulsion and practical energy systems," *Proc. Combust. Inst.*, vol. 33, no. 1, pp. 1–40, Jan. 2011, doi: 10.1016/j.proci.2010.09.007.

[3] R. J. Tancin, G. C. Mathews, and C. S. Goldenstein, "Design and application of a high-pressure combustion chamber for studying propellant flames with laser diagnostics," *Rev. Sci. Instrum.*, vol. 90, no. 4, p. 045111, Apr. 2019, doi: 10.1063/1.5081671.

[4] W. Cai and C. F. Kaminski, "Tomographic absorption spectroscopy for the study of gas dynamics and reactive flows," *Prog. Energy Combust. Sci.*, vol. 59, pp. 1–31, Mar. 2017, doi: 10.1016/j.pecs.2016.11.002.

[5] F. N. Egolfopoulos, N. Hansen, Y. Ju, K. Kohse-Höinghaus, C. K. Law, and F. Qi, "Advances and challenges in laminar flame experiments and implications for combustion chemistry," *Prog. Energy Combust. Sci.*, vol. 43, pp. 36–67, Aug. 2014, doi: 10.1016/j.pecs.2014.04.004.

[6] Li, Yuyang, and Fei Qi. “Recent Applications of Synchrotron VUV Photoionization Mass Spectrometry: Insight into Combustion Chemistry.” Accounts of Chemical Research, vol. 43, no. 1, 25 Aug. 2009, pp. 68–78, https://doi.org/10.1021/ar900130b. Accessed 14 May 2022.

[7] N. Hansen, T. A. Cool, P. R. Westmoreland, and K. Kohse-Höinghaus, "Recent contributions of flame-sampling molecular-beam mass spectrometry to a fundamental understanding of combustion chemistry," *Prog. Energy Combust. Sci.*, vol. 35, no. 2, pp. 168–191, Apr. 2009, doi: 10.1016/j.pecs.2008.10.001.

[8] V. Sick, “High Speed Imaging in Fundamental and Applied Combustion Research.” Proceedings of the Combustion Institute, vol. 34, no. 2, Jan. 2013, pp. 3509–3530, https://doi.org/10.1016/j.proci.2012.08.012. Accessed 15 Feb. 2023.

[9] C.-J. Sung and H. J. Curran, "Using rapid compression machines for chemical kinetics studies," *Prog. Energy Combust. Sci.*, vol. 44, pp. 1–18, Oct. 2014, doi: 10.1016/j.pecs.2014.04.001.

[10] J. Luecke, M. J. Rahimi, B. T. Zigler, and R. W. Grout, "Experimental and numerical investigation of the Advanced Fuel Ignition Delay Analyzer (AFIDA) constant-volume combustion chamber as a research platform for fuel chemical kinetic mechanism validation," *fuel*, vol. 265, p. 116929, Apr. 2020, doi: 10.1016/j.fuel.2019.116929.

[11] P. Kumar and S. Singh Sandhu, "Impact analysis of partially premixed combustion strategy on the emissions of a compression ignition engine fueled with higher octane number fuels: A review," *Mater. Today Proc.*, vol. 45, pp. 5772–5777, Jan. 2021, doi: 10.1016/j.matpr.2021.02.621.

[12] Y. Chen, B. Deng, M. Chen, and K. Hou, "An approach to estimate CCV (cycle-to-cycle variation) of effective energy output of thermal engine: A case study on a high speed gasoline engine," *Case Stud. Therm. Eng.*, vol. 28, p. 101624, Dec. 2021, doi: 10.1016/j.csite.2021.101624.

[13] S. J. Klippenstein, "From theoretical reaction dynamics to chemical modeling of combustion," *Proc. Combust. Inst.*, vol. 36, no. 1, pp. 77–111, Jan. 2017, doi: 10.1016/j.proci.2016.07.100.

[14] J. E. Dec, "Advanced compression-ignition engines—understanding the in-cylinder processes," *Proc. Combust. Inst.*, vol. 32, no. 2, pp. 2727–2742, Jan. 2009, doi: 10.1016/j.proci.2008.08.008.

[15] R. D. Reitz and G. Duraisamy, "Review of high efficiency and clean reactivity controlled compression ignition (RCCI) combustion in internal combustion engines," *Prog. Energy Combust. Sci.*, vol. 46, pp. 12–71, Feb. 2015, doi: 10.1016/j.pecs.2014.05.003.

[16] F. L. Dryer, “Chemical kinetic and combustion characteristics of transportation fuels,” Proceedings of the Combustion Institute, vol. 35, no. 1, pp. 117–144, 2015.

[17] M. B. Toftegaard, J. Brix, P. A. Jensen, P. Glarborg, and A. D. Jensen, "Oxy-fuel combustion of solid fuels," *Prog. Energy Combust. Sci.*, vol. 36, no. 5, pp. 581–625, Oct. 2010, doi: 10.1016/j.pecs.2010.02.001.

[18] A. Cavaliere and M. de Joannon, “Mild Combustion,” *Prog. Energy Combust. Sci.*, vol. 30, no. 4, pp. 329–366, Jan. 2004, doi: 10.1016/j.pecs.2004.02.003.

[19] F. L. Dryer and M. Chaos, "Ignition of syngas/air and hydrogen/air mixtures at low temperatures and high pressures: Experimental data interpretation and kinetic modeling implications," *Combust. Flame*, p. 8, 2008.

[20] P. Pal, A. Mansfield, P. Arias, M. Wooldridge, and H. Im, "A computational study of syngas auto-ignition characteristics at high-pressure and low-temperature conditions with thermal inhomogeneities," *Combust. Theory Model.*, vol. 19, pp. 587–601, Jul. 2015, doi: 10.1080/13647830.2015.1068373.

[21] K. Anand, R. D. Reitz, E. Kurtz, and W. Willems, "Modeling Fuel and EGR Effects under Conventional and Low Temperature Combustion Conditions," *Energy Fuels*, vol. 27, no. 12, pp. 7827–7842, Dec. 2013, doi: 10.1021/ef401989c.

[22] P. Pal, Y. Wu, T. Lu, S. Som, Y. C. See, and A. Le Moine, "Multidimensional Numerical Simulations of Knocking Combustion in a Cooperative Fuel Research Engine," *J. Energy Resour. Technol.*, vol. 140, no. 10, May 2018, doi: 10.1115/1.4040063.

[23] R. D. Reitz, "Directions in internal combustion engine research," *Combust. Flame*, vol. 160, no. 1, pp. 1–8, Jan. 2013, doi: 10.1016/j.combustflame.2012.11.002.

[24] A. F. Wagner, "The challenges of combustion for chemical theory," *Proc. Combust. Inst.*, vol. 29, no. 1, pp. 1173–1200, Jan. 2002, doi: 10.1016/S1540-7489(02)80148-1.

[25] J. A. Miller, "Theory and modeling in combustion chemistry," *Symp. Int. Combust.*, vol. 26, no. 1, pp. 461–480, Jan. 1996, doi: 10.1016/S0082-0784(96)80249-9.

[26] J. A. Miller, M. J. Pilling, and J. Troe, "Unravelling combustion mechanisms through a quantitative understanding of elementary reactions," *Proc. Combust. Inst.*, vol. 30, no. 1, pp. 43–88, Jan. 2005, doi: 10.1016/j.proci.2004.08.281.

[27] Th. Ackermann, "S. W. Benson: Thermochemical Kinetics. Methods for the Estimation of Thermochemical Data and Rate Parameters. John Wiley & Sons, Inc., New York, 1968. XII und 223 Seiten, 4 Abbildungen. Preis: 94 s," *Berichte Bunsenges. Für Phys. Chem.*, vol. 73, no. 2, pp. 241–241, 1969, doi: 10.1002/bbpc.19690730226.

[28] J. A. Miller *et al.*, "Combustion chemistry in the twenty-first century: Developing theory-informed chemical kinetics models," *Prog. Energy Combust. Sci.*, vol. 83, p. 100886, Mar. 2021, doi: 10.1016/j.pecs.2020.100886.

[29] W. H. Green *et al.*, "Computer Construction of Detailed Chemical Kinetic Models for Gas-Phase Reactors," *Ind. Eng. Chem. Res.*, vol. 40, no. 23, pp. 5362–5370, Nov. 2001, doi: 10.1021/ie001088s.

[30] H. Curran, "Developing detailed chemical kinetic mechanisms for fuel combustion," *Proc. Combust. Inst.*, vol. 37, pp. 57–81, Jan. 2019, doi: 10.1016/j.proci.2018.06.054.

[31] R. Van de Vijver and J. Zádor, "KinBot: Automated stationary point search on potential energy surfaces," *Comput. Phys. Commun.*, vol. 248, p. 106947, Mar. 2020, doi: 10.1016/j.cpc.2019.106947.

[32] Gaussian 16, Revision B.01, Frisch, M.J., et al. Gaussian, Inc., Wallingford CT (2016) GaussView 5.0. Wallingford, E.U.A.

[33] J. A. Miller and S. J. Klippenstein, "From the Multiple-Well Master Equation to Phenomenological Rate Coefficients: Reactions on a C3H4 Potential Energy Surface," *J. Phys. Chem. A*, vol. 107, no. 15, pp. 2680–2692, Apr. 2003, doi: 10.1021/jp0221082.

[34] J. M. L. Martin, "Ab initio total atomization energies of small molecules — towards the basis set limit," *Chem. Phys. Lett.*, vol. 259, no. 5, pp. 669–678, Sep. 1996, doi: 10.1016/0009-2614(96)00898-6.

[35] Y. Georgievskii, J. A. Miller, M. P. Burke, and S. J. Klippenstein, "Reformulation and solution of the master equation for multiple-well chemical reactions," *J. Phys. Chem. A*, vol. 117, no. 46, pp. 12146–12154, Nov. 2013, doi: 10.1021/jp4060704.

[36] A. Miyoshi, "Systematic Computational Study on the Unimolecular Reactions of Alkylperoxy (RO2), Hydroperoxyalkyl (QOOH), and Hydroperoxyalkylperoxy (O2QOOH) Radicals," *J. Phys. Chem. A*, vol. 115, no. 15, pp. 3301–3325, Apr. 2011, doi: 10.1021/jp112152n.

Chapter 4: Experimental and theoretical evaluation of the links between structural details and the sooting tendency of methylcyclohexene isomers

4.1 Introduction

Combustion-related air pollution associated with transport, electricity generation, or industrial use is documented to significantly impact mortality and cardiovascular and respiratory health[1]–[6]. Among the primary drivers for the increased ecological risk is the formation of particulate matter (PM) during the combustion of fossil fuels[2]. The presence of particulate matter in the atmosphere is further augmented by the significant release of organic material during wildfires worldwide [7]. The chemical composition and characteristics of these substances must be understood to recognize the long-term effects of these particles on climate, air quality, and health. Hence, the knowledge of kinetics and formation mechanisms for these particles, their interaction with reactive species, and the development of predictive models are critical[2].

Particulate matter in diesel engines originates from the clustering of unburnt fuel, partly burnt lubrication media, water, and sulfates[8], [9]. The levels of PM produced in diesel engines are almost six to ten times higher than in spark ignition engines[9]. However, with the drive to extract larger amounts of power and improve efficiency from SI engines through direct injection, the amount of PM produced by these engines is also rising[10]. Regulatory changes and a general awareness of the ecological impact of these emissions had resulted in the adoption of particulate matter filters in most diesel vehicles. However, the cost and complexity of these devices prevent a

more widespread proliferation of these systems[11]. Changing fuel composition is an alternative solution that could greatly impact internal combustion engine PM emissions, mitigating the need for a costly particle filter solution[12].

The development of alternate fuel compositions has benefitted from applying computational models and numerical indices to predict likely emissions. These methods include the smoke point[13], threshold sooting index[14], oxygen extended sooting index, and the Particulate Matter Index (PMI)[15]. These methods either rely on experimental results, scaled up from simple organic molecules to predict the sooting tendency of different molecules, or through empirical chemical assessments of different chemical tendencies to form fine particles. The Yield Sooting Index (YSI) [16], [17]developed at Yale University is a more precise tool. This technique is agnostic of experimental parameters and links the chemical structure to the sooting tendency. An extension of the YSI is in the form of the quantitative structure-activity relationship (QSAR) model[18], [19]. This predictive tool applies YSI data to guess the likely soot produced from a chemical compound using existing, validated YSI data as training models. This tool is critical to ensuring that a large number of potential fuel candidates can be quickly screened for their tendency to form particulate matter. There are, however, scenarios where the model fails to capture sooting chemistry precisely. This presents an opportunity to add more nuanced exceptions to the training data to improve the fidelity of these predictive tools.

An example of an opportunity to enhance the training dataset of this model was investigated by Kim et al. [12] through an analysis of the YSI of three methylcyclohexene (MCHe) isomers. This study noted that the experimental measurements varied considerably from the predictions of the QSAR model. The model consistently over-predicted the YSI values by 7 to 46 units[19]. Specifically, the experimentally observed value for *3* methyl-1-cyclohexene (3MCHe)

in studies by Das et al. [18] of 85 was significantly higher than that of the other two isomers, *1*-methyl-1-cyclohexene (1MCHe) and *4*-methyl-1-cyclohexene (4MCHe), each with a YSI of ~62 units. Kim et al. [12], through the application of density functional theory (DFT) and flow reactor experiments (T=850-1100 K, Φ=1.0), validated this difference in YSI values by showing that the preferred reaction route for both 1 MCHe and 4 MCHe decompositions to be through the stepwise retro-Diels Alder reactions. In the case of 3MCHe, there were additional competing pathways to form higher amounts of cyclic dienes and aromatics, known as soot precursors. Despite undergoing decomposition through different routes, the activation-energy barrier for the primary reactions is similar in all three isomers, complicating an empirical evaluation. The experimental conditions of the evaluations carried out by Kim et al. [12] could allow for bimolecular reaction reactions in addition to oxidation. This could result in H-atom abstraction reactions from the fuel, obscuring other direct decomposition routes. Figure 4.1 shows the primary decomposition routes for each isomer.

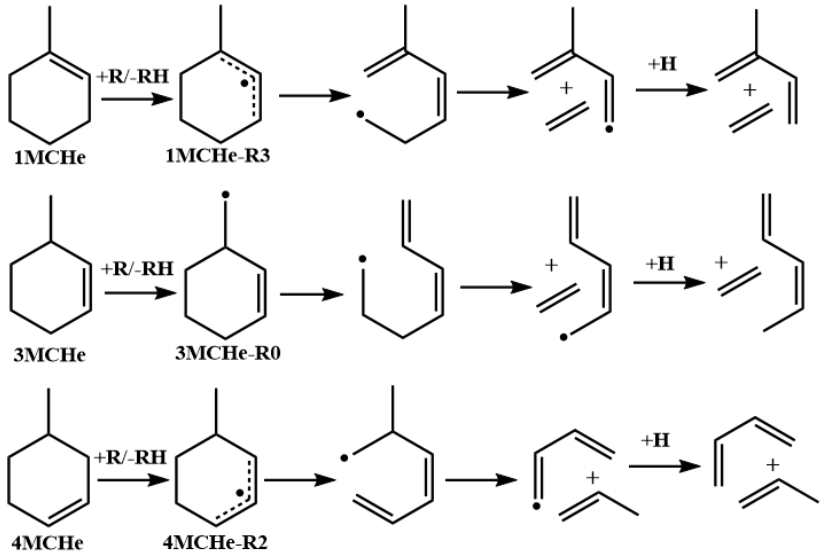

Figure 4.1: The Retro-Diels-Alder stepwise mechanism for each MCHe isomer, as described by Kim et al.[12]. The pathways are initiated through biomolecular reactions where free radicals abstract H-atoms from the fuel.

The oxidative nature of the experimental conditions under which Kim et al.[12] evaluated the decomposition resulted in the H-atom abstraction from the carbon atoms in the ring in the case of 1MCHe and 4MCHe as opposed to the methyl group in the case of 3MCHe. The formation of allylic radicals in the case of 1MCHe and 4 MCHE is followed by a stepwise retro Diels-Alder reaction to form an alkene and a diene. For 3MCHe, since the H-atom abstraction was on the methyl group, the radical formed tended to prefer dehydrogenation to form cyclohexadiene and toluene, known as soot precursors. To fully understand the effects of experimental parameters on the decomposition process, the competition between the formation and decomposition of radical isomers, the stepwise retro Diels-Alder, and the concerted-retro-Diels-Alder pathways are critical to consider in predicting sooting tendency for methyl cyclohexenes.

Isomers of MCHe have primarily been evaluated experimentally in bimolecular environments. While these are critical studies to understanding soot formation in engine-relevant conditions, distinctions between unimolecular decomposition's role and the fuel's abstraction chemistry are clouded. Further insight can be gained by studying the pyrolysis of the MCHe isomers under dilute conditions where bimolecular chemistry is suppressed. There have been limited investigations on understanding the thermal decomposition of the three isomers. Garnett et al.[20], in 1976, evaluated the pyrolysis of 1MCHe, documenting the formation of 1,3 butadiene and ethylene as the retro Diels-Alder products at 495°C. In 2015, Gardiner et al.[21] studied the comparative decomposition of 1MCHE and 4MCHe through velocity map imaging. Kim et al.[12] also studied the unimolecular decomposition pathways and documented the energetics of the possible isomerization of the radicals. These results served as the baseline for an in-depth evaluation of the unimolecular decomposition of 1MCHe, 4MCHe, and 3MCHe to explain their different sooting tendencies.

This chapter presents an experimental evaluation focused on observing the pyrolysis reactions of the three isomers (1MCHe, 3MCHe, and 4MCHe) using the photoionization mass spectrometry (PIMS) time of flight experiment. This evaluation presents an ideal use case to compare the performance of two different ionization sources – the fixed wavelength Nd:YAg laser at 10.487 eV (118.2 nm) and the prototype Hyperion VUV laser. These results are then combined with theoretical calculations of the unimolecular decomposition of the MCHe isomers, and their radicals, the first radicals produced directly from the fuels themselves, are identified, along with the likely pyrolysis pathways that lead to the formation of soot precursors. This approach allows us to resolve which products are directly formed from the fuel itself and help separate that chemistry from the bimolecular chemistry previously observed [12], [22], which can further improve the ability of predictive models for YSI [19].

Dissociative ionization is a challenge encountered while using fixed wavelength ionization sources where pyrolysis products are often indistinguishable from those produced by the interaction of the ionizing photons and the fuel. The operation of the PIMS experiment with a tunable frequency light source enables isomer resolution by selectively ionizing products of decomposition, which is not with the fixed wavelength Nd:YAg system. The ability to operate the laser across a range of wavelengths also reduces the effects of dissociative ionization. Further, by operating at higher energy levels (10.8 eV) it is possible to observe products whose ionization energy is greater than that of the fixed wavelength source.

4.2 Experimental and computational methods

4.2.1 Experimental evaluation of pyrolysis

The experimental data obtained in this study were measured using a microreactor coupled with PIMS detection methods described in detail elsewhere[23]–[26]. Here, we describe the experiment briefly. A microreactor tube that is 1 mm in internal diameter and approximately 3 cm long made of silicon carbide (SiC) is resistively heated, and the wall temperature is monitored using a Type C thermocouple. Silicon carbide is chemically inert with a high melting point, making it a suitable choice for high-temperature pyrolysis studies. The reactor wall temperature uncertainty is estimated to be ± 50 K due to variations in temperature along the length of the reactor wall, and measurements were obtained at steady wall temperatures in 100 K increments along a temperature range of 500-1500 K for all three isomers with an additional measurement at room temperature. Guan et al. [26] reported that the gas centerline peak temperature is approximately 100 K lower than the measured wall temperature of the reactor after passing through approximately one-third of the reactor length. Typical reactor residence times are on the order of 150 ms, and the pressure behind the reactor is ~200-500 Torr [26]. Upon exiting the reactor, the gas expands supersonically into a source chamber held at ~10-4 Torr. The expansion causes near-instantaneous cooling, which limits molecular collisions and suppresses further chemistry. The exiting stream is skimmed to form a molecular beam directed to the ionization chamber held at ~10-6 Torr.

Products of decomposition are measured with PIMS using the 9th harmonic of an Nd: YAG laser, which is generated by taking the 3rd harmonic of the Nd: YAG (Spectra-Physics) through an Ar/Xe tripling cell producing vacuum ultraviolet photons (118.2 nm or 10.487 eV with 0.5 μJ pulse−1 at 30 Hz). The mass spectra are collected using a Jordan reflectron TOF mass

spectrometer. A Channeltron-type electron multiplier detects the ionized species, and the spectra are collected with a digital oscilloscope interfaced with a computer.

Confirmation of the data collected using the Nd: YAG laser system was obtained through PIMS experiments carried out using the 8th harmonic (9.6 eV, 3x1012 photons/s) and 9th harmonic (10.8 eV, 1x1012 photons/s) of a pre-production model of the KMLabs Hyperion VUVTM, which is an ultrafast fiber laser source (the Y-Fi UltraTM) in conjunction with highly cascaded four-wave-mixing harmonic generation in a xenon-filled hollow negative-curvature fiber. In this system, the output of a ytterbium-doped fiber mode-locked oscillator is amplified in three stages by chirped-pulse amplification. This results in approximately 10 W average power at a center wavelength of 1035 nm, 1 MHz repetition rate, and 160 fs pulse duration. A beta-barium borate (β-BBO) crystal is used to generate 4 W (4 μJ pulse energy) of the second harmonic, 517 nm, and focus both the 517 nm and 1035 nm light into a hollow-core negative curvature fused silica fiber. The two-color driving laser enables a cascaded four-wave-mixing process that generates all harmonics of the 1035 nm fundamental up to the 15th harmonic. More details on the operation and applications of the tunable VUV source and setup can be found in work by Couch et al. [27]. Species ionized by intercepting pyrolysis products and this photon source are detected and characterized using the same reflectron system detailed previously. The individual mass spectra obtained for each ionization source in this work are included in Appendix C4 (Figures S4.1-S4.3).

High purity He (99.999%) from Airgas was used as the diluent for each MCHe isomer. 3MCHe was obtained from TCI Chemicals (3MCHe: ≥ 93.0% purity) and 4MCHe and 1MCHe were obtained from Sigma Aldrich (1MCHe: ≥ 96.5% purity, 4MCHe: ≥ 98.5% purity). Dilute gas mixtures were prepared in a stainless-steel cylinder using a Setra Model 280G pressure transducer

to deliver He and an MKS 750B Baratron absolute pressure transducer for the fuels. Gases flow continuously through the reactor at 200 SCCM using an MKS Mass Flow Controller (MFC). The final mixtures were 0.01% of a single MCHe isomer in helium based on partial pressures, and under these conditions, we expect bimolecular chemistry to be minor compared to the unimolecular chemistry with these selected concentrations or reaction conditions.

4.2.2 Computational evaluation of pyrolysis

While the mass spectra produced can provide a snapshot of the key reaction intermediates and radicals present within the microreactor during the experiments, further understanding of the breakdown energetics is necessary to attribute these intermediates to specific mechanistic steps. This work generated a potential energy surface (PES) for the unimolecular decomposition of each MCHe isomer, including all bond dissociation energies and the retro-Diels-Alder pathway. Starting geometries for the retro-Diels-Alder transition states and products were obtained from Kim et al. [12]. For any bond fission routes found active under our experimental conditions (T = 300-1500 K, P ≅ 0.1atm), the resulting radicals were also explored computationally. KinBot [28] was used to provide preliminary PESs of these MCHe radical decompositions at the B3LYP/6-311++G* level of theory. All explored pathways were further refined to obtain more accurate energetics using the following technique.

The rovibrational properties and geometry optimizations of the reactants, products, and transition states were determined at the M06-2X/cc-pVTZ level of theory using Gaussian 16 [29]. 1-D hindered rotor calculations were also performed at the M06-2X/cc-pVTZ level of theory which is a necessary component of the rate constant calculations as they describe the internal rotational motion of a molecule. Higher-level energy estimates for the stationary points were obtained using the CCSD(T)/cc-pV∞Z method, where the infinite basis set limits are estimated

from an extrapolation of results obtained from sequences of cc-pVnZ where n = (D,T) basis sets [30][31]. Final energies are reported at the CCSD(T)/cc-pV∞Z//M06-2X/cc-pVTZ level of theory which includes zero-point correction factors.

The master equation system solver code (MESS) [32] was used to calculate pressure and temperature-dependent rate constants across a wide range of conditions (T= 500-2000 K, P = 0.01 -100 atm). A value of <ΔEd> = 200 cm-1(T/298 K)0.85 was used for the collider He, which helps accurately model the collisional energy transfer. Eckart tunneling corrections were included for the concerted retro-Diels-Alder pathways and important radical decomposition pathways to account for tunneling. The bond fissions were calculated PhaseSpaceTheory feature of MESS, which follows a V=-C/rn model of the potential energy surface as a function of distance. Parameters C and n were calculated by fitting the bond dissociation energy profile as a Morse oscillator between 30-50% past the equilibrium bond length. A full description of this method is found in [33]. The rate constants calculated in this work were fit to PLOG format for use in combustion simulation codes and are included in Appendix C4.

4.3 Results: Pyrolysis kinetics of methylcyclohexene isomers

To discern how the double bond location influences the production of soot precursors for each of the three MCHe isomers under pyrolysis conditions, we applied our combined theoretical and experimental approach to probe the unimolecular decomposition mechanisms. Furthermore, we highlight key observable differences in the radical chemistry between these conditions and those of Kim et al. [12] to help differentiate the soot precursors formed via pyrolysis or an oxidative (bimolecular) environment. We begin our discussion with the 1MCHe and 4MCHe isomers since they have similar measured YSI values (~62) [34]. This is followed by a discussion of the 3MCHe

isomer, which is the outlier of the three isomers having a YSI 22 points higher than the other two [34].

4.3.1 1 methyl-1-cyclohexene

According to Kim et al. [12], under combustion conditions, five radicals are formed via H-atom abstraction from 1MCHe, where the formation of the resonantly stabilized radicals is favored. One of these resonantly stabilized radicals (1MCHe-R3) leads to the stepwise retro-Diels-Alder (Figure 4.1) route, which leads to ring-opening producing isoprene and ethylene and a reduction in sooting tendency. However, under dilute pyrolysis conditions, abstraction reactions play a lessened role. Initiation chemistry from 1MCHe can occur either through the concerted retro-Diels-Alder pathway or through one of seven bond fissions, including a homolytic scission of the methyl group from the ring, as shown in the potential energy surface (PES) for 1MCHe in Figure 4.2.

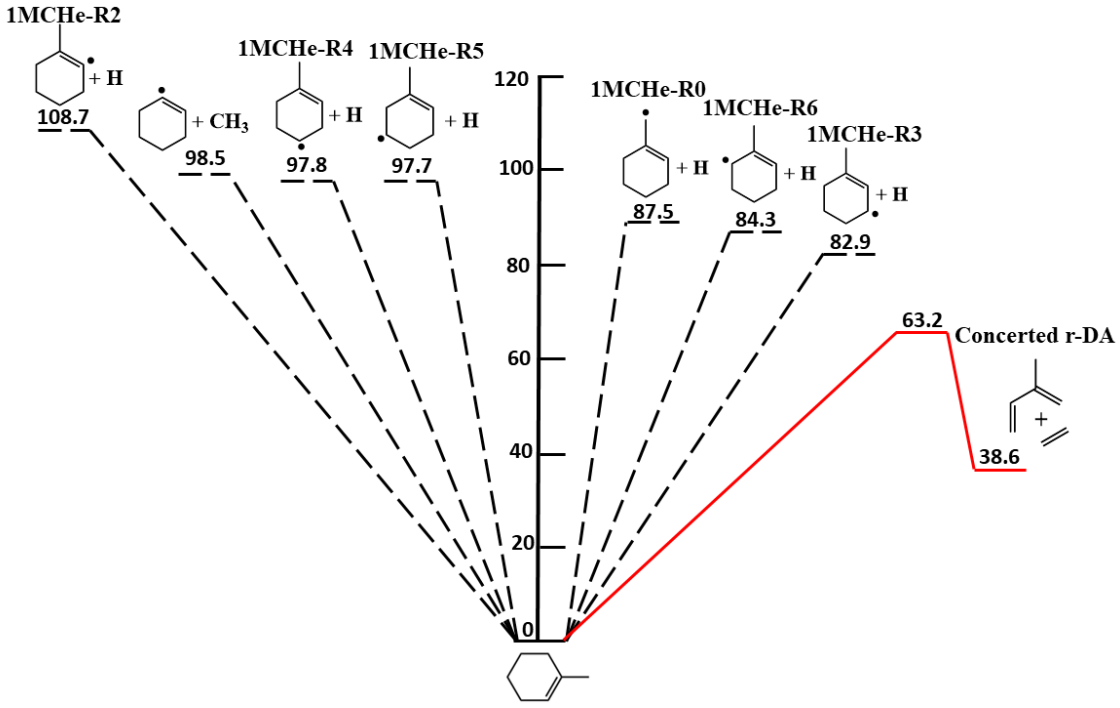

Figure 4.2: Potential energy surface of the unimolecular decomposition of 1MCHe including the bond dissociation pathways and the concerted retro-Diels-Alder (r-DA) route. The energies are

calculated at the CCSD(T)/cc-pV∞Z//M06-2X/cc-pVTZ level of theory and reported in kcal/mol relative to the parent molecule. Solid lines (red) are active, and dashed lines (black) are inactive pathways under our experimental conditions (T=300-1500 K, P≅0.1 atm) according to our rate constant calculations. Branching ratio plots of the decomposition rates can be found in Figure 4.3.

As highlighted by the PES, the concerted retro-Diels-Alder is the lowest energy pathway (63.2 kcal/mol) and has been deemed necessary in previous studies [12] [20]. The energetics show the next likely reactions are one of three C-H bond fissions resulting in a resonantly stabilized radical. In order, the lowest bond dissociation energies are 82.9 kcal/mol to form the 1MCHe-R3 radical, 84.3 kcal/mol to form the 1MCHe-R6 radical, and 87.5 kcal/mol to form the 1MCHe-R0 radical. This is in line with the H-atom abstraction energetics calculated by Kim et al. [12], which also determined that 1MCHe-R3 and 1MCHe-R6 were the most stable abstraction radicals due to their resonantly stabilized structures. Rate constant calculations performed in this work further emphasize that the pyrolysis of 1MCHe is solely dominated by the concerted retro-Diels-Alder reaction under our experimental conditions (see Figure 4.3). The reaction rate for the concerted retro-Diels-Alder reaction is at least an order of magnitude above all other unimolecular reactions for 1MCHe over a temperature range of 500-1500 K. Branching ratio calculations were also performed, where the branching ratio equals the reaction rate constant of interest divided by the sum of all reaction rates, thus yielding a percentage of total unimolecular flux from 1MCHe to products. For 1MCHe, at least 96% of the flux over the 500-1500 K temperature range proceeds through the concerted retro-Diels-Alder path.

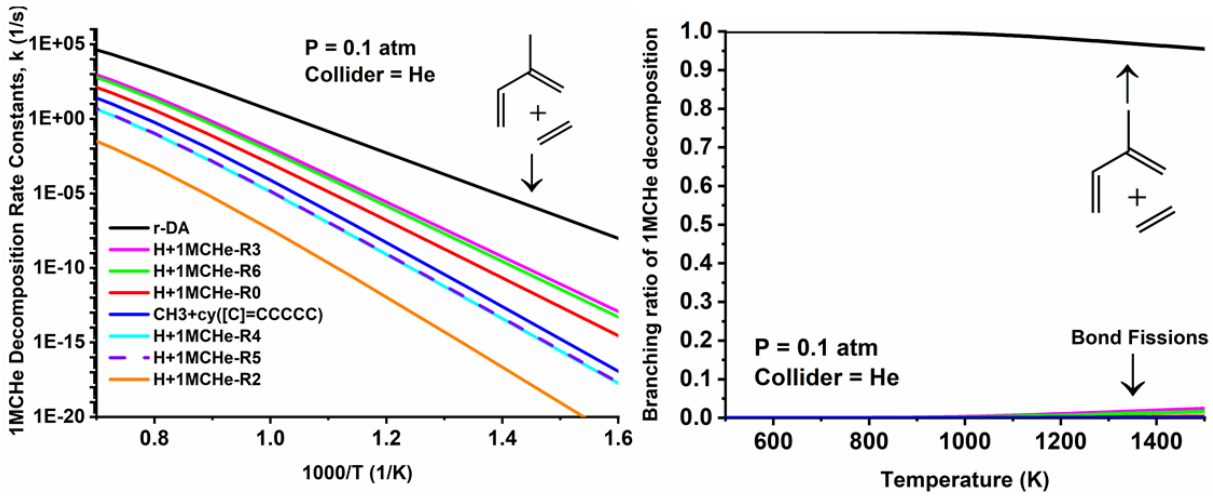

Figure 4.3: Theoretically calculated rate constants (left) and branching ratios (right) for 1MCHe pyrolysis, including bond fissions and the retro-Diels-Alder reaction. Radical names in the legend are the same used in the PES in Figure 2. The most dominant reaction is the concerted retro-Diels-Alder reaction shown in black.

The rates suggest any soot precursors formed during 1MCHe pyrolysis will come from the products of the retro-Diels-Alder reaction, isoprene, and ethylene. Microreactor experiments with 0.01% 1MCHe diluted in He were conducted to confirm our theoretical calculations. Figure 4 4 presents several distinct masses observed experimentally in the PIMS spectra of 1MCHe using the 9th harmonic (10.487 eV) of an Nd: YAg laser, including m/z 96, 81, 78, 68, 52, 40, 39, and 15. Since only the products of the first ionization of each of the respective masses are observed, m/z corresponds to the molecular weight. The data is split into two plots, major species (max peak signal height > 20 %) and minor species (max peak signal height < 20 %), for clarity. The masses in Figure 4.4 are plotted as a percentage (%) of the total maximum peak signal height as a function of temperature at the ionization energy of the Nd: YAg laser (10.487 eV). To obtain the fraction of the total peak signal height for each pass, the maximum signal intensity of the peaks of interest is summed up, and the signal intensity for each mass is divided by the total ion intensity for each temperature sweep. This provides a pseudo-normalization but does not report relative

concentrations since ionization cross-sections are not included. Thus, the data presented in these plots should be considered an indication of the mass presence and not relative mass concentrations.

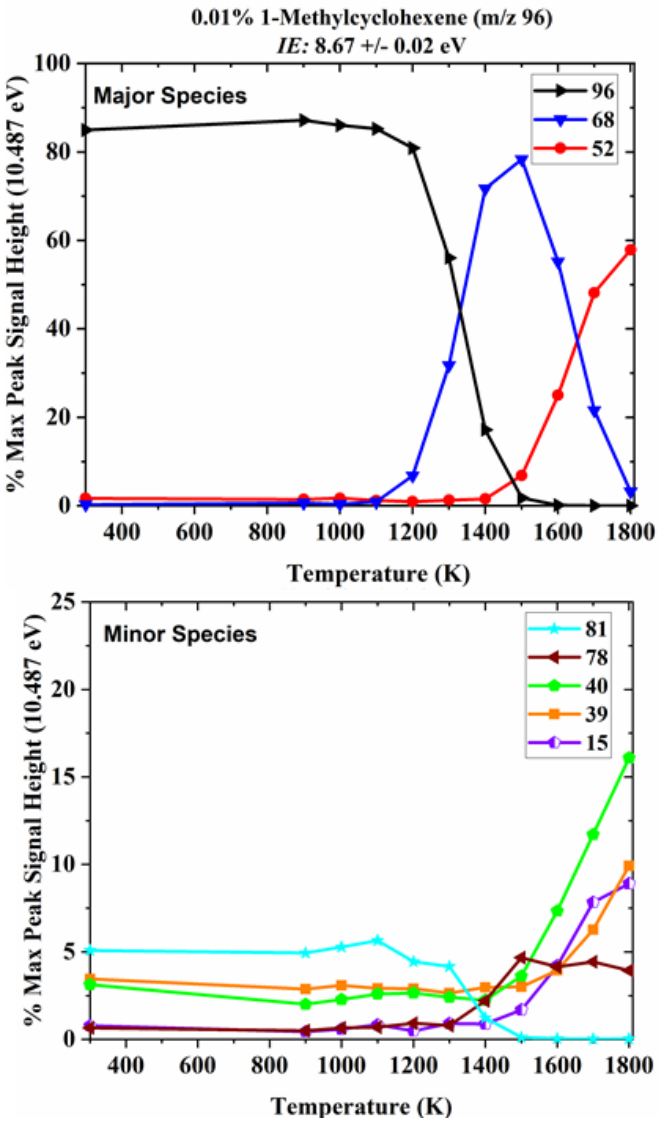

Figure 4.4: Percentage (%) of the total maximum peak signal height as a function of temperature is shown for significant mass values from 1MCHe spectra (IE= 8.67 ± 0.02 eV [35]). *Top:* major species (greater than 20 % flux). *Bottom:* minor species (less than 20 % flux). The presence of dissociative ionization is detected in the 10.487 eV by the presence of m/z 81 at room temperature. PIMS spectra from all three laser intensities used in this work can be found in Appendix C4. C_{13} peaks of the fuel (m/z 97) and isoprene (m/z 69) were left out of the figure for clarity.

1MCHe and Main & Dissociative Ionization Products (Masses 96, 81, and 68): At 500 K the dominant peak is m/z 96, representing the parent peak of 1MCHe. At the same temperature, additional peaks of m/z 39, 40, and 81 are observed, which correspond to the dissociative ionization products of the parent molecule since the IE of 1MCHe at 8.67±0.02 eV [35] is much lower compared to the energy of the ionizing photons (10.487 eV). Since the m/z 81 peak is present at room temperature and decays with increasing temperature, it is not considered a species of note as this is not a pyrolysis product. M/z 39 and 40 remain constant until approximately 1400 K when they begin to increase with temperature, suggesting they are then products of pyrolysis above 1400 K. At 1200 K, an additional peak at m/z 68 is observed. This corresponds to the thermal decomposition of the parent molecule into ethylene m/z 28 (IE of 10.5138 ± 0.0006 eV [36]) and isoprene m/z 68 (IE of 8.85 ± 0.02 eV [37]) via the concerted retro-Diels-Alder reaction which theory indicated to be the only important unimolecular reaction from 1MCHe. Since the ionization energy of ethylene is higher than that of the laser energy (10.487 eV), this peak is visible only in the spectra obtained at the 9th harmonic (10.8 eV) of the Yi-Fi laser, the spectra and plots for which are found in the Appendix C4. The experimental presence of isoprene and ethylene validates the calculated pyrolysis rates showing the retro-Diels-Alder reaction is active under these conditions.

Products of Isoprene Decomposition (Masses 52, 40, 28, and 15): Isoprene production increases up to 1500 K after which the relative signal percentage decreases, suggesting this product is now being consumed via other reactions. The decomposition of isoprene at high temperatures has previously been studied by Weber and Zhang [38]. Above 1200 K, two primary reaction paths are competitive: 1) a bond fission to form methyl radical (m/z 15) plus CH2=C·-CH=CH2 radical (m/z 53), which decomposes to vinyl acetylene (m/z 52), and 2) a unimolecular route forming

ethylene (m/z 28) and allene (m/z 40, IE=9.688 ± 0.002 eV [39]) directly [38]. Figure 4.4 shows evidence of both pathways with masses m/z 52, 40, 28, and 15 all increasing in % max peak signal height above 1500 K as isoprene decays.

Other masses (78, and 39): The remaining masses, m/z 39 and m/z 78 require further investigation. First, m/z 39 is likely propargyl radical formed via an H-atom loss from allene (m/z 40). Excess propargyl could also be formed via H-abstraction from allene via the CH3 radicals produced from the active isoprene bond fission route [38]. Excess amounts of propargyl radical may allow for a recombination reaction of two propargyl radicals to form m/z 78, which was observed experimentally by Weber et al. [38] above 1250 K. The mechanism for propargyl recombination is well known [40] and under the conditions of our experiments, is likely to form the 1,5-hexadiyne (HCºC-CH2-CH2-CºCH), a linear isomer of m/z 78. Thus, all observed masses are explained via the concerted retro-Diels-Alder route and the decomposition of isoprene, and under pyrolysis conditions, the only soot precursors are formed via the formation of propargyl radical and its recombination to form 1,5-hexadiyne. Furthermore, the observed masses substantiate our reaction rate constants, suggesting that under these experimental conditions, the retro-Diels-Alder reaction is the only active pathway.

4.3.2 4 methyl-1-cyclohexene

The same approach of analyzing the thermal decomposition products of 1MCHe was applied to evaluate the other two isomers. Figure 4.5 shows the PES for the unimolecular decomposition of 4MCHe, including the concerted retro-Diels-Alder pathway forming 1,3-butadiene and propene (63.0 kcal/mol). Again, the retro-Diels-Alder reaction has the lowest energy barrier, which is 20 kcal/mol lower than the lowest bond dissociation energy to form 4MCHe-R5.

The 20 kcal/mol difference in energy is approximately the same energy difference calculated for 1MCHe. Like 1MCHe, the resonantly stabilized radicals (4MCHe-R2 and 4MCHe-R5) formed via C-H bond fission have the lowest bond dissociation energies (83.0 and 83.5 kcal/mol, respectively) followed by the methyl bond fission at 86.4 kcal/mol.

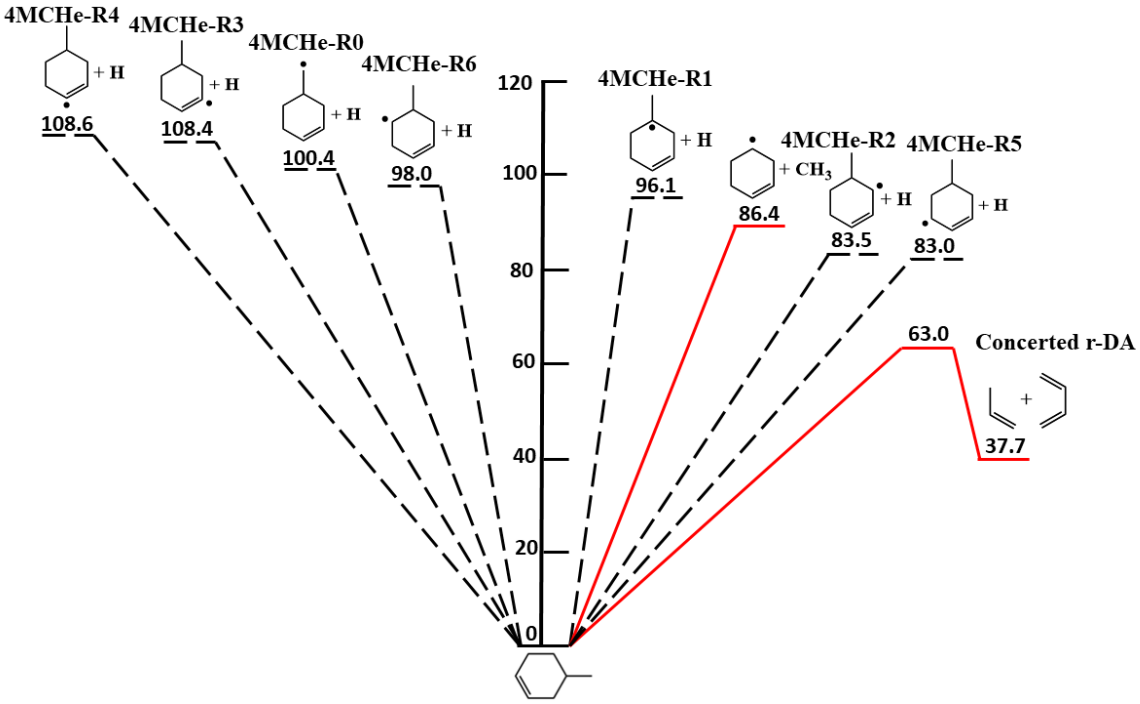

Figure 4.5: Potential energy surface of the unimolecular decomposition of 4MCHe**,**including the bond dissociation pathways and the concerted retro-Diels-Alder route. The energies are calculated at the CCSD(T)/cc-pV∞Z//M06-2X/cc-pVTZ level of theory and reported in kcal/mol relative to the parent molecule Solid lines (red) are active and dashed lines (black) are inactive pathways under our experimental conditions (T=300-1500 K, P≅0.1 atm) according to our rate constant calculations. Branching ratio plots of the decomposition rates can be found in Figure 4.6.

Interestingly, our reaction rate constants in Figure 4.6 suggest two active pathways under our experimental conditions: the concerted retro-Diels-Alder reaction and the methyl bond fission. The retro-Diels-Alder reaction for form 1,3-butadiene and propene is the only active route until ~1000 K, and still is the dominant reaction up to 1500 K. However, at 1000 K, the methyl bond fission starts to play a minor role and reaches a branching fraction of ~22% at 1500 K. Notably

methyl fission from 4MCHe is not the lowest energy bond fission reaction. However, symmetry considerations make methyl fission a more competitive reaction despite the 3.4 kcal/mol increase in bond fission energy over the lowest C-H bond fission.

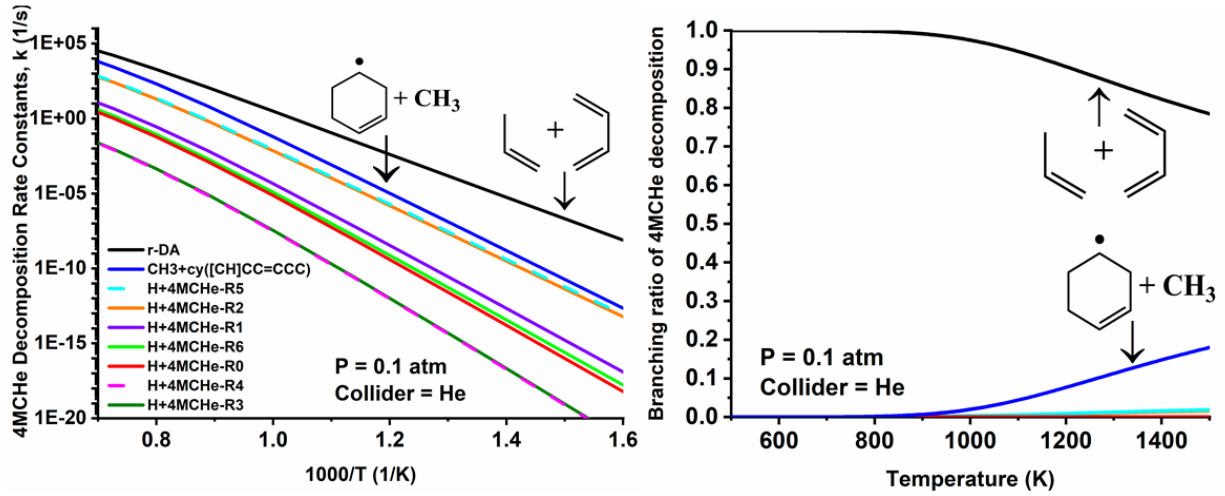

Figure 4.6: Theoretically calculated rate constants (left) and branching ratios (right) for 4MCHe pyrolysis, including bond fissions and the retro-Diels-Alder reaction. Radical names in the legend are the same used in the PES in Figure 4.5. The two active reactions are the concerted retro-Diels-Alder reaction (black) and the methyl bond fission (blue).

4MCHe and Main & Dissociative Ionization Products (Masses 96, 81, 54, and 42): Using the same experimental setup, we can investigate the products formed during the unimolecular decomposition of 4MCHe. Figure 4.7 shows 4MCHe scans run at a concentration of 0.01% in helium at the 10.487 eV laser energy level. In addition to the parent fuel peak at m/z 96, the spectra present an additional peak at m/z 81 at low temperatures, indicating a similar dissociative ionization effect to the one seen in 1MCHe. At 1200 K, peaks at m/z 54 and 42 are observed. As the rate constants suggest, this is evidence of 4MCHe decomposition via the concerted retro-Diels-Alder reaction to form 1,3-butadiene (m/z 54, IE=9.07±0.004eV [41]) and propene (m/z 42, IE=9.7435 ± 0.0005 [42]).

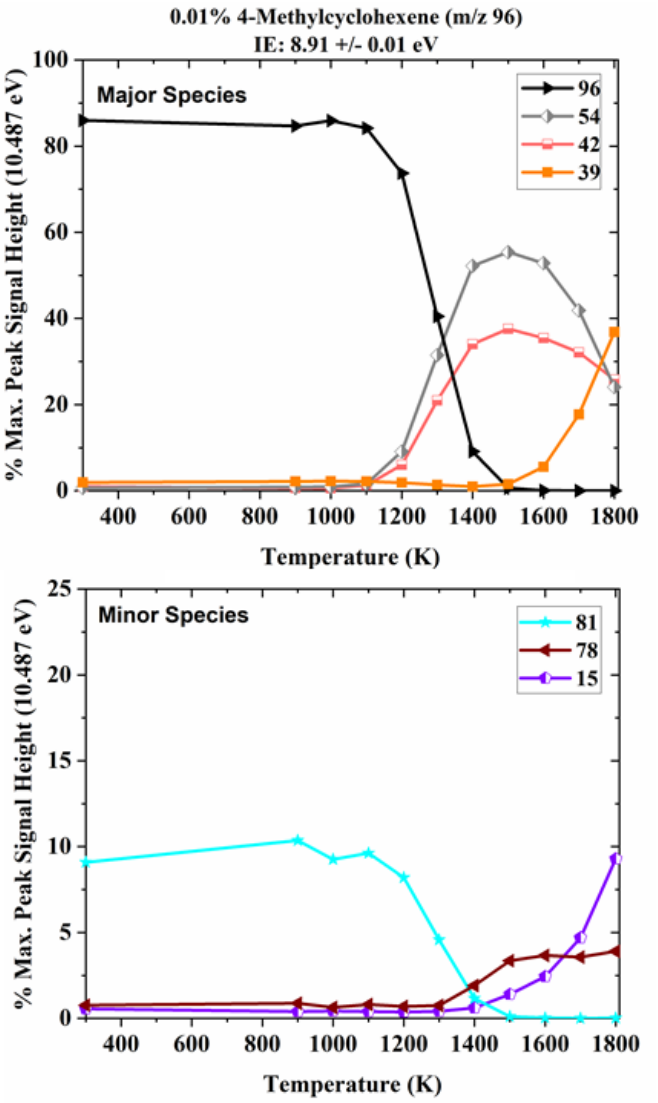

Figure 4.7: Percentage (%) of the total maximum peak signal height as a function of temperature is shown for significant mass values from 4MCHe spectra (IE= 8.91 ± 0.01 eV [35]). *Top:* major species. *Bottom:* minor species. The presence of dissociative ionization is detected in the 10.487 eV by the presence of m/z 81 at room temperature. PIMS spectra from all three laser intensities used in this work can be found in the Appendix C4. C_{13} peaks of the fuel (m/z 97) and 1,3-butadiene (m/z 55) were left out of the figure for clarity.

Products of 1,3-Butadiene (Masses 39 and 15): At 1500 K, 1,3-butadiene (m/z 54) begins to decompose, and peaks at m/z 39 and m/z 15 starts to grow in, suggesting they are direct decomposition products of 1,3-butadiene. This is in line with previous work [43] [44] that demonstrated the primary pyrolysis channel of 1,3-butadiene is to isomerize to 1,2-butadiene,

followed by subsequent C-C bond fission to form methyl radical (m/z 15) and propargyl radical (m/z 39). More recent work by Lockhart et al. [45] suggests a more direct route to form methyl radical and propargyl radical from 1,3-butadiene via direct dissociation, which essentially skips the isomerization step to form 1,2-butadiene.

Other Masses (Mass 78): The remaining mass is m/z 78. As seen in the decomposition of isoprene [38] for 1MCHe and additional studies like that of Scheer et al. [46], when propargyl radicals are produced in excess, a recombination reaction can occur to produce 1,5-hexadiyne (m/z 78). However, our theoretical work suggests a possible second pathway to m/z 78 via the methyl bond fission route. This would involve the remaining radical (m/z 81) to scission of an H-atom forming 2,4-cyclohexadiene (m/z 80). Another H-atom loss followed by a subsequent b-scission of an H-atom would produce benzene (m/z 78). While we cannot distinguish between the isomers of m/z 78 with the current experimental set-up, we believe the route forming benzene is likely a minor route since the 2,4-cyclohexadiene (m/z 80), a stable species with low ionization energy (8.25 eV [47]), is not detected experimentally at any temperature. Additionally, the low fuel concentration (0.01%) used in the study could make observation of this route difficult as the branching ratio only reaches a maximum of 20% at 1500 K.

Considering this, the only definitively observed decomposition route of 4MCHe is the concerted-retro-Diels-Alder reaction, which was verified theoretically and experimentally. While the methyl bond fission route may produce trace amounts of benzene (m/z 78) this would not be distinguishable in our experiment from the linear m/z 78 species likely formed due to propargyl recombination.

4.3.3 3 methyl-1-cyclohexene

Finally, we examine the decomposition of 3MCHe, which has a substantially higher YSI than the other two MCHe isomers. Figure 4.8 shows the PES of the unimolecular decomposition of 3MCHe. Again, the lowest energy pathway is the concerted retro-Diels-Alder reaction (61.1 kcal/mol). However, the lowest bond fission is not a C-H bond, as seen with the previous two isomers. Instead, due to the location of the double bond, the lowest energy bond fission involves breaking the C-C bond to lose the methyl group resulting in a resonantly stabilized 2-cyclohexenyl radical (71.3 kcal/mol). Of note is the difference between this bond dissociation energy and the concerted retro-Diels-Alder energy barrier at only 10.2 kcal/mol, which suggests the lowest energy bond fission is more competitive for 3MCHe than it was for the previous two isomers.

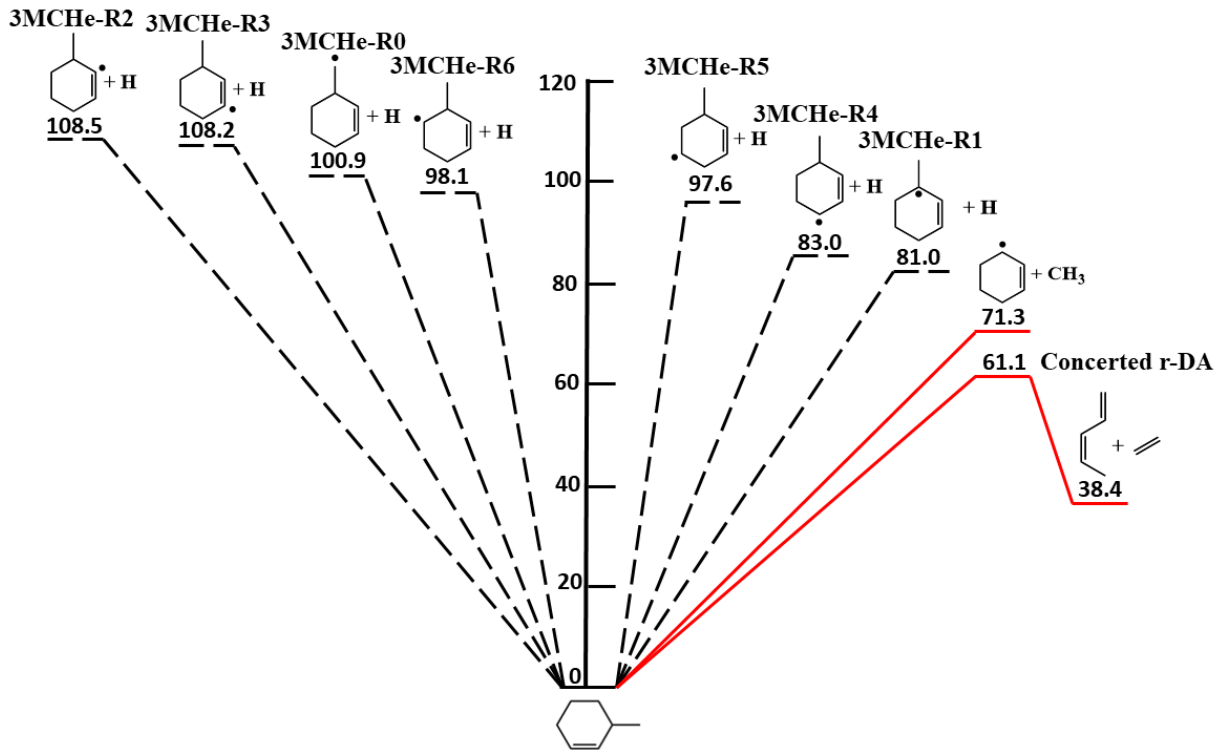

Figure 4.8: Potential energy surface of the unimolecular decomposition of 1MCHe including the bond dissociation pathways and the concerted retro-Diels-Alder (r-DA) route. The energies are calculated at the CCSD(T)/cc-pV∞Z//M06-2X/cc-pVTZ level of theory and reported in kcal/mol relative to the parent molecule. Solid lines (red) are active and dashed lines (black) are inactive pathways under our experimental conditions (T=300-1500 K, P≅0.1 atm) according to our rate constant calculations. Branching ratio plots of the decomposition rates can be found in Figure 4.9.

Rate constant calculations for 3MCHe highlight the competition between the concerted retro-Diels-Alder reaction and the methyl fission pathways at our experimental conditions (T = 300-1500 K, P ≅ 0.1 atm). At lower temperatures, the retro-Diels-Alder reaction is the faster reaction. However, at around T = 750 K, a crossover in branching fraction for 3MCHe decomposition occurs (see Figure 9 right). The methyl cleavage becomes the dominant reaction, leading to a 90/10 split between methyl cleavage and the retro-Diels-Alder reaction at 1500 K. This suggests that both reactions will play a role in the pyrolysis experiments performed in this work, with the production of methyl + 2-cyclohexenyl radical becoming the most important products in the highest wall temperature experiments.

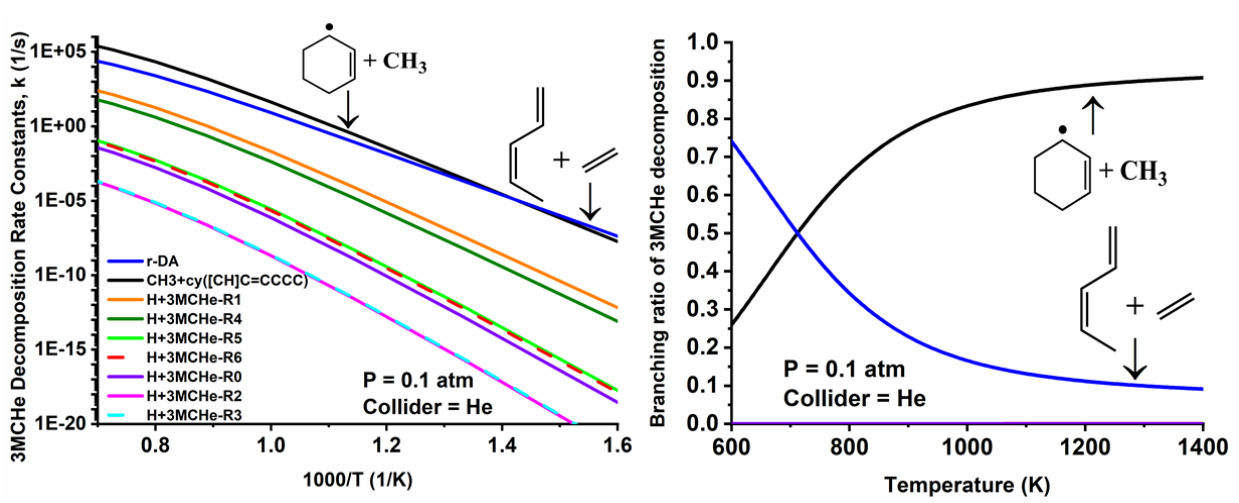

Figure 4.9: Theoretically calculated rate constants (left) and branching ratios (right) for 3MCHe pyrolysis including bond fissions and the retro-Diels-Alder reaction. Radical names in the legend are the same used in the PES in Figure 4.8. The two active reactions are the concerted retro-Diels-Alder reaction (black) and the methyl bond fission (blue).

A similar analysis of 0.01% 3MCHe in helium was carried out using the 10.487 eV ionization source to evaluate thermal decomposition products. The increased number of observed peaks compared to the previous two isomers further confirm that additional chemistry besides the active concerted retro-Diels-Alder reaction under our experimental conditions. Figure 4.10 depicts the observed peaks across all temperatures for the major (top) and minor (bottom) species observed with the 10.487 eV line.

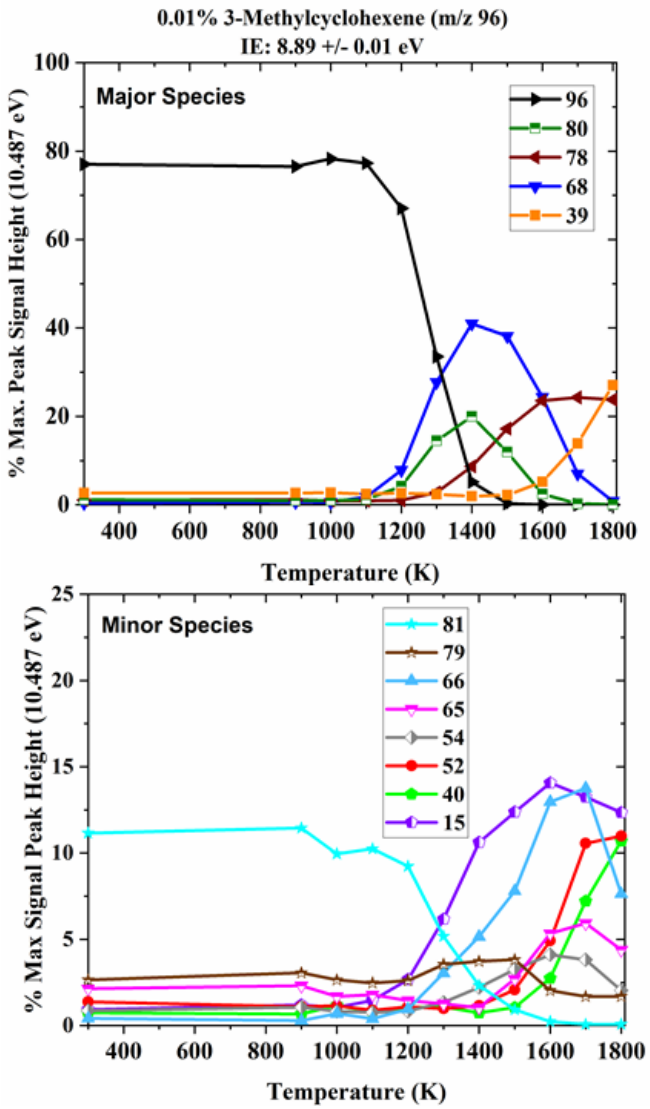

Figure 4.10: Percentage (%) of the total maximum peak signal height as a function of temperature is shown for significant mass values from 3MCHe spectra (IE= 8.89 ± 0.01 eV [35]). *Top:* major species. *Bottom:* minor species. The presence of dissociative ionization is detected in the 10.487 eV by the presence of m/z 81 at room temperature. PIMS spectra from all three laser intensities used in this work can be found in the Appendix C4. C_{13} peaks of the fuel (m/z 97) and 1,3-pentadiene (m/z 69) were left out of the figure for clarity.

3MCHe and Main & Dissociative Ionization Products (Masses 96, 81, 68, and 28): As previously discussed, peaks m/z 96 and m/z 81 correspond to the parent peak of 3MCHe and a peak caused by dissociative ionization respectively. However, the experiments may now be clouded by the fact that methyl-fission to produce m/z 81 is a potential decomposition product of

3MCHe. At 1100 K, peaks at m/z 68 and m/z 28 begin growing together, suggesting the concerted retro-Diels-Alder reaction to form 1,3-pentadiene and ethylene becomes active at this temperature. (As with 1MCHe, the high IE of ethylene allows it to only be detected using the 9th harmonic of the Yi-Fi laser, the figures for which can be found in the Appendix C4). At 1400 K, additional peaks begin to grow in as 1,3-pentadiene begins to decompose. We will separate our experimental product discussions into two parts; first, we discuss the decomposition of the retro-Diels-Alder product 1,3-pentadiene, which is expected to be the first active pyrolysis route followed by the discussion of 2-cyclohexenyl radical decomposition formed via the methyl bond fission.

Products of 1,3-Pentadiene Decomposition (Masses 78, 66, 65, 52, 40, and 39): The decomposition of 1,3-pentadiene, formed via the retro-Diels-Alder route, results in the growth of many distinct peaks. The first possible reactions we discuss are bond fissions of 1,3-pentadiene, which are listed as Rxns 1-3. Using the ALFABET bond dissociation energy prediction tool [48] developed at the National Renewable Energy Laboratory a quick determination of which bond fission reactions are likely active can be made. Rxn. 1 has the lowest bond fission energy predicted at 81.8 kcal/mol. The predicted bond dissociation energies of Rxns 2 and 3 are substantially higher at 102.4 and 115.2 kcal/mol, respectively. Thus, we conclude that Rxn. 1 is likely the dominant bond fission route for 1,3-pentadiene, and the other bond fissions are not contributing to the observed products.

$$CH_2{=}CH\text{-}CH{=}CH\text{-}CH_3 \rightarrow H + CH_2{=}CH\text{-}CH{=}CH\text{-}CH_2^{*} \qquad \text{(Rxn. 1)}$$

$$CH_2{=}CH\text{-}CH{=}CH\text{-}CH_3 \rightarrow CH_3 + CH_2{=}CH\text{-}CH{=}CH^{*} \qquad \text{(Rxn. 2)}$$

$$CH_2{=}CH\text{-}CH{=}CH\text{-}CH_3 \rightarrow C_2H_3 + {}^{*}CH{=}CH\text{-}CH_3 \qquad \text{(Rxn. 3)}$$

In Rxn. 1 the C-H bond on the terminal methyl group breaks and produces H + a C5H7 radical (m/z 67). The resultant 1,3-pentadienyl radical readily cyclizes to form a cyclopentenyl radical (m/z 67) via Rxn 4 and subsequently loses an H-atom via b-scission to form cyclopentadiene (m/z 66) via Rxn 5. This stable cyclic species is observed in our experimental spectra, as is the product of another subsequent H-atom loss (Rxn 6), the cyclopentadienyl radical (m/z 65). Given its resonance stabilization, it is reasonable to assume that this radical (m/z 65) is stable enough for detection under our high dilution conditions and lends credence to the assignment of cyclopentadiene to m/z 66. A theoretical study by Bacskay and Mackie [49] shows both cyclopentadiene and cyclopentadienyl radicals can decompose to form acetylene (m/z 26) and either propyne (m/z 40) via Rxn 7, allene (m/z 40) via Rxn 8, or propargyl (m/z 39) via Rxn 9. (Acetylene (m/z 26) is not detectible in our experimental setup due to its high ionization energy (IE=11.4006±0.0003 [50])).

CH_2=CH-CH=CH-CH_2^* → cy(-CH_2-CH^*-CH=CH-CH_2-) (Rxn. 4)

cy(-CH_2-CH^*-CH=CH-CH_2-) → H + cy((-CH=CH-CH=CH-CH_2-) *(m/z 66)* (Rxn.5)

cy(-CH=CH-CH=CH-CH_2-) → H + cy((-CH=CH-CH=CH-CH^*-) *(m/z 65)* (Rxn. 6)

cy((-CH=CH-CH=CH-CH_2-) → CH≡CH + CH≡C-CH_3 *(m/z 40)* (Rxn. 7)

cy((-CH=CH-CH=CH-CH_2-) → CH≡CH + CH_2=C=CH_2 *(m/z 40)* (Rxn. 8)

cy((-CH=CH-CH=CH-CH^*-) → CH≡CH + HC≡C-CH_2* (m/z 39) (Rxn. 9)

An additional route to form many of the observed species is via the isomerization of 1,3-pentadiene to 1,2-pentadiene via a carbene intermediate via Rxn 10, which is a mechanism similar

to the isomerization of 1,3-butadiene to 1,2-butadiene discussed in 1MCHe. Once formed, 1,2-pentadiene could scission off the terminal methyl group via Rxn 11, forming CH2=C=CH-CH· which could b-scission another H-atom to form butatriene (m/z 52). Alternatively, 1,2-pentadiene could break the other C-C bond-forming propargyl radical directly (m/z 39) via Rxn 12 and ethyl radical (m/z 29), which readily loses an H-atom to form ethylene (m/z 28). Both the isomerization and bond fission routes were active in a shock tube study of 1,2-pentadiene by Herzler et al. [51].

CH_2=CH-CH=CH-CH_3 $\rightarrow$ CH_2=C=CH-CH_2-CH_3 (Rxn. 10)

CH_2=C=CH-CH_2-CH_3 $\rightarrow$ CH_3 + CH_2=C=CH-CH_2^* (Rxn. 11)

CH_2=C=CH-CH_2-CH_3 $\rightarrow$ CH_2=C=CH^* + $^*CH_2$-CH_3 (Rxn. 12)

The complex chemistry of 1,3-pentadiene and the possible isomerizations and decompositions of the molecule and its subsequent products make it difficult to discern which reactions in the Rxn 1-12 mechanism dominate without conducting a detailed study on 1,3-pentadiene itself. What is clear is the role of the retro-Diels-Alder reaction, from which m/z 68, 66, 65, 40, 39, and 28 must originate. Observation of these masses supports the theoretical rate constant calculations showing the retro-Diels-Alder reaction is the first active pyrolysis reaction as the temperature is increased. Furthermore, these decomposition paths, like with 1MCHe and 4MCHe, produce propargyl (m/z 39) which can polymerize to 1,5-hexadiyne (m/z 78). This linear m/z 78 structure can further isomerize eventually to a critical soot precursor, benzene. The similarity of all three MCHe isomers producing m/z 78 via propargyl makes this route unlikely to explain the enhanced sooting tendency of 3MCHe. Considering all these possible decomposition

pathways of 1,3-pentadiene, the retro-Diels-Alder reaction can explain all observed masses except m/z 54, 79, 80, and 81.

Products of Cyclohexenyl Radical (Masses 81, 80, 79, and 78): As theory revealed, the second-lowest reaction barrier for 3MCHe is the fission of the C-C bond to cleave off the methyl group (m/z 15) leaving a 2-cylcohexenyl radical (m/z 81). While this was mentioned as important in the work by Kim et al. [12], they did not go into detail about its decomposition since the H-atom abstraction chemistry dominated under their experimental conditions. For pyrolysis conditions this route becomes highly important; thus, this radical was studied in-depth here. Figure 4.11 shows the branching ratios of the decomposition of the product 2-cyclohexenyl radical, the corresponding PES can be found in Appendix C4.

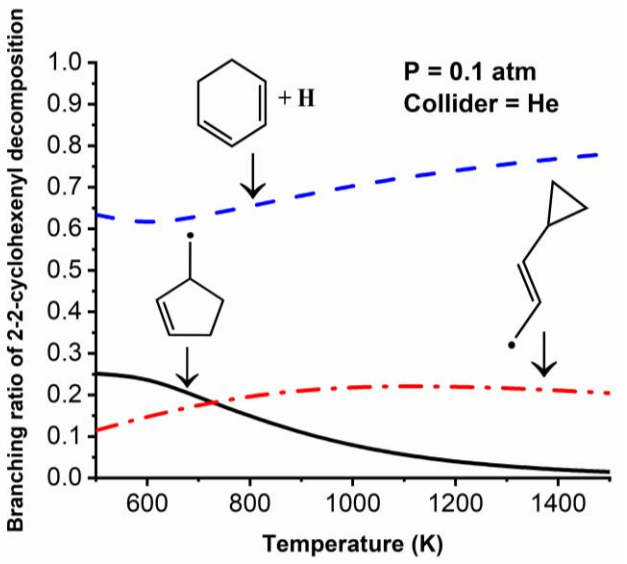

Figure 4.11: Branching ratio for calculated rates of 2-cyclohexenyl radical unimolecular decomposition at P=0.1 atm with He as the collider.

The lowest energy b-scission route of the 2-cyclohexenyl radical is to form 1,3-cyclohexadiene (m/z 80) + H, which is the dominant reaction pathway having above a 60%

branching ratio between T = 500 – 1500 K at P = 0.1 atm according to our rate constant calculations. An additional H-loss would form a resonantly stabilized radical (m/z 79), which will quickly b-scission off another H-atom to form benzene (m/z 78). M/z 80, 79, and 78 are all experimentally observed, strengthening the argument that this is the preferred mechanism for 2-cyclohexenyl radical to decompose and that the methyl-fission from 3MCHe is indeed active, as theory suggests. This provides a dominant and direct pathway to benzene formation for 3MCHe pyrolysis not easily accessible for the other two isomers under our experimental conditions. Thus, as theory indicates, the two lowest energy pathways for 3MCHe can explain all observed products (except for m/z 54) in the PIMS experiments and suggest both are soot precursor-producing pathways, with a faster, more direct link to benzene (m/z 78) via the methyl fission reaction from 3MCHe.

Remaining masses (m/z 54): M/z 54 is a minor product, reaching only a maximum of 5% max signal peak height. The production of this mass could not be explained via the retro-Diels-Alder reaction or the methyl bond fission route. Since the theoretical work shows these are the only two active pathways, we believe m/z 54 is not a primary product of 3MCHe decomposition. There are a few possible explanations for the origin of m/z 54. The 3MCHe fuel sample used in the experiments had the lowest purity of 93% with impurities of uncertain types. One plausible explanation for m/z 54 is that cyclohexene (m/z 82) is an impurity in the sample. The dominant pyrolysis pathway of cyclohexene is to form ethylene (m/z 28) and butadiene (m/z 54) which are both observed masses [52]. Evidence of mass m/z 82 is clouded because of the broad peak between m/z 82-85 which is an artifact of dissociative ionization. Additionally, it is possible wall catalyzed reactions are playing a role in the formation of m/z 54 but this hypothesis cannot be tested at this point. While there may be other possible explanations for m/z 54 ultimately its origin is unclear,

but we can conclusively determine from the theory that is not a primary product of 3MCHe pyrolysis.

4.4 Implications on the sooting tendency of the methylcyclohexene isomers

In our experiments, reactant concentrations were kept low (0.01%) in an inert bath gas to reduce any bimolecular chemistry. This is in contrast to previous work on MCHe isomers [12] [21], where the higher fuel concentrations indeed resulted in soot production but also resulted in obscuring precisely which unimolecular elementary reactions result in soot precursor species. Identification of these pathways informs the origins of soot formation based on structure, a direct contrast to estimation tools that are trained based on structure-property relationships. Figure 4.12 outlines the key reactions of each isomer that lead to the production of known soot precursors: propargyl radical, cyclopentadienyl, and benzene.

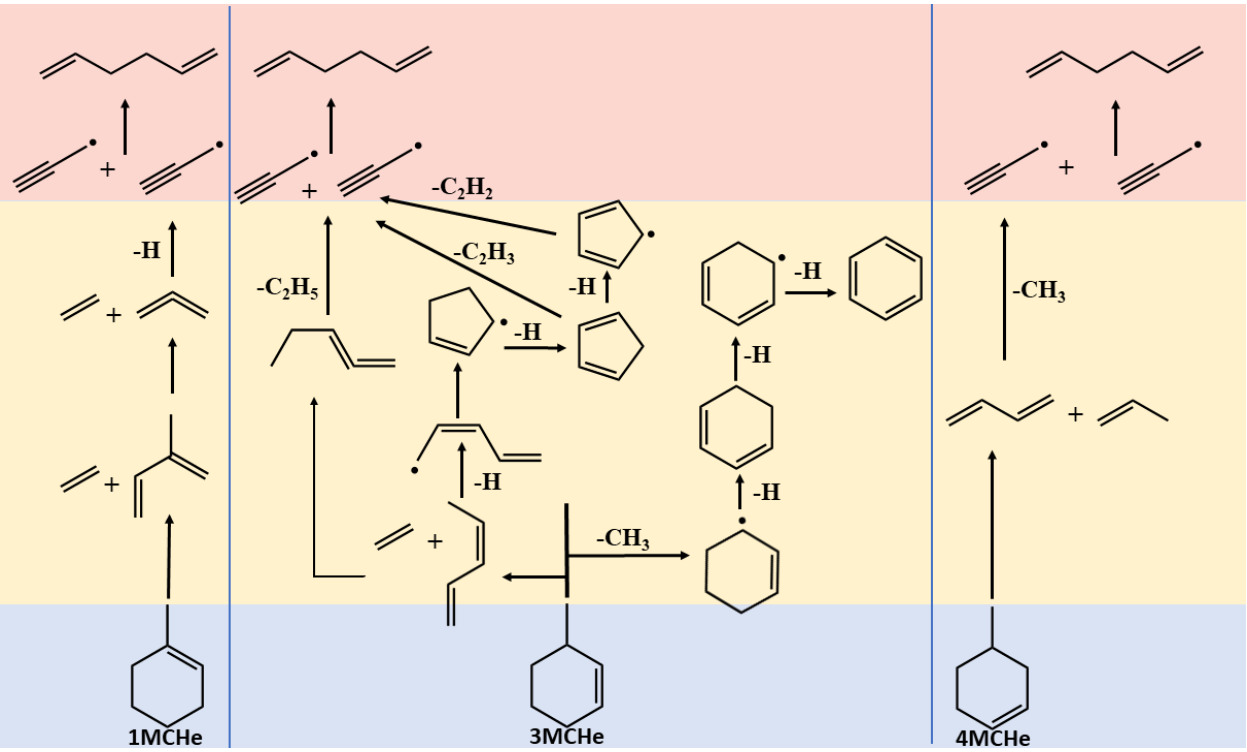

Figure 4.12: Summary and comparison of the main soot precursors producing pathways for each isomer of methylcyclohexene.Species fall into color-coded bins corresponding to the wall temperature at which they are formed: blue: $T_{wall} < 800$ K, yellow: 800 K $\leq T_{wall} \leq$ 1100 K, red: $T_{wall} >$ 1100 K. As discussed, the centerline gas temperature is ~100 K lower than the measured wall temperature of the reactor [26].

Under dilute reaction conditions where unimolecular decomposition dominates, the barrier to the concerted retro-Diels-Alder reactions was consistently the lowest energy pathway to reaction, breaking apart the ring rather than further unsaturation of the ring. For 1MCHe and 4MCHe, the retro-Diels-Alder pathways were the dominant pathways active under our dilute, low-pressure reactor conditions. Therefore, the ability to form soot precursors is limited. Both isomers have routes to form a substantial amount of propargyl radical,0 which can undergo a recombination reaction to form a linear C6H6 species that has the ability to isomerize eventually to an important soot precursor, benzene, but the path to form benzene is less direct than via the reactions of 3MCHe.

Due to the location of its double bond, 3MCHe has a much smaller difference between the energy barrier of the concerted retro-Diels-Alder reaction and the lowest bond fission to form methyl + 2-cyclohexenyl (~10.3 kcal/mol). This allows the bond fission route to become the dominant reaction above 700 K which in turn can produce unsaturated aromatic rings such as 1,3-cyclohexadiene, and benzene directly. Additionally, both propargyl and cyclopentadienyl are formed via the decomposition of 1,3-pentadiene, further increasing the variation and quantity of soot precursors formed during 3MCHe pyrolysis. These findings help to explain the higher YSI value and direct correlation to the molecular structure of this isomer.

4.5 Conclusions

Structural implications on sooting tendency were examined using 1-, 3-, and 4-methylcyclohexene isomers. Breakdown mechanisms for all three isomers were explored using PIMS experiments evaluating products of pyrolysis in a microreactor, in conjunction with computed potential energy surfaces produced bond dissociation energy calculations. The significantly higher sooting tendency of 3MCHe was attributed to the prevalence of forming known sooting precursors including propargyl, 1,3-cyclohexadiene, cyclopentadiene, and benzene quickly, while 1MCHe and 4MCHe were only able to form propargyl radical. For 1MCHe and 4MCHe, smaller quantities of C6H6 were observed and were likely due to propargyl recombination at higher temperatures. This highlights the subtle impact of the double bond placement of otherwise identical structures. Importantly, for 3MCHe, the placement of the double bond allows for a resonantly stabilized radical to form via methyl loss. This resonance stabilization of the 2-cyclohexenyl radical highlights the energetic favorability of the loss of the methyl group and subsequent further unsaturation of the ring in comparison to the other isomers where C-C bond

dissociation energies are at least 15.1 kcal/mol stronger. This opens additional channels for direct unsaturated ring formation in 3MCHe that are not competitive in the 1MCHe and 4MCHe isomers. This observation is in complement to the density functional theory work from Kim et al. [12], in which the authors conclude that the stability of the radicals in pathways towards linear, non-sooting products is much greater in 1MCHe and 4MCHe than in 3MCHe, while the opposite is true for pathways which retain or re-form the cyclic structure of the isomers. Both pyrolysis and abstraction chemistry play an important role in the full understanding of YSI predictions. Thus, the findings presented in this work can help better inform yield sooting index estimations of varied structures and be incorporated into prediction tools for yield sooting index to improve intrinsic sooting estimations.

This work has been adapted for journal publication with the tentative title,' *Evaluating the Sooting Tendency Differences of Methylcyclohexene Isomers Using Microreactor Experiments and Computational Chemistry in Tandem'*.

4.6 References

[1] J. Lelieveld, K. Klingmüller, A. Pozzer, R. T. Burnett, A. Haines, and V. Ramanathan, "Effects of fossil fuel and total anthropogenic emission removal on public health and climate," *Proc. Natl. Acad. Sci.*, vol. 116, no. 15, pp. 7192–7197, Apr. 2019, doi: 10.1073/pnas.1819989116.

[2] S. Fuzzi *et al.*, "Particulate matter, air quality and climate: lessons learned and future needs," *Atmospheric Chem. Phys.*, vol. 15, no. 14, pp. 8217–8299, Jul. 2015, doi: 10.5194/acp-15-8217-2015.

[3] R. Beelen *et al.*, "Effects of long-term exposure to air pollution on natural-cause mortality: an analysis of 22 European cohorts within the multicentre ESCAPE project," *The Lancet*, vol. 383, no. 9919, pp. 785–795, Mar. 2014, doi: 10.1016/S0140-6736(13)62158-3.

[4] T. D. Gordon *et al.*, "Secondary organic aerosol production from diesel vehicle exhaust: impact of aftertreatment, fuel chemistry and driving cycle," *Atmospheric Chem. Phys.*, vol. 14, no. 9, pp. 4643–4659, May 2014, doi: 10.5194/acp-14-4643-2014.

[5] R.-J. Huang *et al.*, "High secondary aerosol contribution to particulate pollution during haze events in China," *Nature*, vol. 514, no. 7521, Art. no. 7521, Oct. 2014, doi: 10.1038/nature13774.

[6] R. Burnett *et al.*, "Global estimates of mortality associated with long-term exposure to outdoor fine particulate matter," *Proc. Natl. Acad. Sci.*, vol. 115, no. 38, pp. 9592–9597, Sep. 2018, doi: 10.1073/pnas.1803222115.

[7] K. Kohse-Höinghaus, "Combustion in the future: The importance of chemistry," *Proc. Combust. Inst. Int. Symp. Combust.*, Sep. 2020, doi: 10.1016/j.proci.2020.06.375.

[8] I. A. Khalek, M. G. Blanks, P. M. Merritt, and B. Zielinska, "Regulated and unregulated emissions from modern 2010 emissions-compliant heavy-duty on-highway diesel engines," *J. Air Waste Manag. Assoc.*, vol. 65, no. 8, pp. 987–1001, Aug. 2015, doi: 10.1080/10962247.2015.1051606.

[9] İ. A. Reşitoğlu, K. Altinişik, and A. Keskin, "The pollutant emissions from diesel-engine vehicles and exhaust aftertreatment systems," *Clean Technol. Environ. Policy*, vol. 17, no. 1, pp. 15–27, Jan. 2015, doi: 10.1007/s10098-014-0793-9.

[10] T. G. Leone *et al.*, "The Effect of Compression Ratio, Fuel Octane Rating, and Ethanol Content on Spark-Ignition Engine Efficiency," *Environ. Sci. Technol.*, vol. 49, no. 18, pp. 10778–10789, Sep. 2015, doi: 10.1021/acs.est.5b01420.

[11] T. W. Chan, E. Meloche, J. Kubsh, and R. Brezny, "Black Carbon Emissions in Gasoline Exhaust and a Reduction Alternative with a Gasoline Particulate Filter," *Environ. Sci. Technol.*, vol. 48, no. 10, pp. 6027–6034, May 2014, doi: 10.1021/es501791b.

[12] S. Kim *et al.*, "Experimental and theoretical insight into the soot tendencies of the methylcyclohexene isomers," *Proc. Combust. Inst.*, vol. 37, no. 1, pp. 1083–1090, Jan. 2019, doi: 10.1016/j.proci.2018.06.095.

[13] E. J. Barrientos, J. E. Anderson, M. M. Maricq, and A. L. Boehman, "Particulate matter indices using fuel smoke point for vehicle emissions with gasoline, ethanol blends, and butanol blends," *Combust. Flame*, vol. 167, pp. 308–319, May 2016, doi: 10.1016/j.combustflame.2016.01.034.

[14] Y. Yang, A. L. Boehman, and R. J. Santoro, "A study of jet fuel sooting tendency using the threshold sooting index (TSI) model," *Combust. Flame*, vol. 149, no. 1, pp. 191–205, Apr. 2007, doi: 10.1016/j.combustflame.2006.11.007.

[15] K. Aikawa, T. Sakurai, and J. J. Jetter, "Development of a Predictive Model for Gasoline Vehicle Particulate Matter Emissions," *SAE Int. J. Fuels Lubr.*, vol. 3, no. 2, pp. 610–622, Oct. 2010, doi: 10.4271/2010-01-2115.

[16] C. S. McEnally and L. D. Pfefferle, "Improved sooting tendency measurements for aromatic hydrocarbons and their implications for naphthalene formation pathways," *Combust. Flame*, vol. 148, no. 4, pp. 210–222, Mar. 2007, doi: 10.1016/j.combustflame.2006.11.003.

[17] C. S. McEnally and L. D. Pfefferle, "Sooting Tendencies of Oxygenated Hydrocarbons in Laboratory-Scale Flames," *Environ. Sci. Technol.*, vol. 45, no. 6, pp. 2498–2503, Mar. 2011, doi: 10.1021/es103733q.

[18] D. D. Das, P. C. St. John, C. S. McEnally, S. Kim, and L. D. Pfefferle, "Measuring and predicting sooting tendencies of oxygenates, alkanes, alkenes, cycloalkanes, and aromatics on a unified scale," *Combust. Flame*, vol. 190, pp. 349–364, Apr. 2018, doi: 10.1016/j.combustflame.2017.12.005.

[19] P. C. St. John, P. Kairys, D. D. Das, C. S. McEnally, L. D. Pfefferle, D. J. Robichaud, M. R. Nimlos, B. T. Zigler, R. L. McCormick, T. D. Foust, Y. J. Bomble, and S. Kim, “A quantitative model for the prediction of sooting tendency from molecular structure,” Energy & Fuels, vol. 31, no. 9, pp. 9983–9990, 2017.

[20] J. L. Garnett, W. D. Johnson, and J. E. Sherwood, "Pyrolysis of 1-methylcyclohexene and methylenecyclohexane," *Aust. J. Chem.*, vol. 29, no. 3, pp. 599–607, 1976, doi: 10.1071/ch9760599.

[21] S. H. Gardiner, M. L. Lipciuc, and C. Vallance, "Gas-Phase Retro-Diels-Alder Reactions of Cyclohexene, 1-Methylcyclohexene, and 4-Methylcyclohexene following Photoexcitation at 193 nm: A Velocity-Map Imaging Study," *J. Phys. Chem. A*, vol. 119, no. 50, pp. 12218–12223, Dec. 2015, doi: 10.1021/acs.jpca.5b06185.

[22] J. L. Garnett, W. D. Johnson, and J. E. Sherwood, "Pyrolysis of 1-methylcyclohexene and methylenecyclohexane," *Aust. J. Chem.*, vol. 29, no. 3, pp. 599–607, 1976, doi: 10.1071/ch9760599.

[23] Z. Tian, S. Zhu, J. Li, and Y. Yan, "Decomposition of 3-methylcyclohexene radicals: Beginning of its mechanism development," *Fuel*, vol. 271, p. 117591, Jul. 2020, doi: 10.1016/j.fuel.2020.117591.

[24] T.K.Ormond., et al. “Pyrolysis of Cyclopentadienone: Mechanistic Insights from a Direct Measurement of Product Branching Ratios.” The Journal of Physical Chemistry A, vol. 119, no. 28, 17 Feb. 2015, pp. 7222–7234, https://doi.org/10.1021/jp511390f. Accessed 8 Apr. 2023.

[25] Vasiliou, AnGayle, et al. “The Products of the Thermal Decomposition of CH3CHO.” The Journal of Chemical Physics, vol. 135, no. 1, 7 July 2011, p. 014306, https://doi.org/10.1063/1.3604005. Accessed 8 Apr. 2023.

[26] Q. Guan, K. N. Urness, T. K. Ormond, D. E. David, G. Barney Ellison, and J. W. Daily, "The properties of a micro-reactor for the study of the unimolecular decomposition of large molecules," *Int. Rev. Phys. Chem.*, vol. 33, no. 4, pp. 447–487, Oct. 2014, doi: 10.1080/0144235X.2014.967951.

[27] D. E. Couch *et al.*, "Detection of the keto-enol tautomerization in acetaldehyde, acetone, cyclohexanone, and methyl vinyl ketone with a novel VUV light source," *Proc. Combust. Inst.*, vol. 38, no. 1, pp. 1737–1744, Jan. 2021, doi: 10.1016/j.proci.2020.06.139.

[28] R. Van de Vijver and J. Zádor, "KinBot: Automated stationary point search on potential energy surfaces," *Comput. Phys. Commun.*, p. 106947, Oct. 2019, doi: 10.1016/j.cpc.2019.106947.

[29] Gaussian 16, Revision B.01, Frisch, M.J., et al. Gaussian, Inc., Wallingford CT (2016) GaussView 5.0. Wallingford, E.U.A.

[30] J. M. L. Martin, "Ab initio total atomization energies of small molecules — towards the basis set limit," *Chem. Phys. Lett.*, vol. 259, no. 5, pp. 669–678, Sep. 1996, doi: 10.1016/0009-2614(96)00898-6.

[31] J. A. Miller and S. J. Klippenstein, "From the Multiple-Well Master Equation to Phenomenological Rate Coefficients: Reactions on a C3H4 Potential Energy Surface," *J. Phys. Chem. A*, vol. 107, no. 15, pp. 2680–2692, Apr. 2003, doi: 10.1021/jp0221082.

[32] Y. Georgievskii, J. A. Miller, M. P. Burke, and S. J. Klippenstein, "Reformulation and solution of the master equation for multiple-well chemical reactions," *J. Phys. Chem. A*, vol. 117, no. 46, pp. 12146–12154, Nov. 2013, doi: 10.1021/jp4060704.

[33] S. Jacobs *et al.*, "A Comprehensive Experimental and Kinetic Modeling Study of the Combustion Chemistry of Diethoxymethane," *Energy Fuels*, vol. 35, no. 19, pp. 16086–16100, Oct. 2021, doi: 10.1021/acs.energyfuels.1c01988.

[34] D. D. Das, P. C. St. John, C. S. McEnally, S. Kim, and L. D. Pfefferle, "Measuring and predicting sooting tendencies of oxygenates, alkanes, alkenes, cycloalkanes, and aromatics on a unified scale," *Combust. Flame*, vol. 190, pp. 349–364, Apr. 2018, doi: 10.1016/j.combustflame.2017.12.005.

[35] R. E. Winters and J. H. Collins, "Mass spectrometric studies of structural isomers. I. Mono- and bicyclic C7H12 molecules," *J. Am. Chem. Soc.*, vol. 90, no. 5, pp. 1235–1239, Feb. 1968, doi: 10.1021/ja01007a022.

[36] B. A. Williams and T. A. Cool, "Two-photon spectroscopy of Rydberg states of jet-cooled C2H4 and C2D4," *J. Chem. Phys.*, vol. 94, no. 10, pp. 6358–6366, May 1991, doi: 10.1063/1.460314.

[37] G. Bieri, F. Burger, E. Heilbronner, and J. P. Maier, "Valence Ionization Energies of Hydrocarbons," *Helv. Chim. Acta*, vol. 60, no. 7, pp. 2213–2233, 1977, doi: 10.1002/hlca.19770600714.

[38] K. H. Weber and J. Zhang, "Mechanistic Study of Thermal Decomposition of Isoprene (2-Methyl-1,3-Butadiene) Using Flash Pyrolysis Supersonic Jet VUV Photoionization Mass Spectrometry," *J. Phys. Chem. A*, vol. 111, no. 45, pp. 11487–11492, Nov. 2007, doi: 10.1021/jp075689+.

[39] Z. Z. Yang, L. S. Wang, Y. T. Lee, D. A. Shirley, S. Y. Huang, and W. A. Lester, "Molecular Beam Photoelectron Spectroscopy of Allene," Aug. 1989, Accessed: Sep. 29, 2021. [Online]. Available: https://escholarship.org/uc/item/5xp6476b

[40] J. A. Miller and S. J. Klippenstein, "The Recombination of Propargyl Radicals and Other Reactions on a C6H6 Potential," *J. Phys. Chem. A*, vol. 107, no. 39, pp. 7783–7799, Oct. 2003, doi: 10.1021/jp030375h.

[41] W. G. Mallard, J. H. Miller, and K. C. Smyth, "The ns Rydberg series of 1,3-trans-butadiene observed using multiphoton ionization," *J. Chem. Phys.*, vol. 79, no. 12, pp. 5900–5905, Dec. 1983, doi: 10.1063/1.445770.

[42] A. B. Burrill and P. M. Johnson, "Torsional analyses of trans-2-butene and propene cations: A comparative investigation of two prototypical ions with different degrees of symmetry," *J. Chem. Phys.*, vol. 115, no. 1, pp. 133–138, Jul. 2001, doi: 10.1063/1.1376634.

[43] Y. Hidaka, T. Higashihara, N. Ninomiya, H. Masaoka, T. Nakamura, and H. Kawano, "Shock tube and modeling study of 1,3-butadiene pyrolysis," *Int. J. Chem. Kinet.*, vol. 28, no. 2, pp. 137–151, 1996, doi: 10.1002/(SICI)1097-4601(1996)28:2<137::AID-KIN9>3.0.CO;2-W.

[44] S. D. Chambreau, J. Lemieux, L. Wang, and J. Zhang, "Mechanistic studies of the pyrolysis of 1,3-butadiene, 1,3-butadiene-1,1,4,4-d4, 1,2-butadiene, and 2-butyne by supersonic jet/photoionization mass spectrometry," *J. Phys. Chem. A*, vol. 109, no. 10, pp. 2190–2196, Mar. 2005, doi: 10.1021/jp045010r.

[45] J. P. A. Lockhart, C. F. Goldsmith, J. B. Randazzo, B. Ruscic, and R. S. Tranter, "An Experimental and Theoretical Study of the Thermal Decomposition of C4H6 Isomers," *J. Phys. Chem. A*, vol. 121, no. 20, pp. 3827–3850, May 2017, doi: 10.1021/acs.jpca.7b01186.

[46] A. M. Scheer, C. Mukarakate, D. J. Robichaud, G. B. Ellison, and M. R. Nimlos, "Radical Chemistry in the Thermal Decomposition of Anisole and Deuterated Anisoles: An Investigation of Aromatic Growth," *J. Phys. Chem. A*, vol. 114, no. 34, pp. 9043–9056, Sep. 2010, doi: 10.1021/jp102046p.

[47] Kimura, Katsumi. Handbook of HeI Photoelectron Spectra of Fundamental Organic Molecules. Halsted Press, 1981.

[48] P. C. St. John, Y. Guan, Y. Kim, S. Kim, and R. S. Paton, "Prediction of organic homolytic bond dissociation enthalpies at near chemical accuracy with sub-second computational cost," *Nat. Commun.*, vol. 11, no. 1, Art. no. 1, May 2020, doi: 10.1038/s41467-020-16201-z.

[49] G. B. Bacskay and J. C. Mackie, "The pyrolysis of cyclopentadiene: quantum chemical and kinetic modelling studies of the acetylene plus propyne/allene decomposition channels," *Phys. Chem. Chem. Phys.*, vol. 3, no. 12, pp. 2467–2473, Jan. 2001, doi: 10.1039/B101317N.

[50] S. T. Pratt, P. M. Dehmer, and J. L. Dehmer, "Zero-kinetic-energy photoelectron spectroscopy from the Ã 1Au state of acetylene: Renner–Teller interactions in the trans-bending vibration of C2H+2 X̃ 2Πu," *J. Chem. Phys.*, vol. 99, no. 9, pp. 6233–6244, Nov. 1993, doi: 10.1063/1.465888.

[51] J. Herzler, J. A. Manion, and W. Tsang, “1,2-Pentadiene decomposition,” *Int. J. Chem. Kinet.*, vol. 33, no. 11, pp. 755–767, 2001, doi: 10.1002/kin.1072.

[52] M. Uchiyama, T. Tomioka, and A. Amano, "Thermal Decomposition of Cyclohexene," *J. Phys. Chem.*, vol. 68, no. 7, pp. 1878–1881, Jul. 1964, doi: 10.1021/j100789a036.

Chapter 5: Probing the pyrolysis of Polyoxymethylene Ethers (POM-E)

5.1 Polyoxymethylene Ethers (POM-E) as diesel fuel additives

The constraints of electric mobility are exacerbated in the case of freight transportation. Range limitations and reduced infrastructure render most long-distance ground shipping routes (>250 miles) unviable for electrification. A large fraction of existing ground-based freight transportation is powered by diesel engines. These Internal Combustion Engines (ICE) provide high efficiency and low operating costs, making them suitable for large-volume freight movement. However, the typical exhaust gas emissions from the combustion of conventional diesel fuel make further development inevitable if future air quality regulations are to be met. Various eco-friendly fuels have been suggested as replacements for traditional diesel in the internal combustion engine, including gaseous fuels, such as natural gas (compressed and liquefied natural gas, or CNG and LNG, respectively), hydrogen, and propane; liquid fuels, such as biodiesel, alcohols such as ethanol, butanol, and methanol; and ethers, such as methyl tertiary butyl ether (MTBE), dimethyl ether (DME). The alternative fuel and fuel additives are termed Electrofuels (E-fuels).

Dibutyl ether (DBE) and oxymethylene ethers (OME) are among the many oxygen-containing fuel and additive candidates. Polyoxymethylene dimethyl ethers (POM-DME, also called oxymethylene ethers or OME) provide almost soot-free combustion. Their wide-scale usage might eliminate diesel engine constraints by reducing emissions and improving efficiency. OMEs possess very high ignitability and an advantageous molecule structure[1]. POM-DME can be synthesized at a large scale from methanol, which can be produced by biomass gasification and subsequent syngas conversion[2].

Most OME combustion investigations in the literature discuss dimethoxymethane (DMM) or mixtures of conventional fuel and DMM. The general chemical structure (H_3C-O-(CH_2-O)$_n$-CH_3) for these molecules includes a large amount of molecular oxygen, ranging from 42 wt% for DMM to nearly 50 wt% for longer chain OMEs. The high oxygen content and the absence of multiple carbon-to-carbon bonds lead to practically soot-free combustion, demonstrated in various studies. In the early '90s, Dodge and Naegeli [3] tested DMM-fossil fuel blends in an unmodified diesel engine and reported a substantial soot reduction with increasing DMM content in the fuel. Svensson et al. [4] investigated pure DMM in a high-pressure optical chamber, reporting that soot could not be detected within the detection limit of the optical setup. Härtl et al. [11] compared a variety of oxygenates, including dimethoxymethane finding it to have the highest soot reduction potential among all investigated fuels. Recently, Omari et al. [5] investigated the soot reduction potential of DMM-Diesel blends, reporting a particulate matter mass reduction of more than 80%, already with a 35% volumetric dimethoxymethane share in diesel fuel. In a further work by Deutz et al. [6], the authors investigated a DMM-Diesel fuel blend with 35 vol%. DMM in a single-cylinder engine via a global design of experiments approach.

While extensive studies have considered the production [7], [8], and fuel properties [9], [10] of long-chain POM-DMEs, investigations of their combustion are relatively rare. Härtl et al. [11] investigated pure longer-chain POM-Es in a heavy-duty single-cylinder diesel engine reporting soot-free combustion similar to DMM. Wang et al. [12] studied the potential of OME3-4 (H_3C-O-(CH_2-O)$_n$-CH_3 where n = 3,4,5) in a homogeneous charge compression ignition engine achieving ultra-low NOx emissions (<10 ppm) at soot-free combustion. Nevertheless, investigations addressing pure long-chain OMEs in a blend with diesel are not available yet.

However, the blending approach is of high interest for the initial stages of phasing out fossil fuel. In a blend with high sooting fossil fuels, the mentioned improvements in fuel properties of long-chain OMEs might reduce the soot reduction potential compared to short-chain OMEs.

5.2 Research into the pyrolysis and oxidation of Polyoxymethylene Ether (POM-E) with diesel

Along with engine test experiments exploring emission characteristics of diesel engines using different POM-Es, several research efforts have been undertaken to understand the chemical kinetics involved during pyrolysis and combustion of POM-E molecules[13]–[16]. In 2001, Daly et al. [17] proposed the first detailed kinetic mechanism (511 reactions, 75 species) for the oxidation of dimethoxymethane (DMM), the smallest in the family of POM-Es. This mechanism was primarily based on analogy to corresponding reactions of molecules such as dimethyl ether (DME), diethyl ether (DEE), ethane (C_2H_6), and propane (C_3H_8). The proposed mechanism matched the species concentration profiles obtained from jet-stirred reactor experiments in the temperature range of 1000-1200K. However, the model significantly underpredicted the rate of DMM consumption at temperatures below 1000 K. Daly et al. [17] hypothesized that at low temperatures, DMM consumption must be taking place via a surface-catalyzed molecular pathway having low activation energy to form formaldehyde (CH_2O), DME, methanol (CH_3OH) and acetaldehyde (H_3CHCO).

Daly's mechanism was further updated by Dias et al. [18] in 2010 by incorporating OH abstraction reactions to account for the missing low-temperature combustion chemistry. Dias's mechanism served as the basis for a more detailed kinetic modeling study on DMM combustion performed by Marrodan et al.[19], [20], Alexandrino et al. [21] and Sun et al [22]. It is to be noted that these studies are primarily based on mechanisms having rate constants estimated using

analogy to similar molecules rather than theoretically calculated. The first attempt at calculating rate constants using methods based on first principles was performed by Vermeire et al. [23] in 2018. The author performed quantum mechanical (QM) calculations using CBS-QB3 level of theory to predict potential energy surfaces (PES) for important reactions involving peroxy species (R−O−O) relevant to low-temperature oxidation of DMM. Unlike earlier studies, Vermeire et al. [23] comprehensively validated the proposed mechanism by comparing numerical simulations against various experimental data sets across different conditions and using different reactor types. Although the mechanism was able to predict could predict species concentration trends of all experimental datasets, demonstrating the strength of these first principle calculations, it highly overpredicted the mole fractions of hydrocarbons such as methane, ethane, and ethylene formed during DMM oxidation. In 2018, another study based on first-principle calculations was performed by Kopp et al.[24]. In this study, the authors performed highly accurate QM calculations using CCSD(T)/cc-pV(D+T) Z level of theory to explore the PESs of two important DMM radicals involved in pyrolysis and the high-temperature combustion, $\dot{C}H_2OCH_2OCH_3$ (Ṙ1) and $CH_3O\dot{C}HOCH_3$ (Ṙ3). It was observed that the QM calculated rate constants vary in the range of one to two orders of magnitude relative to the values in the mechanism previously proposed by Daly et al.[17] and Dias et al.[18]. The difference is most significant for reactions involving the Ṙ3 radical indicates the unique behavior of the methylenedioxy group (O–CH_2–O) in POM-E molecules. Furthermore, it was observed that in contrast to previous studies, quantum mechanical calculations suggest that radical Ṙ3 is always favored to form during hydrogen atom abstraction from DMM by Ḣ and ĊH3 radicals. This presents a clear discrepancy between the previous mechanisms compared to the more accurate quantum mechanical simulations. While the previously proposed mechanisms suggest that the reaction pathway forming CH_2O and DME

radical is dominant, QM calculations show that the route forming CH_3 radical and methyl formate (CH_3OOOCH) is more favorable. Another ab-initio evaluation using the CCSD(T)/pV-TZ level of theory was published by Golka et al. [25],[26] in 2021. Here the authors' calculated rate constants for two important initiation steps involved during the pyrolysis of DMM:

R1. DMM ↔ ĊH3 + ȮCH2OCH3

R2. DMM ↔ CH3Ȯ + ĊH2OCH3.

Based on QM calculations, Golka et al. [25], [26] concluded that during the initial phase of DMM pyrolysis, **R2** is the dominant pathway with a branching ratio of 0.98 across the temperature and pressure range of 1100-1600 K and 0.4-4.7 bar respectively. This is in sharp contrast to the previous conclusion by Vermeire et al.[23], Marrodan et al. [19], [20] and Sun et al.

Multiple engine test experiments [1-3] have been performed using different POM-E molecules (n=1-6) to understand their emission characteristics as a diesel fuel additive. However, a gap exists in the literature where a comprehensive analysis of the chemical kinetics involved in the process is yet to be presented. These studies would be essential to elucidate emission formation mechanisms and the effect of the ($-CH_2-O-$) moiety. Existing chemical kinetic analyses have mostly emphasized DMM's performance, which is not considered among the optimal diesel fuel additives. The use of dimethoxymethane as a diesel additive is complicated by its lower cetane number and high vapor pressure, which can lead to issues with engine integration. The primary reason for the extensive evaluation of DMM is its short-chain structure. This makes it computationally cheaper and chemically easier to evaluate as a representative POM-E molecule. Despite this exhaustive evaluation of the kinetics of DMM pyrolysis and oxidation, a comprehensive mechanism based purely on theoretical calculations still does not exist. Thus, it is evident that additional studies are required to unravel the complex chemical kinetics involved

during the pyrolysis of DMM and different POM-E molecules containing more than one oxymethylene unit (-CH_2-O-).

Another challenge to working with these molecules is synthesizing large volumes of pure long-chain OMEs. The cost and time associated with building scalable production methods for each candidate OME can be offset by first identifying the best candidate for blending with diesel at the molecular level. This chapter details micro-reactor experiments with laser diagnostics are used in conjunction with computational modeling to identify the fundamental decomposition routes for these molecules. Reaction rates are calculated through computational modeling and experimental data evaluation to pinpoint the most likely products of thermal decomposition. By identifying the potential products of pyrolysis, it is possible to develop chemical kinetic mechanisms to link the effects of varying the end group or the number of $(CH_2\text{-}O)_n$ to global observables. These mechanisms can narrow down the list of potential OMEs used as additives and identify the optimum percentage of OMEs in blends with diesel fuel. [22]. In addition to DMM, this work aims to develop a detailed reaction mechanism for longer chain-length POM-Es. Unlike engine tests performed extensively to understand emission characteristics of different long-chain POM-E molecules, very few studies have been done so far to understand the kinetics involved during pyrolysis or combustion of POM-E molecules other than DMM.

5.3 Chemical kinetic investigation of chain length effects of polyoxymethylene ethers (POM-E) during pyrolysis

The following section presents results from Photoionization Mass Spectrometry (PIMS) experiments and quantum mechanical calculations modeling the thermal decomposition of three POM-E molecules: dimethoxymethane (CH_3-O-CH_2-O-CH_3, POM-E1), 2,4,6 trioxaheptane (CH_3-

$O\text{-}CH_2\text{-}O\text{-}CH_2\text{-}O\text{-}CH_3$, POM-E2) and 2,4,6,8 tetraoxanonane ($CH_3\text{-}O\text{-}CH_2\text{-}O\text{-}CH_2\text{-}O\text{-}CH_2\text{-}O\text{-}CH_3$, POM-E3). While the experiments provided important information regarding intermediates formed during decomposition, QM calculations provided a detailed representation of the pathways involved in forming these intermediates and allowed us to develop. Based on master equation analysis using Argonne National Laboratory's code MESS, dominant reaction pathways involved in the early phase of decomposition are also identified in this study. QM calculations match well with the experimentally observed [26] decomposition characteristics of the three POM-E molecules studied in this work. Based on both experiments and theoretical calculations, this study is intended to provide a detailed insight into the chemical kinetics involved during the early phase decomposition of the three distinct POM-E molecules. Furthermore, this work elucidates the effect of chain length on the kinetics as the number of oxymethylene units increases from 1 to 3.

5.3.1 Experimental methods

Pyrolysis experiments, used to confirm initial decomposition pathways, were performed in a micro-reactor in tandem with photoionization mass spectrometry (PIMS) for mass detection. Details of the experimental setup and process have been described in Chapter 2. In summary, Poly Oxymethylene Ethers are studied by entraining a dilute sample of the molecule in helium. This sample mixture is flowed continuously through the reactor at 200 SCCM using an MKS 4B013202RB70 Mass Flow Controller. The following molecules were analyzed - dimethoxymethane (Sigma Aldrich >99% purity), 2,4,6 Trioxaheptane (Asta Tech Chemicals >99% purity), and 2,4,6,8 Tetraoxanonane (synthesized at CSU >95% purity). Each of these molecules' vapor pressure is large enough to prepare static sample volumes of between 0.025% and 0.1% reactant in standard lecture bottles.

The micro-reactor assembly consists of a tubular silicon carbide reactor of 30 mm in length with a 1 mm inner diameter. The reactor material is chosen for its ability to withstand very high temperatures and thermal cycling while remaining inert and not participating in any of the pyrolysis reactions. The reactor is resistively heated to 1800K through Carbon discs fitted to the reactor's outer diameter. These discs are approximately 15 mm apart and form the contact points for the electrical circuit used to heat the reactor resistively. The temperature at the exterior surface of the reactor is monitored by a TIM Microtek thermal camera between the two heating points (details of the camera and the measurement process are provided in Chapter 2). The residence time is roughly 100 μs enabling the identification of the first decomposition products.

The flow properties in the reactor were modeled using CFD by Guan et al. [27]. The temperature was calculated to reach within 100 K of the measured wall temperature by 1/3 of the reactor length. This temperature profile and the falling pressure profile affect the product distribution as the reaction rates are temperature and pressure-dependent. A low Peclet number of the flow results in any wall reactions being constrained to the thin layer of fluid directly adjacent to the walls and not affecting the bulk of the flow.

In the PIMS experiment, gases flow continuously through the reactor, with the products exiting the reactor entering a 0.2 mm diameter molecular beam skimmer. The resulting beam is intersected and ionized by the 9th harmonic of an Nd:YAG laser (118.2 nm or 10.487 eV). The laser is aligned with the flow entering an ionization chamber maintained at 5 X 10-7 torr by a 1200 L/s Pfieffer TPU 1201 P turbomolecular pump. The internal frequency tripled the output of an Nd: YAG laser is directed into a cell that is pressurized to 150 Torr with a 10:1 argon: xenon mixture. This mixture is optimized to promote sum-frequency generation that creates 118.2 nm VUV photons, which have sufficient energy to ionize most hydrocarbon molecules. The generation of

118.2nm photons by Xe/Ar tripling cells has been studied at great length. We expect the use of 30 mJ pulse per pulse power at 355 nm from the YAG laser and the established tripling efficiency of 1×10-5 in pure Xenon and the transmission efficiency of the MgF2 lens to produce roughly 30 nJ per pulse at 118.2 nm light. Post ionization, the molecules in the expansion are accelerated into a Jordan reflectron time of flight spectrometer with a Micro Channel Plate (MCP) detector producing voltage signals which are converted to digital traces in an interfacing computer. This data is converted into a spectra format and is analyzed for the decomposition products.

5.3.2 Computational modeling methods

In this evaluation, quantum mechanical (QM) calculations are performed to identify relevant species and unimolecular reaction pathways during the initial pyrolysis phase of the three POM-E molecules studied in this section. Details of the computational method are presented in Chapter 3, and a brief sequence of operations is shown here. Using the commercially available KinBot [28] code, automated scanning of potential energy surface (PES) at B3LYP/6-311++(d,p) level of theory is performed to identify important reactions that occur during the initial phase of pyrolysis. 1-D hindered rotor scans are then performed for all the associated species to identify the lower energy conformer and the barrier involved in internal rotation for all stationary points involved in the reactions of interest. Finally, single-point energy calculations performed at the CCSD(T)/cc-pV(D+T)Z level of theory, are utilized to obtain high accuracy energies Finally the master equation is solved using Argonne National Laboratory's (ANL) Master Equation System Solver (MESS) to calculate pressure and temperature-dependent rate constants of the reaction pathways involved during pyrolysis.

5.3.3 Experimental results

5.3.3.1 Dimethoxymethane (DMM/M-1-M)

The experimental results from the decomposition of the POM-E molecules in the heated micro-reactor experiments are presented first, followed by the electronic structure calculations. Figure 5.1 shows PIMS Spectra for 0.1% dimethoxymethane in He at four temperatures, labeled on the right. Two peaks are observed at room temperature when ionized by the light source at 10.47 eV. All three POM-E molecules chosen in this experimental study show strong dissociative ionization. The presence of an easily ionizable lone pair of electrons on the multiple oxygen atoms results in a direct elimination of hydrogen in the form of a radical from the parent molecule. This manifests in a large peak at m/z 75 corresponding to $CH_3OCH_2OCH_2$+ and the associated Carbon 13 peak at m/z 76. At 900K, an additional peak at m/z 45 (methyl methoxy radical CH_3OCH_2+) appears. This is due to breaking the weak oxygen-carbon bond-forming methoxy radical (m/z 31 with I.E 10.704 eV[31]) and the fragment at m/z 45. Since the methoxy radical's ionization energy is beyond the laser's capability, it is not observed. However, the formation of methyl methoxy radical indicates its presence indirectly. As the temperature is raised further, the parent peak reduces in signal intensity, indicating a complete breakdown within the reactor into multiple fragments. Due to the laser's conditions, most of these fragments undergo decomposition to formaldehyde (m/z 30, IE = 10.880eV[31]) and methyl radical through multiple intermediate radical forms. The laser energy at 10.487eV places a lot of these radical fragments outside the ionizability envelope, resulting in only the methyl peak (IE) being seen at temperatures greater than 1300K and growing in intensity as the temperature is raised. A comprehensive analysis carried out at a tunable synchrotron light

source, which eliminates the challenge of dissociative ionization and can access products beyond the capability of the tabletop Nd:YAg laser agrees with these results.

A set of concentration trials was carried out to confirm that none of the products observed (or pathways were being suppressed) due to bimolecular reactions. This involved assessing spectra from evaluations carried out at 0.15% dimethoxymethane as a high concentration limit, followed by trials at 0.1%, 0.05%, and 0.025%. All four evaluations confirmed that none of the observed peaks were due to bimolecular reaction, with peaks across concentrations being identical in mass over charge and varying only in signal intensity.

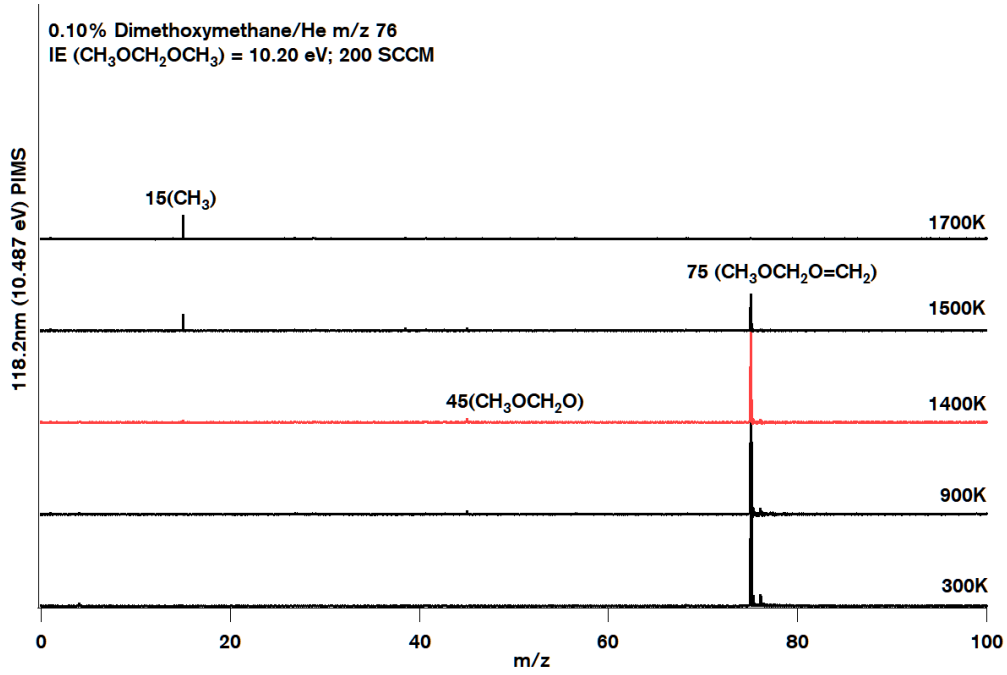

Figure 5.1: PIMS of 0.1% Dimethoxymethane in He in the micro-reactor at 200 SCCM heated from 300 to 1700 K and ionized by 118.2 nm (10.487 eV) photons

5.3.3.2 2,4,6 Trioxanonane (M-2-M)

The next member of the methyl end group POM-E evaluated was 2,4,6 Trioxanonane (POM-E2) - this molecule differs from dimethoxymethane in having an additional O-CH2 group in the chain. A sample at 99% purity was obtained from Asta Tech for this evaluation and Figure

5.2 shows PIMS spectra for 0.1% of the molecule in a Helium carrier gas. At room temperature, a weak parent peak is observed at m/z 105 (the result of the removal of hydrogen through oxygen lone pair ionization) due to a strong dissociative ionization effect. Laser intensity coupled with additional oxygen in the second methoxy group results in intense dissociative ionization at room temperature, with peaks at m/z 77 (formyl radical elimination), m/z 76 (formaldehyde elimination), m/z 75(secondary C-O bond fission), m/z 74 (methanol elimination). These dissociative ionization peaks persist till 1500K, with intensity decreasing with increasing temperature. At 900K, the first pyrolytic decomposition product is observed at m/z 45 (CH_3OCH_2 *) and 61 (CH_3OCH_2O*). With a further increase in temperature, the fragment peaks persist with a progressive reduction in parent peak intensity. At 1300K, the first sign of methyl peak (m/z 15) is observed - with peak height growing with increasing temperature, consistent with observations made with dimethoxymethane. By 1500K, all other pyrolytic fragmentation peaks disappear, with only the methyl peak and weak fragmentation peaks at m/z 74 and m/z 75. This indicates the strong tendency of the molecule at elevated temperatures to fragment in the short residence time of the reactor to form methyl radical and formaldehyde (m/z 30, IE 10.88 eV[31]). At temperatures beyond 1500K, the parent peak at m/z 105 disappears, and only the methyl peak at m/z 15 endures.

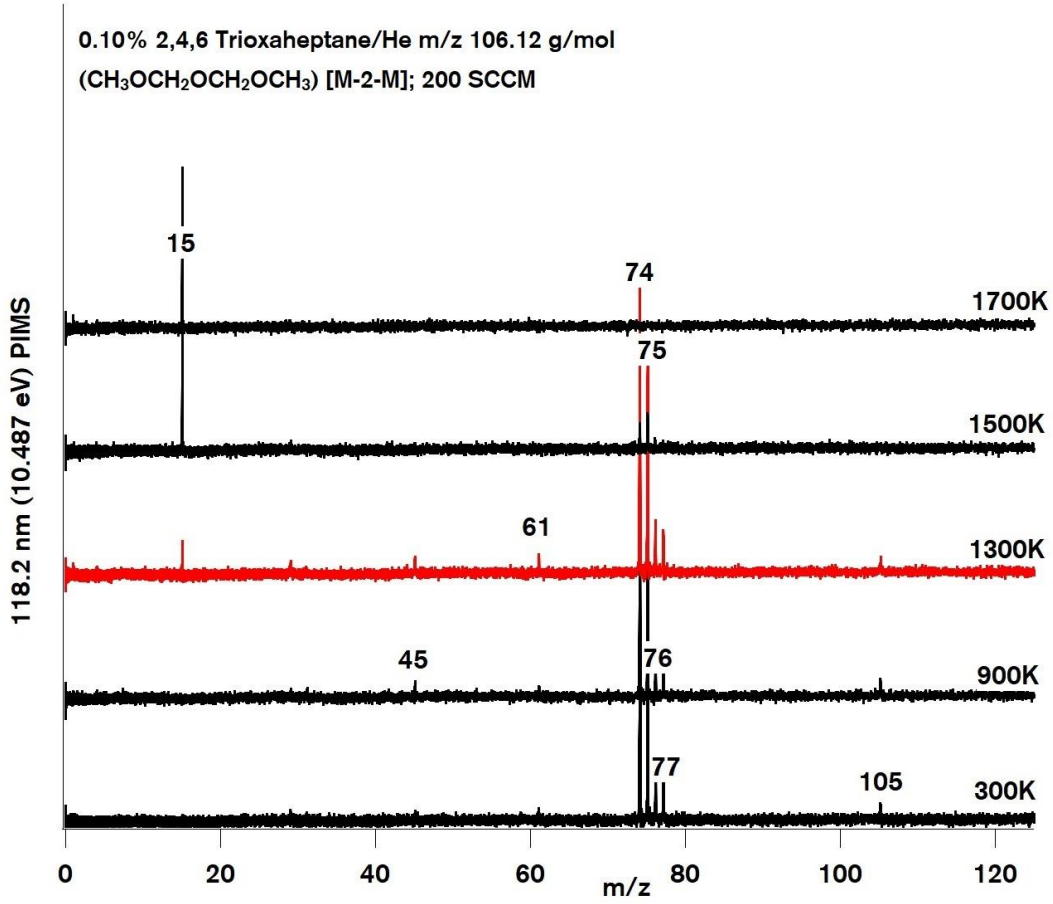

Figure 5.2: PIMS of 0.1% 2,4,6 Trioxanonane in He in the micro-reactor at 200 SCCM heated from 300 to 1700 K and ionized by 118.2 nm (10.487 eV) photons

5.3.3.3 2,4,6,8 Tetraoxanonane (M-3-M)

The third compound evaluated using the photoionization mass spectrometry setup was 2,4,6,8 Tetraoxanonane [M-3-M], containing two O-CH2 groups more than dimethoxymethane and weighing 136 g/mol. The sample evaluated was synthesized at CSU to a purity of >96%. Figure 5.3 shows PIMS spectra for 0.1% of the molecule in helium. Like the previous two molecules evaluated, M-3-M also undergoes a very high degree of dissociative ionization. The photon energy of 10.487eV is strong enough to completely break down the parent peak at room temperature into multiple fragments, with a minimal parent peak at m/z 136. Major peaks are

observed at m/z 107, m/z 106, m/z 105, and m/z 104, with the peak at m/z 105 being the strongest in relative intensity. These peaks correspond to the elimination of methoxy (CH_3O), formaldehyde (CH_2O), and methanol (CH_3OH) from the parent molecule. The peak at m/z 91 is $CH_3OCH_2OCH_2O$*, with the other fragment at m/z 45 (CH_3OCH_2). Unlike the other two compounds, where the bond cleavage between the oxygen and carbon atoms is driven through thermal cracking, in this case, bond breakage is achieved through photon impact. A set of peaks is observed at m/z 74, m/z75 ($CH_3OCH_2OCH_2$), m/z 76, and m/z 77 caused by the bond breakage between the oxygen and carbon at different sites along the molecule. The corresponding fragments associated with these masses are also seen at m/z 59, m/z60, and m/z 61. The peak at m/z 44 may be assigned to *C_2H_4O. These dissociative ionization fragments persist up to 1400K, with most peaks disappearing beyond this temperature. The appearance of methyl radical (*CH_3 m/z 15) is first noted at 1200K. This is lower than the 1300K seen across the previous two molecules and concentration evaluations. This can be attributed to the longer chain length of the molecule with relatively weaker bonds binding individual fragments leading them to break down more easily into methyl and formaldehyde at elevated temperatures. By 1800K, the only peaks visible are at m/z 15, which increases in intensity between the temperature range of 1200K to 1800K.

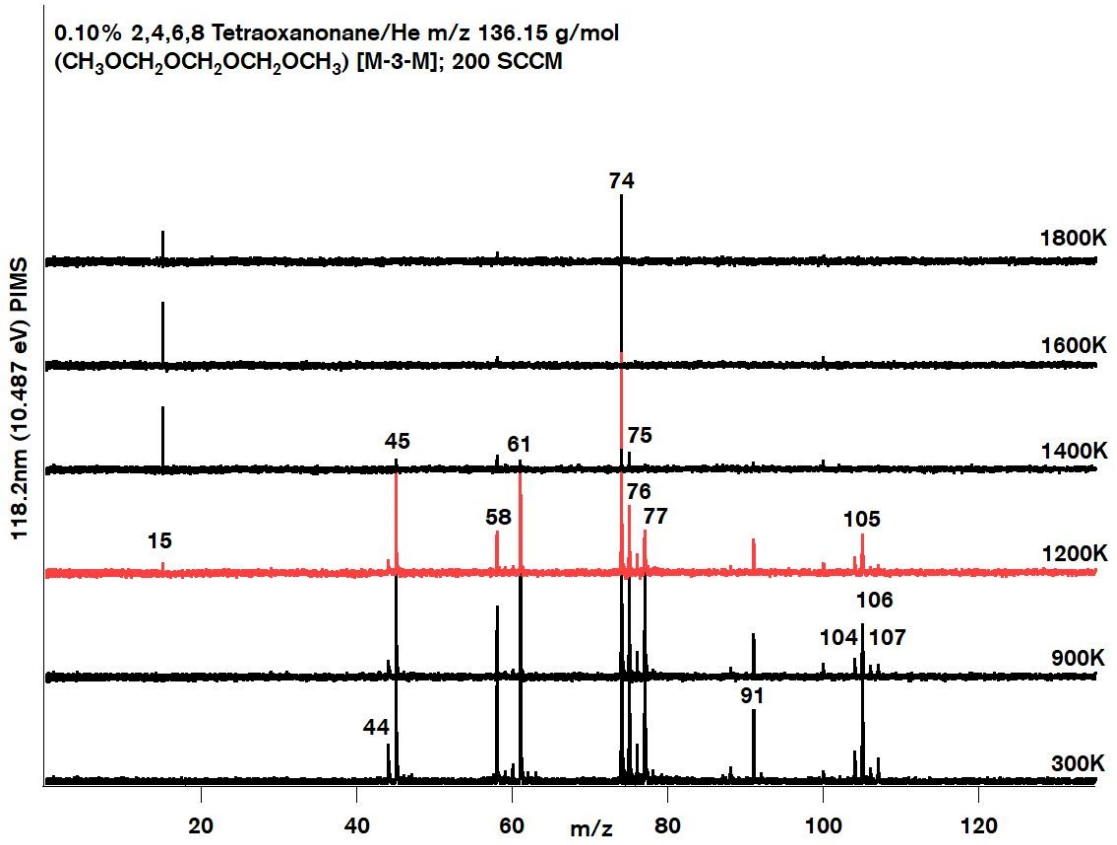

Figure 5.3: PIMS of 0.1% 2,4,6,8 Tetraoxanonane in He in the micro-reactor at 200 SCCM heated from 300 to 1800 K and ionized by 118.2 nm (10.487 eV) photons

5.3.4 Computational Results

Various initiation reactions involved in the pyrolysis of POM-E1-3 molecules are studied using QM calculations. Initiation steps include C-H and C-O bond fission routes as well as molecular routes forming CH_2O via transition state (TS) structure. The details of the reactions studied are shown in Table 5.1. Based on the barrier of bond fission routes calculated using CCSD(T)/cc-pV(D+T)Z level of theory, bond dissociation energies (BDEs) of C-H and C-O bonds involved in POM-E1-3 molecules and the effect of chain length on BDEs as the number of oxymethylene units (-CH_2-O-) increases from one to three. This section gives us a sense of what abstractions will play a bigger role and what unimolecular bond fissions may be competitive. After

we explain the effect of increasing POM-E chain length on the strength of chemical bonds, we discuss the chemical kinetics involved during the initial phase of pyrolysis of POM-E1-3 molecules. In this section, we discuss dominant initiation pathways based on the rate constants calculated using ANL's code MESS and elucidate the change in reactivity as the number of CH_2O moiety increases in POM-E molecules.

5.3.4.1 Bond dissociation energy (BDE)

Using CCSD(T)/cc-pV(D+T) Z level of theory, bond dissociation energies (BDEs) are calculated for three different POM-Es studied in this work, the details of which are provided in Figure 5.4. As can be observed from this figure, the BDEs for C-H bonds are much higher than that of C-O bonds for all POM-Es. For DMM containing only one oxymethylene unit, BDEs for C-H bonds are ~96 kcal/mol for both terminal and central carbon belonging to CH_3O and CH_2O moieties in the molecule, respectively. However, for C-O bonds, there exist significant differences in BDEs for the terminal (~81.4 kcal/mol) and central carbon (87.9 kcal/mol), which is ~6.5 kcal/mol stronger than the other. A similar conclusion was made by Kopp et al. [24] and Golka et al. [25], [26]by performing CCSD(T) calculations.

From Figure 5.5, which shows the comparison of BDEs for POM-E_{1-3}, it can be observed that as the number of oxymethylene units increases by one, BDE for C-H bond in the CH2O moiety (or secondary carbon) tends to increase by ~1-2 kcal/mol, although there is no significant change in BDE for C-H bond in CH_3O moiety (or terminal carbon) of the molecule (~96 kcal/mol). Therefore, POM-E molecules have the strongest C-H bond belonging to CH_2O moiety rather than the terminal carbon. It is to be noted that the above-mentioned trend in POM-E molecules contrasts with that of conventional hydrocarbon fuels, where primary or terminal C-H bonds are stronger

than that of secondary or tertiary. This can be explained in terms of electron delocalization due to the presence of multiple oxygen atoms in POM-E molecules, which imparts extra stability to the central carbon atom[22].

Like C-H bonds, the C-O bond belonging to CH_3O moiety (terminal C-O bond) has the lowest BDE and all the C-O bonds belonging to CH_2O moiety in the POM-E molecule are significantly stronger than that of the terminal C-O bond (ΔBDEs ~6 kcal/mol for POM-E1 and ~8 kcal/mol for POM-E3). It is also to be noted that for all three POM-Es, differences in BDEs of C-O bonds in CH_2O moiety is only approximately 1 kcal/mol and the strongest C-O bond in the structure always belongs to the first CH_2O moiety (central C-O bond in DMM) in the molecule. Furthermore, like BDE trends observed for C-H bonds in POM-Es, BDE of terminal C-O bond remains approximately the same (~81 kcal/mol) for all three POM-Es and other C-O bonds in the structure, BDE tends to increase by ~1 kcal/mol with the addition of one oxymethylene unit in the chain. These results are partially validated by the experimental observations made where the primary products of decomposition are the elimination of the end methyl group seen at temperatures above 1000K. The decreasing bond strength of these terminal methyl groups is observed with the progressive reduction in temperature at which the first methyl peaks are observed. Observation of other dissociation products is not possible due to the fixed energy of the ionization source, which puts products such as formaldehyde (CH_2O) and methoxy radical (CH_3O^*) outside the ionizable threshold.

From the above discussion, it is evident that the inclusion of additional CH_2O units in the structure makes the strongest C-H and C-O bond in the POM-Es even stronger; however, it does not change or impact the weakest bond. This indicates that all POM-Es are likely to initiate decomposition via a similar dominant reaction pathway which is discussed in detail in the next

section. Moreover, as BDE is closely related to the stability of the radicals formed and high bond dissociation energies reflect the formation of unstable free radicals, from the above discussion it can also be concluded that as chain length increases, POM-E molecules will start forming less stable radicals during pyrolysis which can undergo decomposition at a faster rate to form β-scission products. Quantum mechanical calculations at the same level of theory regarding radical decomposition pathways will be discussed in the next sections regarding the chain effects of POM-E radicals on kinetics. The competition between bond dissociation and abstraction is critical in the case of blending with diesel fuels. During compression ignition, the creation of fuel-rich pockets could result in pyrolysis dominating. At other zones, abstraction reactions will be prevalent. With the experimental results unable to fully elucidate likely reaction pathways, a more detailed analysis of the competing reaction rates will be required to evaluate POM-E decomposition. This is presented in the following sections.

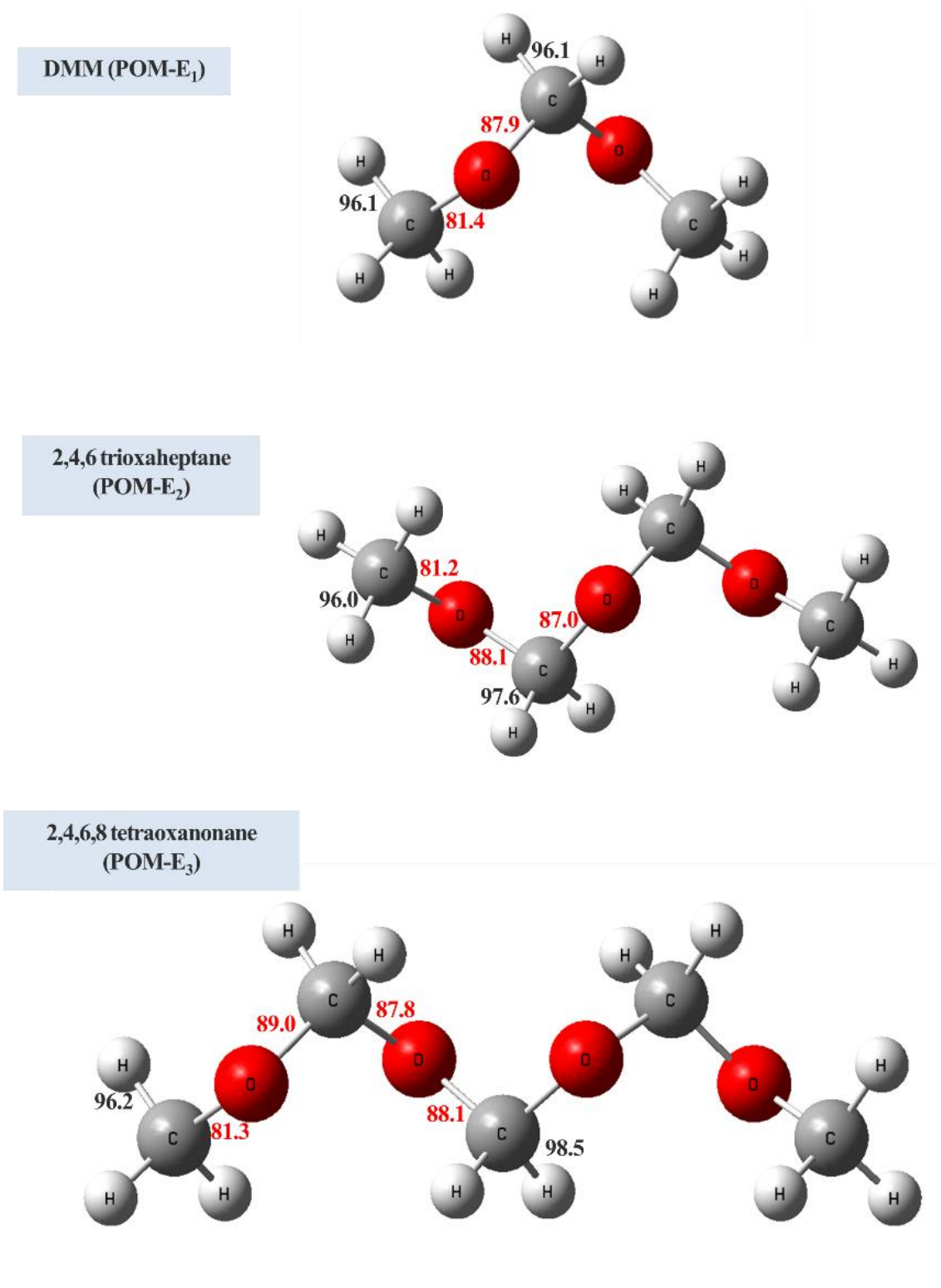

Figure 5.4: BDEs (kcal/mol) for three POM-E molecules

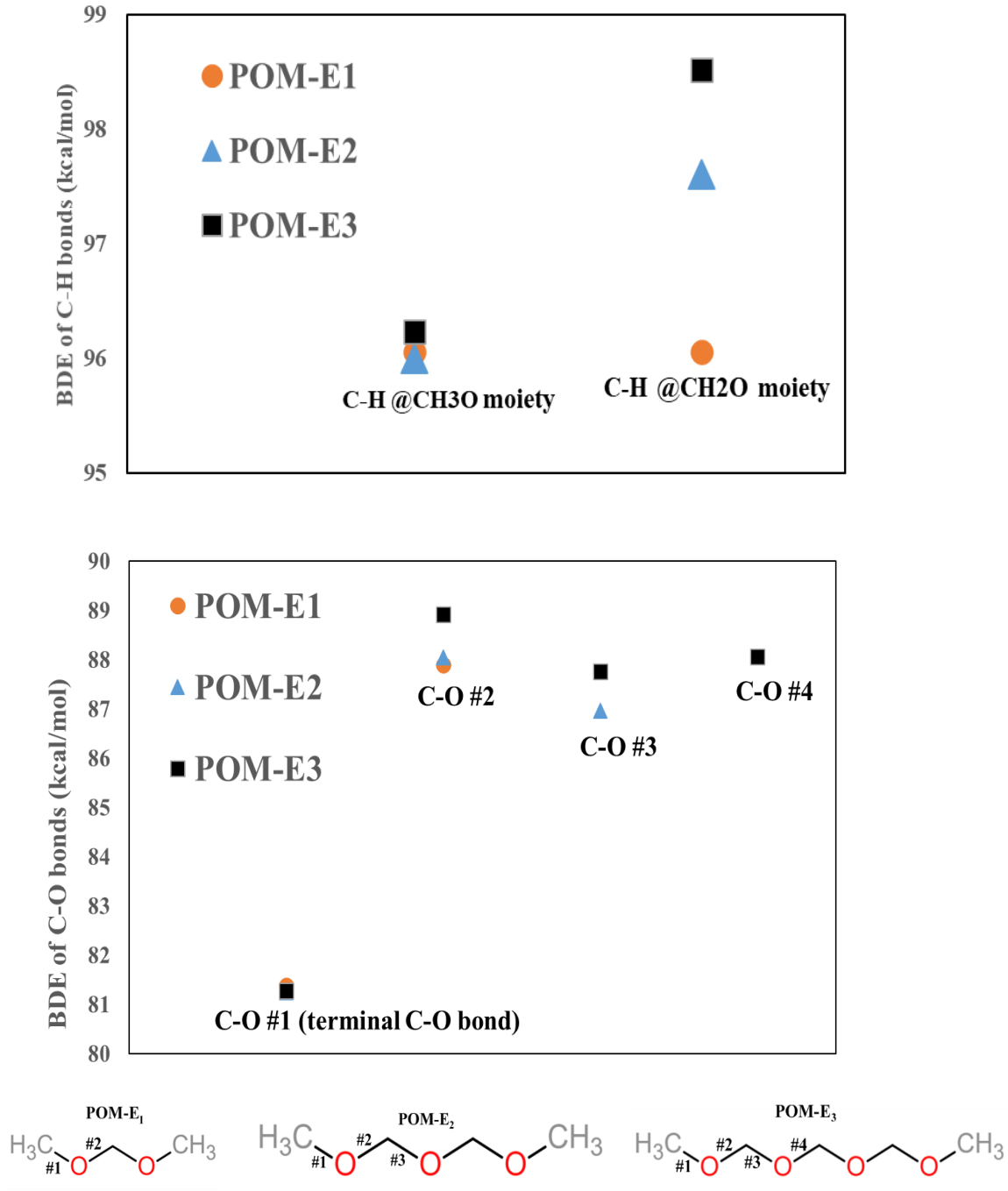

Figure 5.5: Comparison of BDEs (kcal/mol) for three POM-E molecules

5.3.4.2 Initiation steps and rate constant comparison

Using KinBot, scanning of potential energy surface (PES) is performed to identify unimolecular initiation reactions involved during the pyrolysis of three different POM-E_{1-3} molecules. The details of the reactions are shown in Table 5.1, and a simplified PES for three POM-Es is shown in Figure 5.6 to Figure 5.8.

Table 5.1 Barriers (kcal/mol) of important unimolecular reactions involved during the initial phase of pyrolysis of three different POM-E molecules (n=1, 2, 3)
(QM method: CCSD(T)/cc-pV(D+T) Z)

POM-E molecule	n	No.	Reactions	Barrier (E)*
$CH_3OCH_2OCH_3$	1	R1.1	$H + \dot{C}H_2OCH_2OCH_3$	96.06
		R1.2	$H + CH_3O[\dot{C}H]OCH_3$	96.06
		R1.3	$\dot{C}H_3 + \dot{O}CH_2OCH_3$	81.38
		R1.4	$CH_3\dot{O} + \dot{C}H_2OCH_3$	87.90
		R1.5	$CH_2O + CH_3OCH_3$	77.10
$CH_3OCH_2OCH_2OCH_3$	2	R2.1	$H + \dot{C}H_2OCH_2OCH_2OCH_3$	96.00
		R2.2	$H + CH_3OCH_2O[\dot{C}H]OCH_3$	97.61
		R2.3	$\dot{C}H_3 + \dot{O}CH_2OCH_2OCH_3$	81.24
		R2.4	$CH_3\dot{O} + \dot{C}H_2OCH_2OCH_3$	88.05
		R2.5	$CH_3O\dot{C}H_2 + \dot{O}CH_2OCH_3$	86.97
		R2.6	$CH_2O + CH_3OCH_2OCH_3$	65.45
$CH_3OCH_2OCH_2OCH_2OCH_3$	3	R3.1	$H + \dot{C}H_2OCH_2OCH_2OCH_2OCH_3$	96.24
		R3.2	$H + CH_3OCH_2O[\dot{C}H]OCH_2OCH_3$	98.52
		R3.3	$\dot{C}H_3 + \dot{O}CH_2OCH_2OCH_2OCH_3$	81.28
		R3.4	$CH_3\dot{O} + \dot{C}H_2OCH_2OCH_2OCH_3$	88.92
		R3.5	$CH_3O\dot{C}H_2 + \dot{O}CH_2OCH_2OCH_3$	87.76
		R3.6	$CH_3OCH_2\dot{O} + \dot{C}H_2OCH_2OCH_3$	88.06
		R3.7	$CH_2O + CH_3OCH_2OCH_2OCH_3$	79.40

*For bond-fission reactions involved in Pathways 1 and 2, barrier (E)=$E_{product}$-$E_{reactant}$
For reactions involving TS, barrier (E)=E_{TS}-$E_{reactant}$

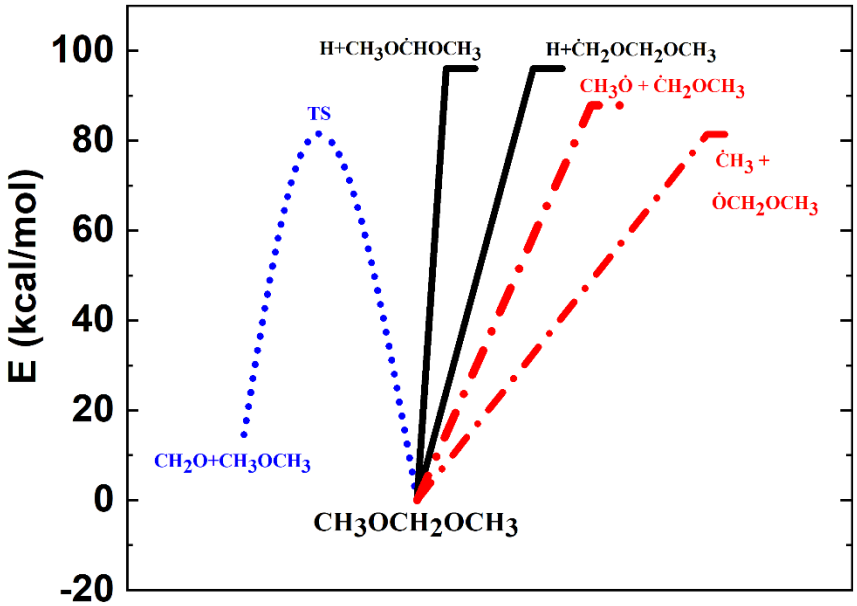

Figure 5.6: Potential energy surface (PES) of important unimolecular reactions involved during the initial phase of pyrolysis of $CH_3OCH_2OCH_3$

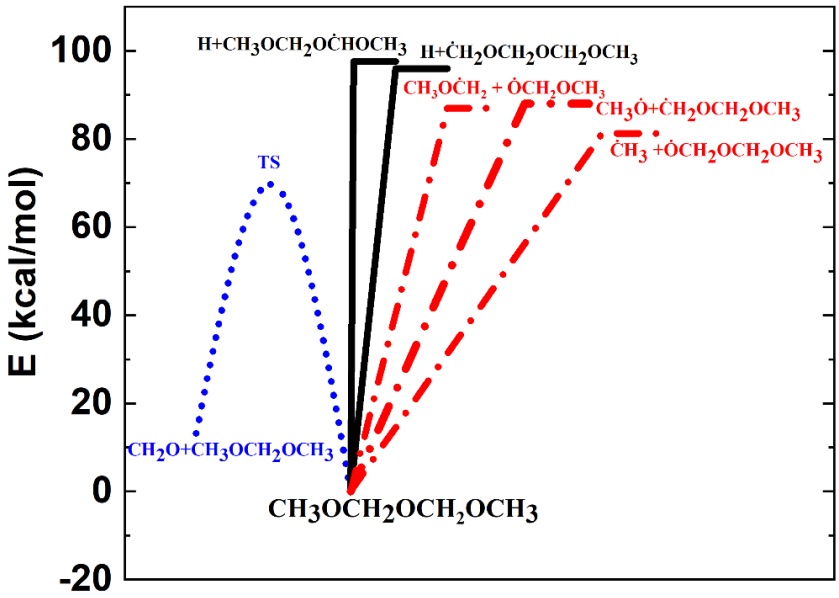

Figure 5.7: Potential energy surface (PES) of important unimolecular reactions involved during the initial phase of pyrolysis of $CH_3OCH_2OCH_2OCH_3$ (n=2)

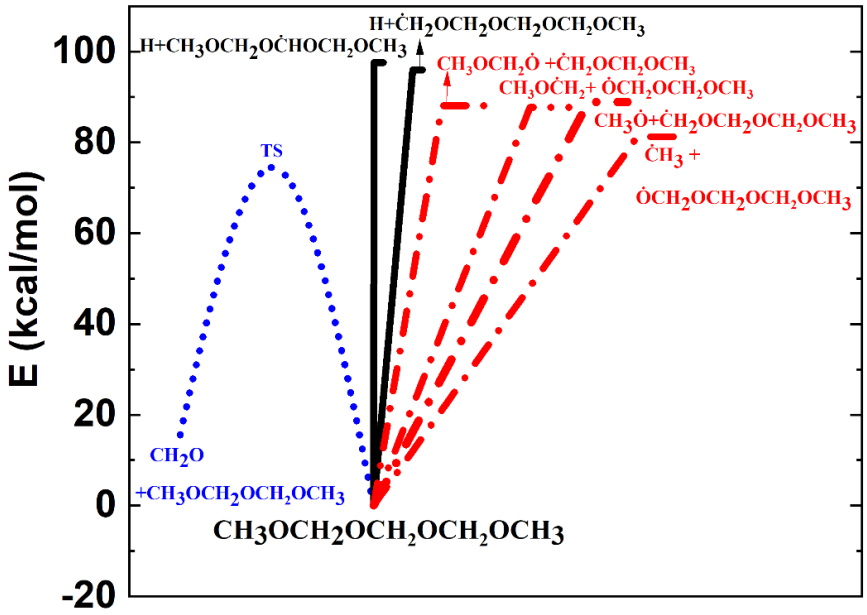

Figure 5.8: Potential energy surface (PES) of important unimolecular reactions involved during the initial phase of pyrolysis of $CH_3OCH_2OCH_2OCH_2OCH_3$ (n=3)

From the PES, it is observed that POM-E (n=1, 2, 3) molecules undergo unimolecular decomposition via three different pathways:

1) *Pathway 1* consists of reactions involving C-H bond fission at the terminal and central methyl groups forming H radical and corresponding POM-E radicals.

2) *Pathway 2* involves breaking of C-O bond belonging to CH_3O and CH_2O moieties along the chain-forming different radicals such as methyl radical ($H_3C\cdot$), methoxy radical ($CH_3O\cdot$), methoxymethyl radical ($CH_3OCH_2\cdot$), $CH_3OCH_2O\cdot$, etc.

3) *Pathway 3* involves the formation of formaldehyde (CH_2O); in the process, dimethoxymethane (DMM, CH_3-O-CH_2-O-CH_3, n=1) forms dimethyl ether (CH_3OCH_3); 2,4,6 trioxaheptane (CH_3-O-CH_2-O-CH_2-O-CH_3, n=2) and 2,4,6,8 tetraoxanonane (CH_3-O-CH_2-O-CH_2-O-CH_2-O-CH_3, n=3) breaks down to form DMM (n=1) and 2,4,6 trioxaheptane (n=2) respectively.

Pathway 1 and *Pathway 2 are solely* comprised of bond fission reactions, and *Pathway 3* proceeds via a transition state (TS). Figure 5.9 shows the molecular structure of TS involved in *Pathway 3* for all three POM-E molecules studied in this work. As the figure shows, for POM-E1 and POM-E3, terminal CH3 approaches the atom O of CH_2O moiety next to it, and formaldehyde (CH2O) forms in the process. For POM-$E_{2,}$ atom O of terminal CH_3O moiety approaches the CH_2 group, and in the process, formaldehyde (CH_2O) forms.

While *Pathway 1* and *Pathway 2* comprise bond fission reactions involving no distinct TS structure, *Pathway 3* proceeds via a transition state (TS). Figure 5.9 shows the molecular structure of TS involved in *Pathway 3* for all three POM-E molecules studied in this work. As can be observed from the figure, for POM-E_1 and POM-E_3, terminal CH_3 approaches the atom O of CH_2O moiety next to it, and in the process, formaldehyde (CH_2O) forms. For POM-$E_{2,}$ atom O of terminal CH_3O moiety approaches the CH_2 group, and in the process, formaldehyde (CH_2O) forms.

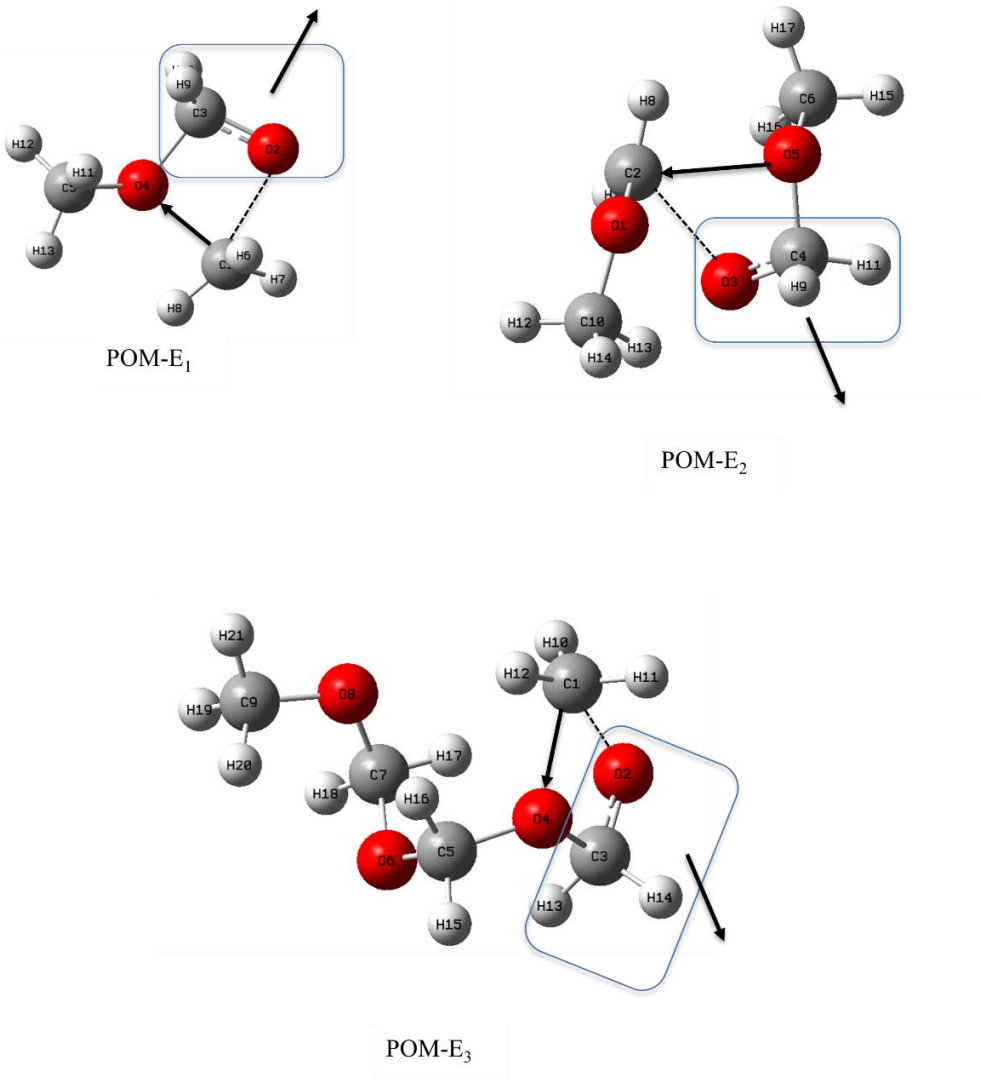

Figure 5.9: Molecular structures of TS involved in Pathway 3 for all three POM-E molecules (n=1-3)

Using Argonne National Laboratory's code MESS, the rate constants of the above-mentioned reaction pathways are calculated over a temperature range of 500-200K at different pressures (0.00001 to 100 atm). Figure 5.10 shows the rate constant calculated at different temperatures at pressure, P=10 atm. From Figure 5.10, it can be observed that among the three pathways, *Pathway 2* is the most dominant through which POM-E molecules can undergo decomposition in the temperature range of 500-2000 K. This is even though the energy for CH_2O elimination is lower than the bond fission routes. It is to be noted that predictably based on BDEs discussed in the

previous section, terminal C-O bond fission reaction forming CH_3 radical is the most critical initiation step for all three POM-Es.

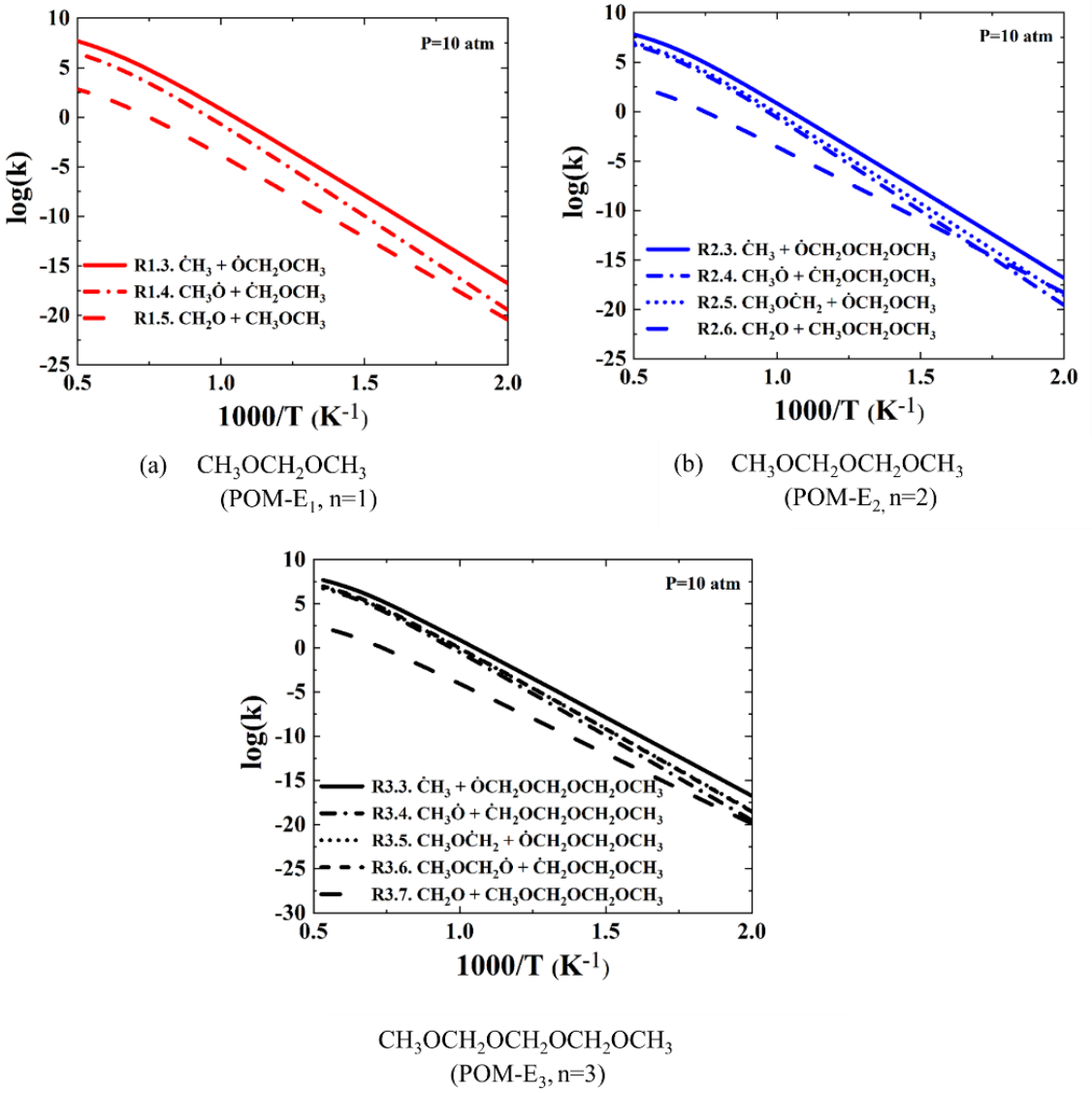

Figure 5.10: Temperature (T) dependent rate constants (k) for reactions involved in Pathway 2 and Pathway 3 at pressure, P =10 atm

A similar conclusion was made by Golka et al. [25],[26] for DMM pyrolysis Figure 5.11 and Figure 5.12 show the comparison of rate constants and branching ratio (BR) calculated in this

study for C-O bond fission reactions of DMM with that of existing literature. As can be observed from these figures, high-pressure rate constants and BRs calculated in this work matches very well with that of Golka et al. [25],[26] who performed experiments as well as QM calculations using CCSD(T)/ cc-pV(D+T) Z level of theory to study initiation reactions involved during DMM pyrolysis. In addition to Golka et al.'s [25], [26] QM calculated rate constants, Figure 5.12 also shows rate constant and BR from other studies on DMM where rate constants are estimated based on analogy to similar molecules.

These preliminary rates have been updated with additional routes evaluated, with rate constants and branching ratios for the decomposition of DMM being plotted at a pressure of 1 atm. These evaluations have been performed with both argon and nitrogen and are shown in Appendix C5.

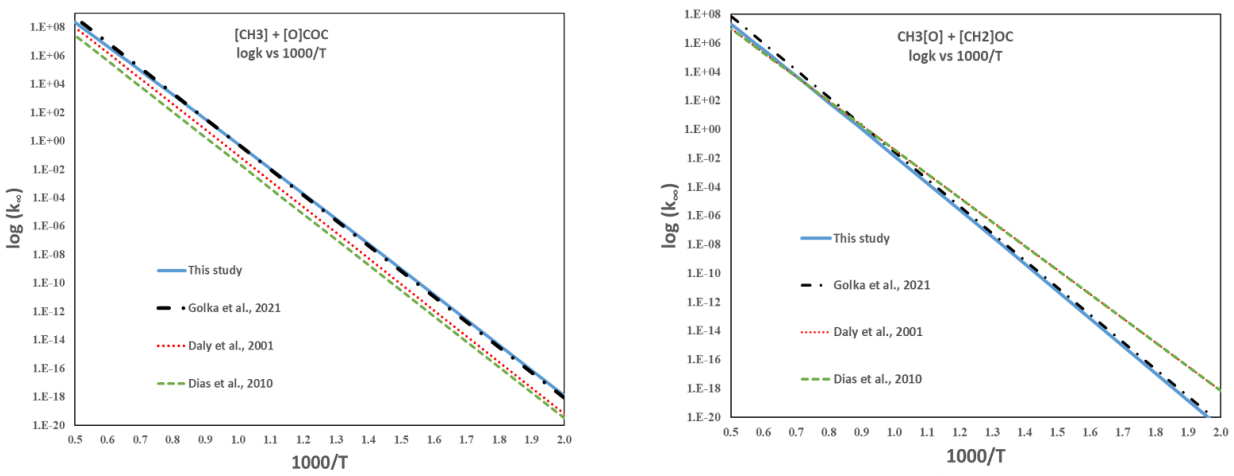

Figure 5.11: Comparison of QM calculated rate constant in this study with existing literature

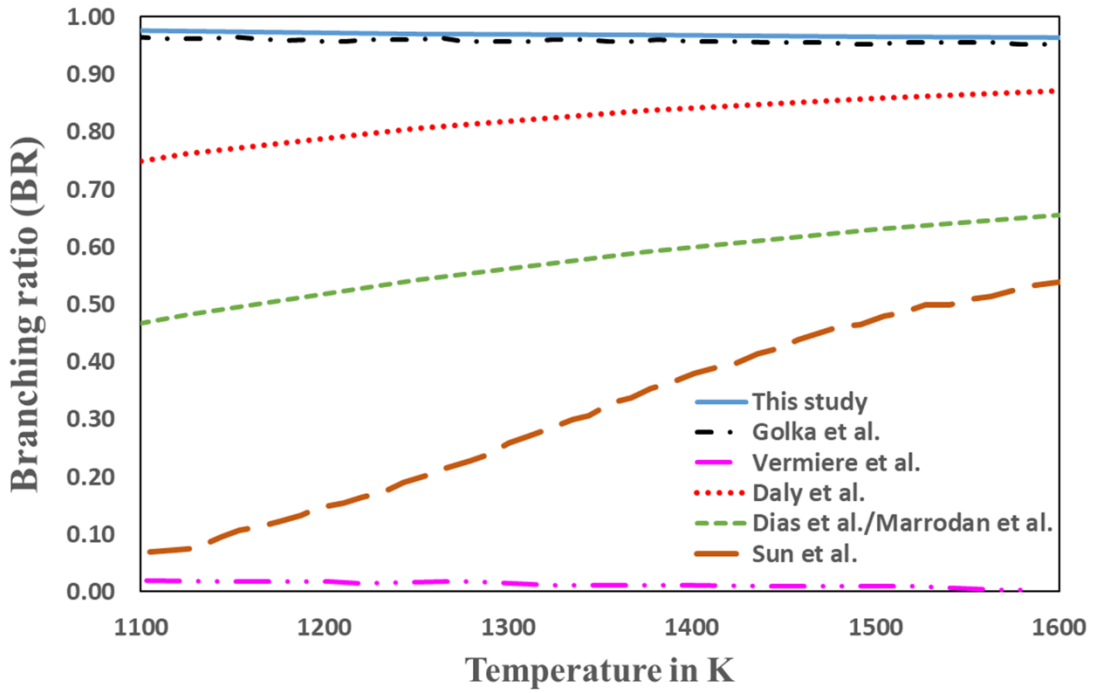

(a) BR for $\dot{C}H_3$ + $\dot{O}CH_2OCH_3$

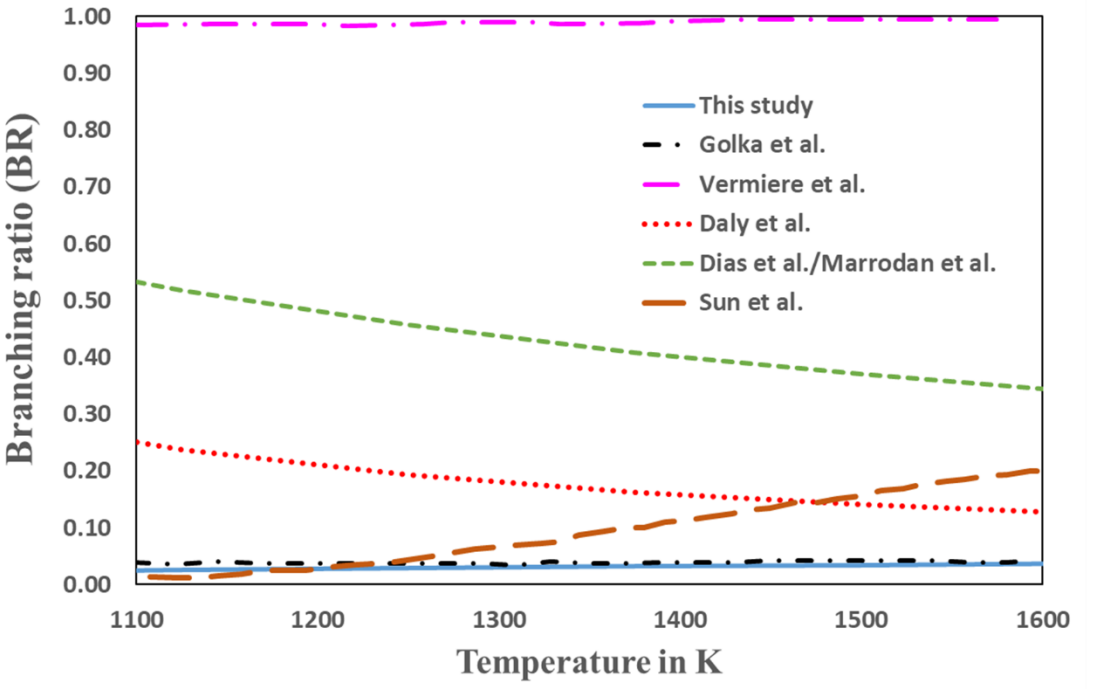

(b) BR for CH_3 $\dot{O}$ + $\dot{C}H_2OCH_3$

Figure 5.12: Comparison of QM calculated BRs in this study with existing literature

It is to be noted that the estimated rate constants proposed by Daly et al.[17] and Dias et al.[18] based on analogy to DME and DEE underpredicts significantly (by almost ten times and especially at low temperatures) the key initiation reaction, R1.3: $[CH_3]$ +[O]COC. It is to be noted, however, that despite the estimated rate constants by Daly et al. [17] and Dias et al. [18] for reaction R1.3 being significantly lower than this work, it does capture the slope of log(k∞) vs. 1000/T very well. For R1.4. CH_3O+$[CH_2]$ COC, the estimated rate constants based on analogy, overpredicts the rate of the reaction at low temperatures and underpredicted it at temperature T>1000K. In the case of C-O bond fission reaction R1.4. CH_3O+$[CH_2]$ COC for which C-O bond belongs to the CH_2O unit of the chain, the rates estimated by analogy ([17], [18]) do not match either the shape of the slope of the rates calculated in this work or the individual values. This discrepancy in results highlights the unique behavior of the oxymethylene (CH_2O) group in POM-E molecules. From Figure 5.12 which shows the comparison of BR calculated in this study with that of existing literature, it can be observed that there exist significant differences in QM calculated branching rations with that of previous mechanisms based on analogous molecule rate constant estimation. This highlights the inability of these rates to be extended to longer chain POM-Es based on the significant differences that exist with the smallest member of this group of molecules. Moreover, there exists no consensus in the existing literature regarding the branching between two important bond fission reactions involved in the initial phase of DMM pyrolysis.

Upon comparison of the various POM-E kinetics, two trends appear in the reaction analysis. First, thermal decomposition for all molecules is dominated by knocking off the terminal methyl group from the chain. This is highlighted by the fact that this reaction has the highest branching ratio for all three POM-Es studied so far. However, as the chain length increases, other C-O bond fissions become increasingly important, and correspondingly the branching ratio associated with

the reaction forming methyl radical reduces. This signifies that as chain length increases, many more reaction pathways become active, producing other radicals besides the methyl radical. Figure 5.13 shows the branching ratio for different reactions involved in Pathway 2 forming various radicals during pyrolysis of POM-E molecules (n=1-3). Secondly, with the increase in accessible thermal decomposition pathways, the total destruction rate of the POM-E molecules (POM-E -> Products) increases with chain length. For all C-O bond fissions, the resultant radicals can quickly β scission to form CH_3, H, and CH_2O, creating a rapid production in molecules. This is consistent with the observation that as chain length increases, YSI for the POM-E molecules decreases. With the increase in chain length, reaction times and an increased dilution effect become shorter. Combined, this may explain the observed decrease in YSI with chain length. The total rate constants for each of the three POM-E molecules is shown in Figure 5.14.

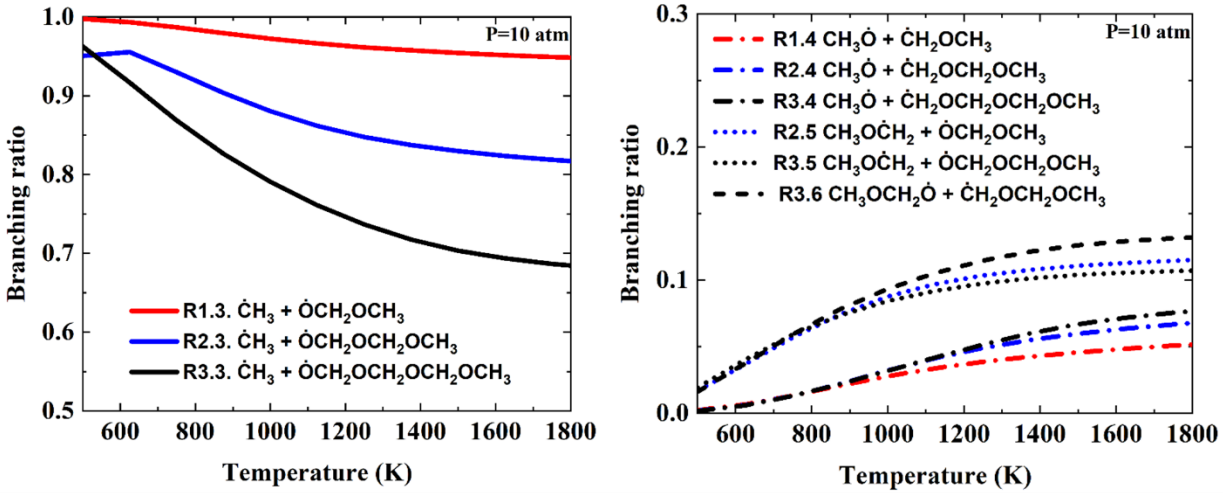

Figure 5.13: Branching ratio plots for three different POM-E molecules (n=1-3) at pressure, P=10 atm.Left**:** The dominant reaction for all three POM-E molecules is the cleavage of the CH_3 terminal group from the molecule. Right: As chain length increases, the contribution from other C-O bond cleavages also becomes more important.

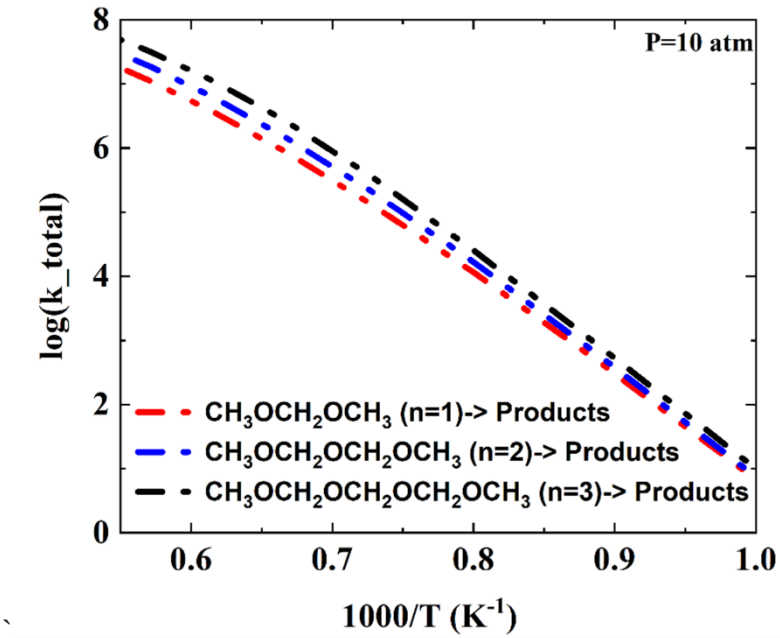

Figure 5.14: Temperature (T) dependent total rate constants (k_total) for three different POM-E molecules (n=1-3) at pressure, P=10 atm.

5.4 Chemical kinetic investigation of end-group effects of polyoxymethylene ethers (POM-E) during pyrolysis

The simplest OME, Dimethoxymethane (CH3-O-[CH2O]$_n$-CH3 where n=1), is comprised of one oxymethylene unit bonded to oxygen with terminating methyl groups. In the next few sections, we refer to Dimethoxymethane (DMM, POM-E1) as M-1-M, where the letters refer to the alkyl end group type, and the number refers to the number of oxymethylene units present in the molecule. A considerable amount of work has been put into understanding the kinetics and ignition properties of M-1-M, as well as similar molecules with more oxymethylene units, up to seven (CH_2-O) units. The high oxygen content and increasing cetane number with the length of these molecules have been highlighted as reasons for their propensity to decrease sooting. However, some major concerns about methyl-terminated OMEs, including low lower heating value (LHV),

high water solubility, and poor sealing material compatibility, may be addressed with longer alkyl end groups.

In a recent paper, Batholet et al. [6] tested various fuel properties, including biodegradability, water-solubility, cetane number, yield sooting index (YSI), and LHV on different OME combinations and showed that ethyl, propyl, and butyl end groups with 1-3 oxymethylene units provide for a substantial reduction in soot emissions while retaining ideal diesel blend properties. The two simplest molecules that fit those criteria are diethoxymethane (E-1-E) and dipropoxymethane (P-1-P). The unimolecular decomposition and oxidation pathways of E-1-E have been studied through shock-tube experiments and high-level quantum chemical calculations [7-8-Leur, Kroger, etc.], and chemical kinetic models of E-1-E by analogy to n-heptane have been proposed for low and high temperatures [28]. Meanwhile, little to no work has been done on the thermal decomposition of P-1-P.

In this work, an investigation of the thermal decomposition of different OME end groups during the first stages of combustion is presented. This is intended to discern the main reaction channels for each of the three different end-group OMEs. Pressure (0.01atm – 100atm) and temperature (500K-2000K) dependent reaction rate constants were calculated for various bond fission and isomerization-decomposition reactions for M-1-M, E-1-E, and P-1-P using quantum chemical calculations at the CCSD(T)/cc-pV∞Z/M06- 2X/cc-pVTZ level of theory. These results are validated against previous experimental and computational work and draw analogies with dipropyl ether for P-1-P.

5.4.1 Experimental methods

The experimental method employed for this work is identical to the technique described in section 5.3.1. Photoionization Mass Spectrometry was used to identify the primary products of

thermal decomposition. The synthesis of diethoxymethane and dipropoxymethane was carried out as part of the DOE Co-Optima project effort at CSU. The synthesis of these variable end-group POM-Es was done using the trans-acetalization reaction of methyl-terminated OMEs (DMM) with higher chain length alcohols. This synthesis technique produced samples with purities of more than 95%. The two samples of diethoxymethane and dipropoxymethane were run at a concentration of 0.1% to prevent any bimolecular reactions. Spectra were obtained across a temperature range of 300K (room temperature) up to 1800K.

5.4.2 Computational modeling methods

The computational method used to model the thermal decomposition of dimethoxymethane, diethoxymethane, and dipropoxymethane is identical to the approach described in section 5.3.2. The Quantum Mechanical calculations featured the same series of operations aimed at producing rates of reactions across a range of pressures in the temperature range of 500 – 2000K.

5.4.3 Experimental results

5.4.3.1 Dimethoxymethane (M-1-M)

PIMS spectra and results for the thermal decomposition of dimethoxymethane are described in section 5.3.3 (A). These results were obtained by running 0.1% samples of dimethoxymethane procured from Sigma Aldrich

5.4.3.2 Diethoxymethane (E-1-E)

Room temperature spectra for diethoxymethane shows significant dissociative ionization with fragments formed at m/z 89 (methyl bond breakage) and m/z 74 (formaldehyde elimination).

The first time thermally activated decomposition pathways are reached is between 1300 and 1400K reactor surface temperatures. The presence of m/z 28 also confirms the validity of the transition state route at 67.9 kcal/mol. Other short-lived products fragment into methyl radicals (m/z 15) and formaldehyde (m/z 30, but not ionizable at 10.487 eV). The PIMS spectra are shown in Figure 5.15.

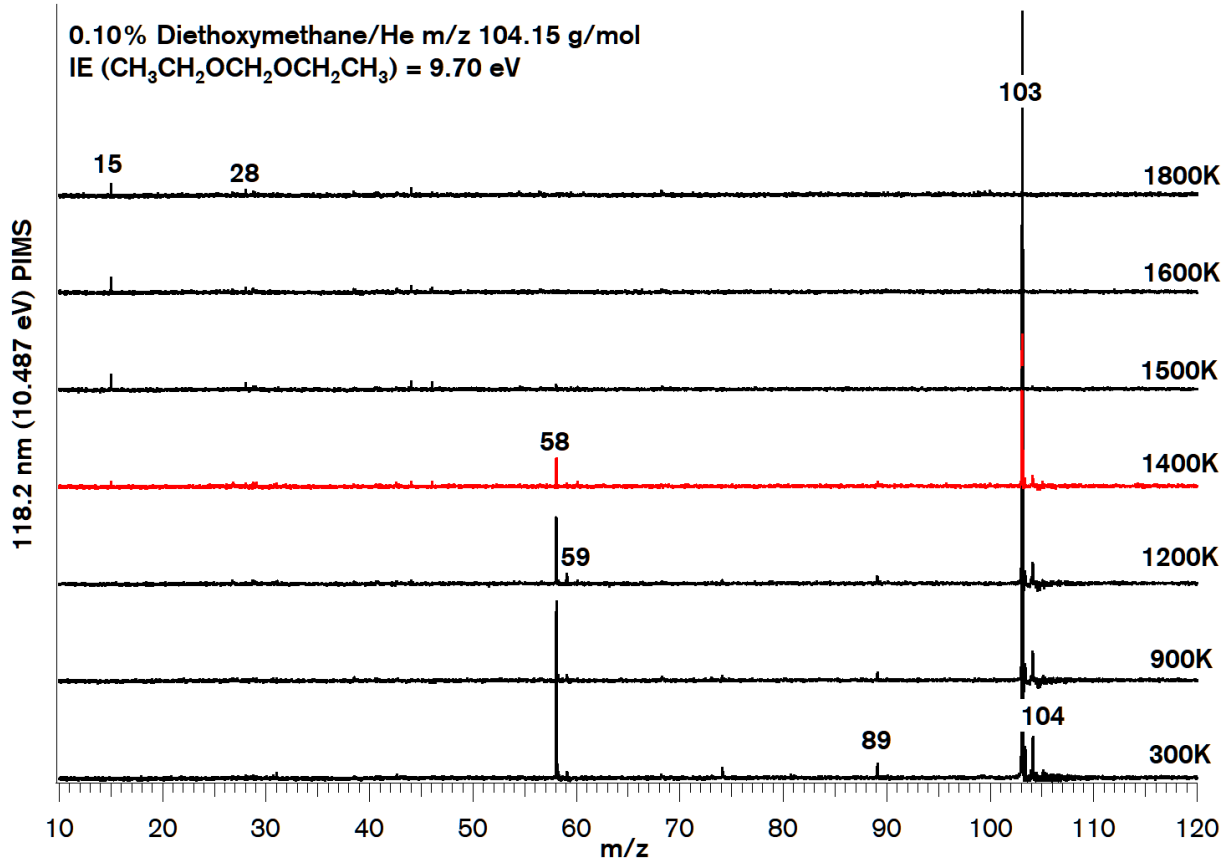

Figure 5.15: PIMS of 0.1% diethoxymethane in He in the micro-reactor at 200 SCCM heated from 300 to 1800 K and ionized by 118.2 nm (10.487 eV) photons

5.4.3.3 Dipropoxymethane (P-1-P)

Room temperature spectra obtained at 300K shows significant dissociative ionization with multiple peaks observed in addition to the parent peak. A weak parent peak signal is seen at m/z

132, with a much larger signal corresponding to the abstraction of a hydrogen atom from the parent molecule internally at m/z 131. A cluster of peaks is observed at m/z 104 (ethylene elimination), m/z 102 (CH_3-CH_2* elimination), and m/z 102 (formaldehyde elimination). The formaldehyde elimination peak is the most dominant route among these three (based on signal intensity). Additional peaks observed at m/z 73 and m/z 72 are due to the fragmentation of the first carbon-oxygen bond and the elimination of propanol. Additional peaks seen at m/z 58 (Propanal) and m/z 43 (CH_3-CH_2-CH_2*) are fragment remnants produced by the laser. The PIMS spectra are shown in Figure 5.16.

As the temperature is raised, the primary decomposition route of elimination of the end propyl and methyl groups is observed at temperatures above 1300K. At these temperatures, the influence of the ionizing medium on the fragmentation is reduced, with bond fission peaks at m/z 43 (CH_3-CH_2-CH_2*) and m/z 15 (CH_3*) becoming dominant.

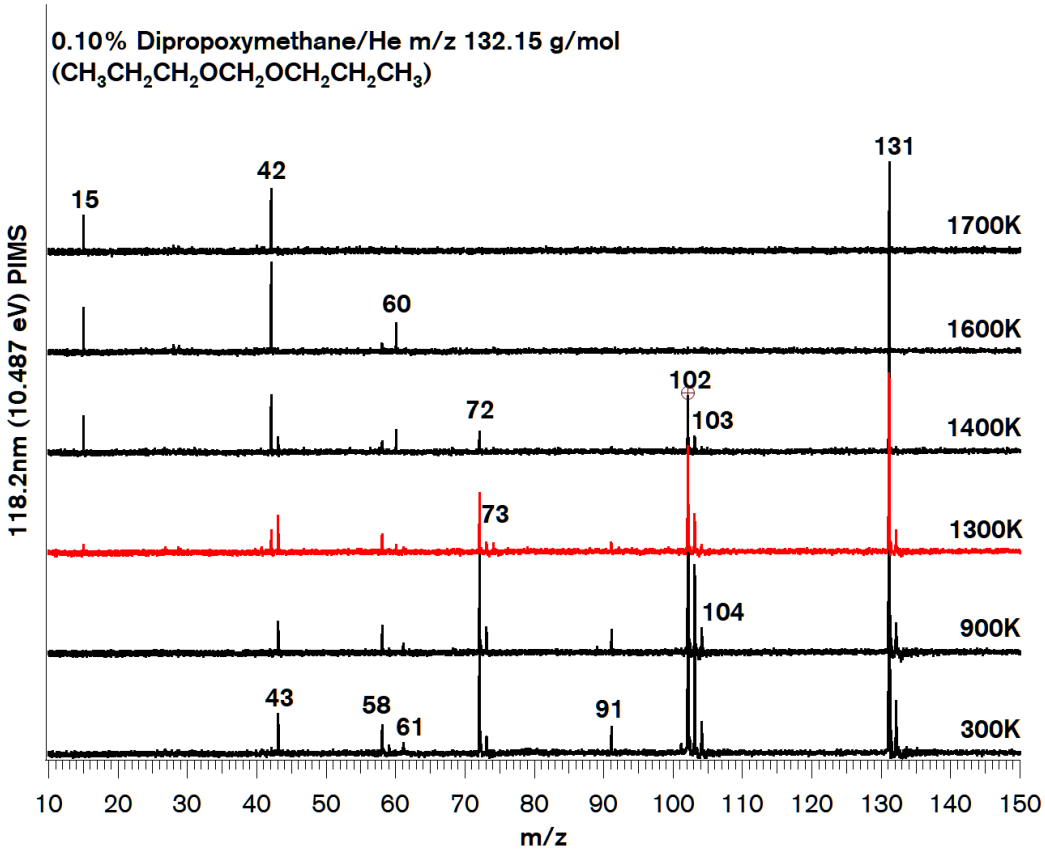

Figure 5.16: PIMS of 0.1% dipropoxymethane in He in the micro-reactor at 200 SCCM heated from 300 to 1700 K and ionized by 118.2 nm (10.487 eV) photons

5.4.4 Computational results

The results from the quantum mechanical calculations were used to determine the individual bond energies for the different carbon-hydrogen, carbon-carbon, and carbon-oxygens bonds in all three molecules. The weakest bond in the case of diethoxymethane is the carbon-carbon bond between the terminal methyl group and the CH_2 group. For dipropoxymethane, the weakest bond is at the C-C bond between the secondary and tertiary carbon atoms in the molecule. The strongest bond in both molecules is the carbon-hydrogen bond in the terminal methyl groups. With an increase in end group length, we observe an increase in the lowest bond energy and a

decrease in the strongest bond energy. A representation of the bond energies is presented in Figure 5.17.

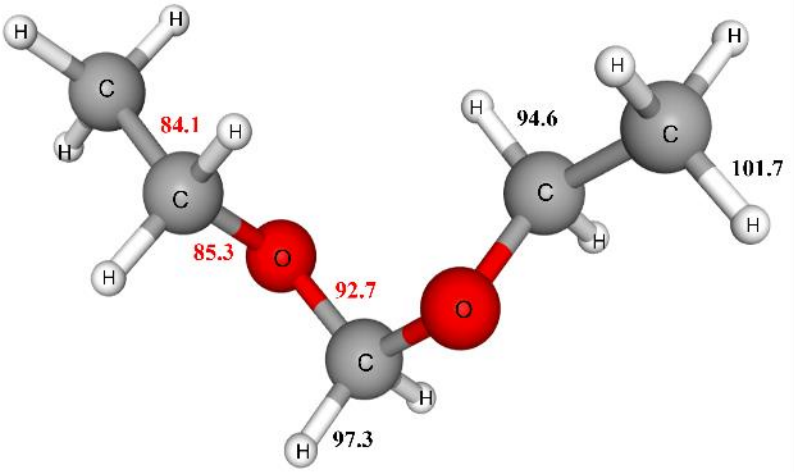

Diethoxymethane (E-1-E)

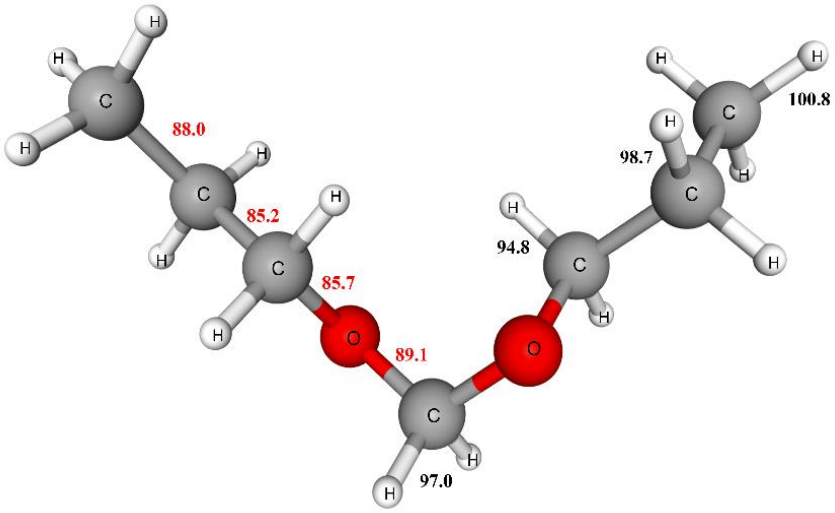

Figure 5.17: Bond Dissociation Energies of diethoxymethane and dipropoxymethane

Dipropoxymethane (P-1-P)

An analysis of the individual reaction rates and branching ratios for diethoxymethane showed that the rate of decomposition of the parent molecule through the breaking of the terminal ethyl and methyl bonds was the fastest. When compared to other likely decomposition reactions, these two rates were orders of magnitude faster across the temperature range. When analyzed as a function of the total decomposition, it was concluded that approximately 99% of the reaction flux is accounted for by these two bond fission routes. The oxygen radicals produced as a result of these bond fissions undergo further decomposition or β scission to produce formates. These reaction rates and branching ratios at a pressure of 1 atm are shown in Figure 5.18 and Figure 5.19.

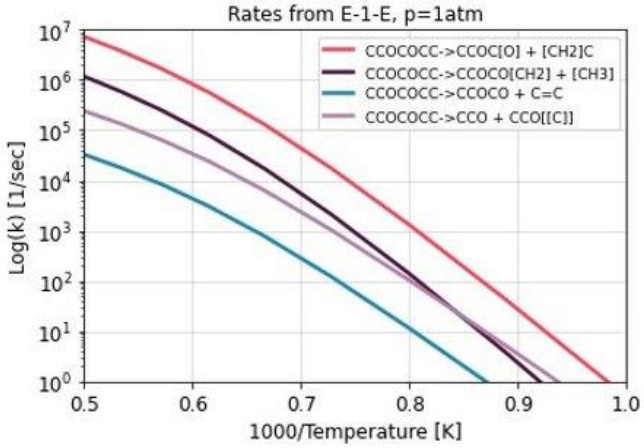

Figure 5.18: Rates of thermal decomposition for diethoxymethane as a function of temperature at 1 atm pressure

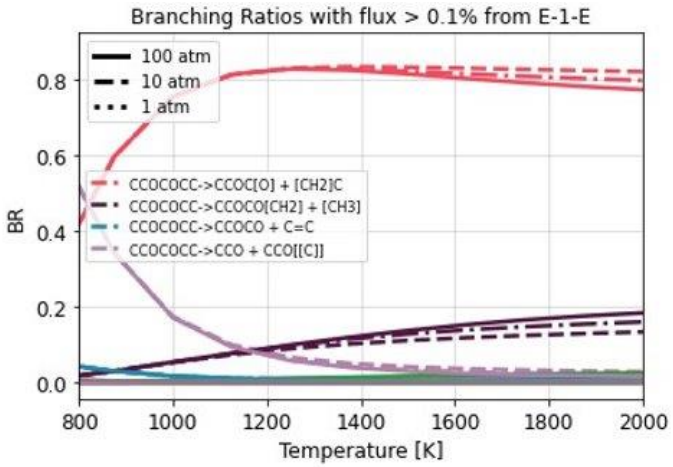

Figure 5.19: Branching ratio for the primary routes of decomposition of diethoxymethane as a function of temperature at 1 atm.

A similar analysis of the reaction rates and branching ratios for dipropoxymethane indicate that most of the reaction flux (greater than 75%) is caused by the bond fission of the terminal ethyl and propyl group. As the temperature is increased beyond 1000K, the breakage of the terminal methyl group and the propoxyl groups become more competitive. The oxygenated radicals produced by the elimination of the methyl, ethyl, and propyl groups undergo a series of further decompositions and β scissions at engine-relevant temperatures to produce formaldehyde and propylene. These reaction rates and branching ratios are shown in Figure 5.20 and Figure 5.21.

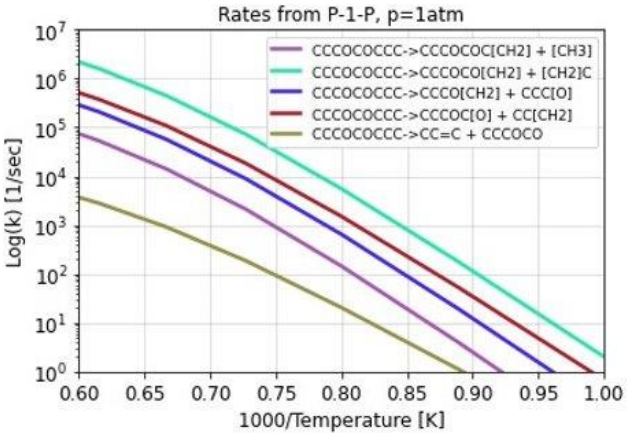

Figure 5.20: Rates of thermal decomposition for dipropoxymethane as a function of temperature at 1 atm

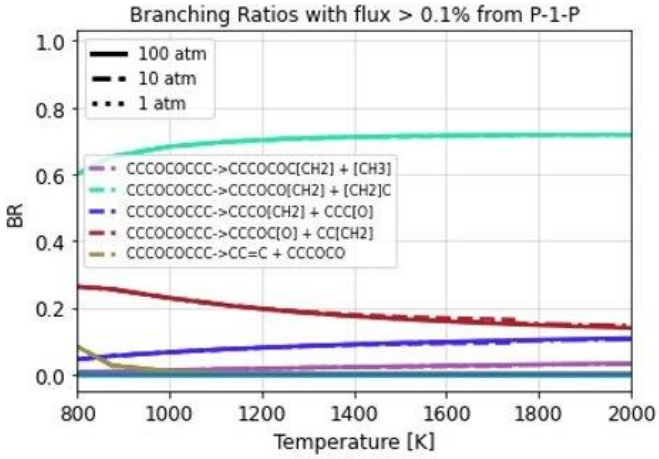

Figure 5.21: Branching ratio for the primary routes of decomposition of dipropoxymethane as a function of temperature at 1 atm.

The results from the experimental observations and modeling calculations confirm that as the length of the end group is increased, the temperature at which the first products of bond fission are observed decreases. This is consistent with a lowering in the bond energies between the three molecules with an increase in the chain length. As the temperature is raised beyond 1000 K the molecular pathways become unimportant and the bond fission routes dominate. Among the three molecules evaluated as part of this study, the rate of consumption (the rate at which the parent molecule is broken down through thermal decomposition) is higher for dipropoxymethane as

compared to diethoxymethane which is higher than dimethoxymethane. For the largest molecule evaluated (dipropoxymethane), as the temperature is raised, bond fissions involving carbon-oxygen bonds become more active, contributing to a large pool of radicals being formed. This is especially relevant at higher temperatures (where combustion normally occurs). The additional radicals produced can form oxygen-containing radicals through H-abstraction. These open further pathways to OH formation and accelerate ignition and combustion chemistry.

5.5 Exploration of secondary decomposition products of methyl-terminated polyoxymethylene ethers

5.5.1 Computational modeling of secondary decomposition

Results from the experimental and computational modeling of the primary decomposition of methyl-terminated polyoxymethylene ethers (dimethoxymethane, 2,4,6 trioxaheptane, and 2,4,6,8 tetraoxanonane) confirmed that the fastest pyrolysis reaction is associated with the breaking of the terminal methyl group from the parent molecule. These routes resulted in the creation of methyl radical ($*CH_3$) and the $*O(CH_2O)_nCH_3$ radical. Ab-initio quantum mechanical calculations were carried out at the CCSD(T)/cc-pV(D+T)Z // M06-2X/CC-pVTZ level of theory to determine the further decomposition of the oxygen-containing radicals. The computational method employed to carry out these reactions is similar to the process described in Chapter 3.

5.5.2 Results and discussion

The results from the analysis carried out are shown in Figure 5.22. This figure shows the relative rates between the different secondary decomposition reactions of the oxygen-containing radical produced by the pyrolysis of dimethoxymethane. The route involving the beta scission of

the radical to form methyl formate and a hydrogen atom is shown to be the fastest. Labbe et al. [29] showed that methyl formate decomposes largely into methanol and carbon monoxide under pyrolysis conditions, which explains the detection of methanol in experimental results of dimethoxymethane pyrolysis. The observation of methanol in the spectra was previously attributed to a hydrogen migration [30] through a transition state to form a carbene which quickly decomposes into methanol.

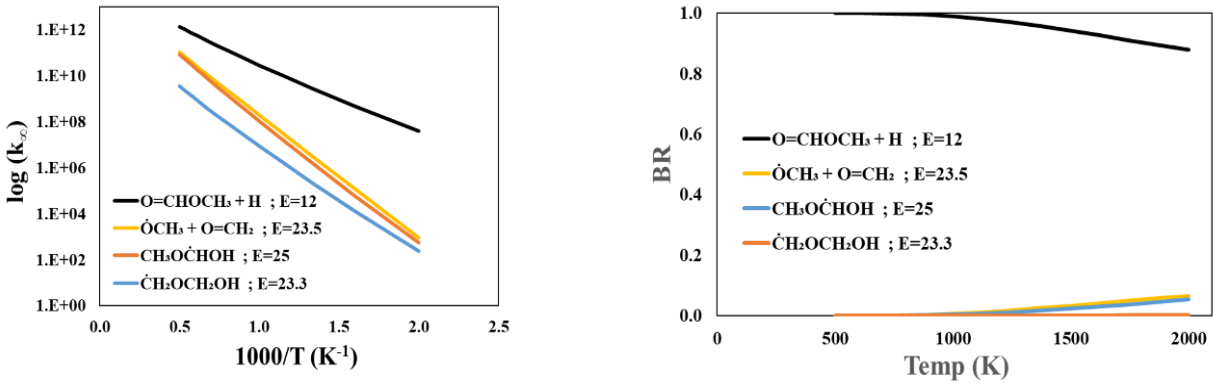

Figure 5.22: (left) Rate comparison of the significant secondary decomposition routes of $[O](CH_2O)nCH_3$; (right) Branching ratio plot of the different secondary decomposition routes $[O](CH_2O)nCH_3$

A similar analysis of the high-temperature pyrolysis of 2,4,6 trioxaheptane (M-2-M) and 2,4,6,8 tetraoxanonane (M-3-M) indicated an analogous decomposition pathway to dimethoxymethane. First, the terminal methyl C-O bond fission forms [O](CH2O)nCH3 radical and the methyl radical, with the former undergoing beta scission to produce formate and the hydrogen radical. Unlike methyl formate, the decomposition of the formates associated with M-2-M and M-3-M decomposition (methoxy methyl formate and methoxymethoxy methyl formate) has not been studied extensively in the literature. Ab-initio Quantum Mechanical (QM) calculations to determine the energies of the different pyrolysis reactions and products of these formates are underway. The results from these modeling efforts are shown in the potential energy

surfaces (PES) Figure 5.23. This PES shows that the lowest transition state (TS) for O=COCOC goes to form methyl formate and formaldehyde. Another pathway to these products is the 3rd lowest energy transition state. The 2nd lowest transition state goes to form formaldehyde, methanol, and carbon monoxide, which is a similar route to the lowest energy TS but includes the subsequent methyl formate decomposition.

The rate calculations for the bond fission reactions are currently underway. However, the relative energies of the lowest energy TS and the lowest energy bond fission can provide insight into possible rate comparisons. Unlike the initial decomposition of the M-2-M fuel molecule, which only has about a 10 kcal/mol energy difference between the lowest energy TS and lowest energy bond fission, methoxy methyl formate has an equivalent difference of about 30 kcal/mol. This larger difference increases the likelihood that the TS reactions will be faster than the bond fission reactions. A similar decomposition trend can be seen in Figure 5.24, which shows the pyrolysis of the M3M formate, O=COCOCOC. These figures show that the dominant early pyrolysis pathway of methyl end group polyoxymethylene ethers (before other radicals are present in significant amounts) leads through formate molecules that "unzip," creating formaldehyde and smaller formate, in addition to hydrogen and methyl radicals.

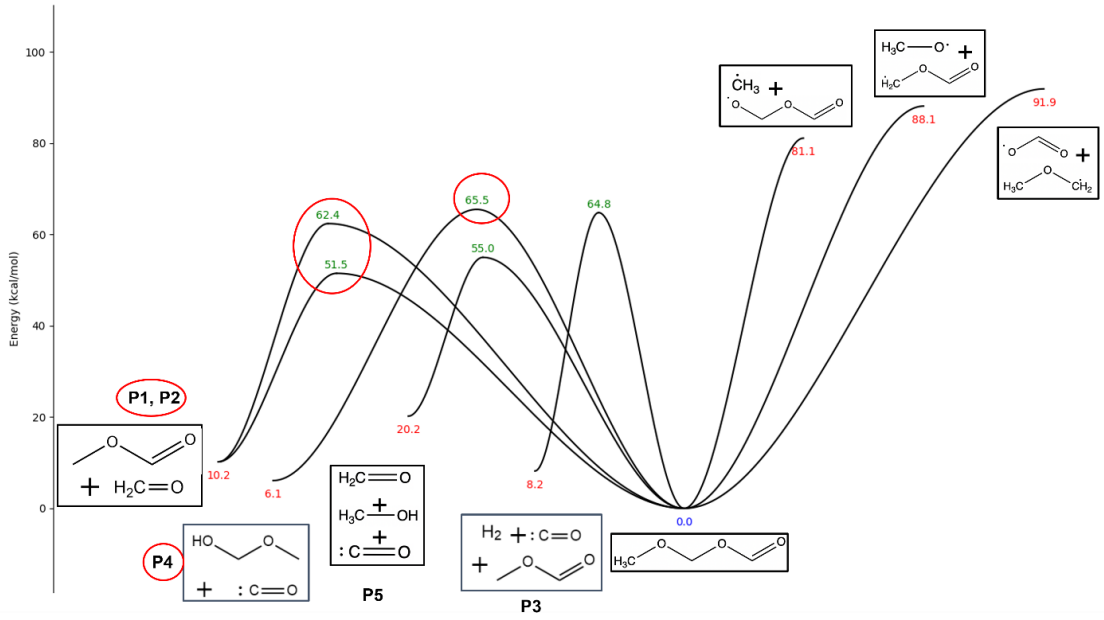

Figure 5.23: Potential Energy Surfaces (PES) for the decomposition of oxygen-containing radical formed by the decomposition of 2,4,6 trioxahpetane (M-2-M)

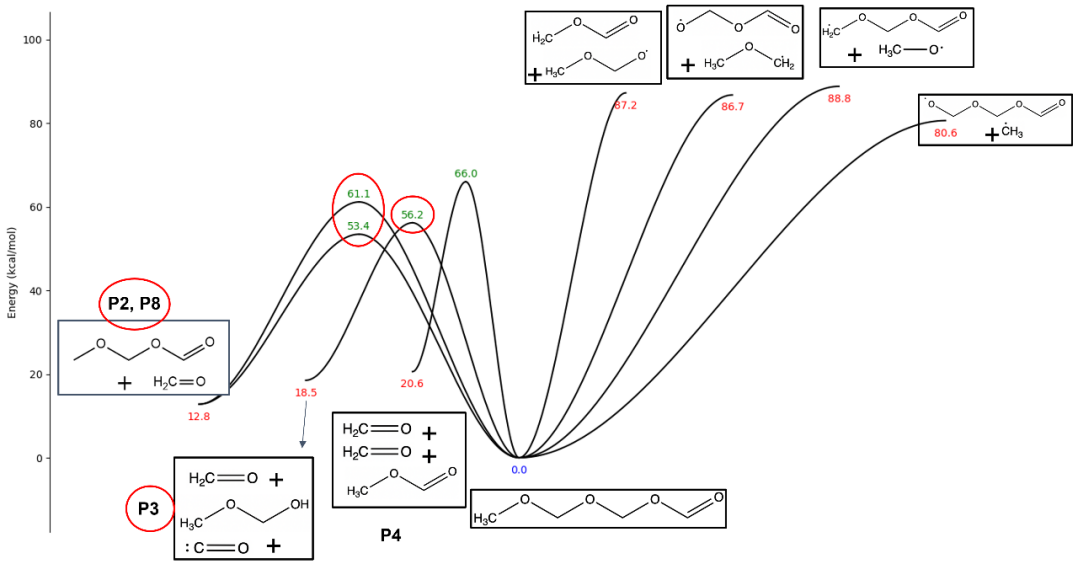

Figure 5.24: Potential Energy Surfaces (PES) for the decomposition of oxygen-containing radical formed by the decomposition of 2,4,6 tetraoxanonane (M-3-M)

5.6 Conclusions

Polyoxymethylene ethers (POM-E) have been recognized as a family of molecules which have demonstrated a reduction in soot emission when blended with diesel. This reduction in carbonaceous emission has been attributed to the presence of oxygen in the ether molecules, which results in complete combustion. Previously a large number of in-engine experiments had been used to demonstrate this improvement in emission characteristics. These tests focused on showcasing the improved performance of these engines when operated with blends of polyoxymethylene molecules in diesel. A fundamental exploration of the reason for these reductions was attempted by early kinetic modeling and experimental evaluations. These studies characterized the decomposition of dimethoxyethane (the smallest member of this group of molecules). Many of these preliminary investigations relied on analogies with other ethers like dimethyl ether and dibutyl ether to produce kinetic mechanisms. These results were then used as the basis to predict the behavior of longer chain lengths and different end-group POM-E molecules. These studies, while being important in establishing the fundamental molecular basis for the effectiveness of these molecules, did not describe the behavior of these larger molecules in sufficient detail. This work represents the first effort to understand the difference in pyrolysis between different POM-E molecules using a combination of spectroscopic analysis and computational modeling. High-level ab-initio quantum mechanical models have been developed to predict the preliminary and secondary decomposition of these molecules. To identify the most suitable compromise between performance, manufacturability, and in-engine efficiency, these studies provide the basis for the selection of a suitable molecule for blending with diesel.

Comparisons of the pyrolysis of different chain-length polyoxymethylene ethers indicated that the rate of decomposition of the longest chain molecules 2,4,6,8 tetraoxanonane was the

fastest. This increased decomposition rate and the formation of a pool of activated radicals could be essential in ensuring that sustained and complete combustion is achieved. These radicals have also been shown to make improvements in the ignition capabilities of these molecules, making them suitable for blending with diesel with reduced performance.

In addition to probing the pyrolysis of the POM-E molecules, an effort has been made to understand the decomposition behavior of secondary radicals produced from the pyrolysis of these POM-E molecules. Computational modeling has been applied to demonstrate the primary reaction paths to forming radicals that have been identified as combustion promoters. Abstraction reaction and oxidation studies are also planned to produce detailed kinetic mechanisms for POM-E molecules. The modeling of these reactions will be essential in demonstrating the suitability of one or more POM-E molecules in blends with diesel.

An analysis of POM-E molecules with different end groups has also been attempted. Experimental measurements and computational modeling have been critical in producing reaction rates to compare different methyl, ethyl, and propyl end group POM-Es for their effectiveness in decomposing to form radicals that can promote further reactions. This research effort presents a comprehensive analysis of the high-temperature pyrolysis of these molecules and their impact on combustion properties when blended with diesel or other fossil fuels.

This work has been adapted for journal publication with the tentative title,' *Chemical kinetic investigation of chain length effects of polyoxymethylene ethers (POM-E) during pyrolysis'.*

5.7 References

[1] K. Hakimov *et al.*, "Ignition delay time and speciation of dibutyl ether at high pressures," *Combust. Flame*, vol. 223, pp. 98–109, Jan. 2021, doi: 10.1016/j.combustflame.2020.09.028.

[2] F. Yuchuan, S. Qing, and S. Jianyi, "Synthesis and Reforming of Dimethoxymethane," *Chin. J. Catal.*, vol. 30, no. 8, pp. 791–800, Aug. 2009.

[3] L. Dodge and D. Naegeli, "Combustion Characterization of Methylal in Reciprocating Engines," National Renewable Energy Lab. (NREL), Golden, CO (United States), NREL/TP-425-6345, Jun. 1994. doi: 10.2172/10157045.

[4] K. I. Svensson, M. J. Richards, A. J. Mackrory, and D. R. Tree, "Fuel Composition and Molecular Structure Effects on Soot Formation in Direct-Injection Flames Under Diesel Engine Conditions," *SAE Trans.*, vol. 114, pp. 594–604, 2005.

[5] M. Härtl, P. Seidenspinner, E. Jacob, and G. Wachtmeister, "Oxygenate screening on a heavy-duty diesel engine and emission characteristics of highly oxygenated oxymethylene ether fuel OME1," *fuel*, vol. 153, pp. 328–335, Aug. 2015, doi: 10.1016/j.fuel.2015.03.012.

[6] S. Deutz *et al.*, "Cleaner production of cleaner fuels: wind-to-wheel – environmental assessment of CO_2 -based oxymethylene ether as a drop-in fuel," *Energy Environ. Sci.*, vol. 11, no. 2, pp. 331–343, 2018, doi: 10.1039/C7EE01657C.

[7] N. Schmitz, J. Burger, E. Ströfer, and H. Hasse, "From methanol to the oxygenated diesel fuel poly(oxymethylene) dimethyl ether: An assessment of the production costs," *fuel*, vol. 185, pp. 67–72, Dec. 2016, doi: 10.1016/j.fuel.2016.07.085.

[8] J. Burger, M. Siegert, E. Ströfer, and H. Hasse, "Poly(oxymethylene) dimethyl ethers as components of tailored diesel fuel: Properties, synthesis and purification concepts," *Fuel*, vol. 89, no. 11, pp. 3315–3319, Nov. 2010, doi: 10.1016/j.fuel.2010.05.014.

[9] L. P. Lautenschütz, "Neue Erkenntnisse in der Syntheseoptimierung oligomerer Oxymethylendimethylether aus Dimethoxymethan und Trioxan," 2015. https://archiv.ub.uni-heidelberg.de/volltextserver/19210/ (accessed Feb. 02, 2022).

[10] L. Lautenschütz, D. Oestreich, P. Seidenspinner, U. Arnold, E. Dinjus, and J. Sauer, "Physico-chemical properties and fuel characteristics of oxymethylene dialkyl ethers," *fuel*, vol. 173, pp. 129–137, Jun. 2016, doi: 10.1016/j.fuel.2016.01.060.

[11] M. Härtl, K. Gaukel, D. Pélerin, and G. Wachtmeister, "Oxymethylenether als potenziell CO2-neutraler Kraftstoff für saubere Dieselmotoren Teil 1: Motorenuntersuchungen," *MTZ - Mot. Z.*, vol. 78, no. 2, pp. 52–59, Feb. 2017, doi: 10.1007/s35146-016-0170-9.

[12] Z. Wang, H. Liu, X. Ma, J. Wang, S. Shuai, and R. D. Reitz, "Homogeneous charge compression ignition (HCCI) combustion of polyoxymethylene dimethyl ethers (PODE)," *Fuel*, vol. 183, pp. 206–213, Nov. 2016, doi: 10.1016/j.fuel.2016.06.033.

[13] H. Chen, X. Su, J. Li, and X. Zhong, "Effects of gasoline and polyoxymethylene dimethyl ethers blending in diesel on the combustion and emission of a common rail diesel engine," Energy, vol. 171, pp. 981–999, Mar. 2019, doi: https://doi.org/10.1016/j.energy.2019.01.089.

[14] Han, D. Y., et al. "Influence of Polyoxymethylene Dimethyl Ethers on Diesel Fuel Properties." Energy Sources, Part A: Recovery, Utilization, and Environmental Effects, vol. 38, no. 18, 16 Sept. 2016, pp. 2687–2692, https://doi.org/10.1080/15567036.2015.1110646. Accessed 8 Apr. 2023.

[15] J. Liu, J. Yang, P. Sun, W. Gao, C. Yang, and J. Fang, "Compound combustion and pollutant emissions characteristics of a common-rail engine with ethanol homogeneous charge and polyoxymethylene dimethyl ethers injection," *Appl. Energy*, vol. 239, pp. 1154–1162, Apr. 2019, doi: 10.1016/j.apenergy.2019.02.036.

[16] C. Barro, M. Parravicini, K. Boulouchos, and A. Liati, "Neat polyoxymethylene dimethyl ether in a diesel engine; part 2: Exhaust emission analysis," *fuel*, vol. 234, pp. 1414–1421, Dec. 2018, doi: 10.1016/j.fuel.2018.07.108.

[17] C. A. Daly, J. M. Simmie, P. Dagaut, and M. Cathonnet, "Oxidation of dimethoxymethane in a jet-stirred reactor," *Combust. Flame*, vol. 125, no. 3, pp. 1106–1117, May 2001, doi: 10.1016/S0010-2180(01)00227-9.

[18] V. Dias and C. Renard, "Modeling of Rich Premixed C2H4/O2/Ar and C2H4/Dimethoxymethane/O2/Ar Flames".

[19] L. Marrodán, E. Royo, Á. Millera, R. Bilbao, and M. U. Alzueta, "High Pressure Oxidation of Dimethoxymethane," *Energy Fuels*, vol. 29, no. 5, pp. 3507–3517, May 2015, doi: 10.1021/acs.energyfuels.5b00459.

[20] L. Marrodán, F. Monge, Á. Millera, R. Bilbao, and M. U. Alzueta, "Dimethoxymethane Oxidation in a Flow Reactor," *Combust. Sci. Technol.*, vol. 188, no. 4–5, pp. 719–729, May 2016, doi: 10.1080/00102202.2016.1138826.

[21] K. Alexandrino, Á. Millera, R. Bilbao, and M. U. Alzueta, Gas and soot formed in the dimethoxymethane pyrolysis. Soot characterization," *Fuel Process. Technol.*, vol. 179, pp. 369–377, Oct. 2018, doi: 10.1016/j.fuproc.2018.07.021.

[22] W. Sun, T. Tao, M. Lailliau, N. Hansen, B. Yang, and P. Dagaut, "Exploration of the oxidation chemistry of dimethoxymethane: Jet-stirred reactor experiments and kinetic modeling," *Combust. Flame*, vol. 193, pp. 491–501, Jul. 2018, doi: 10.1016/j.combustflame.2018.04.008.

[23] F. H. Vermeire, H.-H. Carstensen, O. Herbinet, F. Battin-Leclerc, G. B. Marin, and K. M. Van Geem, "Experimental and modeling study of the pyrolysis and combustion of dimethoxymethane," *Combust. Flame*, vol. 190, pp. 270–283, Apr. 2018, doi: 10.1016/j.combustflame.2017.12.001.

[24] W. A. Kopp *et al.*, "Detailed kinetic modeling of dimethoxymethane. Part I: Ab initio thermochemistry and kinetics predictions for key reactions," *Combust. Flame*, vol. 189, pp. 433–442, Mar. 2018, doi: 10.1016/j.combustflame.2017.07.037.

[25] L. Golka, I. Weber, and M. Olzmann, "Pyrolysis of dimethoxymethane and the reaction of dimethoxymethane with H atoms: A shock-tube/ARAS/TOF-MS and modeling study," *Proc. Combust. Inst.*, vol. 37, no. 1, pp. 179–187, Jan. 2019, doi: 10.1016/j.proci.2018.05.036.

[26] L. Golka, D. Gratzfeld, I. Weber, and M. Olzmann, "Temperature- and pressure-dependent kinetics of the competing C–O bond fission reactions of dimethoxymethane," *Phys. Chem. Chem. Phys.*, vol. 22, no. 10, pp. 5523–5530, Feb. 2020, doi: 10.1039/D0CP00136H.

[27] Q. Guan, K. N. Urness, T. K. Ormond, D. E. David, G. Barney Ellison, and J. W. Daily, "The properties of a micro-reactor for the study of the unimolecular decomposition of large molecules," *Int. Rev. Phys. Chem.*, vol. 33, no. 4, pp. 447–487, Oct. 2014, doi: 10.1080/0144235X.2014.967951.

[28] R. Van de Vijver and J. Zádor, "KinBot: Automated stationary point search on potential energy surfaces," *Comput. Phys. Commun.*, vol. 248, p. 106947, Mar. 2020, doi: 10.1016/j.cpc.2019.106947.

[29] Labbe, N. J.; Sivaramakrishnan, R.; Klippenstein, S. J. The Role of Radical+fuel-Radical Well-Skipping Reactions in Ethanol and Methylformate Low-Pressure Flames. Proceedings of the Combustion Institute 2015, 35 (1), 447–455. https://doi.org/10.1016/j.proci.2014.05.107.

[30] T. Yu, X. Wu, X. Zhou, A. Bodi, and P. Hemberger, "Hydrogen migration as a potential driving force in the thermal decomposition of dimethoxymethane: New insights from pyrolysis

imaging photoelectron photoion coincidence spectroscopy and computations," Combust. Flame, vol. 222, pp. 123–132, Sep. 2020, doi: 10.1016/j.combustflame.2020.08.040.

[31] J. P. Porterfield et al., "Thermal Decomposition of Potential Ester Biofuels. Part I: Methyl Acetate and Methyl Butanoate," J. Phys. Chem. A, vol. 121, no. 24, pp. 4658–4677, Jun. 2017, doi: 10.1021/acs.jpca.7b02639.

Chapter 6: Redesigning the micro-reactor

6.1 Introduction

To model and evaluate the chemical reactions in devices such as the micro-reactor requires understanding the flow field within the reactor. Particularly the pressure and temperature of the gaseous molecule as it transits through the reactor undergoing thermal decomposition. The reaction rate constant of the unimolecular decomposition (k) of different gas-phase species can be modeled using the simplified Arrhenius equation [1].

$$k = Ae^{\frac{-Ea}{RT}} \tag{6.1}$$

Where A is the pre-exponential factor, T is the temperature, n is the temperature exponent, Ea is the activation energy, and R is the universal gas constant. The pre-exponential factor (also termed the frequency factor) is dependent on how often molecules in the gas phase collide[2]. This is directly related to the pressure and temperature of the sample. Thus, developing reaction rate models and kinetic mechanisms depends on an error-free prediction of parameters such as the pressure and temperature at all points along the flow field.

The dimensions of the micro-reactor (three centimeters in length and 1 mm inner diameter) prevent a direct sampling of these parameters using probes as they would disrupt the fluid flow. Optical access to the flow field is also restricted as operational requirements mandate using opaque materials (usually ceramics). While the reactor is a large aspect ratio straight tube of constant diameter, the flow within it cannot be considered a simple Poiseuille flow for pressure evaluations. The tube is resistively heated to high temperatures using attached electrodes. Through simulation

and experimental observation, it was shown that the portion of the tube outside the span of the electrodes is at a lower temperature due to convective and radiative cooling. Therefore, there is a strong axial gradient in the wall temperature, usually starting at the inlet, further complicating the flow field, and making an accurate temperature measurement a challenge. The heating also accelerates the flow, and if the mass flow rate is high enough, the local Mach number of the flow will increase rapidly, and the fluid can choke near the exit.

Predicting the pressure across the length of the microreactor also has associated challenges. A computational study by Guan et al.[3] identified that since the chamber pressure downstream of the tube exit is so low, the local Knudsen number (Kn) within the tube can increase to the point where the continuum Navier-Stokes equations break down. When this occurs, one must account for "slip" both in momentum and thermal energy at the walls, as this affects the radial velocity and temperature profiles. Taking the above into account, it was found that accounting for slip permits the simulation of the flow using computational fluid dynamics (CFD). The ability to recreate the pressure boundary conditions and mass flow rate by reversing the calculations validated the developed model's accuracy. These CFD simulations predict that the pressure profile inside the reactor rapidly decreases along the length of the reactor. Simulations of centerline pressure as a function of the reactor length show a steady decline from an inlet pressure of 275torr (at a wall temperature of 1500 K) down to zero within the first 2.5 cm of the reactor. The wall temperature is shown to impact the inlet pressure with a higher wall temperature corresponding to higher inlet pressure. The strong temperature dependence of the viscosity causes the elevation in pressure with temperature. This behavior is consistent across the range of wall temperatures simulated (1300 -1600 K).

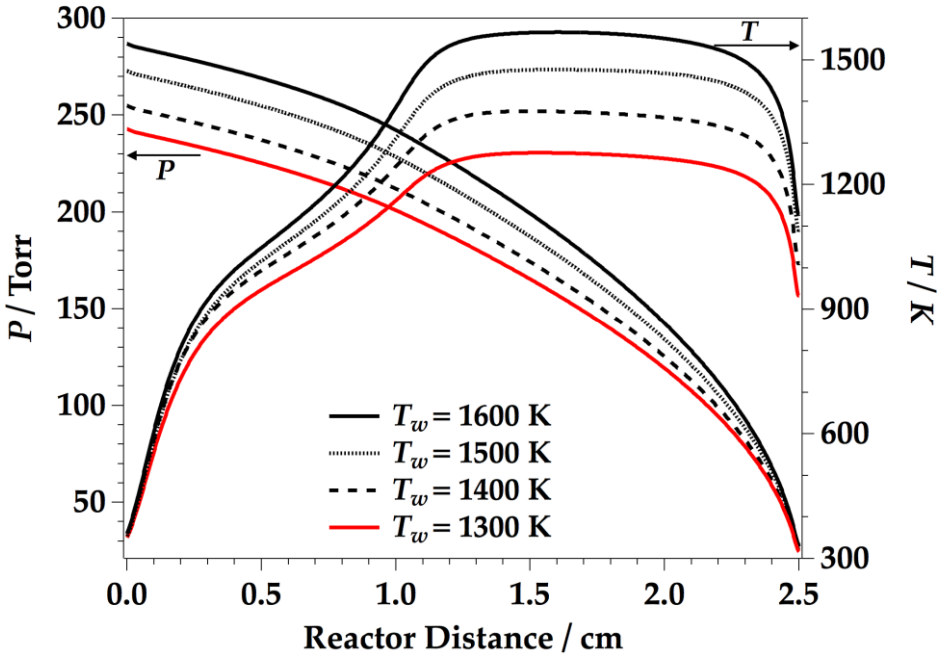

Figure 6.1: Simulated centerline pressure (left) and temperature (right) profiles for a 280 sccm continuous flow of helium along the length of a 2.5 cm reactor (0.66 mm I.D) as a function of wall temperature (T_w) [1]. The electrodes for resistive heating are placed at 1 cm and 24 cm (adapted from [3])

The primary contributor to this drop in pressure within the reactor is the flow acceleration produced by the extreme differential in pressure boundary conditions. These simulations also show that the temperature of the gas along the centerline of the reactor is relatively constant between the electrodes (placed roughly at 10 mm and 25 mm along the reactor). Initial experimental results showed a differential in the temperature of about 150K between the wall temperature and centerline fluid temperature. These measurements were made using a longer-length reactor with a thicker wall section and lowered flow rate of 25 sccm. More recent simulations carried out at 280 sccm mass flow rate and a standard 1 mm I.D reactor showed that the temperature difference is more in the 25-50K range between the external wall and the 'chemical temperature' inside the reactor. These simulations also confirm that most of the relevant chemistry happens between 5 mm

to 2 mm of the total length of the reactor, where both the temperature and pressure are elevated. Towards the exit of the reactor (the last 5 mm), all reactions are quenched due to the fall-off in pressure.

The centerline velocity of the fluid was also modeled in this work across a range of temperatures at an inlet mass flow rate of 280sccm. The velocity rises steadily from the inlet reaching supersonic speeds of about 2 cm from the inlet before ramping up to almost 2000ms^{-1} at the exit.

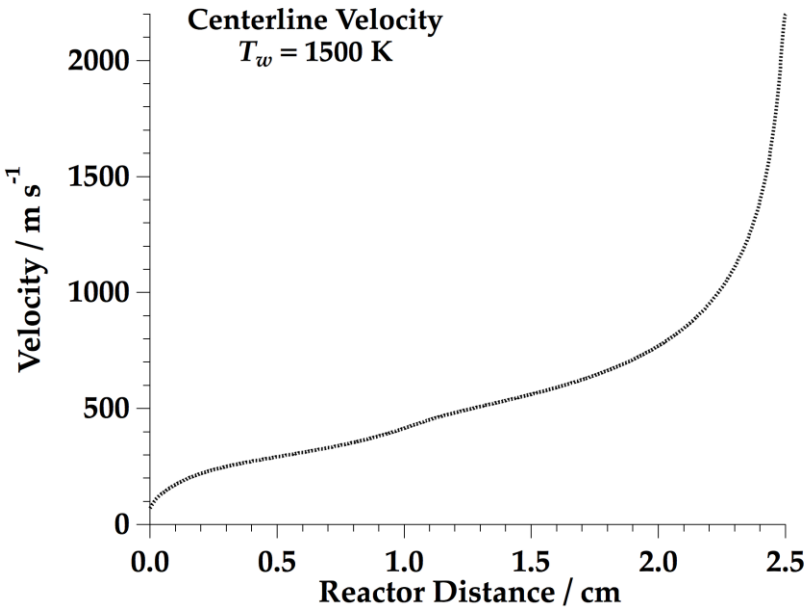

Figure 6.2: Simulated centerline velocity profile for a 280 sccm continuous flow of He along the length of a 2.5 cm reactor (0.66 mm i.d.) at Tw = 1500 K [49]. The electrodes for resistive heating are placed at 1 cm and 2.4 cm. (adapted from [3])

Another important factor in modeling chemical reactions within the reactor is the residence time in the heated portion of the micro-reactor. Longer residence times increase the likelihood of radical-radical reactions and radical abstraction or addition reactions with the precursors being investigated. These bimolecular reactions greatly complicate the analysis of the desired

unimolecular process. One way to assess the possibility of bimolecular reactions is based on collisions. Considering the single-particle collisional frequency z_{ii}:

$$z_{ii} = \frac{N_i}{V}\sigma\sqrt{2}\left(\frac{8\mathrm{kT}}{\pi m_i}\right)^{\frac{1}{2}} = \frac{P}{kT}\sigma\sqrt{2}\left(\frac{8\mathrm{kT}}{\pi m_i}\right)^{\frac{1}{2}} \quad (\text{collisions s}^{-1}) \tag{6.2}$$

with an intermediate temperature (T) and pressure (P) of 1200 K and 200 Torr assumed (see Figure 6.1), the collisional frequency in the reactor (z_{ii}) is on the order of 100 collisions μs^{-1} (assuming a collisional cross-section (σ) of 0.4 nm^2 and a molecular weight (mi) of 40 amu, values between He and CO2; *k* is the Boltzmann constant with a value of $1.38(10^{-23})$ J K^{-1}). Incorporating a dilution of 0.1% (a partial pressure of 0.2 Torr) and a fixed residence time of 100 μs, a rough estimate of the collisions between potentially reactive species is 100 collisions. Reactions at the gas kinetic rate could be influential under these conditions, but most rates will be at least an order of magnitude lower. They, therefore, won't be significant compared to the unimolecular reaction scheme of interest. Decreasing the residence time in the reactor is not a viable way to avoid bimolecular reactions because it is essentially a fixed experimental parameter due to limited pumping capabilities. Instead, this task is accomplished through dilution.

The challenges associated with consistently predicting the conditions within the reactor complicate the extension of the results obtained from these experiments to develop chemical kinetic models. Providing a stabilized pressure environment and controlling reaction residence time are hard to achieve, both major deficiencies of the current reactor design. To address these shortcomings, a novel reactor design and geometry are necessary.

6.2 Redesigning the Chen Reactor

Modification to the design of the micro-reactor was initiated by analyzing the flow phenomena within the Chen reactor by first applying a theoretical model by Fan[4]. Fan's geometry used for these evaluations was a simple tubular structure with a length of 3 cm and an inner diameter of 1 mm. The wall thickness was set to 600 µm with a concentric inner cavity. For these initial evaluations, the flow within the reactor is assumed to be laminar, and the pressure drop was modeled by calculating the friction factor, and the Reynolds number of the flow within the given dimensions of the reactor[5].

$$\Delta P = \frac{\overline{f_{f\,d,h}}.L.\rho.|\vec{U}|^2}{2D} \tag{6.3}$$

$$\overline{f_{f\,d,h}} = \frac{64}{Re_D} \tag{6.4}$$

where $f_{fd,h}$ is the friction factor, L and D are the length and internal diameter of the cylindrical tube, and Re_D is the Reynold number for internal flow. These equations are applied to typical conditions of an inlet pressure of 230 torr and a mass flow rate of 300 sccm. It is observed that the pressure inside the reactor drops several orders of magnitude from the inlet value to zero at the exit, confirming the results observed in previous simulations. As previously described the drop in pressure is not ideal for chemical kinetic evaluation as it can cause localized effects on the decomposition process leading to the formation of products and radicals that are not truly the result of thermally driven decomposition. To produce a more stabilized pressure profile within the reactor a modification to the geometry at the exit of the reactor is proposed. This modification is in the form of a converging-diverging nozzle which is commonly used in other engineering

applications where a change in flow parameters is desired. The reduction in diameter acts as a choking device influencing the pressure around it and upstream of the constriction.

The analysis of this modification is accomplished by applying equation 6.5 [6] linking the mass flow rate and choke diameter for an isentropic flow in a converging nozzle

$$\dot{m} = A * P_0 * \sqrt{\frac{\gamma}{RT_0}} \left(\frac{2}{\gamma+1}\right)^{\frac{\gamma+1}{2(\gamma-1)}} \tag{6.5}$$

Where $\dot{m}$ is the mass flow rate, A is the nozzle outlet area, P_0 is the upstream pressure, and γ is the ratio of specific heats. This equation demonstrates that it is possible to affect the upstream pressure by modifying the choke area.

The newly proposed converging-diverging nozzle design was modeled by Fan [4]. This design featured transition lengths G1 and G2, as shown in Figure 6.3. With the initial assessment of the flow conditions and behavior completed, a more rigorous assessment required the application of numerical methods and CFD. These evaluations were used to identify the effects of varying individual geometric parameters on flow behavior.

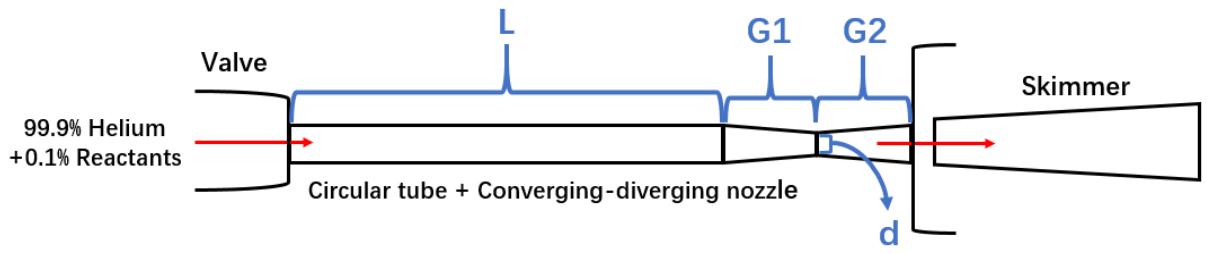

Figure 6.3: Redesigned reactor structure diagram (adapted from [4])

For CFD calculations, helium is chosen as the carrier gas since it is inert, non-atomic, and has a high thermal conductivity. Helium is also the carrier gas used in the experiment. The dilution rates used (0.1% of the fuel in helium) lent themselves well to the approximation of pure helium as the inlet gas. The microreactor wall is heated to temperatures between 1300-1700 K during experiments. The carrier gas, which is typically at room temperature at the inlet, experiences a dramatic temperature change within the short residence time of the reactor. Thus, valid thermodynamic functions for the thermal conductivity and dynamic viscosity of helium are necessary to obtain reliable simulation results.

These parameters have been previously determined experimentally and are adapted as follows [7]:

$$k = 2.682 \cdot 10^{-3}(1 + 1.123 \cdot 10^{-3}P)\, T^{(0.71(1-2.10\hat{}(-4)P))} \quad [W/(m*K)]$$

$$\mu = 3.67 \text{ X } 10^{-7} \cdot T^{0.7} \quad [Pa.s]$$

where k is the thermal conductivity and μ the dynamic viscosity and the temperature and pressure have units of Kelvin and Bar respectively.

A description of the CFD method used by Fan is described in brief here, a more detailed explanation can be found at [4]. Fan [4] implemented the system of equations defining the continuity equation, conservation of linear momentum, conservation of energy for a steady-state, and compressible ideal gas flow in MATLAB. ANSYS Fluent was applied since it could achieve the highest convergence speed and solution accuracy at the lowest computational cost among

multiple CFD tools. Three-dimensional models of reactors with different structure parameters were built in ICEM (an ANSYS meshing tool) [8]. This configuration is a general mesh style for three-dimensional models. This meshing method was chosen as it is suitable for many model profiles while being easy to build with a low probability of error concerning structural geometry. To study the microreactor design numerically, models with different structure parameters were built and calculated in a short amount of time. The choice of a tetrahedral mesh was influenced by the relatively simple shape of the reactor geometry. The reduced accuracy compared to a hexahedral mesh is offset by gains in the reduction of computational time and cost. A density-based solver was applied with a SIMPLE scheme using a second-order-upwind discretization method [9]. The integration of a revised algorithm extended the applicability of the SIMPLE scheme to compressible flow allowing a detailed evaluation of flow parameters within the new geometry.

6.3 Parametric evaluation of the redesigned reactor

6.3.1 Geometric parametric evaluation

The redesigned reactor was then analyzed using CFD tools described in [4] to understand the impact of varying geometric parameters on the fluid flow properties within the reactor. This was to optimize the new configuration while establishing tolerance bands for the fabrication of the geometry. The effect of varying the choke diameter, d, from 0.100 mm to 0.300 mm was compared with the straight tube configuration. Upon addition of the nozzle structure, the pressure distribution becomes stable within the main body of the microreactor, and the maximum centerline pressure is directly affected by changing the choke diameter, d. Similarly, the projected velocity profiles plateau within the microreactor main body with the addition of the nozzle structure. The assessment of the impact of changing the exit diameter also indicated a degree of tunability that

could be engineered into the micro-reactor by selecting different exit diameters to produce stabilized and specific fluid properties.

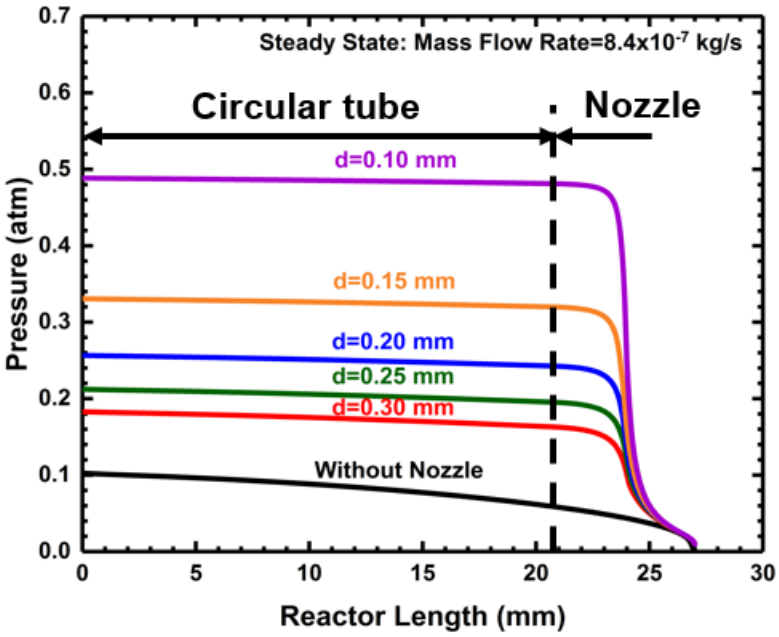

Figure 6.4: Centerline pressure distribution for various choke diameters d.(adapted from [4])

T. Fan further calculated the effect of the lengths of both the converging and diverging sections G1 and G2 for their impact on fluid flow properties. The simulation results for the centerline pressure indicated that the length of G1 and G2 have minimal influence on the fluid properties when altered across a range of 3 mm. Both these features showed no significant impact on the residence time of the fluid or velocity profile when varied. To ease manufacturability, the diverging section of length G2 was eliminated. The allowed tolerance on the length of the converging section was extended by 2 mm to improve ease of fabrication.

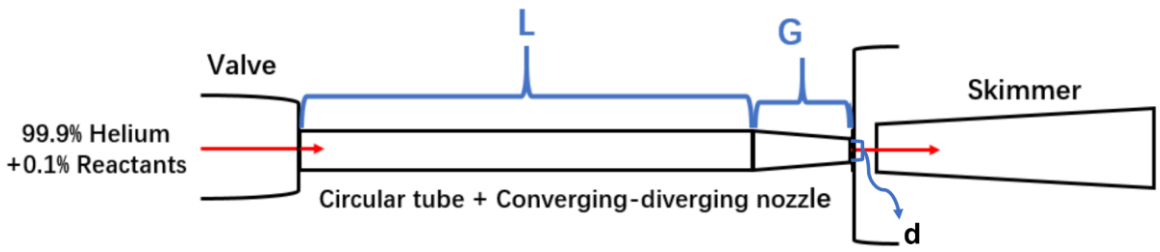

Figure 6.5: Redesigned reactor structure with a single converging section

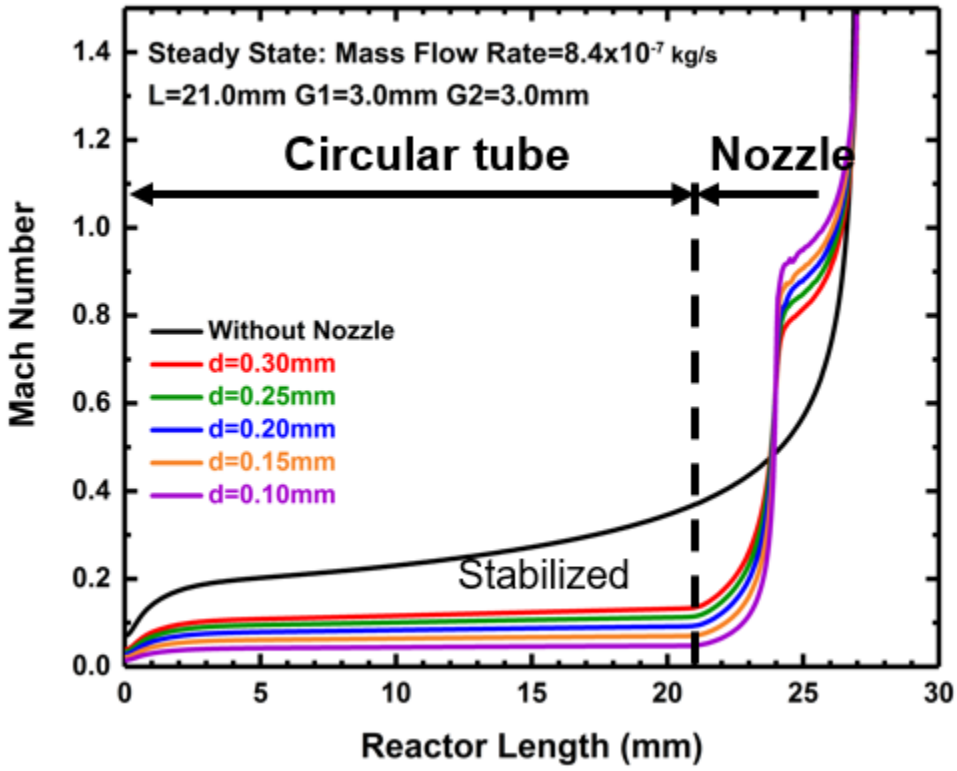

Figure 6.6: Central line Mach number distribution along the reactor length for various choke diameters, d.(adapted from [4])

The length of the main body of the reactor L was evaluated between 20 mm to 30 mm to understand its impact on the fluid flow properties. These simulations confirmed that the only change observed was to the residence time of the fluid within the reactor. This provides an additional tunable parameter that can be altered to understand the impact of how long the fluid is retained in the reactor environment on pyrolysis reactions.

6.3.2 Thermodynamic evaluation

The geometric parametric evaluation provided a baseline configuration (L=20 mm, G1 = 5 mm, d =0.15 mm) which was then analyzed from a thermodynamics perspective in contrast to the tube reactor. Comparisons of the temperature, pressure, velocity profile, and Kn under continuous flow rate conditions of 300sccm were carried out between the Chen reactor and the redesigned geometry by Fan [4]. The Kn provided a convenient dimensionless parameter to compare fluid characteristics between both reactors.

$$Kn = \frac{\lambda}{D} = 1.26\sqrt{\gamma}\frac{Ma}{Re_D} \tag{6.6}$$

Typically, the Navier Stokes equations are applicable at Kn less than 0.01, and the fluid is said to be in continuum flow. Fluid in this domain is easy to model and analyze to develop accurate chemical kinetic mechanisms. The fluid remains in this continuum regime throughout the reactor for the redesigned micro-reactor with the nozzle. In contrast, the Kn in the straight tube reactor quickly rises beyond 0.01 within the first 5 mm. Additionally, the centerline pressure and velocity profiles remain stable throughout the main body of the reactor, and a maximum temperature (1500K) is reached at 6 mm from the inlet. These initial design evaluations made it apparent that the optimized micro-reactor geometry produced stabilized fluid profiles while retaining all the characteristics of the Chen reactor that make it a highly useful experimental tool.

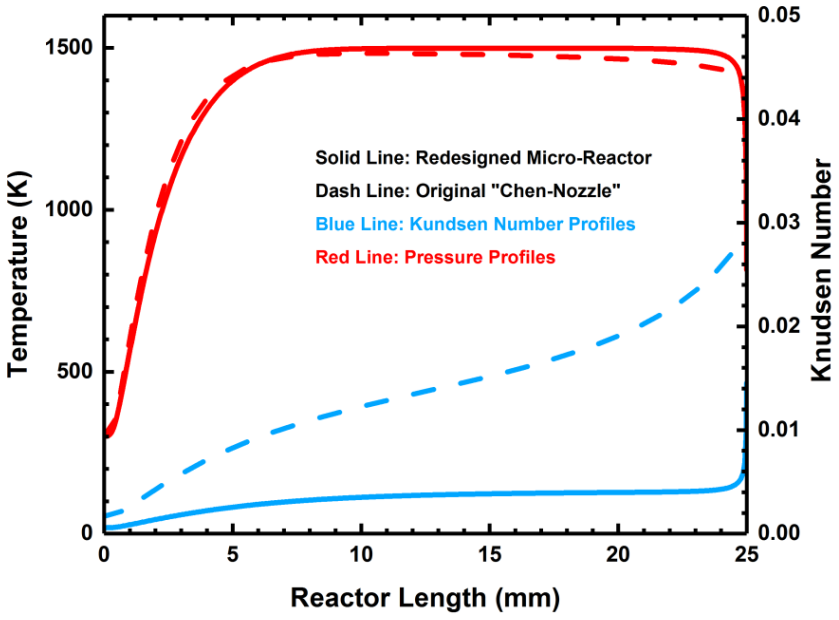

Figure 6.7: Centerline temperature and Knudsen number distribution along with the reactor of both redesigned micro-reactor and original "Chen nozzle" (adapted from [4])

6.4 Prototype redesigned micro-reactor

To validate the proposed redesign, a prototype micro-reactor featuring a specialized modification to simulate the effect of a nozzle transition was fabricated and utilized in the in-house PIMS experiment at CU Boulder. This prototype was manufactured at the Integrated Instrument Development Facility (IIDF) in the Cooperative Institute for Research in Environmental Sciences (CIRES) at the University of Colorado Boulder. Two prototype versions were produced, one by inserting a 1 mm outer diameter (O.D), 0.5 mm inner diameter (I.D), and 0.8 mm long alumina ceramic tubing into the standard Chen reactor. The second prototype featured a 1 mm O.D alumina tube with a 0.5 mm I.D segment that was epoxied onto the end of a 28 mm silicon carbide tube. The result is a microreactor with a built-in rectangular step nozzle structure, which is different in geometry compared to the ideal nozzle's tapered shape.

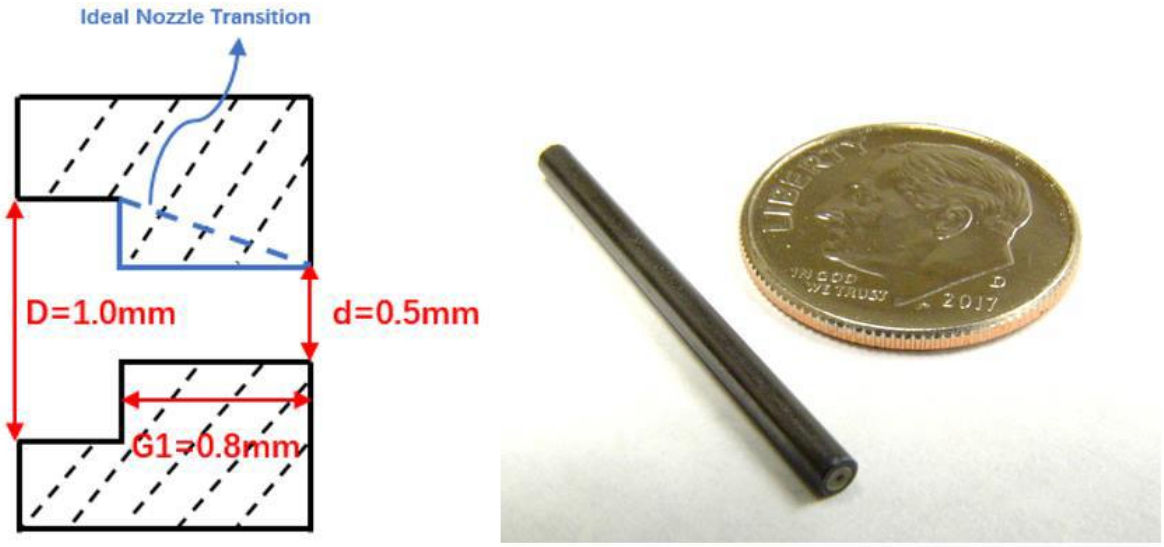

Figure 6.8: A photo and structure diagram of the novel reactor prototype (adapted from [4])

The impact of the new configuration was evaluated in the PIMS experiment by analyzing the thermal decomposition of propionaldehyde [4]. These experiments were used to confirm that the operating characteristics of the microreactor continue to be like that of the tube reactor. Initial spectra showed a similar distribution of products observed across temperature scans. The resistive heating performance and temperature measurements correlated well with previous experiments. These initial results and numerical models formed the basis for the next stages in the fabrication of these nozzle micro-reactors.

6.5 References

[1] S. R. Logan, "The origin and status of the Arrhenius equation," *J. Chem. Educ.*, vol. 59, no. 4, p. 279, Apr. 1982, doi: 10.1021/ed059p279.

[2] K. J. Laidler, "The development of the Arrhenius equation," *J. Chem. Educ.*, vol. 61, no. 6, p. 494, Jun. 1984, doi: 10.1021/ed061p494.

[3] Q. Guan, K. N. Urness, T. K. Ormond, D. E. David, G. Barney Ellison, and J. W. Daily, "The properties of a micro-reactor for the study of the unimolecular decomposition of large

molecules," *Int. Rev. Phys. Chem.*, vol. 33, no. 4, pp. 447–487, Oct. 2014, doi: 10.1080/0144235X.2014.967951.

[4] T. Fan, "Design of a Novel Microreactor to Study Short Residence Time Combustion.", 2016

[5] J. Holman, *Heat Transfer*, 10th Edition. McGraw-Hill Education, 2009.

[6] C. Boles, *Thermodynamics - An Engineering Approach*, 8th Edition. McGraw Hill Education, 2019.

[7] H. Petersen, "The Properties of Helium: Density, Specific Heats, Viscosity, and Thermal Conductivity at Pressures from 1 to 100 bar and from Room Temperature to about 1800 K," p. 46.

[8] I. C. ANSYS, "13: geometry and mesh generation preprocessor," *Ansys Inc*, 2012.

[9] L. Mangani and C. Bianchini, "HEAT TRANSFER APPLICATIONS IN TURBOMACHINERY," p. 12, 2007.

Chapter 7: Fabrication of the novel micro-reactor geometry

7.1 Evaluating the ideal nozzle geometry

With the range of geometric parameters for the nozzle decided (exit diameter, length, and transition region length) [1], different nozzle configurations were evaluated. Two final designs were compared for their effectiveness in stabilizing pressure and velocity profiles of the fluid in the reactor and are shown in Figure 7.1. The first design incorporates a step nozzle (similar to the prototype) with a sharp transition in diameter from 1 mm to 0.5 mm at the exit. The length of the smaller diameter section represents the transition length. It was identified that sharp transitions could lead to localized product recirculation. Thus, the second design features a more gradual angular transition into the constriction region.

Additional comparisons of the two reactor geometries highlighted the potential for creating better surface finishes with the tapered geometry. An improved surface finish would prevent radical trapping, reduce boundary effects, and improve the reliability of the reactor in general. Further, having a large material zone would result in a non-uniform heating effect, disrupting the chemical reaction. Based on these conclusions, it was decided to manufacture the reactor with a tapered constriction.

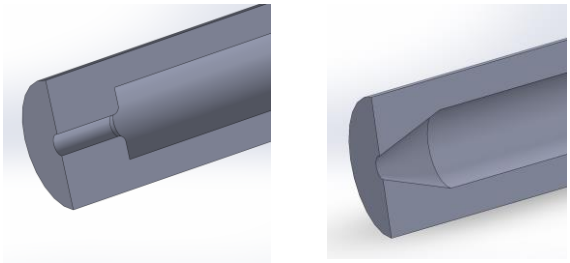

Figure 7.1: The CAD rendering of the redesigned reactor shows a step nozzle (left) and a tapered nozzle (right).

variants are proposed, featuring exit diameters ranging from 0.500 mm to 0.100 mm in steps of 0.100 mm. All other geometrical parameters are identical in these reactors, except for a change in transition length for exit diameters 0.200 mm and 0.100 mm to accommodate the extreme change in diameters. Silicon carbide is retained as the primary material system for the new reactor design to ensure continued compatibility with the experimental setups described in Chapter 2. Silicon carbide also possesses exceptional wear resistance, high thermal conductivity, low coefficient of thermal expansion, and high hardness[2] – [4]. These properties, in combination with excellent thermal shock resistance[5], [6], and chemical stability[7], [8] make it an ideal material for corrosive environments.

7.2 Shortcomings of traditional manufacturing using silicon carbide

Traditional ceramic compaction methods incorporate rigid tooling and expensive fabrication techniques. Techniques like casting[9]–[11], extrusion[12], [13], and injection molding[14], [15] are applied, including multiple intermediate stages of processing, each relying on specialized components[16], [17] to produce parts for a range of applications. These elaborate methods have limited small-component silicon carbide manufacturing to relatively simple geometries with more intricate configurations requiring a host of specialized modifications that can be cost-prohibitive. The inflexible nature of the tooling further curtails customizability, a

significant factor in low-volume production and one-off prototype manufacturing. These current processing techniques feature machined tooling made of stainless steel and tool steel, which are not amenable to modification. Even minor alterations to the final product's design can have an expensive cascading effect on other processing equipment due to the rigidity of the tooling involved in these processes. Thus, many factors of traditional ceramic processing methods contribute to their inherent incompatibility with iterative design changes [18], [19].

Additive ceramics and silicon carbide manufacturing has emerged as an alternative to the more orthodox manufacturing methods but is still limited in applicability[20]. Multiple generative manufacturing methods like extrusion-free forming, binder jetting[21], [22], Selective Laser Sintering (SLS), robocasting [23]–[25], and Stereolithography (SLA)[26]–[28] have been explored for their ability to generate basic shapes using SiC. While significantly faster than conventional methods in producing near-net forms, these processes suffer fundamental material challenges[29]. To be compatible with the fabrication process, modifications of the precursor composition may be necessary, impacting the finished component properties, altering the sintering time, and causing outgassing, which can affect the furnace atmosphere. The deposition of ceramic layers as part of the compaction process also introduces inconsistencies in the product, with pores and discontinuities being more prevalent in components produced through these techniques. A critical downside to additive manufacturing is the constraints imposed by the technique's resolution. The ability to create details smaller than 0.500 mm inside a geometry, especially in high aspect ratio designs as required by many microfluidic applications, is firmly beyond the capacity of currently accessible techniques for most ceramics[29]. Multistage processing has been explored for these forms, but the time and cost involved quickly approach that of more dedicated conventional processing methods.

To address this gap in capability, this chapter describes a novel high throughput, iterative processing route for manufacturing small, high aspect ratio silicon carbide geometries at a low cost. This fabrication sequence integrates a hybrid manufacturing technique that harnesses the rapid iterability of additive manufacturing, combining it with the knowledge base for conventional ceramic processing. A bottom-up approach was used, beginning with the bulk silicon carbide, followed by a systematic investigation of other batch components for the potential to introduce modifications. This resulted in creating a unique silicon carbide precursor composition, tailored to be compatible with a range of compaction processes and optimized for small feature sizes. With customizability at the core of this technique, polymer, and metal additive manufacturing are utilized to create tooling. This supports the Fabrication of final structures across a range of dimensions with the tooling design supporting sizes from 500 mm to 30 mm (length). Generative manufacturing enables the design of fabrication tooling to be made independent of the ceramic type, permitting it to manufacture various ceramic parts. The evolution and design of tooling are discussed in detail, focusing on its versatility – across the material composition and compaction technique. A new approach to achieving compaction is presented, highlighting the reduced cycle time and the ability to produce a range of configurations. The broad applicability of this process is showcased with components of different geometries and material types produced. Emphasis is placed on manufacturing geometries with extremely thin wall thicknesses, highlighting this technique's ability to produce near-net configurations in a single processing step. Additionally, material characterization studies are presented, highlighting the superior performance of components produced using this new technique compared to currently available alternatives.

7.3 Manufacturing process overview

The following section details the process steps, characteristics of the precursor material, the powder preparation sequence, compaction tooling, and compaction process as applicable to silicon carbide, focused on creating the configurations required by the microreactor geometry.

Figure 7.2 presents a section view of the target geometry to be manufactured to meet the experimental requirements. The geometry features a large aspect ratio (a much bigger dimension in one axis than the other two), with the key characteristic being an internal tapering of the cavity inside the structure. In addition to the geometry, the experimental conditions mandate smooth interior surfaces that would not disrupt the reactor's fluid flow. High component strength and lowered porosity are further prerequisites that are factored into the choice of the manufacturing method. The presence of voids or high porosity could result in 'radical trapping,' making the new microreactor unusable within the context of the experiment. High component density would also improve the ability of the reactor to be resistively heated and extend the product's usable life within the experiment.

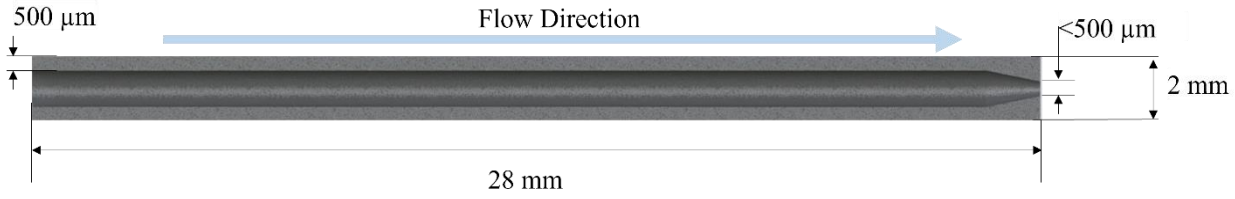

Figure 7.2: CAD rendering of a section view of the target reactor geometry featuring internal taper from 1 mm to 0.500 mm

A hybrid processing route is proposed combining the repeatability and robustness of conventional ceramics processing and the rapid turnaround time of polymer and metal additive manufacturing. Figure 7.3 shows the sequence of operations involved in producing the

microreactor geometry. The features of the reactor and the requirement of manufacturing using SiC necessitated the development of a precursor composition tailored to the chosen forming route. Developing a specialized blend of SiC for this process was done in collaboration with Calix Ceramic Solutions. These components are mixed in an aqueous medium using high-purity water that is either reverse osmosis (R.O.) treated or deionized to prevent secondary reactions with the precursor mixture. For compatibility with the chosen compaction route, the volume of water added is adjusted to ensure the rheological properties before spray drying. The goal after spray drying is a free-flowing powder such that the final bulk density is 0.9 g/cm3, the final tap density at 1.1 g/cm3 with an average final particle size of 0.070 mm.

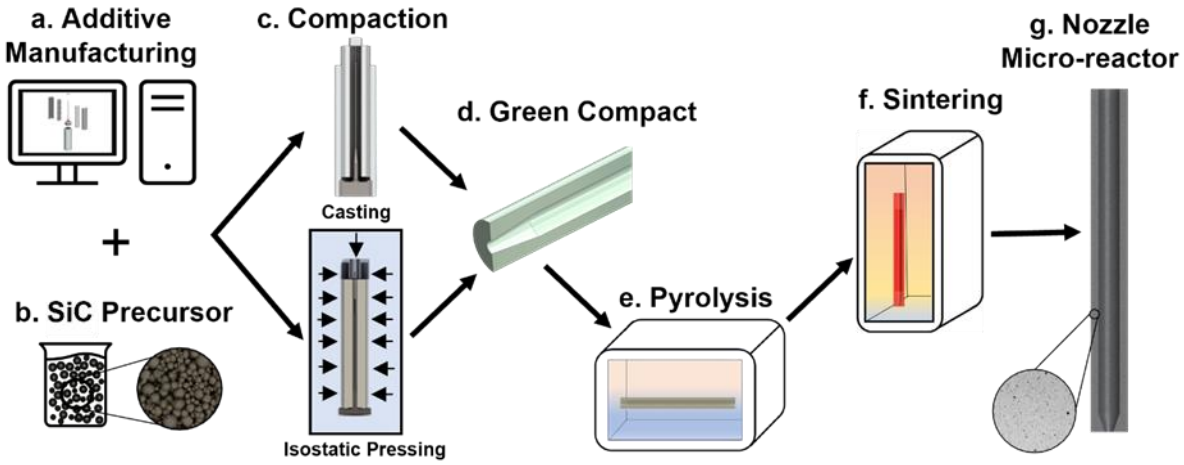

Figure 7.3: Process flow for creating microreactor geometry. (A) Creation of a digital tool geometry applying the principles of design for manufacturability and tailored for production using both polymer additive manufacturing (Stereolithography) and metal additive manufacturing (Direct metal laser sintering). (B) A specialized raw material composition custom-made using a spray drying process for compaction. (C) Casting and isostatic pressing are two compaction methods chosen for their compatibility with the final geometry and precursor composition. (D) The component post-compaction is in a 'green state'. (E) Pyrolysis is carried out in a Lindberg M Blue Retort at 650°C. (F) Final component sintering is completed in a Thermal Technology Furnace Model 1000-3560-FP24 at 2150°C. (G) Component post-processing is completed to finish edge surfaces and verify hole dimensions.

7.3.1 Precursor development

Silicon carbide forming processes require a precursor material with a uniform size distribution and high flowability[30], [31]. This ensures that the 'green-state' product produced possesses the desired density and predictable shrinkage post-sintering. This is achieved using a spray drying process to produce a dry powder with uniform size distribution and spherical shape. Spray drying is carried out using a PTX Pentronix Roto-Clean Spray Dryer 9500 system, producing particle sizes in the range of 0.020 – 0.200 mm. The particle size of the RTP powder was adjusted to be suitable for both isostatic pressing and conventional casting. In the isostatic process, RTP powder in the dry form was used in the isostatic process – with the grain size being altered to meet the density requirements of greater than 3.10g/m3. For compatibility with the casting process, the RTP powder can be converted to an aqueous form by mixing with RO/DI water. Care is taken to ensure that the rheological parameters of the blend are maintained for optimum castability.

The specifications of the microreactor geometry demanded the creation of a slurry system that pushed the limits of the spray drying process. The fundamental composition of the silicon carbide precursor was iterated to produce the small features of the reactor. This involved adjusting the percentage of boron carbide to <1% to stabilize the small volumes of the slurry used. Further modifications were carried out to the α-SiC particle size to produce finer blends to achieve higher compaction. With the wall thickness dimensions approaching the α-SiC particle size, modifications were made to produce finer blends by lowering the average size to less than 0.0005 mm. This had the added benefit of producing finished geometries with a higher density value approaching the theoretical limit. A constant challenge to working with these types of minute geometries was the complications in extracting the compacted green state component from the tooling; this was overcome by experimenting with variations in the fugitive binders. By increasing

the percentage of the binder media to 12% by volume, it was possible to produce stronger green-state components that could be separated from the tooling system. The last iterated component of the mixture was the type of carbon sources. The high aspect ratio of the design leads to post-sintering warping and charring of the component during the sintering process. To avoid the buildup of carbon during this phase, the carbon source was identified as a possible candidate for alteration. After exploring multiple alternatives, sucrose was identified as an alternative to phenolic resin with the final stabilized blend, with the percentage of the carbon source adjusted to 4% for use with both isostatic pressing and casting. These modifications produced an RTP powder with an average grain size (D50) of less than 0.040 mm.

7.3.2 Compaction tooling development

Tooling design and development were carried out for two compaction routes – isostatic pressing and conventional casting. This effort focused on achieving maximum commonality between the two processes and was tailored to be produced using generative manufacturing techniques applied to both metal and polymers. Feature sizes on the order of 0.150 mm in the microreactor geometry necessitated extremely tight tolerances (+/- 0.030 mm) on the tooling design and manufacture, limiting the types of material and additive manufacturing processes that could be used. The tubular configuration also required the tooling to be designed with an emphasis on ease of assembly and post-compaction disassembly. All tooling elements incorporate allowances to accommodate shrinkage factors of around 18% for sintered SiC. The tooling used to produce all internal features of the reactor was manufactured using stainless steel to ensure sufficient rigidity and enable the creation of smooth interior walls. Exterior components were made using WaterShed XC 11122 (an ABS-like translucent polymer) to reduce cost and facilitate quick modifications. These parts are produced with tolerances in the X/Y dimension of 0.05 mm for the

first inch 25.4 mm plus ±0.001 in./in.mm/mm and Z-dimension tolerances of (0.127 mm) for the first inch 25.4 mm plus 0.001 mm/mm. Minimum wall thickness for this material and printing system is set at 0.0635 mm and a minimum feature size of 0.0635 mm in the X-Y direction.

7.3.2.1 Casting

The core of the tooling setup used in casting is the stainless-steel mandrel. This component is designed to produce the inner cavity of the reactor, including the tapered section. The mandrel (component A in Figure 7.4) is fabricated using stainless steel (17-4 P.H.) and Direct Metal Laser Sintering (DMLS) methods. The 3D printed component is heat-treated post-manufacturing for additional strength and is corrosion resistant allowing for multiple use cycles. The mandrel is 110 mm tall, with a base diameter of 20 mm. The upright section features a series of reducing diameters starting at 4 mm and stepping down to 0.81 mm at the upper segment. The central segment measures 1.18 mm and represents the major inner diameter of the reactor. The mandrel is intentionally designed to produce progressively smaller internal cavities while integrating features for increased ease of disassembly. It is designed to be assembled upright, with the base incorporating locating features for the rest of the tooling setup. The reactor's exterior is produced through a split mold design with two mating halves (component B in Figure 7.4) of a jacket (or casting block) located on the base of the mandrel. These components measure 105 mm in height and have an inner diameter of 2.36 mm, forming the main cavity into which the SiC precursor is poured. This cavity represents the outer diameter of the reactor geometry. Locating pips 2mm in diameter are provided on each half of the mold for easy assembly and to prevent any offset of the two halves. The parting line created by this design is mostly superficial and is removed during the finishing process. All polymer components used in this tooling setup are manufactured using WaterShed XC 11122 through Stereolithography (SLA). The WaterShed XC 11122 polymer is

chosen to produce these tooling components for its water-resistant and atmospheric sealing capabilities preventing the egress of moisture out through the tooling and stopping the ingress of air into the tooling setup reducing bubbling. To ensure that sufficient levels of rigidity are maintained once all the components are assembled, an exterior polymer shell (component C in Figure 7.4) is fabricated using stereolithography, and WaterShed XC 11122 is attached to the tooling assembly. This shell is anchored into a groove designed into the base of the mandrel, and it measures 105 mm in height with an outer diameter of 20 mm. Concentricity of the cavity inside the reactor is ensured by centering the mandrel; this is accomplished through a dual-purpose WaterShed XC 11122 polymer lid (component E in Figure 7.4) manufactured through stereolithography measured at 2 mm in diameter and 5 mm in height. The lid is positioned at the top of the mandrel. It has a central tapering hole 0.81 mm in diameter and 2 mm deep, allowing it to be inserted into the mold cavity while aligning the mandrel. The lid also prevents contaminants from infiltrating the tooling setup once the precursor has been introduced into the tooling apparatus. A third WaterShed XC 11122 polymer cylinder (component D in Figure 7.4) which is 110mm in height and has an inner diameter of 21 mm, also produced using stereolithography, is slipped onto the setup to provide additional points of attachment to the lid. The CAD model used to create all described components is detailed in Figure 7.4.

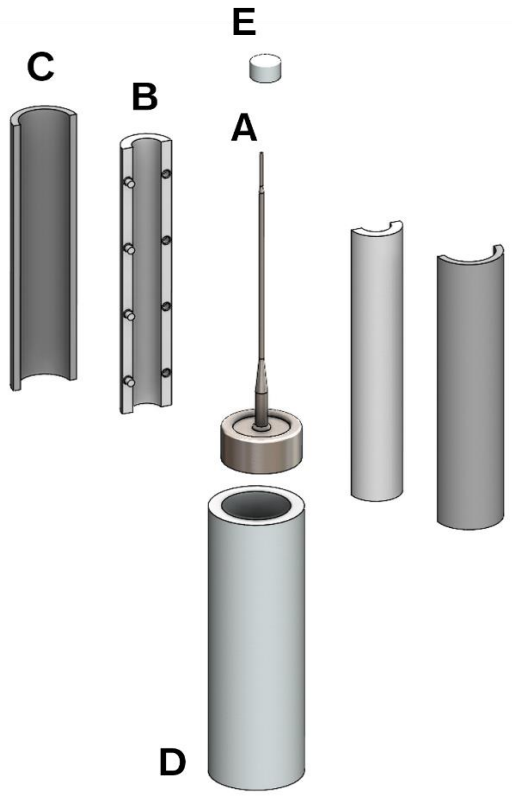

Figure 7.4: Casting tooling assembly with components labeled in the order of assembly (A) Stainless steel mandrel produced using DMLS. (B)Primary split casting block made with Watershed XC 11122 using SLA featuring location pips. (C) Secondary casting block made using ABS and SLA. (D) Support jacket made using Watershed XC 11122 and SLA used to stabilize the setup. (E) Watershed XC 11122 lid to seal the assembly and prevent contaminant entry.

The casting process involves converting the spray-dried Ready to Press (RTP) granulate to an aqueous slurry by mixing with 40% volume of D.I water. The conversion to aqueous form requires close monitoring to prevent the formation of granulate clumps while ensuring that the stirring does not introduce any inconsistencies in the form of air or contaminant bubbles. The slurry is then carefully introduced into the mold cavity of the casting setup. Care is taken to ensure that the slurry is introduced into the mold cavity uniformly until the upper neck of the mandrel is covered. The lid is used to locate the mandrel's upper end, completely sealing the mold from contaminants. Mold design accounts for the volume change due to the evaporation of water

shrinkage factors during compaction. The green strength of the compact is achieved 6 – 12 hours after drying.

Assessment of the dryness of the component is completed visually, followed by the disassembly of all the tooling components. At this point, the compact is held in place only by the mandrel and the casting blocks. The casting blocks incorporate identifying features for the location of the seam to part the interior casting block. The assembly is kept in an upright position to ensure that even in the relatively stabilized green state, no lateral forces are applied. With the compact exposed externally, the inner mandrel is removed by drawing it downwards. The mandrel integrates facets in its configuration, enabling smooth release from the assembly. This is critical to ensure the integrity of the taper post-tool removal. After extraction from the tooling, the compact is allowed to air dry for 2 hours.

7.3.2.2 Isostatic Pressing

The second compaction method chosen to produce the reactor design is isostatic pressing. Compaction in this method is accomplished by applying uniform pressure on the silicon carbide powder inside the tooling assembly. As with the casting process, a stainless-steel mandrel of identical dimensions and manufacturing method is used to create the interior cavity of the reactor. An elastomeric bag, also called the isostatic pressing jacket, is used to transfer compacting pressure to the silicon carbide powder used in this setup. In a process like the one described for casting the reactor, the molded bag is produced using additively manufactured tooling. A two-component mast and jacket design are created to produce the isostatic pressing bag. The mast has a base dimension of 21 mm and an upright section with a height of 115 mm and a diameter of 2.18 mm. The jacket has an outer diameter of 18.5 mm and an inner diameter of 8 mm. Both these parts are produced using stereolithography and the WaterShed XC 11122 polymer. A range of polyurethane

durometers was evaluated to ensure the optimum pressure transfer to produce a fully densified compact. To make a non-porous elastomer bag, the polyurethane mix is introduced into the mast and jacket construction. The filled assembly is placed on a vibrating stand ensuring uniform fill density. Each elastomeric bag used in the assembly of the finished components is tested to verify impermeability to fluids by sealing both ends and immersing them into a tank of isopressing fluid. The CAD model of the tooling components used in this process is shown in Figure 7. 5.

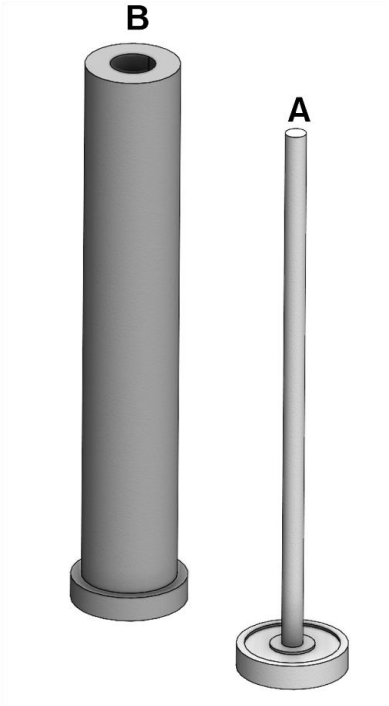

Figure 7.5: Additively manufactured tooling components to produce isopressing mold bags. (A) Mold mast produced using WaterShed XC 11122 and SLA 3D printing. (B) Mold jacket produced using WaterShed XC 11122 and SLA 3D printing

Tooling assembly for the isostatic pressing process is similar to the one used for casting with the elastomer bag forming the outer jacket and located onto the assembly features on the base of the stainless-steel mandrel. The precursor used in this case is not mixed with water and is used directly in the dry Ready to Press (RTP) form. The grain size of the RTP allows for a high degree of flowability, enabling an easy introduction to the tooling setup. Post-filling the mold with RTP,

the assembly is then enclosed in a WaterShed XC 11122 polymer supporting jacket, also produced using stereolithography to ensure rigidity inside the pressing device. The supporting jacket is 110 mm tall, with a base of 21 mm and an inner cavity of 8 mm. The supporting jacket features rectangular cutouts at the upper and lower ends measuring 2 mm in height and 4mm in length to help alleviate any imbalances in pressure due to the geometry of the components. This is then further reinforced by a WaterShed XC 11122 polymer perforated jacket. This component has multiple circular holes cut out to stabilize the pressure applied and to reinforce the setup.

Both the support jacket and the perforated jacket are intended to fit around the base of the stainless-steel mandrel, adding two layers of protection from the ingress of the isopressing fluid. They also ensure that the components do not warp under the applied loads and that the pressure is uniformly transmitted to the entire setup. A custom lid made of a softer polymer is used to 'cap' the assembly and secure the mandrel, concentric to the molded bag. CAD models of the components are shown in Figure 7.6.

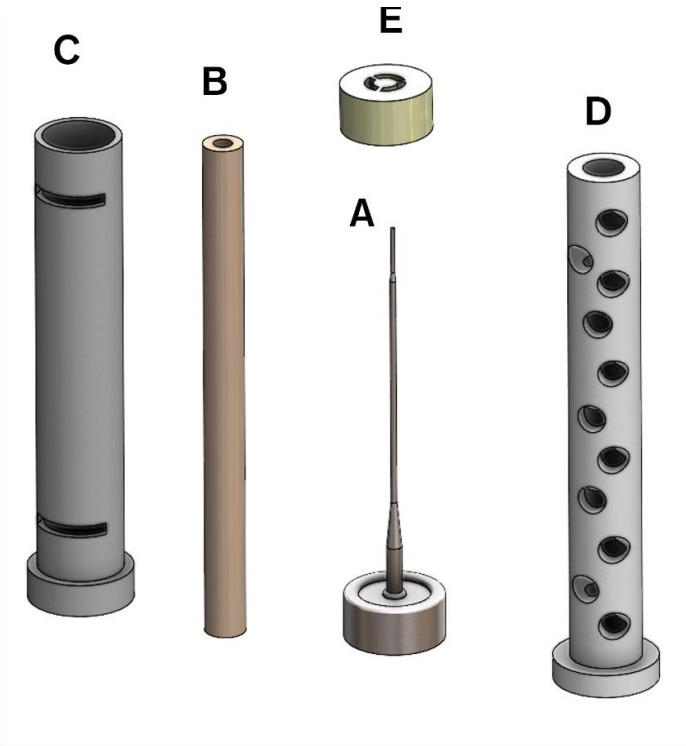

Figure 7.6: Isopressing tooling assembly with components labeled in the order of assembly. (A) Stainless steel mandrel produced using DMLS. (B)Iospressing jacket made of polyurethane cast in-house. (C) Support jacket made using WaterShed XC 11122 and printed using SLA. (D) Perforated jacket was made using WaterShed XC 11122 and SLA was used to stabilize the pressure application on the setup. (E) Polyurethane lid to seal the assembly and prevent contaminant entry.

Initial trials were carried out in a commercial large-scale isopressing apparatus. These setups are intended for use with much higher wall thickness (>76.2 mm). This resulted in parts being warped and fragmented when used with the reactor tooling. Further, significant spring-back in the initial mandrel designs led to post-pressing fissures and defects in the internal cavity of the reactor. To support the production of a component with extremely thin wall sections, a custom isopressing apparatus was developed. The design of this device allows for components of a very thin cross-section (<0.500 mm) and a high aspect ratio to be isopressed. This specialized setup features a miniaturized pressure cell of 6 cubic inches volume, with a variable pressure setting

ranging from 3000 psi to 30000 psi. Central to the compatibility of the device with these smaller, more intricate designs is the finer variable pressure control, which can be adjusted either manually (through a hand crank) or automatically through a motorized system. Compaction in this setup is achieved at pressure ranges from 18000 to 21000 psi, depending on the granulate size and composition. Post compaction, tool disassembly involves removing the components in the order of assembly, followed by a careful release of the mandrel from the base.

Applying 3D printing to produce all tooling components enabled a highly iterative design and manufacturing approach. Issues with spring back, the rigidity of tooling parts, and the warping of the assembly were addressed by quickly modifying the design and producing components additively. Developing two compaction methods concurrently enabled learning from one process route to be transferred to the other, especially in tackling challenges with distortion and component densification. Multiple trials were carried out to support using these non-conventional processing techniques and tooling, combined with a new raw material composition. This involved significantly relaxing the tolerances on the final component to understand the interaction between the tooling and chosen processing method. Standard specimens were produced in solid rod forms using both techniques to verify the finished product features compared to traditional processing methods such as extrusion and squeeze casting.

Additive manufacturing also facilitated trials with multiple materials for tooling components. These enabled rapid evaluations of the design features while keeping costs and turnaround times low. The mandrel alone went through over eight design updates to produce parts with the specified finish and ease of disassembly required by the application. The evolution of this design is shown in Figure 7.7.

Figure 7.7: CAD renderings of the geometry of the mandrel highlighting the changing geometry with the evolution of process capabilities (left: oldest, right: newest)

The evolution of the mandrel design also enabled the incorporation of features such as localized fillets and chamfers for compatibility with the high-resolution setting of the printing process. This allowed feature sizes as small as 0.045 mm to be created using direct metal laser sintering techniques. Similarly, each support component was manufactured over various dimensions to choose the optimum configuration. Wherever possible, tooling features enable locking and sealing to prevent environmental contamination. Locating details prevents cross-assembly or offsetting of stacked components. Minimum material mass designs are preferred to reduce processing time and handle challenges. In addition to the tooling in the form of release media applied to the mandrel, the design of sealing lids was made simultaneously to improve the ease of extraction and feature production within the reactors. Both compaction processes benefited from having a similar baseline tooling design. These enabled learnings in one process to be quickly transferred to the other, reducing risk and the overall development time. The choice of using a single material for the exterior of the tooling was aimed at ensuring uniform load transfer, especially during isostatic pressing, and ensuring harmony with the silicon carbide precursor.

Prototyping the internal taper required scaling up the geometry to understand tooling and slurry interaction. This necessitated creating segments of the tooling at larger dimensions and

modeling the impact of pressure on these features. The final blueprint wall thickness requires extremely low tolerances around the 0.400 mm dimension. To achieve this, the individual processes needed to be studied for their ability to be progressively shrunk in the lateral dimension. To produce parts with these extreme cross-sections, the mandrel is designed with a series of 'joggles.' These reductions in cross-sections allow the slurry to densify, enabling the segment above it to layer effectively. Compared to more conventional tool manufacturing, additive manufacturing proved vital in allowing rapid changes and evaluating them on the test bench.

7.3.3 Pyrolysis and Sintering

Post compaction, the component is described to be in the green state. To enable safe handling of the part, it is first pyrolyzed. This process is common to parts produced using isostatic pressing and casting. It is accomplished in a Linberg/Blue M Box Furnace Atmosphere retort with a do not exceed temperature of 1250 °C. The components are heated in a Nitrogen atmosphere with continuous pumping in steps of 2 °C per minute up to 650 °C. The component is held at this temperature for two hours. The binder material is burnt out of the reactor during this process, partially sintering it. Ambient cooling allows the component to return to room temperature in 6 hours. Once pyrolysis is completed, the component is safe to handle, and exterior surface flaws can be removed manually using 1200-grit silicon carbide sandpaper.

The sintering procedure achieves post-pyrolysis, final densification, and establishment of the geometry's final dimensions. The sintering stage is common to components produced by the isostatic pressing and casting. Sintering is the application of heat to a partially densified component (green state) to produce properties that approach the theoretical values. The effect of the atmosphere in which the component is sintered impacts its final facets. The presence of Nitrogen while sintering influences the microstructural evolution of SiC with oxide additives. It was noted

that the percentage of Nitrogen in the atmosphere impacts the resistivity and thermal conductivity of the sintered component. Sintering is achieved in a Thermal Technology Model 1000-3560-FP24 Furnace with a hot zone size of 152.4 mm in diameter and 152.4 mm in height. Here the green component is heated to a temperature of 2150°C, with a never exceed temperature of 2650°C. The sintering process is completed in an atmosphere of Argon. The component is heated in steps of 5 °C per minute, with the final sintering temperature reached in 7 hours, where the component is held at this temperature for 30 minutes. Component cooldown is completed in an ambient atmosphere in 14 hours.

The component is fully densified and visually inspected, followed by sizing to meet the specifications laid down by experimental requirements. This involves cutting the sample from 60 mm in length to 30 mm and grinding to ensure perpendicularity of the end faces.

7.4 Materials Characterization

To quantify the performance of parts produced using this process and to validate the properties of the finished component in comparison to the currently used Hexoloy silicon carbide reactors a series of material characterization experiments were conducted. In these experiments, the reactor configuration produced using Calix High Strength 2 and the hybrid digital process is referred to as the nozzle reactor, and the standard Hexoloy reactor is referred to as the tube reactor.

7.4.1 Modulus of Rupture (MOR) evaluation

Sintered density of the finished component was identified as a key characteristic of the reactor affecting its performance in the experimental setup. To evaluate this a series of comparative evaluations were carried out. These experiments looked at the modulus of rupture (in MPa)

between the sintered SiC produced by this process (Calix High strength 2) and the sintered Hexoloy reactor currently used in the experiment.

These evaluations were carried out per ASTM 1161 which is the standard test method for flexural strength of advanced ceramics at ambient temperature. The specimens tested as per this specification conform to type B configuration with a support span of 40mm, thickness of 3 mm, and a four-point fully articulated loading at room temperature. Loading rates were chosen not to exceed a strain rate of $1.0 \text{ X } 10^{-4} \text{ s}^{-1,}$ and loading was sustained till fracture. Samples tested were produced using dry pressing methods, and the relative modulus of rupture (MOR) is presented in Figure 7.8.

7.4.2 X-Ray Diffraction

Powder samples were prepared by grinding one reactor sample produced by each process (this work and extrusion using Hexoloy) to a particle size of less than 44 μm (sub-325 mesh). Diffraction patterns of back-loaded powder samples were collected with a diffractometer (D2 Phaser, Bruker, Germany) using copper Kα radiation (λ=1.54 Å). Patterns were collected from 15 to 60 °2θ with a 0.04 °2θ step size and a 4-second count time. Analysis software (Jade, v.9, Materials Data Inc., Livermore, CA, USA) was used for qualitative analysis and mineral identification. Data obtained from these evaluations were also used for qualitative comparison to other XRD data published using Hexoloy SiC material and is presented in Figure 7.9.

7.4.3 Micro Computerized tomography (μ-CT)

Micro CT imaging was used to observe the internal features of the reactor produced using this process as compared to the tube reactor created using Hexoloy material. Reactor samples were

imaged using x-ray microscopy (Zeiss Xradia 520 Versa). Settings for the scans included: 4× objective, 80 kV voltage, 7 W power, no filter, 1601 projections, 2 second exposure time. Images were reconstructed for microCT assessment and visualization.

These settings produced an approximate field of view of 2048 pixels by 2048 pixels with a voxel size of 13.11252 µm with a binning of 1. The total scan time for both samples was 2 hours. Automated centering and beam hardening corrections were applied using Scout-and-Scan Control System Reconstructor software (v 14.0.14829.38124). Reconstructions were imported into Dragonfly Pro (version 4.1, Object Research Systems), and histograms were manually adjusted for visualization. Section views along the centerline were stitched together for both reactors to observe interior features and confirm the taper section's integrity and dimensional accuracy (2 mm in length and taper from 1 mm to 0.480 mm). A section view of the nozzle reactor is presented in Figure 7.10.

7.4.4 Scanning Electron Microscopy (SEM)

The tube reactor that was produced using Hexoloy and the nozzle reactor that was produced using Calix High Strength 2 and the process described in this work were sputter-coated with Au-Pd to provide a conducting surface. Imaging was in either secondary electron (S.E.) or backscatter electron (BSE) mode, or a mixture of the two, depending on what gave the best contrast and image quality. BSE provides some relative chemistry information, with higher atomic number elements producing a brighter BSE signal due to a higher probability of an incident electron being reflected back to the detector.

Electrons are generated using a LaB_6 filament with accelerating voltages ranging from 10kV to 25kV. All images were collected in an environmental SEM (ESEM, Quanta 200, FEI

Company, Hillsboro, OR). Images were produced at magnification levels from 500X to 2000X and a selection of these are shown in Figure 7.11.

7.4.5 Optical Microscopy Imaging

The exterior surfaces of the reactor samples were imaged using the Olympus Vanox -S Research Photomicrographic Microscope System. Illumination is provided by a tungsten-halogen lamp housed in a lamp housing at the lower rear base of the microscope. Light emitted from the lamp is first passed through a collector lens, then reflected by a mirror through a field diaphragm and into the substage condenser. There were a variety of condensers available for this model, including brightfield and darkfield, throughout the full range of optical corrections. The reactor surface was prepared by cleaning with acetone and air drying to remove any surface contaminants. Imaging was carried out in the range of 10X – 100X. Image visualization was accomplished in a computing system running the Leica Exalta micro imaging software with lighting and focus manually adjusted to produce the best contrast and image quality. A selection of the images obtained is presented in Figure 7.12.

7.4.6 Characterization Results and Discussion

Modulus of rupture evaluations indicated the superior performance of the Calix High Strength 2 material as compared to the Hexoloy grade of silicon carbide. The results are presented in Figure 7.8. A higher modulus of rupture translates to better resistive heating characteristics combined with a longer experimental life cycle. The currently used Hexoloy reactors are discarded after approximately 20 cycles of use due to reduced thermal response and fracturing at electrical contact points. With the higher component density achieved using this composition and compaction process, it is expected to double the usable life cycle of these new reactors. A higher

strength also confirms that this material system can approach the theoretical density limit, producing parts with fewer pores and reducing the chance of failure during operation.

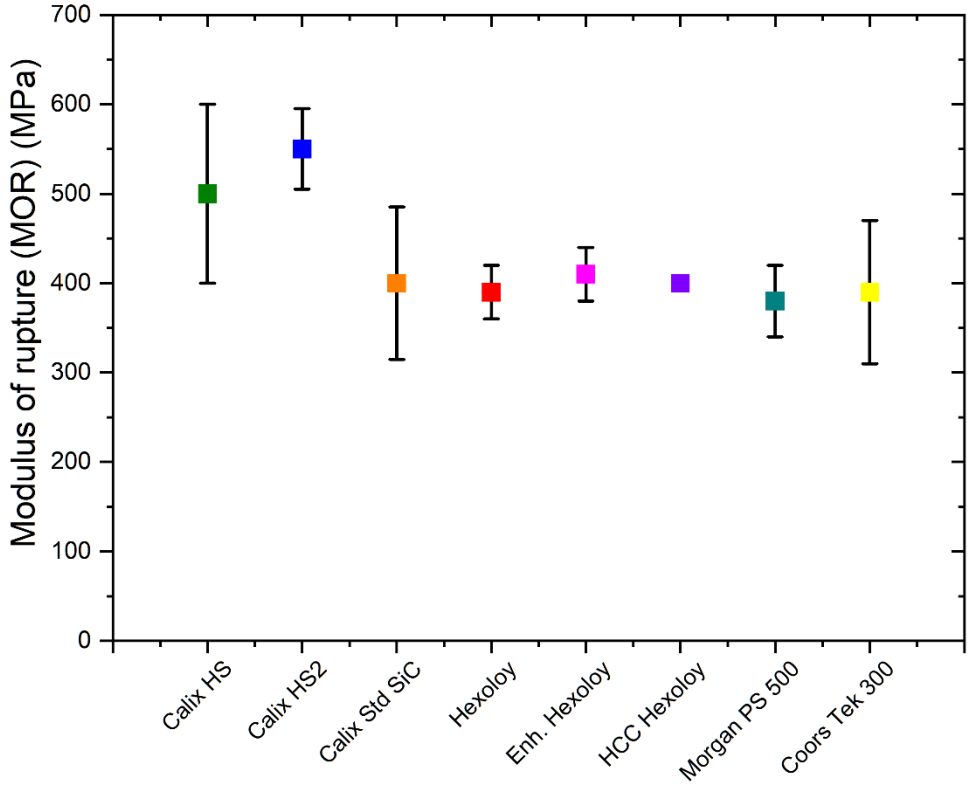

Figure 7.8: Modulus of rupture tests carried out on cast rod samples of different silicon carbide grades. The material used in this process is Calix High Strength 2, and the material used in the tube reactor is Hexoloy.

X-ray Diffraction results validated that the processing method described in this work does not introduce any material inconsistencies as compared to currently used components. These results are presented in Figure 7.9. The data obtained confirm that the nozzle reactor's fundamental composition is identical to the tube reactor. This ensures that the new reactor will not require any modifications for integration with the application. Existing protocols for reactor handling and heating can be continued with the nozzle reactor composition ratification.

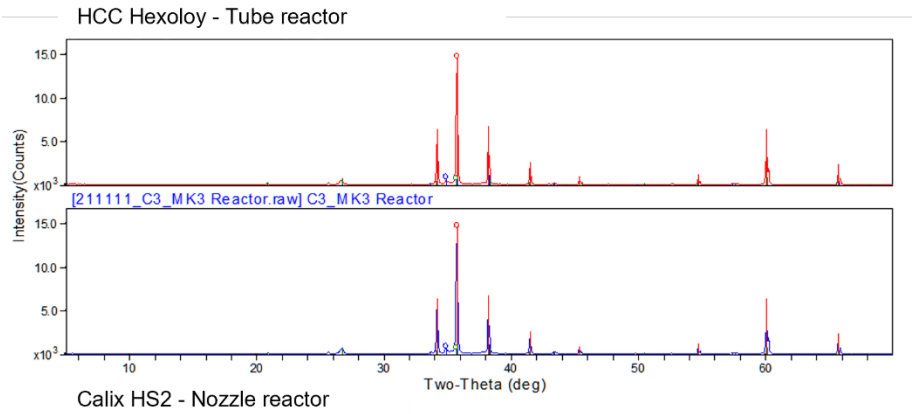

Figure 7.9: X-ray diffraction results for material used to manufacture the tube reactor (in red) and the material used to manufacture the nozzle reactor (blue).

Micro-CT and SEM imaging enabled a non-destructive method to observe the taper inside the nozzle reactor and verify the cavity's linearity inside the reactor. These images are shown in Figure 7.10 and Figure 7.11, respectively. Concentricity of the cavity within the reactor was another parameter that was studied, and feedback from initial images was used to inform the tooling design of both processes and the anchoring methods used to center the mandrel. Both imaging techniques showed a clean, straight cavity devoid of any tool indentations and internal voids for the nozzle reactor produced using the process detailed in this work. This is in direct contrast to the tube reactor, where the cavity was not concentric with the outer diameter. The images show significant pitting inside the reactor cavity along with flow lines consistent with tooling age on the extrusion dies. Also clear from the images is the irregularity of the interior walls of the reactor coupled with large voids of the order size of 0.040 mm. This has also been previously confirmed in a study using X-ray fluorescence and absorbance and has been identified as a factor affecting flow characteristics and hence kinetic modeling.

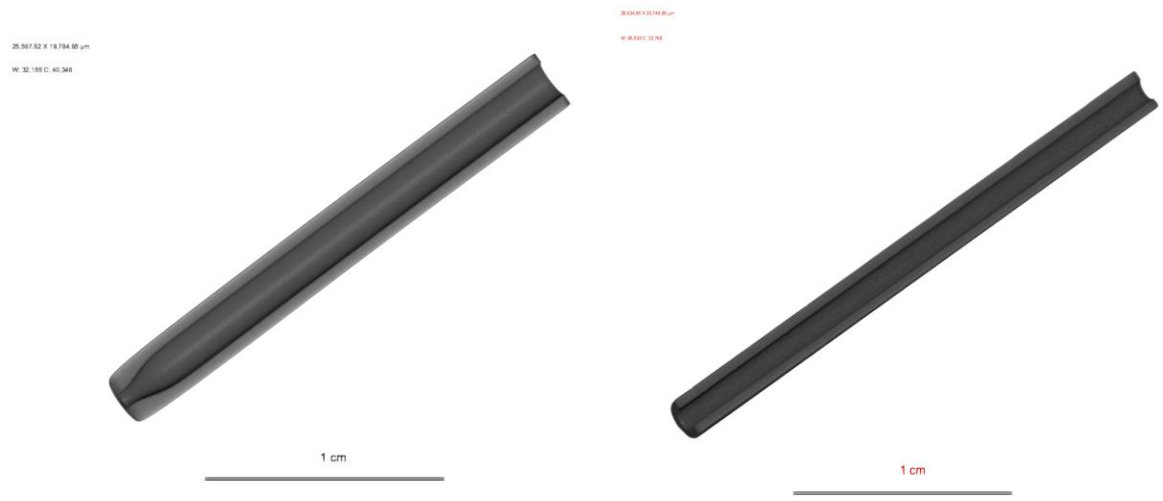

Figure 7.10: Composite Micro Contrast Tomography (Micro-CT) showing a section view of the reactor produced using the technique described in this work. (nozzle reactor, left and tube reactor, right)

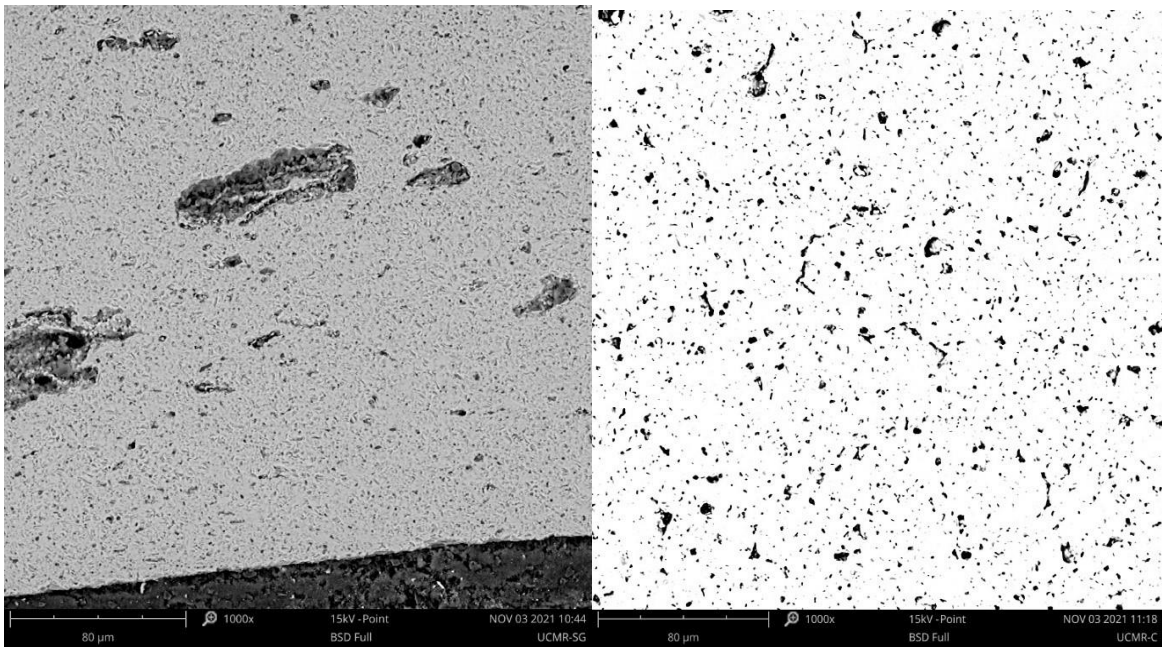

Figure 7.11: Scanning Electron Microscope (SEM) images at 1000X showing internal defects in the tube reactor (left) as compared to the reactor (right) produced using the technique described in this work.

Optical imaging highlighted the exterior surface features of the reactors. These images are presented in Figure 7.12. This technique shows the presence of superficial flaws (which can result

in regions of low strength localized around these defects) on the tube reactor. This is in direct contrast to the smooth surface of the nozzle reactor, with almost no pores visible even at maximum magnification. The effect of these flaws on the tube reactor extends beyond lowered density and can also affect the maximum temperature to which the reactor can be heated resistively (1800 K for the tube reactor as compared to 2100K with the nozzle reactor), limiting experimental applicability.

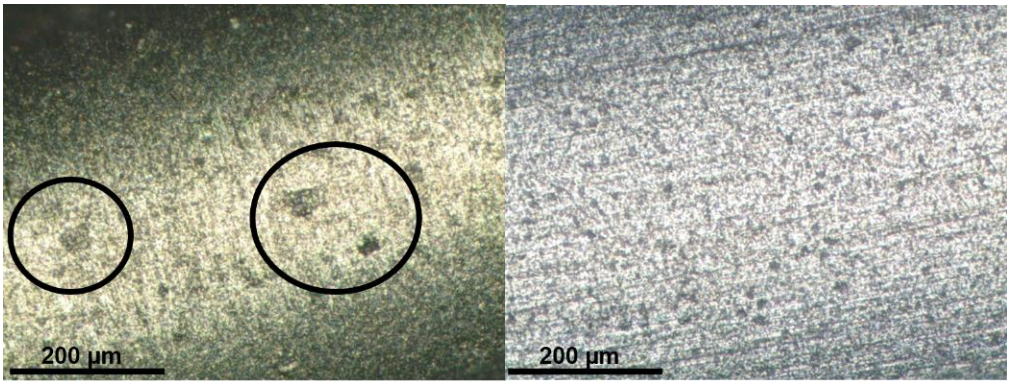

Figure 7.12: Optical microscope images at 50 X zoom showing the tube reactor (left) and the reactor produced using the process (right) described in this work.

7.5 Experimental Validation of the nozzle micro-reactor

The molecule chosen to evaluate the performance of the nozzle reactor as compared to the tube reactor was cyclohexene. This involved observing the signal change due to the variation in the mole fraction of the decomposition of cyclohexene as a function of fluid pressure at different temperatures. Identical experimental conditions were set up with 0.1 % of cyclohexene run first through the tube reactor (Chen reactor) and the nozzle reactor across a temperature range of 300K to 1700K. The thermal decomposition of cyclohexene through the retro Diels-Alder method to butadiene and ethylene is a reaction that has been identified as pressure and temperature-sensitive [42],[43]. Therefore, at the higher stabilized pressures of the nozzle reactor (as compared to the

tube reactor), we expect to see a greater fraction of cyclohexene decomposing to form butadiene and ethylene. It is also shown that the increased pressure within the reactor will result in the decomposition reaction beginning at a lower temperature in the nozzle reactor.

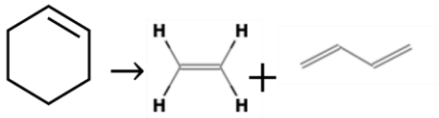

$$C_6H_{10} \rightarrow C_2H_4 + C_4H_6$$

m/z 28 m/z 54

Figure 7.13: Cyclohexene decomposition reaction producing ethylene and 1,3 - butadiene

Results from the two experimental runs are presented in the plot shown in Figure 7.14. The X-axis represents micro-reactor surface temperature change in increments of 100 K starting at room temperature up to 1800 K. The Y-axis represents the ratio of the normalized signal height of 1,3-butadiene compared to cyclohexene's signal height. The nozzle reactor chosen for this evaluation features a constriction with an exit diameter of 0.400 mm. The data points corresponding to the ratio of signal heights for the nozzle reactor indicate how the amount of butadiene produced is significantly higher between 1300-1700 K as compared to the tube reactor. The maximum ratio of signal heights (the amount of decomposition achieved) is higher for the nozzle reactor in contrast to the tube reactor. At temperatures beyond 1500 K, the stabilized pressure enables access to decomposition pathways with much higher thermal barriers. This results in a drop-off in the ratio of signal heights because other secondary decomposition products are formed. A similar switching of primary decomposition paths is achieved only at temperatures greater than 1700 K in the case of the tube reactor. The shift in temperature for the onset of decomposition can be attributed to the presence of a constriction in the case of the nozzle reactor.

This reduction in exit diameter results in a modification in the fluid flow behavior throughout the reactor, resulting in a change in the residence time and pressure of the fluid within the reactor. These alterations make for a more reproducible, consistent flow field, which in turn, makes numerical modeling these reactors more facile, highlighting the value of incorporating this nozzle using this manufacturing method. Prior to the application of this method, such an intricate design change lay outside the fabrication envelope for this material type, both from a cost and time perspective.

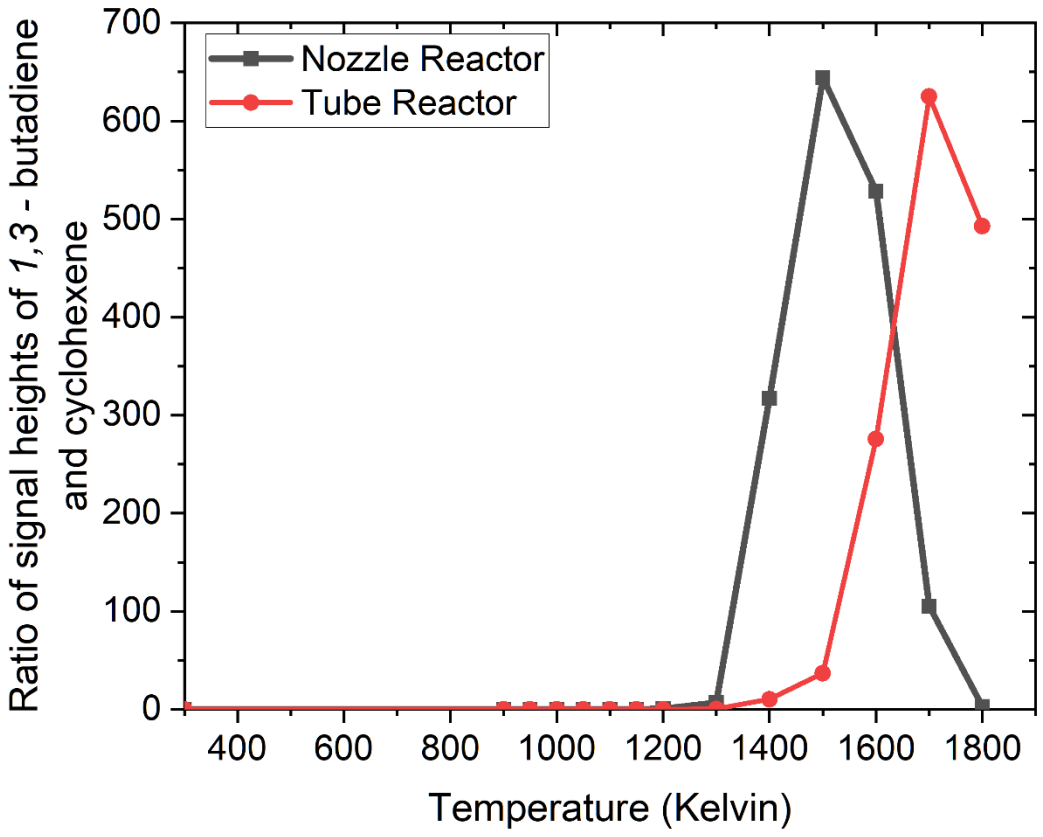

Figure 7.14: Ratio of the signal height of butadiene to cyclohexene versus temperature in the nozzle reactor as compared to the tube reactor

7.6 Multi-Material Capability

In addition to producing high aspect ratio silicon carbide geometries the application of this technique has been expanded to include additional engineering ceramic materials as well. The same process flow has been applied to produce components with the reactor geometry using alumina and Yttria Stabilized Zirconia (YSZ). Standard RTP powders with minor modifications have successfully produced components with wall thicknesses lower than 0.500 mm and feature sizes as small as 0.300 mm. Compositional changes to the raw material include reducing grain sizes of the major component ceramic to less than 0.040 mm. All other processing parameters and sequences are kept common across materials. This capability allows for multiple materials to be fabricated simultaneously, highlighting the processing methodology's versatility. An example of reactor geometries manufactured using the process described in this work is shown in Figure 7.15 (B).

7.7 Multi-Geometry Capability

The digital aspect of this technique enables it to be extended to a range of geometries in addition to the reactor configuration. This has been evaluated by producing multiple components in addition to the standard nozzle reactor shape. The tool design philosophy of this process focused on integrating modularity into the manufacturing technique. This allowed modifications to the final geometry by altering a minimal number of tooling elements. An example of this modular capability is creating a tubular structure with a tapped internal cavity.

This was achieved by altering the design of the stainless-steel mandrel by integrating tapping threads on the external surface of the tooling element. A manufacturing sequence like what is described in Figure 7.3 was carried out, and post-compaction, the mandrel was extracted by unscrewing it out of the cavity of the component. The green compact was then sintered to produce

a fully densified tube with an exterior diameter of 3 mm and internal threads of 2 mm pitch along a length of 30 mm. This component was manufactured to showcase the flexibility of the process and its ability to be easily modified to produce vastly different and challenging shapes. An example of the tooling developed for the fabrication of a high aspect ratio component featuring internal threads is shown in Figure 7.15 (A) with a rendering of the cross-section of the geometry shown in the inset.

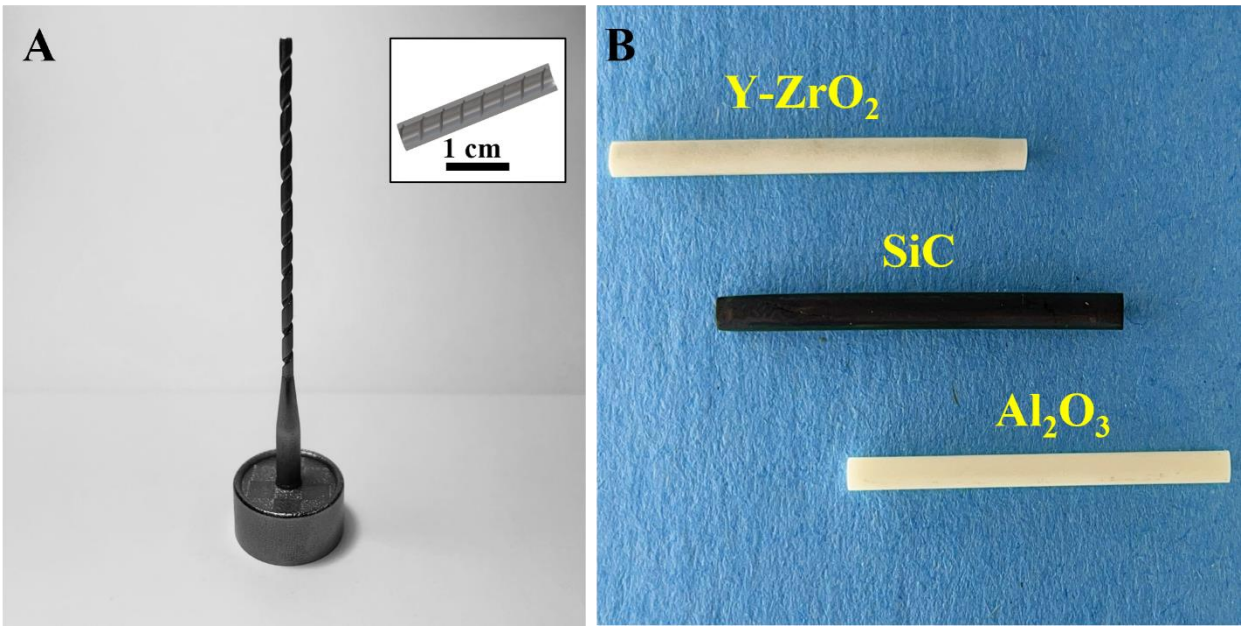

Figure 7.15: Image showing the tooling component featuring a helical thread produced using direct metal laser sintering with the inset image showing a rendering of the cross-section of the geometry fabricated using this tooling. B.) Silicon carbide SiC, alumina, and Yttria stabilized Zirconia reactor geometries fabricated using the method described in this work.

7.8 Conclusions

This chapter documented the digital manufacturing technique created to manufacture high aspect ratio silicon carbide geometries. The development of specialized ceramic precursors, tooling, and compaction techniques is detailed. The technique has been applied to produce a range of reactor geometries featuring an internal taper designed to optimize fluid flow parameters within the reactor. Material characterizations have been used to compare the features of the reactor

produced using this process and the currently used Chen reactor. These results conclusively demonstrated the higher density, hardness, and superior finish of the new design and the features of the constriction in the design. Experimental validation using the PIMS experiment was used to demonstrate and explain the variation in results obtained because of the superior flow characteristics produced in the new design. It is expected that the enhanced capabilities provided by the new reactor, coupled with enhanced diagnostic techniques, would be crucial in providing insight into developing future fuels.

This work has been adapted for journal publication with the tentative title,' *Rapid prototyping of high-resolution silicon carbide devices using digital manufacturing; demonstrated using flow reactors.*'

7.9 References

[1] K. Yamada and M. Mohri, "Properties and Applications of Silicon Carbide Ceramics," in Silicon Carbide Ceramics—1: Fundamental and Solid Reaction, S. Sömiya and Y. Inomata, Eds. Dordrecht: Springer Netherlands, 1991, pp. 13–44. doi: 10.1007/978-94-011-3842-0_2.

[2] K. Biswas, "Solid State Sintering of SiC-Ceramics," Mater. Sci. Forum, vol. 624, pp. 71–89, 2009, doi: 10.4028/www.scientific.net/MSF.624.71.

[3] G. R. Sawyer and T. F. Page, "Microstructural characterization of 'REFEL' (reaction-bonded) silicon carbides," J. Mater. Sci., vol. 13, no. 4, pp. 885–904, Apr. 1978, doi: 10.1007/BF00570528.

[4] X. Li, K. Zhang, H. Konietzky, Y. Wang, and X. Li, "Experimental study on the dynamic mechanical behaviors of silicon carbide ceramic after thermal shock," Nucl. Mater. Energy, vol. 24, p. 100774, Aug. 2020, doi: 10.1016/j.nme.2020.100774.

[5] S. Ding, Y.-P. Zeng, and D. Jiang, "Thermal shock resistance of in situ reaction bonded porous silicon carbide ceramics," Mater. Sci. Eng. A, vol. 425, no. 1, pp. 326–329, Jun. 2006, doi: 10.1016/j.msea.2006.03.075.

[6] R. Gutierrez, T. Frauenheim, T. Köhler, and G. Seifert, "Stability of silicon carbide structures: from clusters to solid surfaces," J. Mater. Chem., vol. 6, no. 10, pp. 1657–1663, Jan. 1996, doi: 10.1039/JM9960601657.

[7] R. Moene, M. Makkee, and J. A. Moulijn, "High surface area silicon carbide as catalyst support characterization and stability," Appl. Catal. Gen., vol. 167, no. 2, pp. 321–330, Feb. 1998, doi: 10.1016/S0926-860X(97)00326-8.

[8] V. A. Izhevskyi, L. A. Genova, J. C. Bressiani, and A. H. A. Bressiani, "Review article: silicon carbide. Structure, properties and processing," Cerâmica, vol. 46, pp. 4–13, Mar. 2000, doi: 10.1590/S0366-69132000000100002.

[9] W. Wesch, "Silicon carbide: synthesis and processing," Nucl. Instrum. Methods Phys. Res. Sect. B Beam Interact. Mater. At., vol. 116, no. 1, pp. 305–321, Aug. 1996, doi: 10.1016/0168-583X(96)00065-1.

[10] P. Zhang, J. Liang, L. Yin, and S. Guo, "The synthesis of micro-sized silicon carbide whiskers and the application for heat transfer enhancement," Sci. China Technol. Sci., vol. 57, no. 12, pp. 2371–2378, Dec. 2014, doi: 10.1007/s11431-014-5704-0.

[11] M. Willander, M. Friesel, Q. Wahab, and B. Straumal, "Silicon carbide and diamond for high temperature device applications," J. Mater. Sci. Mater. Electron., vol. 17, no. 1, p. 1, Jan. 2006, doi: 10.1007/s10854-005-5137-4.

[12] X. She, A. Q. Huang, Ó. Lucía, and B. Ozpineci, "Review of Silicon Carbide Power Devices and Their Applications," IEEE Trans. Ind. Electron., vol. 64, no. 10, pp. 8193–8205, Oct. 2017, doi: 10.1109/TIE.2017.2652401.

[13] F. F. Wang and Z. Zhang, "Overview of silicon carbide technology: Device, converter, system, and application," CPSS Trans. Power Electron. Appl., vol. 1, no. 1, pp. 13–32, Dec. 2016, doi: 10.24295/CPSSTPEA.2016.00003.

[14] Q. An, J. Chen, W. Ming, and M. Chen, "Machining of SiC ceramic matrix composites: A review," Chin. J. Aeronaut., vol. 34, no. 4, pp. 540–567, Apr. 2021, doi: 10.1016/j.cja.2020.08.001.

[15] D. T. D. Karimbaev, A. Y. Ezhov, and M. A. Mezentsev, "DEVELOPMENT OF BREAKTHROUGH TECHNOLOGIES FOR CREATING NODES AND DETAILS FROM

CERAMIC AND POLYMER COMPOSITE MATERIALS FOR SMALL-SIZED AIRCRAFT ENGINES," p. 10, 2017.

[16] Luo, Z.H., et al. “Preparation of Reaction-Bonded Silicon Carbide with Well Controlled Structure by Tape Casting Method.” Ceramics International, vol. 38, no. 3, Apr. 2012, pp. 2125–2128, https://doi.org/10.1016/j.ceramint.2011.10.053. Accessed 30 Nov. 2021.

[17] U. Paik, H.-C. Park, S.-C. Choi, C.-G. Ha, J.-W. Kim, and Y.-G. Jung, "Effect of particle dispersion on microstructure and strength of reaction-bonded silicon carbide," Mater. Sci. Eng. A, vol. 334, no. 1, pp. 267–274, Sep. 2002, doi: 10.1016/S0921-5093(01)01897-4.

[18] C. h. Carter Jr., R. f. Davis, and J. Bentley, "Kinetics and Mechanisms of High-Temperature Creep in Silicon Carbide: I, Reaction-Bonded," J. Am. Ceram. Soc., vol. 67, no. 6, pp. 409–417, 1984, doi: 10.1111/j.1151-2916.1984.tb19726.x.

[19] Chaonan Xu, Chong Xu, Feng Han, Feng Zhang, Wei Wei, Zhaoxiang Zhong, Weihong Xing,' Fabrication of high performance macroporous tubular silicon carbide gas filters by extrusion method,' Ceramics International,Volume 44, Issue 15,2018.

[20] Z. Yong, H. Xinbo, X. Qu, and Z. Zhen, "Research on ceramic injection molding of silicon carbide," RARE Met. Mater. Eng., vol. 36, pp. 326–329, Aug. 2007.

[21] Z. Zhang et al., "Influence of Carbon Content on Ceramic Injection Molding of Reaction-Bonded Silicon Carbide," Int. J. Appl. Ceram. Technol., vol. 13, no. 5, pp. 838–843, 2016, doi: 10.1111/ijac.12570.

[22] M. Iqbal, M. Konneh, A. Y. B. M. Said, and A. F. B. M. Zaini, "Surface Quality of High Speed Milling of Silicon Carbide by Using Diamond Coated Tool," in Advanced Research in Material Science and Mechanical Engineering, Pts 1 and 2, Durnten-Zurich, 2014, vol. 446–447, pp. 275-+. doi: 10.4028/www.scientific.net/AMM.446-447.275.

[23] C. Gao, G. Liu, and H. Wang, "Experimental Investigations of Drilling Silicon Carbide Using Brazed Diamond Tools," Mater. Perform. Charact., vol. 8, no. 1, pp. 329–343, Jul. 2019, doi: 10.1520/MPC20180190.

[24] J.-H. Eom, Y.-W. Kim, and S. Raju, "Processing and properties of macroporous silicon carbide ceramics: A review," J. Asian Ceram. Soc., vol. 1, no. 3, pp. 220–242, Sep. 2013, doi: 10.1016/j.jascer.2013.07.003.

[25] T. Whalen, W. Trela, and J. Baer, "Injection-Molding of Silicon-Carbide - Statistical Design of Experiments," Int. J. Powder Metall., vol. 27, no. 2, pp. 155–158, Apr. 1991.

[26] R. He et al., "Progress and challenges towards additive manufacturing of SiC ceramic," J. Adv. Ceram., vol. 10, no. 4, pp. 637–674, Aug. 2021, doi: 10.1007/s40145-021-0484-z.

[27] I. Polozov, N. Razumov, D. Masaylo, A. Silin, Y. Lebedeva, and A. Popovich, “Fabrication of Silicon Carbide Fiber-Reinforced Silicon Carbide Matrix Composites Using Binder Jetting Additive Manufacturing from Irregularly-Shaped and Spherical Powders,” Materials, vol. 13, no. 7, p. 1766, Apr. 2020, doi: 10.3390/ma13071766.

[28] A. Fleisher et al., "Reaction bonding of silicon carbides by Binder Jet 3D-Printing, phenolic resin binder impregnation and capillary liquid silicon infiltration," Ceram. Int., vol. 45, no. 14, pp. 18023–18029, Oct. 2019, doi: 10.1016/j.ceramint.2019.06.021.

[29] S. Meyers, L. De Leersnijder, J. Vleugels, and J.-P. Kruth, "Direct laser sintering of reaction bonded silicon carbide with low residual silicon content," J. Eur. Ceram. Soc., vol. 38, no. 11, pp. 3709–3717, Sep. 2018, doi: 10.1016/j.jeurceramsoc.2018.04.055.

[30] R. S. Evans, D. L. Bourell, J. J. Beaman, and M. I. Campbell, "Rapid manufacturing of silicon carbide composites," Rapid Prototype. J., vol. 11, no. 1, pp. 37–40, Jan. 2005, doi: 10.1108/13552540510573374.

[31] K. Cai et al., "Geometrically Complex Silicon Carbide Structures Fabricated by Robocasting," J. Am. Ceram. Soc., vol. 95, no. 8, pp. 2660–2666, 2012, doi: 10.1111/j.1551-2916.2012.05276.x.

[32] A. Ortona, C. D'Angelo, S. Gianella, and D. Gaia, "Cellular ceramics produced by rapid prototyping and replication," Mater. Lett., vol. 80, pp. 95–98, Aug. 2012, doi: 10.1016/j.matlet.2012.04.050.

[33] G. Ding, R. He, K. Zhang, N. Zhou, and H. Xu, "Stereolithography 3D printing of SiC ceramic with potential for lightweight optical mirror," Ceram. Int., vol. 46, no. 11, pp. 18785–18790, Aug. 2020, doi: 10.1016/j.ceramint.2020.04.196.

[34] H. Zhang, Y. Yang, K. Hu, B. Liu, M. Liu, and Z. Huang, "Stereolithography-based additive manufacturing of lightweight and high-strength C-f/SiC ceramics," Addit. Manuf., vol. 34, p. 101199, Aug. 2020, doi: 10.1016/j.addma.2020.101199.

[35] Z. Chen et al., "3D printing of ceramics: A review," J. Eur. Ceram. Soc., vol. 39, no. 4, pp. 661–687, Apr. 2019, doi: 10.1016/j.jeurceramsoc.2018.11.013.

[36] R. A. Alliegro, L. B. Coffin, and J. R. Tinklepaugh, "Pressure-Sintered Silicon Carbide," J. Am. Ceram. Soc., vol. 39, no. 11, pp. 386–389, 1956, doi: 10.1111/j.1151-2916.1956.tb15609.x.

[37] S. Suyama, T. Kameda, and Y. Itoh, "Development of high-strength reaction-sintered silicon carbide," Diam. Relat. Mater., vol. 12, no. 3, pp. 1201–1204, Mar. 2003, doi: 10.1016/S0925-9635(03)00066-9.

[38] Haswell, Stephen J., et al. "The application of micro reactors to synthetic chemistry." Chemical Communications 5 (2001): 391-398.

[39] Roberge, Dominique M., et al. "Micro-reactor technology: a revolution for the fine chemical and pharmaceutical industries?" Chemical engineering & technology 28.3 (2005): 318-323.

[40] Chen, Peter, et al. "Flash pyrolytic production of rotationally cold free radicals in a supersonic jet. Resonant multiphoton spectrum of the 3p2A2". rarw. X2A2" origin band of methyl." The Journal of Physical Chemistry 90.11 (1986): 2319-2321.

[41] Vasiliou, A.; Nimlos, M. R.; Daily, J. W.; Ellison, G. B. "Thermal Decomposition of Furan Generates Propargyl Radicals" J. Phys. Chem. A 2009, 113, 8540–8547

[42] Uchiyama et al,' Thermal Decomposition of Cyclohexene', 1964

[43] Tsang et al,'Unimolecular Rate Expression for Cyclohexene Decomposition and Its Use in Chemical Thermometry under Shock Tube Conditions', 2015

[44] Tang, Zhu Xing, Xia Zhao, Hui Hui Tan, and He Zhang. "Technology Research of Silicon Carbide by Extruding." Advanced Materials Research. Trans Tech Publications, Ltd., September 2011. https://doi.org/10.4028/www.scientific.net/amr.335-336.717.

Chapter 8: Exploring the effects of pressure and residence time on unimolecular decomposition reactions in nozzle micro-reactors

8.1 Introduction

Unimolecular decomposition reactions are a common component of the reaction mechanisms used for combustion or atmospheric systems. Each of these reactions is, in principle, both temperature and pressure-dependent [1]. Additionally, when these reactions are studied using micro-reactors where the residence time at elevated temperatures is 100 – 125 microseconds, the impact of how long the reaction occurs becomes critical. Consequently, to achieve accurate kinetic predictions of complex chemical systems, it is necessary to incorporate this pressure and indirect residence time into kinetic models[1]. This requires developing tools enabling chemical kinetic evaluations where the reaction pressure is controllable.

The pressure-dependent reaction rates primarily arise from collisional energy transfer for gas phase decomposition reactions. According to the mechanism proposed by Lindemann and Christiansen, unimolecular decomposition reactions involve the following phases[2]:

1. Collisional energy transfer between reactant (AB) and bath-gas (M) molecules

   Collisional activation $AB + M \longrightarrow AB^* + M$

   Collisional deactivation $AB^* + M \longrightarrow AB^* + M$

2. Intramolecular rearrangement

   Molecular fragmentation $AB^* \longrightarrow$ Products

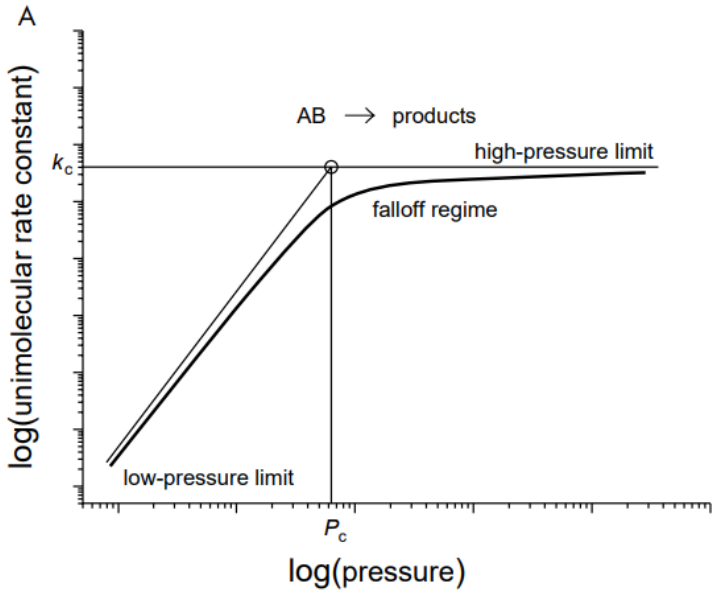

Figure 8.1: Typical pressure dependence of unimolecular reactions [2]

The rate coefficient for the overall reaction depends on bath gas pressure. This impact is due to the competition between collisional energy transfer and intramolecular rearrangement processes, producing three distinct domains of pressure dependence.

At the high-pressure limit (which depends on the reactant, temperature, and the nature of the bath gas) the number of collisions between the reactants and bath gas molecules is so large that the energy and angular momentum populations maintain an equilibrium Boltzmann distribution. Therefore, the reaction rate coefficient is pressure-independent at this high pressure, rendering information about the collisional activation and deactivation unnecessary.

At the low-pressure limit, the reactant bath gas collisions do not happen often enough for the Boltzmann distribution of energy and angular momentum to be at equilibrium. Therefore, the number of molecules with enough energy to decompose is reduced, and the rate coefficient falls under the steady state value achieved at the high-pressure limit. This results in the collisional

activation and deactivation and, in turn, the pressure to become rate-limiting or rate-influencing parameters.

At intermediate pressures, the relationship between the reaction rate coefficient of the reactant and bath gas mixture is no longer linear with changing pressure. At intermediate pressures, both collision-induced transition and decomposition rates play an important role in the kinetics. This is referred to as the 'falloff region,' a state at which an accurate evaluation of the pressure conditions of the reaction becomes critical to determining the rate parameters of the decomposition process. The ability to predict this pressure dependence of the reaction is an important part of chemical kinetic modeling and the validation of these models through experimental results [3]. Prior theoretical kinetics work has employed simple estimation models for the collisional transition rates, with parameters modified to match available experimental data[4], [5]. This simplification limits the utility of theoretical kinetics as a mechanism development tool. Empirical theories are effectively limited to interpolations and extrapolations of the pressure and temperature ranges for reactions that have already been studied experimentally[3]. Correlation of the energy transfer parameters with physical properties (e.g., molecular size, collision bath gas, reaction temperature) provides some predictive ability, but currently, such correlations are not well determined and introduce additional uncertainties in the rate estimates.

This is further complicated in the case of micro-reactor experiments where the effective pressure value experiences a strong axial gradient [6]. As described in Chapter 6, the acceleration of flow produced due to the strong differential in inlet and outlet pressures in the experimental setup obscures the accurate determination of pressure along the reactor. Additionally, Guan et al.[6] showed through computational fluid modeling simulations that the pressure varies strongly as a function of the wall temperature of the micro-reactor. This makes the accurate validation of

theoretical models using experimental data produced from these experiments challenging. To address this shortcoming, the modified nozzle reactor geometry described in Chapter 6 and fabricated using the novel processing method detailed in Chapter 7. The nozzle reactor achieves stabilization in the fluid flow profile within the reactor, making it possible to estimate the pressure inside the device. Further, compared to the tube reactor, the nozzle reactor's enhanced surface finish reduces any localized flow disruptions that improve the pressure estimation and reaction modeling.

In addition to the stabilization of fluid flow characteristics within the reactor, simulation results by T. Fan [7] showed that it is possible to ‘tune’ the pressure inside the reactor geometry by altering the exit diameter of the nozzle reactor. This was validated by producing a series of silicon carbide nozzle micro-reactors with a range of exit diameters. The following section describes the computational fluid modeling studies on these reactor geometries and experimental validation studies.

8.2 Computational Fluid Modeling (CFD) Evaluations

Table 8.1 summarizes the dimensions of the four reactors evaluated as part of the computational fluid modeling efforts. Three prototype evaluation reactors were produced featuring an internal taper with a major diameter tapering to a smaller exit diameter. All reactors feature an exit diameter of 2 mm to interface with the experimental setup described in Chapter 2. All four geometries are of the same length (28 mm) to reduce any dimensional impact on the residence time. The wall thickness of each of these geometries is also identical to ensure that the heat transfer across the walls of these reactors is also similar. These geometries are produced using the Calix High Strength 2 SiC materials system using the isostatic pressing method detailed in Chapter 7.

Table 8.1: Summary of the prototype reactor dimensions utilized as part of the micro-reactor validation studies.

Reactor Type	Major Diameter	Exit Diameter	Length	Transition Length
Tube Reactor (Chen)	1 mm	1 mm	28 mm	-
Nozzle Reactor (P1650)	1 mm	0.650 mm	28 mm	1.5 mm
Nozzle Reactor (P1400)	1 mm	0.400 mm	28 mm	1.5 mm
Nozzle Reactor (P1200)	1 mm	0.200 mm	28 mm	1.5 mm

The validation of fluid flow behavior within the manufactured reactors was carried out using ANSYS FLUENT using the method described in Chapter 6 and detailed in work by T. Fan. [7] FLUENT[8] is a commercially available CFD package that enables modeling across a range of cases from applicable cases from uncompressible to highly compressible flow. The choice of FLUENT was motivated by the convergence speed and accuracy of the tool, in addition to reducing any software-based inconsistencies with previously calculated values. The use of the inbuilt meshing tool further reduced computational time and improved solution consistency across runs.

A simplified reactor geometry was developed to simulate fluid flow behavior upstream of the reactor as well as the region downstream of the reactor. A representation of the reduced MESH geometry is shown in Figure 8.2.

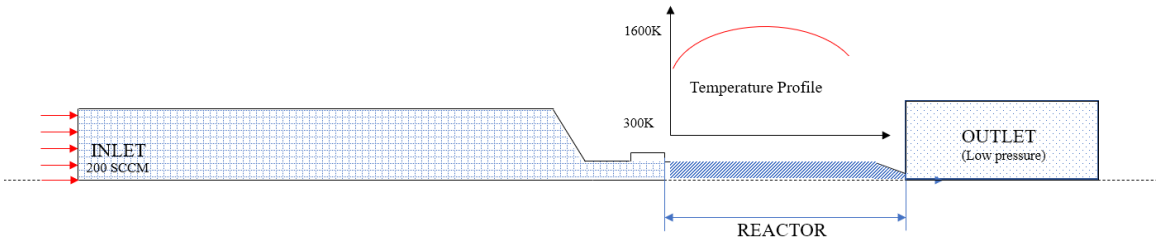

Figure 8.2: MESH geometry generated using SpaceClaim in ANSYS to model flow into the reactor geometry. Average mesh sizes at all regions outside of the reactor is 0.15 mm with the reactor mesh size at 0.01 mm

The geometric dimensions of these spaces are chosen to be large enough that they accurately capture fluid flow features before and after the reactor while being small enough to be computationally cost-effective. The geometry is defined to be axis-symmetric to ensure that all critical measurements are made along the axis of the reactor. The mesh generated features a 0.3 mm node size, with the grid dimensions decreased to 0.1 mm at the reactor location to produce more accurate results. The inlet boundary conditions are specified downstream of the reactor geometry, with the outlet set at the exit of the reactor. The inlet conditions are defined through a flow rate value of 3.527 e-7 kg/s of helium. This translates to a volumetric flow rate of 200 sccm, miming actual experimental conditions where at least 99.9 % of all the fluid entering the reactor by volume is helium. A temperature profile is applied to the exterior wall of the reactor with the peak temperature set at 1600K. A plot of the variation in internal wall temperature as a function of axial length is inset in Figure 8.2.

Simulations were carried out with the reactor material conditions defined per the specifications of the Calix High Strength 2 SiC system. The standard energy transfer model is employed with the total energy calculated as a sum of the internal, kinetic, and potential energy. The energy equation is solved by the application of the standard equation of state and thermodynamic relations. Calculations are made while treating the helium flowing through the system as an ideal gas with

the viscous model set to laminar flow. At the inlet, pressure is defined by the inlet flow rate with a temperature of 300 K to simulate experimental conditions. The outlet of the reactor is set to mimic the very low-pressure conditions of the experiment by choosing a pressure value of -999 Pa.

Initial simulations were used to validate the results obtained against the work of T. Fan. This was accomplished through the creation of a test geometry featuring an exit diameter of 0.100 mm with an inlet flow rate of 8.4 e-7 kg/s. With this complete, the four reactor geometries in Table 1 were evaluated for the pressure within the reactor as well as the velocity of fluid flow. A comparison of the pressure from the inlet to the outlet is shown in Figure 8.3, with pressure in torr along the y-axis and the centerline axial length. From the plot, it is observed that there is a stabilization in the fluid pressure at approximately 3 cm from the inlet of the reactor. This stabilization continues till roughly the center of the transition to the reduced diameter exit, where there is a steep drop-off in pressure. The stable pressure increases with a reduction in the exit diameter of the reactor, with the P1200 (with a 0.200mm) exit diameter showing the highest stabilized pressure of 80 torr at the inlet of the reactor. The pressure at the inlet of the P1400 nozzle reactor is at 55 torr with the P1650 nozzle reactor at 42 torr.

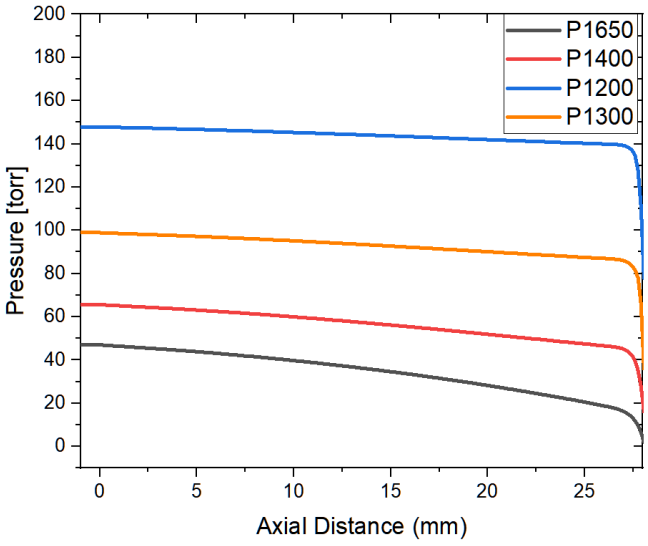

Figure 8.3: Comparison of pressure as a function of axial length between four nozzle reactor geometries evaluated P1650 (0.650 mm exit diameter), P1400 (0.400 mm exit diameter), P1300 (0.300 exit diameter) and P1200 (0.200 exit diameter)

The pressure at the inlet of the P1200 nozzle reactor is about twice the inlet pressure of the Chen reactor (with an inlet pressure is about 46 torr). This is shown in Figure 8.4. At approximately midway through the geometry, pressure in the P1200 nozzle reactor is at 135 torr as compared to the Chen reactor, where the pressure is at 35 torr.

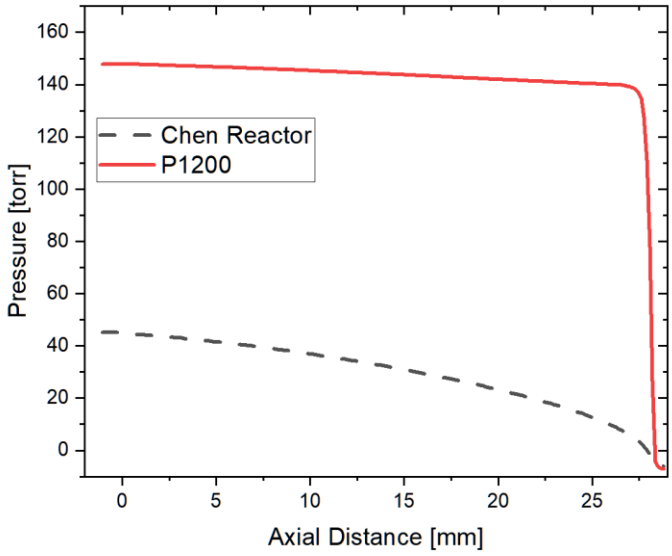

Figure 8.4: Comparison of pressure as a function of axial length between the nozzle reactor geometry P1200 and the Chen reactor (tube configuration)

A similar evaluation of the velocity was carried out to show the stabilized velocity profiles for fluid in the nozzle reactor geometries. A consequence of the reduced diameter of the exit of the reactor is the lowering of the stabilized velocity profile in the reactor. The velocity stabilization is achieved approximately at the same location as the pressure stabilization, indicating a zone of uniform properties within the reactor at which the pressure, velocity, and residence times can be evaluated as a function of temperature. At the inlet, the velocity is at its lowest in the case of the P1200 reactor at an average value of 110 m/s, with the highest being for the P1650 reactor at an average value of 417 m/s. The velocities ramp up at approximately midway through the transition region before reaching the hypersonic speeds in the case of the P1200 at the outlet. A comparison of the velocities is shown in Figure 8.5.

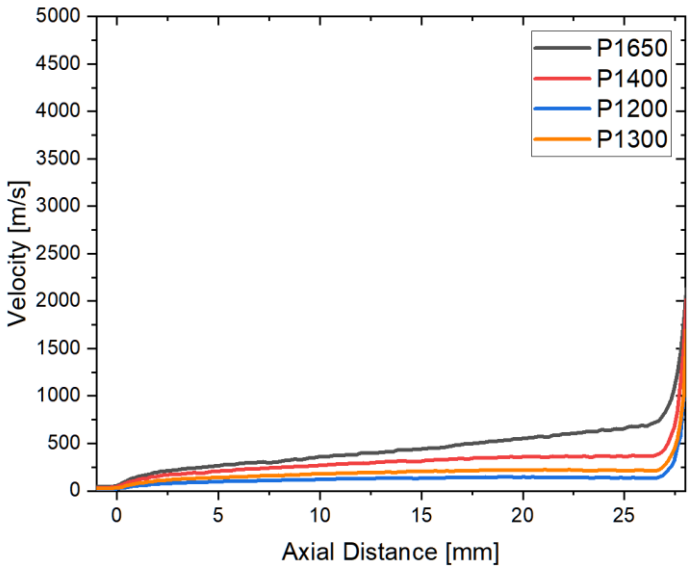

Figure 8.5: Comparison of velocity as a function of axial length between four nozzle reactor geometries evaluated P1650 (0.650 mm exit diameter), P1400 (0.400 mm exit diameter), P1300 (0.300 exit diameter) and P1200 (0.200 exit diameter)

A comparison of velocity profiles between the P1200 reactor and the Chen reactor shows the dramatic rise of velocity in the case of the Chen reactor. This is in direct contrast to the nozzle reactor, where the velocity is stabilized at a value of m/s through most of the reactor. This is shown in Figure 8.6.

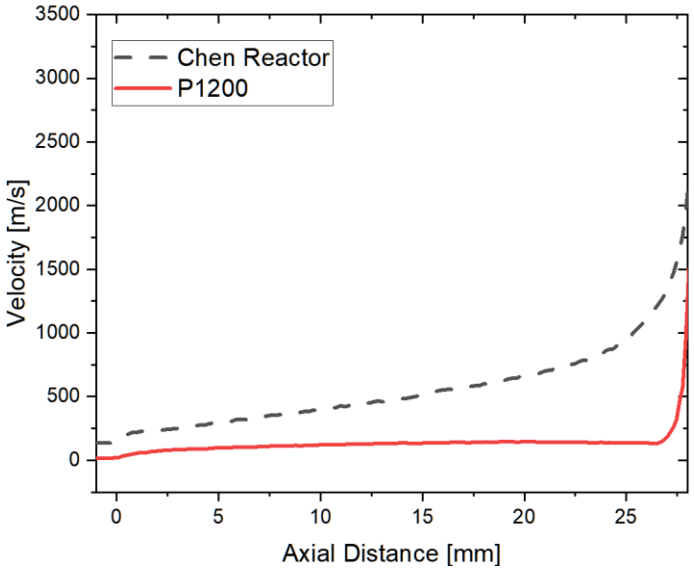

Figure 8.6: Comparison of velocity as a function of axial length between the nozzle reactor geometry P1200 and the Chen reactor (tube configuration)

An important consequence is an increase in the residence time of the fluid within the reactor. This is due to the reduced velocity of the fluid in the system because of the flow being 'throttled' by the presence of the constriction at the exit. Figure 8.7 shows the variation of fluid residence time as a function of varying exit diameters. These results were simulated at 1600K reactor wall temperature with the inlet flow conditions at 200 sccm of helium. The residence time increases non-linearly with reducing exit diameter. The fluid is slowest in the P1200 reactor at 290 microseconds and fastest in the Chen reactor at 115 microseconds.

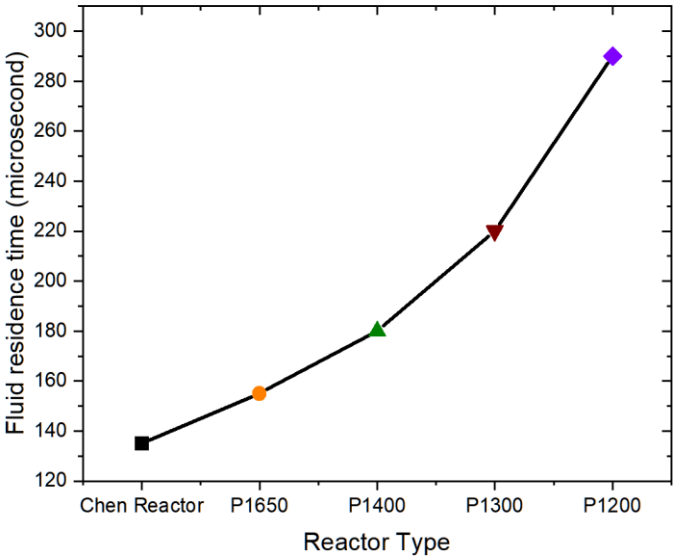

Figure 8.7: Variation of fluid residence time in the nozzle reactor as a function of the exit diameter (P1650 (0.650 mm exit diameter), P1400 (0.400 mm exit diameter), P1300 (0.300 exit diameter) and P1200 (0.200 exit diameter)

These simulations highlight the presence of a stable fluid flow region within the reactor where the pressure, velocity, and temperature within the system can be ascertained through simulation results. These are important parameters in the validation of chemical kinetic models, which rely on experimental data to produce mechanisms that can be scaled to predict complex molecular behavior across a range of conditions. The ability to vary the experimental pressure and temperature by changing the reactor geometry provides experimentalists with a facile tool to study the effects of these conditions on fundamental decomposition chemistry.

8.3 Experimental validation of nozzle reactors using photoionization mass spectrometry

The impact of varying the pressure within the micro-reactor geometry was evaluated using the photoionization mass spectrometry setup on multiple chemical systems. Molecules were chosen

such that there was an observable difference in their unimolecular decomposition or secondary reaction within the pressure and residence time range provided by the three nozzle reactors in comparison to the Chen reactor.

8.3.1 Anisole

Anisole is an important fuel additive that has been demonstrated to reduce the emissions produced in diesel engines, with a 10% anisole–diesel blends producing much lower emissions as compared to neat diesel in a study carried out by Zhou et al. [9]. Tian et al.[10] demonstrated the effective increase in octane number of gasoline when blended with anisole and other lignin-based aromatics. Anisole is a key component of biomass pyrolysis fuels, forming the feedstock for a range of biofuels[11]. It is among the simplest chemical systems that can be used to simulate the decomposition behavior of lignocellulosic biomass in an experimental setup. Additionally, anisole has been identified as an important source for forming numerous reactive intermediates linked with the creation of polycyclic aromatic hydrocarbons (PAHs)[12]. The formation of these PAHs has been the focus of numerous studies for their role in the formation of soot across combustion processes[13], [14].

The generation of the first aromatic ring is a vital step in the formation of PAHs, and the reactive chemistry of resonantly stabilized radicals plays a role in this process[15]. Radicals such as propargyl and cyclopentadienyl are stable under extreme pressure and temperature conditions, allowing them to remain in combustion environments[11]. This results in a significant build-up of these species, thereby influencing the chemistry of these combustion systems. The presence of a weak O-CH_3 bond makes anisole an ideal candidate for evaluating the chemistry of phenoxy, cyclopentadienyl, and propargyl radicals[12].

Previous evaluations have focused on understanding anisole combustion, including the evaluation of rate constants, species profiles, and global combustion parameters. Lin and Lin [16] determined the rate constant for the decomposition of anisole to cyclopentadienyl radical and CO by studying decomposition reactions in the temperature range of 1000-1580K and pressures 0.4 – 0.9 atm. This study highlighted the formation of *ortho*- and *para*-cresols as isomers of toluene at room temperature. Mackie et al. [17] demonstrated that most of the oxygen remains bound to the phenol and cresol after pyrolysis and not in the CO. This result was arrived at by studying pyrolysis between 850-1000K and 0.16 – 1.2 atm pressure. Arends et al.[18] developed the reaction mechanism for the thermolysis of anisole in a hydrogen atmosphere using a flow reaction at temperatures of 793-1020K. In 1997, Pecullan et al. [19] developed a primary reaction mechanism for the decomposition of anisole and validated it against flow reactor pyrolysis and oxidation experiments at atmospheric pressure and a temperature of 1000K. A comprehensive kinetic study of the decomposition and pyrolysis of anisole was carried out by Nowakowska et al.[20] through the creation of a mechanism built on the oxidation of ethylbenzene studied by Husson et al.[21] The main decomposition occurs by the formation of phenoxy radicals, and stable main products are phenol, methane, CO, benzene, and hydrogen. In 2018 Wagnon et al.[22] presented a new mechanism for anisole and validated it through experimental pyrolysis and oxidation studies of anisole in a jet-stirred reactor at atmospheric pressure and 675-1275 K. Yuan et al.[11] also carried out a comprehensive modeling and experimental evaluation of anisole using a flow reactor at 0.04 atm and 1 atm between 850 and 1160 K using a synchrotron vacuum ultra-violet photoionization diagnostic. The study proposed that at lower temperatures, the phenoxy radical is mainly consumed via recombination with methyl radical, producing methyl-cyclohexadienone. As the temperature is raised, decomposition is dominated by the breakdown of phenoxy radical to cyclopentadiene

and carbon monoxide. Bierkandt et al.[23] investigated flame structures of premixed anisole fames using photoionization mass spectrometry and photoelectron spectrometry at two synchrotron sources where tunable vacuum-ultraviolet radiation enables isomer-resolved photoionization. This study concluded that there are three main routes to the destruction of anisole, first, the formation of benzaldehyde at lower temperatures and in leaner flames; second, the formation of phenol, and the unimolecular decomposition to phenoxy and methyl radicals.

In 2001, Friderichsen et al.[24] used the Chen reactor to pyrolyze anisole to understand the decomposition pathways that lead to the formation of known soot precursors in the form of cyclopentadienyl radical and propargyl radical. This study also identified the formation of 9,10 – dihydrofulvalene, the adduct of the reaction of two cyclopentadienyl radicals, in addition to the formation n of naphthalene, confirming the successive reactions to form PAHs. This was followed up by an investigation of anisole pyrolysis by Scheer et al. [12] using photoionization mass spectrometry and resonance-enhanced multiphoton ionization (REMPI) techniques and a Chen micro-reactor. This study showed that benzene formation as a secondary bimolecular reaction product was likely due to methyl radical, and cyclopentadienyl radical reaction compared to direct propargyl recombination.

Investigating the pressure dependence of this bimolecular route to the formation of benzene is a critical step to understanding the influence of combustion conditions on forming PAHs. For the first time, the nozzle reactors enable the investigation of these reactions' pressure dependence by changing the geometry's exit diameter. The likely effects of varying the pressure and providing a stable reacting environment will provide valuable experimental results which can be used to validate chemical kinetic models. Additionally, a deeper understanding of the temperature dependence of the intermediate steps in the decomposition and recombination reactions is of

crucial interest because propargyl radical, cyclopentadienyl radical, and phenoxy radical are important precursors for the formation of PAHs and hence soot.

8.3.1.1 Experimental methods

Pyrolysis experiments were carried out using the nozzle reactor P1650 and P1400, along with comparison runs with the Chen reactor in conjunction with the photoionization mass spectrometry for species detection. Experimental details and the process have been described in Chapter 2. In brief, anisole is studied by entraining a dilute sample of the compound in helium. The following compounds were analyzed – anisole (Sigma Aldrich, > 98% purity), anisole d3 (Sigma Aldrich, > 97% purity), and anisole d8 (Sigma Aldrich, >97% purity). The vapor pressure of these compounds is large enough for mixtures in the concentration range of 0.1%, 0.05%, and 0.025% in helium could be prepared manometrically in standard lecture bottles. The sample mixture flows into the experimental setup and the reactor through an MKS 4B01 series mass flow controller.

The micro-reactor assembly consists of the chosen SiC micro-reactor of 30 mm length with a 1 mm inner diameter. The reactor is resistively heated to 1800K through Carbon discs fitted to the reactor's outer diameter. These discs are approximately 15 mm apart and form the contact points for the electrical circuit used to resistively heat the reactor. The reactor material is chosen for its ability to withstand very high temperatures and thermal cycling while remaining inert and not participating in any of the pyrolysis reactions. The temperature at the exterior surface of the reactor is monitored by a TIM Microtek thermal camera between the two heating points (details of the camera and the measurement process are provided in Chapter 2).

In the PIMS experiment, gases flow continuously through the reactor with the products exiting the reactor entering a 0.2 mm diameter molecular beam skimmer. The resulting beam is

intersected and ionized by the 9th harmonic of a Nd:YAG laser (118.2 nm or 10.487 eV). The laser is aligned with the flow entering an ionization chamber maintained at 5 X 10-7 torr by a 1200 L/s Pfieffer TPU 1201 P turbomolecular pump. The internal frequency tripled output of a Nd:YAG laser is directed into a cell that is pressurized to 150 Torr with a 10:1 argon:xenon mixture. This mixture is optimized to promote sum frequency generation that creates 118.2 nm VUV photons, which have sufficient energy to ionize most hydrocarbons molecules. The generation of 118.2nm photons by Xe/Ar tripling cells has been studied at great length. Use of 30 mJ pulse per pulse power at 355 nm from the YAG laser and the established tripling efficiency of 1×10-5 in pure Xenon as well as the transmission efficiency of the MgF2 lens, we expect to produce roughly 30 nJ per pulse at 118.2 nm light. Post ionization, the molecules in the expansion are accelerated into a Jordan reflectron time of flight spectrometer with a Micro Channel Plate (MCP) detector producing voltage signals which are converted to digital traces in an interfacing computer. This data is converted into a spectra format and is analyzed for the decomposition products.

8.3.1.2 Experimental results

The experimental spectra obtained for the decomposition of 0.1% anisole in helium in the Chen reactor are presented first, followed by the results at the same concentration using the nozzle reactor. The spectra from the evaluations are presented in Figure 8.8. Along the y-axis, signal intensity in arbitrary units is shown with the mass over charge m/z shown in the x-axis. Results are presented at six different temperatures – 300 K (room temperature), 900 K, 1200K, 1400K, 1600K and 1800K. At room temperature, the parent peak is visible at m/z 108, with the C_{13} peak at m/z 109. The molecule shows very little dissociative ionization, as no other major fragmentation peaks are visible at this temperature. As the temperature is raised to 900 K, the parent molecule remains stable inside the Chen reactor, and no fragmentation is observed. There is an increase in

the signal intensity of the parent molecule at m/z 108, this is attributed to the low-temperature isomerization of anisole to cresol (which has a slightly higher ionization cross section as compared to anisole), this is consistent with the flow reactor and synchrotron experiments by Yuan et al. [11]. The first signs of decomposition are observed at 1200K when a peak is seen at m/z 93. This corresponds to the formation of phenoxy radical (m/z 93) after the cleavage of the carbon-oxygen bond in the O-CH_3 group of anisole. This reaction (R1) is shown below:

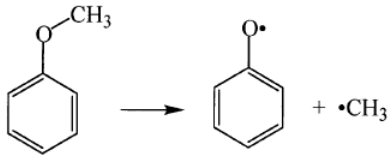

(1)

The formation of phenols is due to the recombination of phenoxy radicals with H-atoms present in the system. This has been shown as a likely recombination pathway in work by Bierkandt et al. [23] and Yuan et al. [11]. However, this is not reported in the previous work by Friderichsen et al. [24] or Scheer et al. [12]. A likely explanation for this could be the increasing likelihood of picking up H-atoms in a continuous flow system as compared to the pulsed valve system used previously at CU Boulder. As temperature increases further to 1400K, anisole undergoes secondary decomposition to produce cyclopentadienyl radical (CPDR) (m/z 65) and CO through reaction R2.

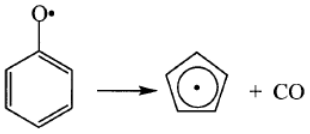

(2)

Carbon monoxide is not visible in this experiment as its ionization energy is greater than what is produced by the fixed wavelength source used in this experiment. The presence of CO, however, has been confirmed previously by Friderichsen et al. [24], Yuan et al. [11], and Bierkandt et al. [23] using the Matrix FTIR experiment and synchrotron ionization sources. At temperatures beyond 1600K, CPDR further decomposes into propargyl radical (m/z 39) and acetylene (m/z 26)

(not visible due to a high IE of). The energy barrier of this reaction was calculated to be about 62.3 kcal/mol by Moskaleva et al. At these elevated temperatures, a recombination reaction occurs between the CPDR and methyl radical to form methylcyclopentadiene (MCPD) (m/z 80).

This reaction is noted in Scheer et al. [12] as being an important route to the formation of high molecular weight precursors to PAH growth through anisole breakdown. The formation of MCPD is also affected by concentration, with the high concentration runs in the Chen reactor showing a larger amount of MCPD followed by the high-temperature decomposition of this molecule to benzene (m/z 78).

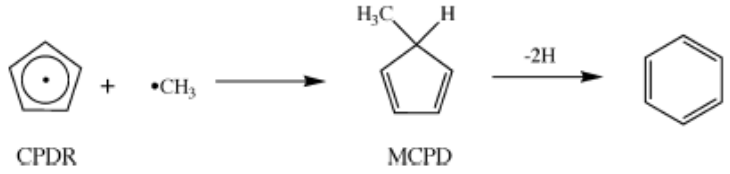

(3)

At temperatures beyond 1600K, nearly all the CPDR is consumed by decomposition reactions to produce propargyl and acetylene, as well as alternative recombination routes featuring diacetylene (m/z 50) and diacetylene (m/z 52)

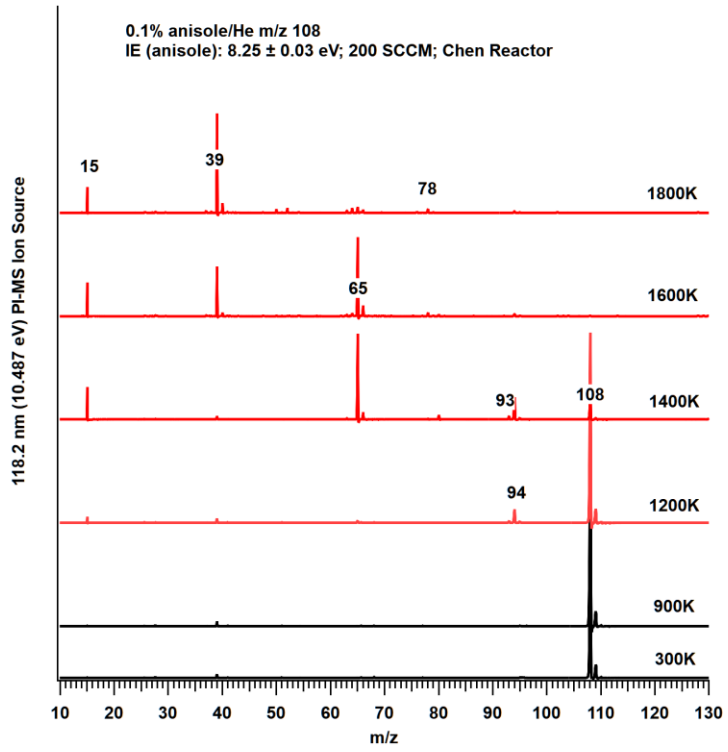

Figure 8.8: PIMS of 0.1% anisole in He in the Chen micro-reactor at 200 SCCM heated from 300 to 1800 K and ionized by 118.2 nm (10.487 eV) photons

A similar series of peaks is observed during the decomposition of acetylene in the P1650 nozzle reactor, at 0.1%, the signal intensities are much higher in the nozzle reactor. This is likely due to the variation in expansion produced at the exit of the nozzle reactor. The 0.650 mm constriction at the exit of the reactor is responsible for stabilizing and raising the pressure inside the reactor. At the elevated pressures of the P1650 nozzle, a higher degree of decomposition is observed at lower relative temperatures to the nozzle reactor. At 1200K, relative peak heights are much larger, with a greater degree of decomposition of the parent molecule (m/z 108). Also observed is a strong peak at m/z 80 corresponding to the recombination of CPDR (m/z 65) and methyl radical (m/z 15) through reaction R3. At 1400K, the presence of a sharp peak at m/z 39 (propargyl radical) is observed, along with a peak at m/z 40 (propyne) is observed. The presence of propyne is attributed to the decomposition of phenol (m/z 94) into 1,4 butadiene (m/z 54) and

propyne. As the temperature is raised, successive decomposition reactions to produce benzene (m/z 78) are noted from the MCPD (m/z 80) through the loss of 2 hydrogen atoms. This is an important reaction due to the link between benzene as a known soot precursor and the relation between the successive decomposition reactions to the elevated pressure within the reactors. At 1800K, only the secondary decomposition and recombination peaks remain, with a sharp peak at m/z 78, confirming the high-temperature stability of benzene and benzyne radicals. The spectra from the evaluations are presented in Figure 8.9.

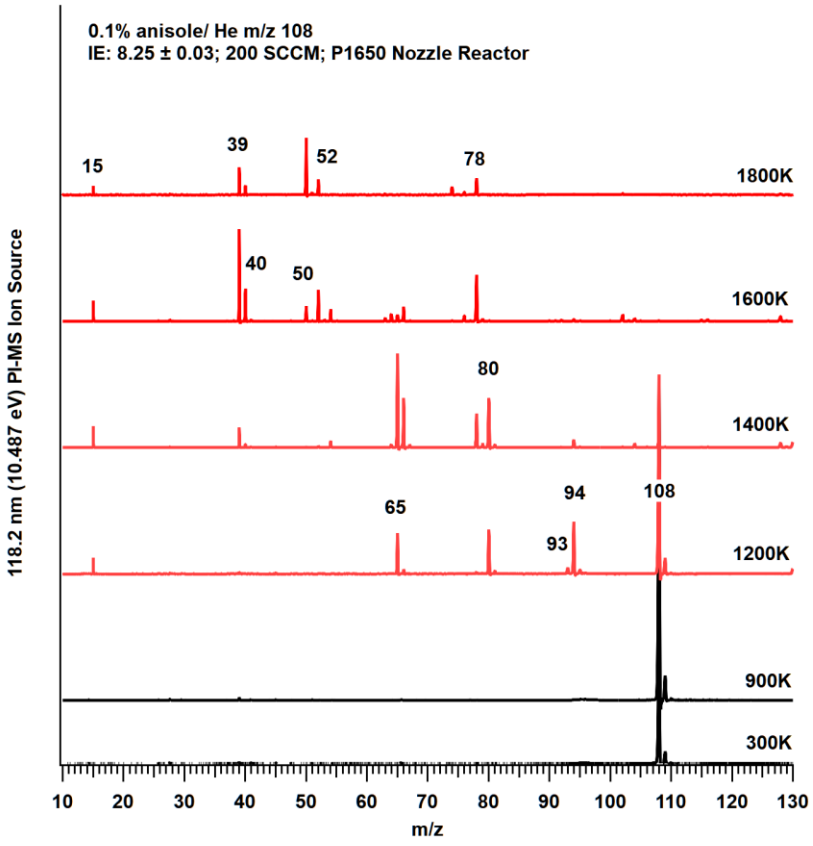

Figure 8.9: PIMS of 0.1% anisole in He in the P1650 nozzle micro-reactor at 200 SCCM heated from 300 to 1800 K and ionized by 118.2 nm (10.487 eV) photons

The recombination of propargyl radicals (m/z 39) to benzene (m/z 78) has been studied extensively as a possible contributor to the formation of polycyclic aromatic hydrocarbons (PAHs). This was probed as a possible route to explain the increased signal fraction of benzene in the

spectra m/z 78. Scheer et al.[12] studied the decomposition of high concentrations of propargyl bromide in the Chen reactor to map the contribution of propargyl recombination to form benzene. Results from these experiments confirmed that this was not a direct route to the formation of benzene in the short residence time and lowered pressure conditions of this system. Additionally, in the nozzle reactor setup, the formation, and consumption of MCPD (m/z 80), provides a more likely direct route to the formation of benzene (m/z 78). A comparison of the normalized signal intensity is shown in Figure 8.10.

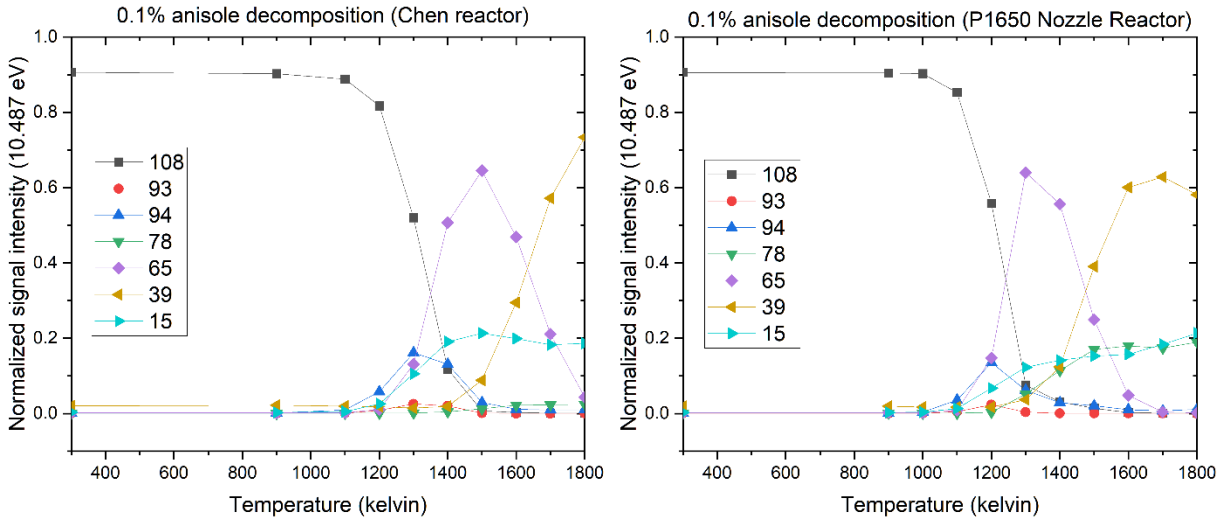

Figure 8.10: Normalized signal height for the decomposition of 0.1% anisole as a function of temperature in the Chen reactor (on the left) and the P1650 nozzle reactor (on the right)

A series of concentration evaluations were conducted using the Chen reactor and P1650 nozzle reactor to understand the impact of concentration on the decomposition pathways and recombination reactions. The decomposition of 0.05% anisole in helium was studied through the Chen reactor, and the spectra obtained in shown in Figure 8.11. At lower concentrations, the signal intensity reduces, along with the formation of MCPD (m/z 80) at increased temperatures beyond 1400K. Due to the lower number of collisions experienced at this condition, the concentration of reactants is shown to play an important role in the formation of recombination products and hence

soot precursors. In contrast to this, the recombination reactions in the P1650 nozzle reactor (spectra shown in Figure 8.12) continue to occur, indicating that at the stabilized pressures in these reactors, the formation of MCPD (m/z 80) and benzene (m/z 78) continues.

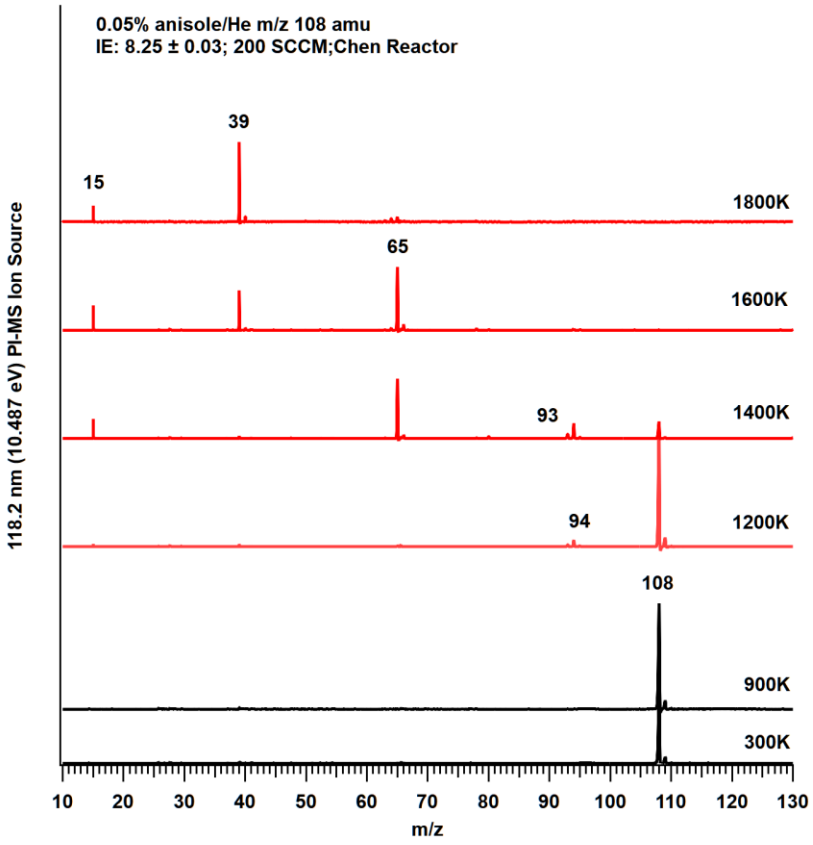

Figure 8.11: PIMS of 0.05% anisole in He in the Chen micro-reactor at 200 SCCM heated from 300 to 1800 K and ionized by 118.2 nm (10.487 eV) photons

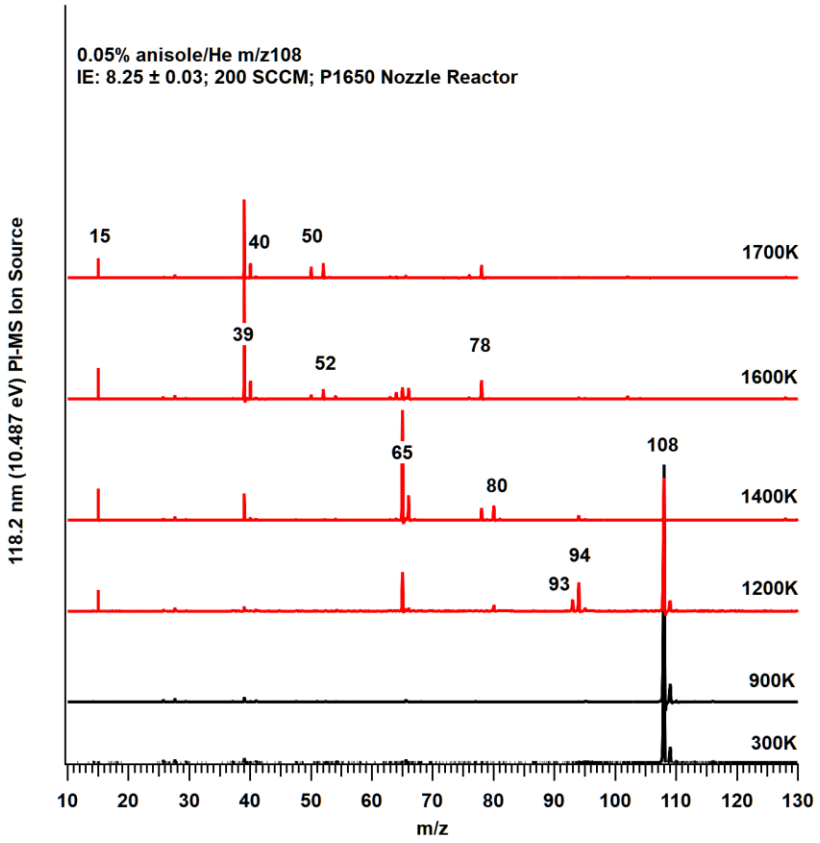

Figure 8.12: PIMS of 0.05% anisole in He in the P1650 nozzle micro-reactor at 200 SCCM heated from 300 to 1800 K and ionized by 118.2 nm (10.487 eV) photons

A comparison of the normalized signal heights between the two reactors indicates that in the Chen reactor at 0.1% of anisole, the amount of benzene (m/z 78) produced is 2% of the total signal, as compared to nearly 18% in the P1650 nozzle reactor. The fraction of benzene formed at 0.05% reduces proportionate to the change in concentration in the case of the Chen reactor at about 1 % of the total signal, but the change is less significant in the case of the nozzle reactor at a maximum of 12%. This is shown in Figure 8.13.

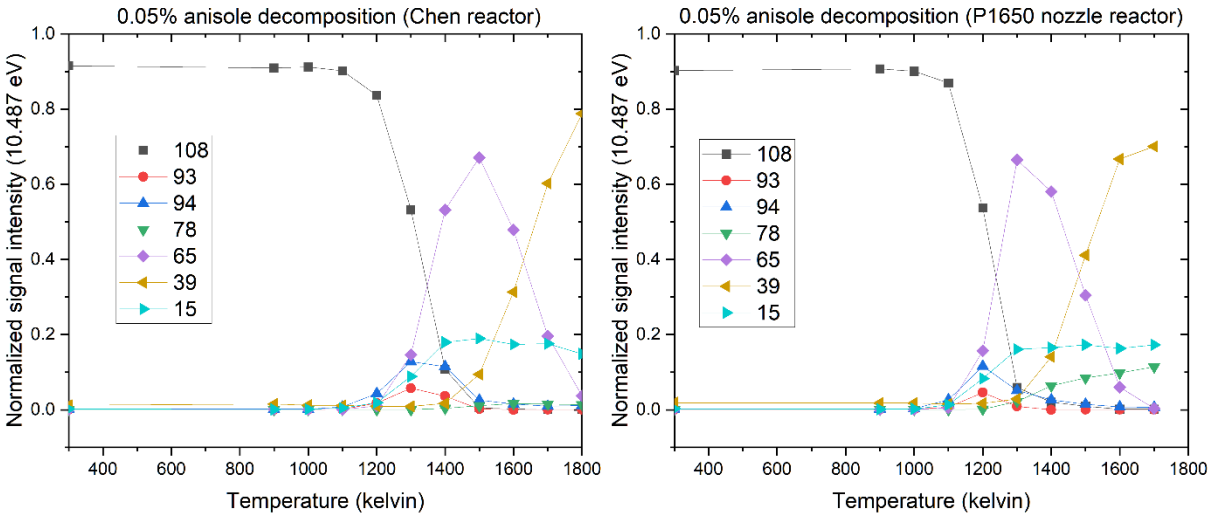

Figure 8.13: Normalized signal height for the decomposition of 0.05% anisole as a function of temperature in the Chen reactor (on the left) and the P1650 nozzle reactor (on the right)

A further reduction in concentration was used to confirm the trends observed previously between the 0.1% and 0.05% runs. At this reduced concentration (0.025%), the amount of benzene formed dropped by a factor of 2 (linearly) with a reduced concentration of 0.05% of the total signal. In the case of the P1650 reactor, the reduction was 4% of the total signal height. The PIMS spectra for the Chen reactor and P1650 nozzle reactor are shown in Figure 8.14 and Figure 8.15, respectively.

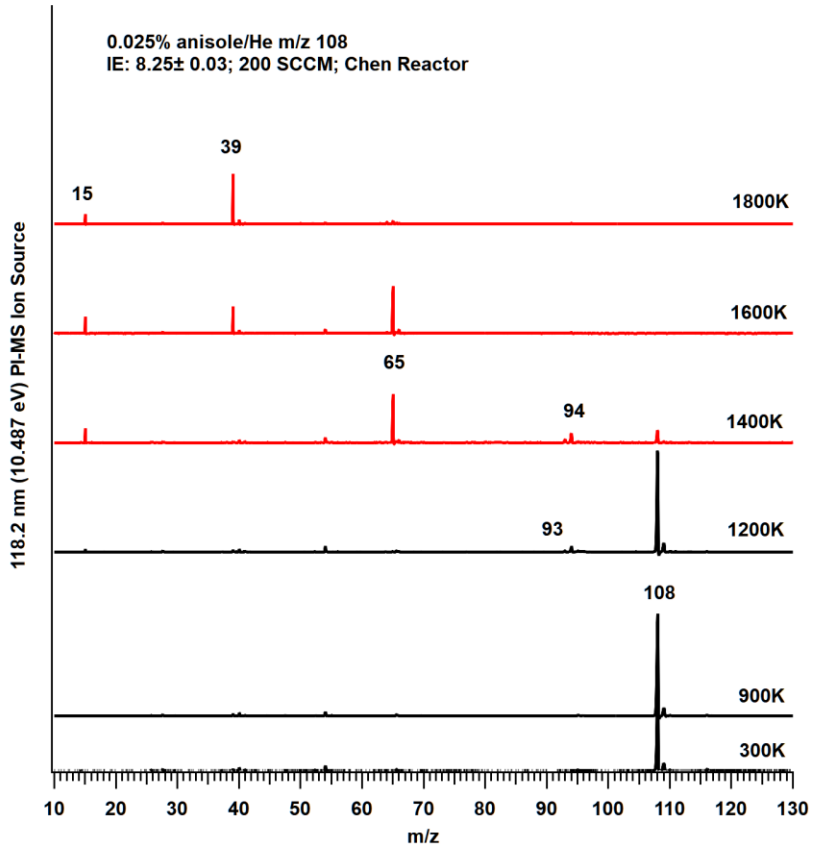

Figure 8.14: PIMS of 0.025% anisole in He in the Chen micro-reactor at 200 SCCM heated from 300 to 1800 K and ionized by 118.2 nm (10.487 eV) photons

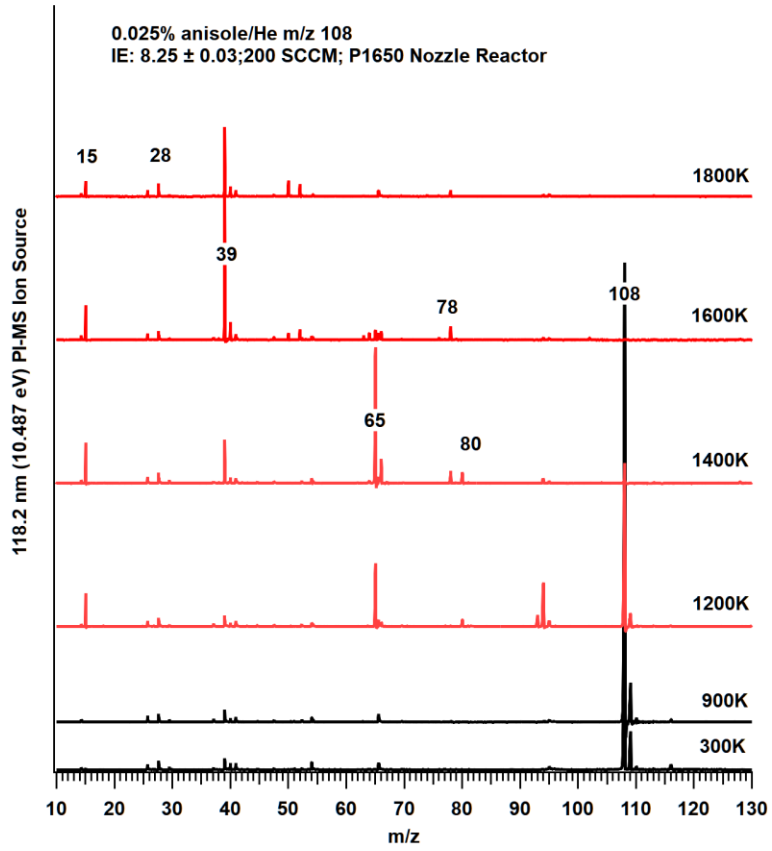

Figure 8.15: PIMS of 0.025% anisole in He in the P1650 nozzle micro-reactor at 200 SCCM heated from 300 to 1800 K and ionized by 118.2 nm (10.487 eV) photons

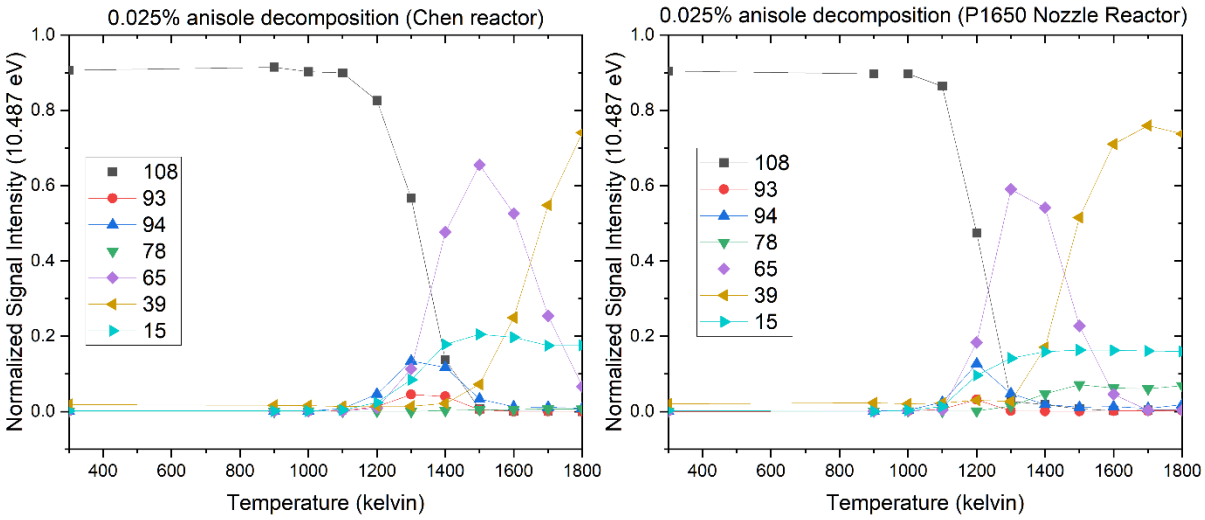

Figure 8.16: Normalized signal height for the decomposition of 0.025% anisole as a function of temperature in the Chen reactor (on the left) and the P1650 nozzle reactor (on the right)

In addition to the Chen reactor and P1650 nozzle reactor, experiments were conducted with the P1400 nozzle reactor. This geometry features a smaller exit diameter of 0.400 mm. This results in a higher stabilized pressure in the reactor coupled with an increased residence time. The spectrum obtained from experiments with 0.025% anisole in helium using the P1400 nozzle reactor is shown in Figure 8.17. A comparison of the percentage of benzene (m/z 78) in the decomposition products indicates values in the range of 15 – 25 %, almost double the values seen in the P1600 reactor. A larger fraction of benzene indicates that the increased stabilized pressure and residence time in the P1400 reactor system encourages recombination reactions between CPDR and methyl radical to produce MCPD, which can then decompose at higher pressures to form benzene (m/z 78).

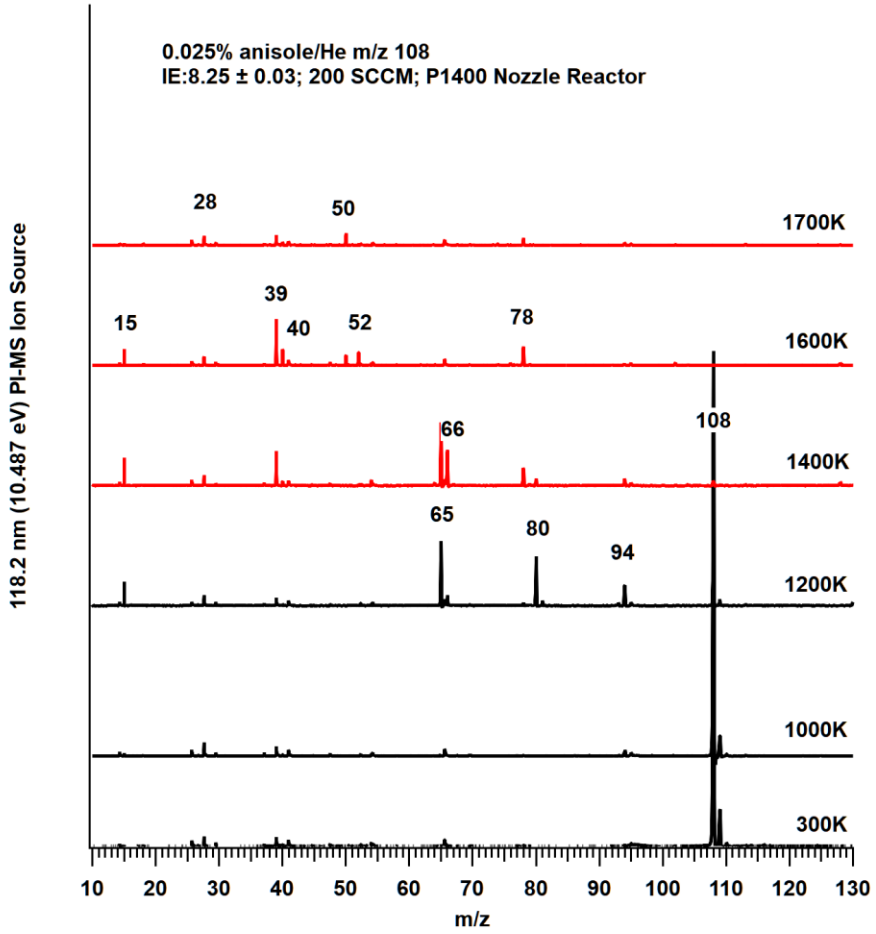

Figure 8.17: PIMS of 0.025% anisole in He in the P1400 nozzle micro-reactor at 200 SCCM heated from 300 to 1800 K and ionized by 118.2 nm (10.487 eV) photons

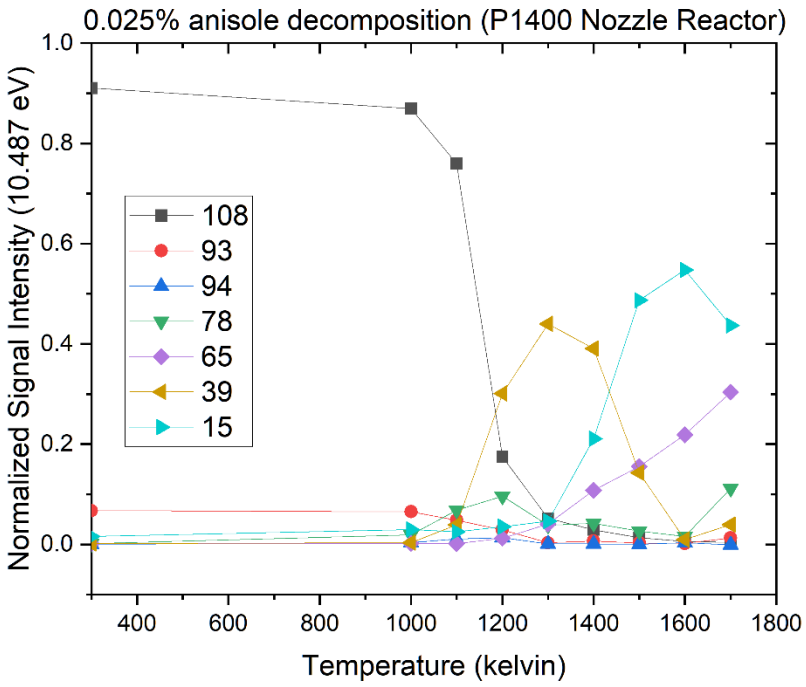

Figure 8.18: Normalized signal height for the decomposition of 0.025% anisole as a function of temperature in the P1400 nozzle reactor (on the right)

Photoionization mass spectrometry (PIMS) experiments were carried out using the Chen reactor and nozzle reactor (P1650 geometry), to study the pyrolysis of two deuterated anisole isomers. The PIMS spectra for the decomposition of 0.1% d3-anisole using the Chen reactor and P1650 nozzle reactor are shown in Figure 8.19 and Figure 8.20. As expected, the primary decomposition and recombination reactions are the same in the case of d3-anisole. The peaks at m/z 94, 93, 65, and 39 are not shifted due to the analogous routes to non-deuterated anisole. The parent d3-anisole and methyl radical peaks are shifted three units with additional peaks at m/z 15 corresponding to alternate decomposition routes of smaller primary pyrolysis fragments. Also of note is the presence of a sharp peak at m/z 83 in the case of the nozzle reactor, confirming the recombination of d3-methyl group with the cyclopentadienyl radical to form an adduct which then decomposes to form partially deuterated ring-like structures.

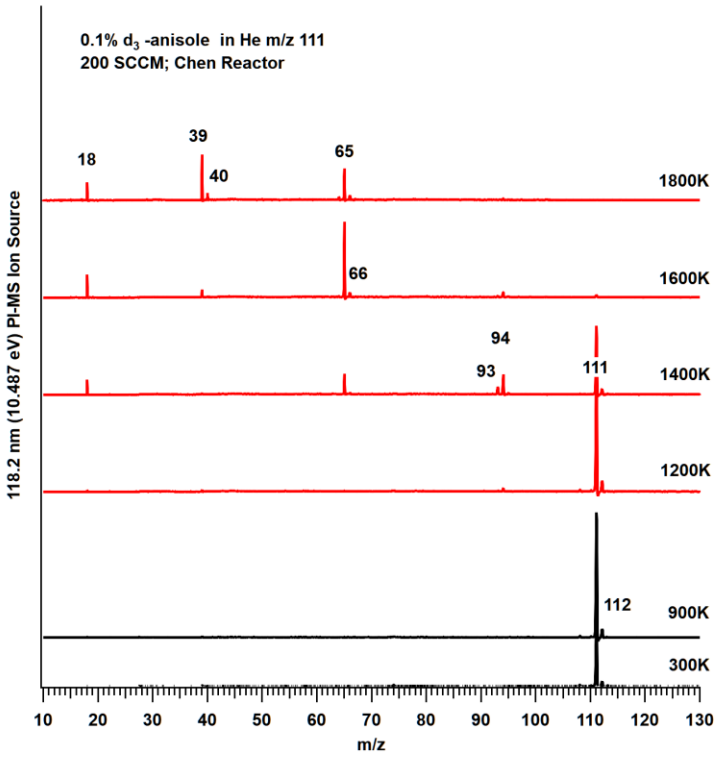

Figure 8.19: PIMS of 0.1% d3-anisole in He in the Chen micro-reactor at 200 SCCM heated from 300 to 1800 K and ionized by 118.2 nm (10.487 eV) photons

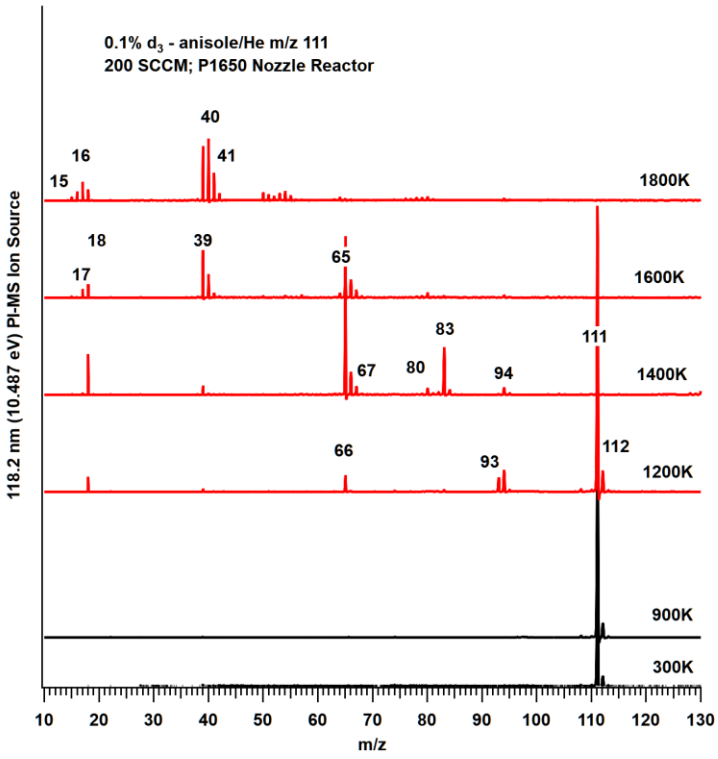

Figure 8.20: PIMS of 0.1% d3-anisole in He in the P1650 nozzle micro-reactor at 200 SCCM heated from 300 to 1800 K and ionized by 118.2 nm (10.487 eV) photons

In the case of d_8 anisole, each peak is shifted as expected according to complete deuteration. Spectra from 0.1% d_8-anisole in the Chen reactor and P1650 nozzle reactor are shown in Figure 8.21 and Figure 8.22.

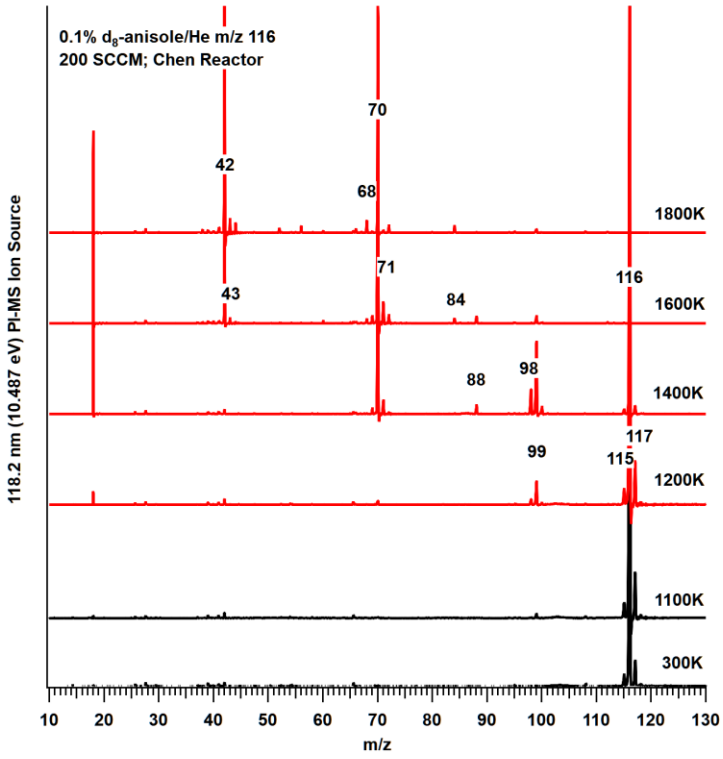

Figure 8.21: PIMS of 0.1% d8-anisole in He in the Chen micro-reactor at 200 SCCM heated from 300 to 1800 K and ionized by 118.2 nm (10.487 eV) photons

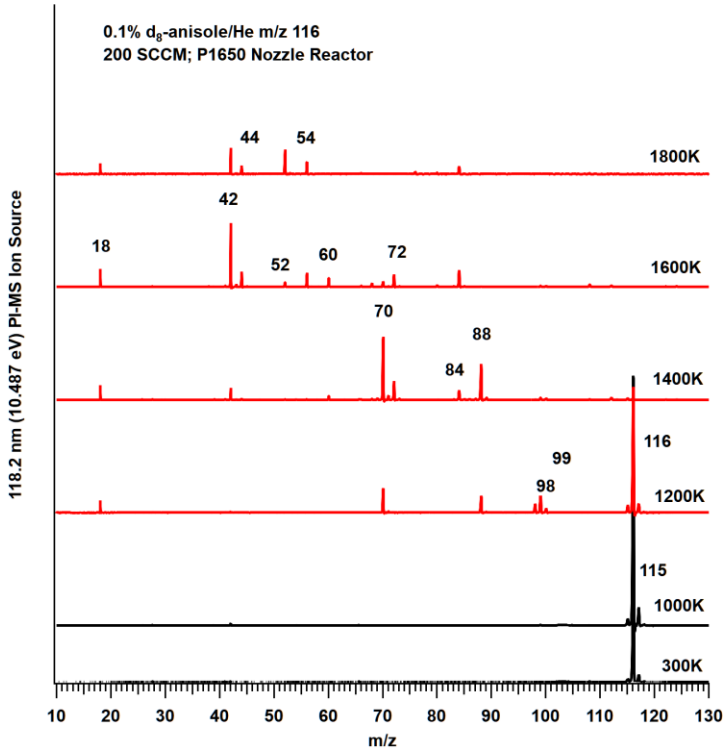

Figure 8.22: PIMS of 0.1% d8-anisole in He in the P1650 nozzle micro-reactor at 200 SCCM heated from 300 to 1800 K and ionized by 118.2 nm (10.487 eV) photons

8.3.2 Furan

The requirement to investigate alternates to primary fossil fuels and first-generation biofuels such as ethanol has resulted in significant research into the production and application of furan and its derivatives, such as dimethylfuran (DMF) and methyl furan (MF). DMF, in particular, is a promising biofuel as its performance rivals gasoline in IC engines while possessing an energy density (approximately 34.8 MJ/kg) similar to gasoline and significantly better than ethanol. Furan is the simplest resonantly stabilized heterocyclic compound with an oxygen atom with a high degree of unsaturation. The presence of unsaturated bonds coupled with the aromatic ring structure has been linked to the formation of soot precursors during the combustion process.

Previous investigations of furan have focused on understanding the primary decomposition routes of furan. Grela et al.[25] were among the first to study the low-pressure pyrolysis of furan,

MF, and DMF in a flow reactor at low pressure (1 mtorr) between 1050 K and 1270K and proposed that the route to forming CO was dominant for all three compounds. They were also among the first to note the formation of biradicals as being important intermediates in the pyrolysis of furan. Lifshitz et al. [26] studied the decomposition of furan behind shock waves at higher pressures of 2-3 atm over a temperature range of 1050-1460K. This effort involves using gas chromatography and mass spectrometry to calculate the rate constants for the decomposition of furan to be eight times the value calculated previously [25]. In 1991, Organ and Mackie [27] extended the shock tube temperature between 1100 – 1700K and at higher pressures of 15 – 22 atm and detected several species as a result of the enlarged temperature and pressure envelope. This work. Fulle et al.[28] further expanded the envelope of the study across a temperature range of 500 – 3000K and used laser-schlieren densitometry and time-of-flight (TOF) mass spectrometry to identify the two primary decomposition channels via the formation of intermediate carbenes. They noted that at lower temperatures, the decomposition channel forming propyne and CO were dominant, while at higher temperatures (approximately 1700K), a channel switch occurs, forming acetylene and methyl ketene. These studies formed the basis for providing valuable experimental data to validate kinetic models developed to predict furan decomposition processes [11], [26], [29]–[32].

Sendt et al.[31] developed a simple pyrolysis model featuring reactions based on theoretical calculation and estimation. Tian et al.[30] developed a comprehensive mechanism including 206 species and 1368 reactions and validated it against low-pressure premixed flame studies and pyrolysis results. In 2013, Somers et al. [33], [34] developed a detailed mechanism which was built upon by Cheng et al.[32], [35]. These studies featured methyl furan decomposition evaluated using a synchrotron-based ionization source. An evaluation of furan decomposition by Cheng et al. [36] in 2017 featured a low-pressure laminar flow reactor (30 torr), where the authors noted

that the primary contributor to the formation of propargyl radical (C_3H_3) was from propyne instead of directly from the β-carbene.

Experimental evaluations of the furan pyrolysis were also carried out using the photoionization mass spectrometry (PIMS) and matrix Fourier transform infrared (FTIR) setups and the Chen reactor, first by Vasiliou et al.[37] and then by Urness et al. [38]. The initial evaluation by Vasiliou et al. [37] showed that the two primary decomposition routes for Furan forming the alpha carbene and beta carbene, could be accessed in the short residence times of the Chen reactor. The combination of mass spectrometry and infrared spectroscopy enabled the identification of all the important decomposition products, except for formyl radical, which was thought to be too short-lived for detection. These studies also demonstrated that in the short residence time of the Chen reactor, the isomerization of propyne (m/z 40) to allene, was not detected. Urness et al.[38] explored the relationship between the temperature of the reaction and the distribution of the two primary decomposition routes shown below. This was carried out using a similar Chen reactor and using a synchrotron-based tunable ultraviolet ionization source.

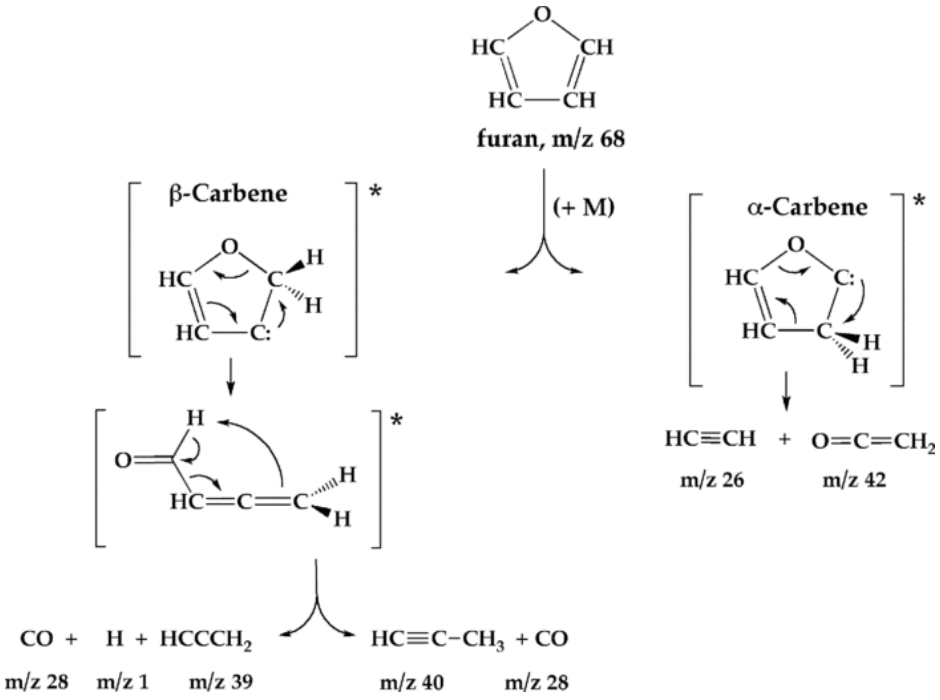

Liu et al.[39] and later Sendt et al.[31] applied computational techniques to be among the first to propose that furan decomposes through two separate pathways that involve a pair of carbenes. The α-carbene was computed to decompose to acetylene (m/z 26) and methyl ketene (m/z 42), while the β-carbene is predicted to isomerize to formyl allene, which breaks down into propyne (m/z 40) and carbon monoxide (m/z 28). These results were confirmed by Fulle et al. [28] and later by independent evaluations using the micro-reactor setup.

Urness et al. [38] examined the pyrolysis of furan -d0 and furan d4 in a micro-reactor using a tunable PIMS setup to arrive at the following reaction scheme, confirming the previous reaction pathway:

$Furan\ (+M) \rightleftharpoons [\alpha - carbene] \rightarrow HC \equiv CH + CH_2 = C = O$ (R 8.1)

$Furan\ (+M) \rightleftharpoons [\beta - carbene] \rightarrow CH_3C \equiv CH + CO$ (R 8.2)

$Furan\ (+M) \rightleftharpoons [\beta - carbene] \rightarrow HCO + HCCCH_2 \rightarrow H + CO + HCCCH_2$ (R 8.3)

They proposed that as temperature increased, the distribution of furan going to the α-carbene route increased from an initial value of less than 10% to approximately 20% of the flux at 1600K. The authors note that the branching ratio of α-carbene to β-carbene could also be affected by the pressure at which pyrolysis occurs. This hypothesis forms the basis for an evaluation of the decomposition of furan using the nozzle reactor geometries – P1650, P1400, and P1200. With a reduction in diameter, the fluid flow pressure in the interior of the reactor is simulated to be stabilized and increased. If the branching ratio is pressure dependent, then the results should indicate an increase in the amount of furan decomposing to α-carbene and its secondary products.

8.3.2.1 Experimental methods

The experimental photoionization mass spectrometry method used to detect the species produced because of pyrolysis is identical to the technique described in Section 3.1.1 and Chapter 2. A summary is presented next; a mixture of 0.025% furan in helium is prepared using a method of partial pressures in a stainless-steel tank. This mixture is then supplied into the experimental setup and the micro-reactor assembly using a commercial mass flow controller (MKS P4B 0–200 sccm N_2) at a flow rate of 200 sccm. The pressure upstream of the reactor is measured using a capacitance manometer. Approximately 1.5 cm of the reactor is resistively heated, and the temperature of the outer wall is measured with a TIM Microtek infrared thermal camera. The molecular beam exiting the reactor is interrogated by synchrotron radiation about 10 cm downstream from the skimmer. The ions were detected using a microchannel plate, and the signal was recorded by ion counting. Four different micro-reactor configurations were evaluated. These geometries are described in Table 1.

8.3.2.2 Measurement of product ratios via photoionization

Photoionization has the ability to quantify the composition of gas mixtures. Ionization of a neutral target such as furan produces an ion signal proportional to the target concentration in the area sampled by the photon source. A detailed explanation of the analysis of the signal is presented in Chapter 2. A summary is described here. The PIMS signal in a dilute gas can be understood by a formulation of Beer's law [38], [40]. For photoionization, the ion signal is a function of the number of molecules in the interaction region, the VUV photon flux through the volume, and the photoionization cross-section. However, the absolute value of neither the volume nor the photon flux is known. The volume can be estimated with some uncertainty; however, it can also be gathered into an empirical constant obtained by calibration, which ultimately cancels when taking ratios. The photon fluxes are measured using a photodiode. In the calculations for furan, since all species are ionized using the same ionization source and ionizing event, these terms cancel out. Therefore, to a first approximation, the photoionization signal S_i^+ due to species i can be written as

$$S_i^+ = C n_i \phi(E) \sigma_i(E) \quad (8.1)$$

Where n_i is the number density of a particular species in the interaction volume, $\phi(E)$ is the photon flux at a given photon energy, and $\sigma i(E)$ is the molecule's photoionization cross-section at the given photon energy. Here the signal Si+ refers to the total ion counts summed over the desired mass peak and normalized on the sampling time or the number of scans. Equation (8.1) ignores that, because of differential diffusion, mass differences, and other factors, molecules of differing mass and collision cross-sections will be detected with different efficiency. This effect is considered by defining a mass discrimination factor D_i that is empirically determined by

calibration. Incorporating the mass discrimination factor and solving for the number density of the neutral target leads to:

$$n_i = \frac{s_i^+}{CD_i \emptyset(E) \sigma_i(E)} \tag{8.2}$$

where the constant C contains all the geometry-dependent factors that do not change with differing masses, which could be obtained by absolute calibration. Using Equation (8.2) to determine the absolute number density of species can be challenging due to the variability in the value of C. However, the equation can determine a ratio of number densities, as common terms get canceled out.

The branching ratio of the pyrolysis products from reaction R 8.1 through R 8.3 as a function of temperature was first proposed by Urness et al.[38] through the following formulation:

$$\left[\frac{\alpha-carbene}{\beta-carbene}\right] = \frac{[HCCH]}{CO} = \frac{[HCCH]}{[HCCCH_2]+[HCCCH_3]} = \frac{[CH_2CO]}{[HCCCH_2]+[HCCCH_3]} = \frac{[CH_2CO]}{[CO]} \tag{8.3}$$

The above formulation was used to plot the ratio of α-carbene products detected to the number of β-carbene products formed as a function of temperature. The results of this evaluation carried out between 1300K and 1600K show an increase in the number of α-carbene products produced as the temperature is increased. This is shown to trend well with simulations by Tian et al.[30], Fulle et al.[28], and Sendt et al.[31] This work features a similar analysis carried out as a function of pressure to understand the effects of varying pressure on the branching ratio for the pyrolysis of furan.

A simplified formulation of Equation 8.1 is applied to relate the signal heights produced through photoionization to the concentration of species. Where the signal of species i, S_i is a function of the time and energy (E). When this relation is integrated over time, the following equation is arrived at:

$$S_i(E) = \Lambda * c_i * \sigma_i(E) * m_i^{\gamma} \tag{8.4}$$

Where Λ is an instrumentation factor, c_i is the time-averaged concentration of species i, σ_i is the ionization cross section and m_i^{γ} is the mass of species I, raised to γ, which is a mass discrimination factor. The ratio of α-carbene to β-carbene is determined by taking a ratio of the two signal intensities to determine the concentration of species. The instrumentation factor is a common term between both calculations. This results in the following equation:

$$\left[\frac{\alpha-carbene}{\beta-carbene}\right]_P = \frac{c_i}{c_j} = \frac{S_i}{S_j} * \frac{\sigma_j}{\sigma_i} * \left(\frac{m_j}{m_i}\right)^{\gamma} \tag{8.5}$$

An expansion of Equation 8.5 in terms of the data obtained from the PIMS experiment is shown in Equation 8.6:

$$\left[\frac{\alpha-carbene}{\beta-carbene}\right]_P = \frac{1}{\frac{c_{39}}{c_{42}}+\frac{c_{40}}{c_{42}}} \tag{8.6}$$

$$\left[\frac{\alpha-carbene}{\beta-carbene}\right]_P = \frac{[CH_2CO\ @10.487\ eV]}{[HCCCH_2\ @10.487\ eV]+[HCCCH_3@10.487\ eV]} \tag{8.7}$$

Where $\frac{c_{39}}{c_{42}} = \frac{S_{39}}{S_{42}} * \frac{\sigma_{42}}{\sigma_{39}} * \left(\frac{m_{42}}{m_{39}}\right)^{\gamma}$, $\frac{c_{40}}{c_{42}} = \frac{S_{40}}{S_{42}} * \frac{\sigma_{42}}{\sigma_{40}} * \left(\frac{m_{42}}{m_{40}}\right)^{\gamma}$, are the ratio of concentrations of propargyl radical (m/z 39)[41] , ketene (m/z 40)[42] and propyne (m/z 40)[43]. The values of ionization cross-section at 10.5 eV for propargyl radical, ketene, and propyne are applied from existing literature. 1700 K is chosen as the temperature of evaluation based on the assumption that nearly all the furan in the system would have decomposed at this temperature. The value of γ is set at 0.51 ± 0.11 for the chosen temperature (1700K) based on the calculations by Urness et al. [38]. The decomposition analysis of furan is carried out at 0.025% furan in helium to reduce the impact of bimolecular reactions on the spectra obtained.

8.3.2.3 Experimental Results

The photoionization spectra obtained from the decomposition of 0.025% of furan in helium, studied using a Chen reactor through a temperature range of 300K to 1800K is shown in

Figure 8.23. To suppress any bimolecular reactions (characterized by the presence of methyl peak (at m/z 15), evaluations were carried out at 0.025% furan in helium, the highest concentration at which no bimolecular reactions were observed. At room temperature, the only observable peak is at m/z 68, corresponding to the parent peak with a small peak at m/z 69, representing the C_{13} peak of furan. As the reactor is heated to temperatures between 1300K and 1400K, signals from m/z 40 (CH_3CCH, propyne) are observed, along with a faint signal at m/z 42 (CH_2CO, ketene). At temperatures above 1500K, the peak at m/z 40 intensifies along with a smaller peak at m/z 39 (C_3H_3, propargyl radical). Additionally, Urness et al. [38] noted the presence of some allene (m/z 40, $H_2C=C=CH_2$) produced through the isomerization of propyne. This is not distinguishable in the fixed wavelength ionization source used in these experiments, but any signal intensity change is factored into the calculation for the contribution to the β-carbene route. At 1700 K, the signal intensity for m/z 39 (propargyl radical) is noted to increase slightly. The origin of the propargyl radical was originally attributed to an independent decomposition route of β-carbene. However, more recent experimental and modeling efforts by Cheng et al. [36] note that the formation of propargyl radical is likely to be from the decomposition of propyne (m/z 40).

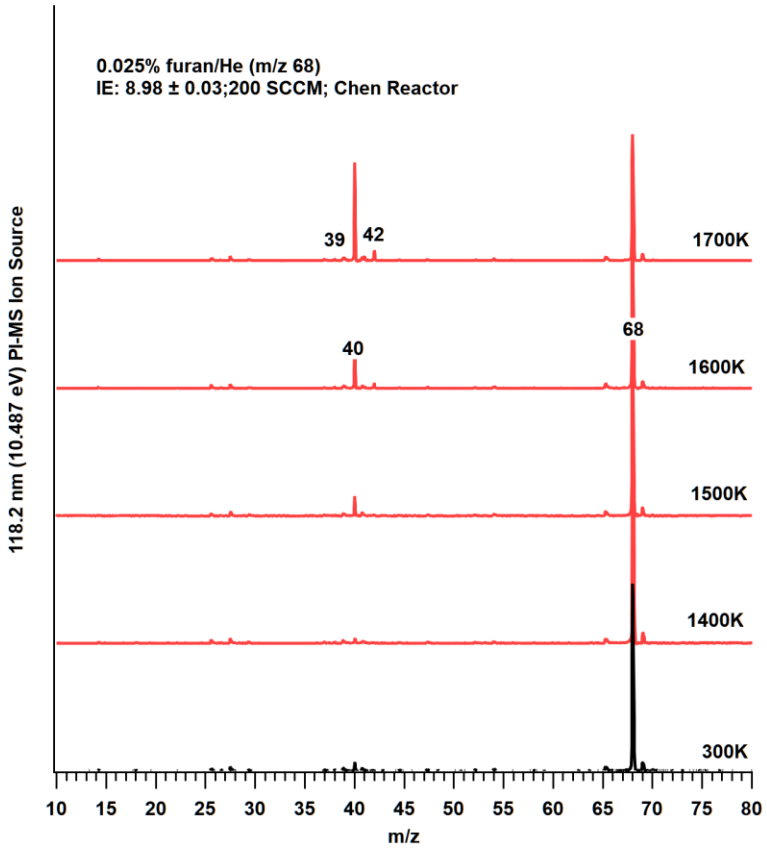

Figure 8.23: PIMS of 0.025% furan in He in the Chen reactor at 200 SCCM heated from 300 to 1700 K and ionized by 118.2 nm (10.487 eV) photons

A similar analysis of the decomposition of furan was carried out using the three nozzle reactor geometries. The spectra from these experiments are shown in Figure 8.24, Figure 8.25 (P1400 nozzle reactor), and Figure 8.26 (P1200 nozzle reactor). Individual signal heights in mili-volt are extracted from these spectra to calculate the ratio of α-carbene to β-carbene.

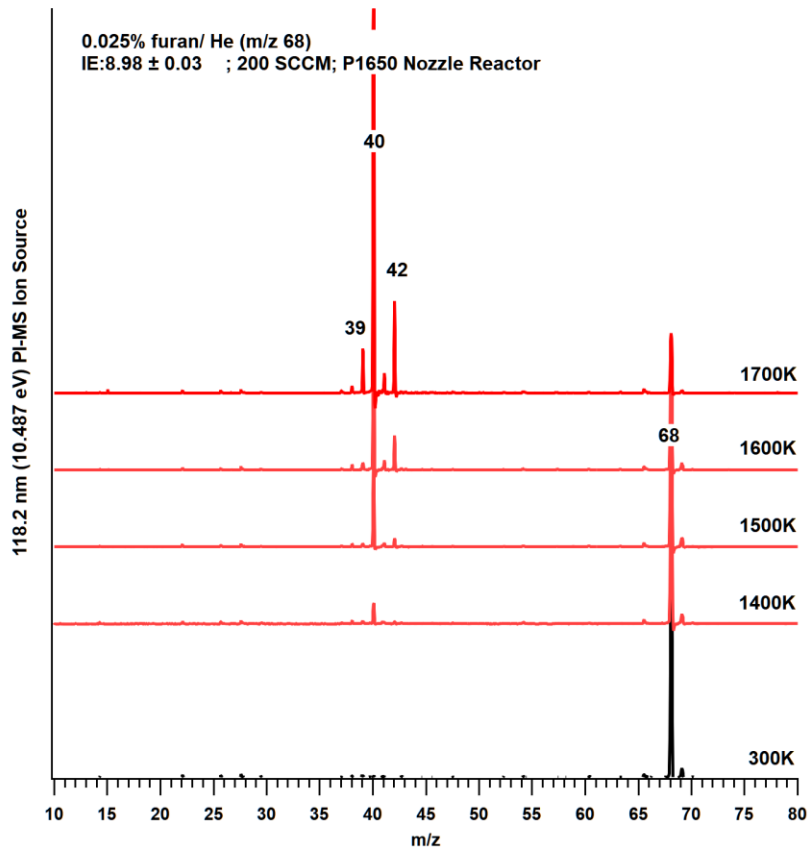

Figure 8.24: PIMS of 0.025% furan in He in the P1650 nozzle micro-reactor at 200 SCCM heated from 300 to 1700 K and ionized by 118.2 nm (10.487 eV) photons

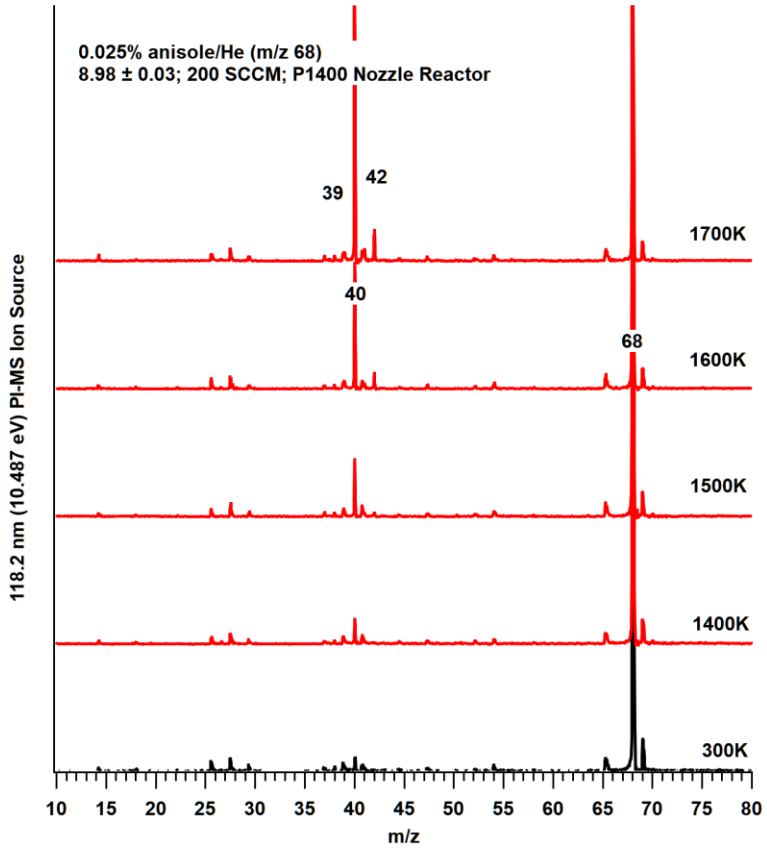

Figure 8.25: PIMS of 0.025% furan in He in the P1400 nozzle micro-reactor at 200 SCCM heated from 300 to 1700 K and ionized by 118.2 nm (10.487 eV) photons

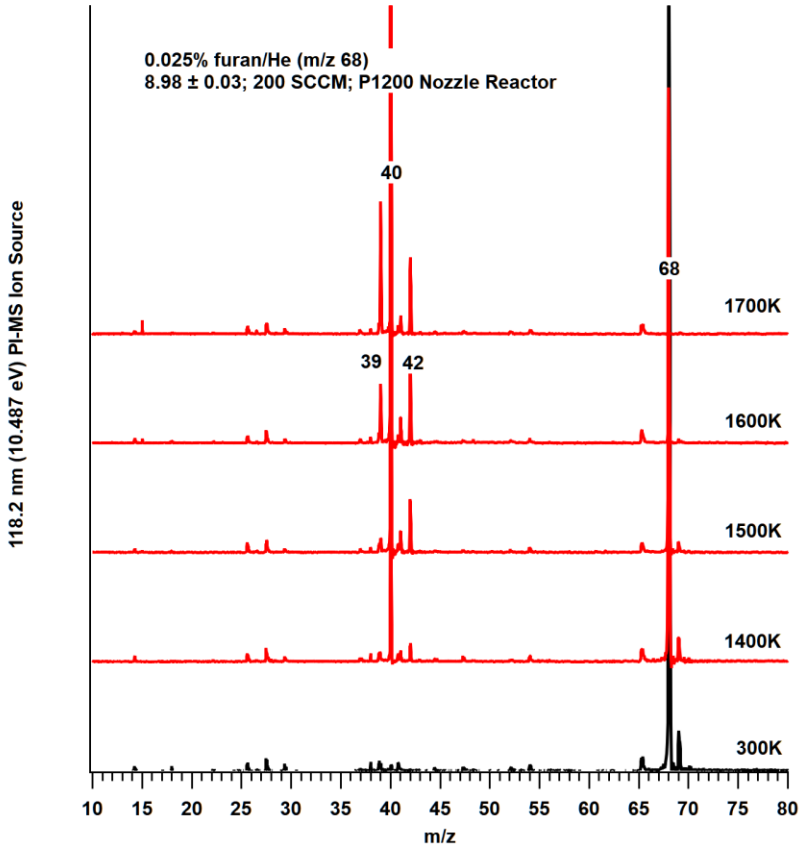

Figure 8.26: PIMS of 0.025% furan in He in the P1400 nozzle micro-reactor at 200 SCCM heated from 300 to 1700 K and ionized by 118.2 nm (10.487 eV) photons

The ratio of α-carbene to β-carbene is calculated using the expression shown in Equation 8.7. The temperature chosen for these evaluations is 1700K across the four reactor geometries. The primary products of α-carbene and β-carbene have an ionization energy that lies within the envelope of what is produced by the fixed wavelength ionization source (10.487 eV). The results from these evaluations are shown in Figure 8.27.

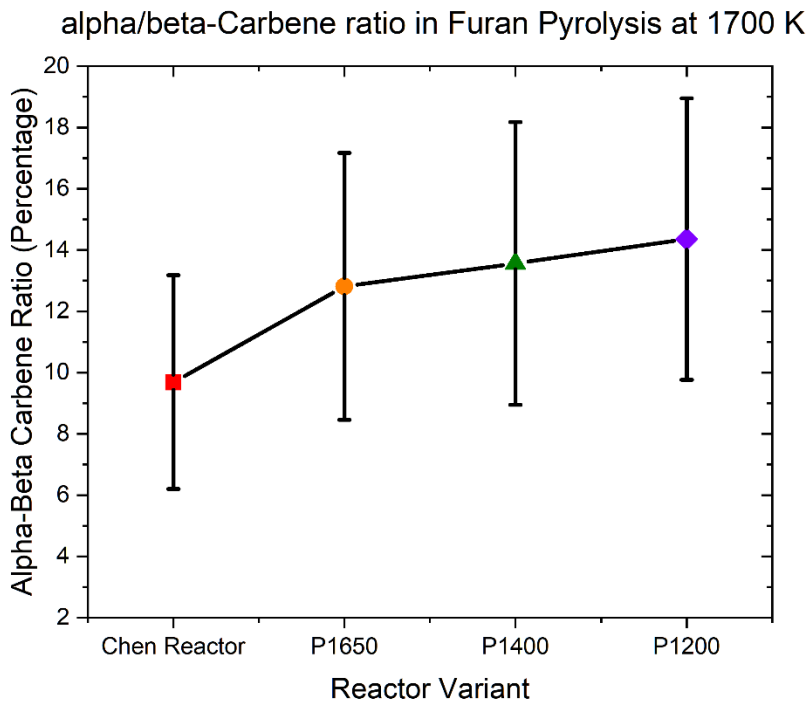

Figure 8.27: Ratio of products measured at 10.487 eV from the α-carbene (m/z 42, ketene) relative to the β-carbene (propargyl, m/z 39 and propyne, m/z 40) as a function of changing reactor exit diameter (and indirectly pressure)

With a reduction in the exit diameter of the nozzle reactor geometry, the ratio of α-carbene to β-carbene increases. There is an increase in the branching of the decomposition reaction towards the α-carbene route, up from about 10 % in the Chen reactor to 14% in the case of the P1200 nozzle reactor. The values shown in Figure 8.27 are arrived at after averaging multiple experimental runs in each micro-reactor geometry. This is done to reduce experimental variability. The error bars shown represent the possibility for variation in results due to the ionization cross-sections for each of the products as well as the mass discrimination factor γ. The results obtained vary within the bounds of the experimental error observed in the calculations performed by Urness et al. [38]

The overall results qualitatively trend with the effects of increasing pressure and are consistent with the CFD simulation results in section 8.2 that, showing that a decreasing nozzle diameter results in a higher stabilized pressure in the reactor system. This increased pressure (and accompanying residence time), could contribute to a larger fraction of the furan in the reactor

decomposing through the α-carbene route forming ketene and acetylene. A computational analysis of these results is currently underway, with reaction rate parameters being determined at the experimental pressures. The goal of these efforts is to present a combined experimental and theoretical evaluation of the decomposition of furan, highlighting the pressure dependence of unimolecular decomposition.

8.4 Conclusion

This chapter outlines the pressure dependence of unimolecular decomposition reactions along with an experimental evaluation of the nozzle reactor geometries manufactured using the process described in Chapter 7. The computational fluid dynamics modeling of fluid flow within four selected reactor geometries is shown. Results from these evaluations highlight the stabilization of pressure and velocity, validating the initial design studies discussed in Chapter 6. These results have enabled, for the first time the estimation of pressure values within the reactor geometry, providing an important parameter crucial for reaction kinetics modeling. Results from the simulation are used to demonstrate the relationship between the reactor geometry, specifically the exit diameter of the reactor, and the reactor pressure and residence time. A demonstration of the impact of this increased pressure and residence time is highlighted through the decomposition reactions of anisole and subsequent high-temperature recombination reactions leading to the formation of important soot precursors. The increased pressure conditions within the smallest exit diameter reactor the P1200, result in a larger fraction of the cyclopentadienyl radical and methyl radical (produced from the decomposition of anisole) to recombine to form methyl cyclopentadiene which has been identified as a known soot precursor. This is the first time that in a micro-reactor environment, a study on the impact of pressure variation has been carried out on

soot precursor and polycyclic aromatic hydrocarbon formation. A second evaluation of the pressure dependence of the pyrolysis of furan is presented. This study details the impact of varying reaction pressure at a fixed temperature on the branching ratio of the thermal decomposition products of furan. An increasing reaction pressure (and residence time) in the system has been shown to trend towards a larger flux of decomposition products towards the formation of ketene and acetylene as opposed to the formation of propyne and carbon monoxide. These experimental results will prove crucial in the validation of computational modeling efforts to build chemical kinetic mechanisms to predict the decomposition behavior of a range of fuels and molecules. For the first time, researchers can 'select' the pressure at which a decomposition or combustion reaction is being studied. Additionally, they can now accurately estimate the value of different reaction parameters, making model validation even more accurate. This makes the nozzle micro-reactor a powerful tool in discerning the combustion chemistry of the fuels of the future.

8.5 References

[1] Carstensen, Hans-Heinrich, and Anthony M. Dean. "Chapter 4 the Kinetics of Pressure-Dependent Reactions." Modeling of Chemical Reactions, vol. 42, no. 2007, 2007, pp. 101–184, https://doi.org/10.1016/s0069-8040(07)42004-0.

[2] S. de Persis, A. Dollet, and F. Teyssandier, "Pressure Dependence of Gas-Phase Reaction Rates," *J. Chem. Educ.*, vol. 81, no. 6, p. 832, Jun. 2004, doi: 10.1021/ed081p832.

[3] A. W. Jasper, K. M. Pelzer, J. A. Miller, E. Kamarchik, L. B. Harding, and S. J. Klippenstein, "Predictive a priori pressure-dependent kinetics," *Science*, vol. 346, no. 6214, pp. 1212–1215, Dec. 2014, doi: 10.1126/science.1260856.

[4] V. D. Knyazev, "Energy Dependence of .ltbbrac..DELTA.E.rtbbrac.down and the Shape of Falloff Curves: Implications for Modeling of Experimental Data," *J. Phys. Chem.*, vol. 99, no. 40, pp. 14738–14741, Oct. 1995, doi: 10.1021/j100040a023.

[5] R. Sivaramakrishnan, et al. “Shock Tube and Theoretical Studies on the Thermal Decomposition of Propane: Evidence for a Roaming Radical Channel.” The Journal of Physical Chemistry A, vol. 115, no. 15, 29 Mar. 2011, pp. 3366–3379, https://doi.org/10.1021/jp2006205. Accessed 27 Feb. 2023.

[6] Q. Guan, K. N. Urness, T. K. Ormond, D. E. David, G. Barney Ellison, and J. W. Daily, “The properties of a micro-reactor for the study of the unimolecular decomposition of large molecules,” *Int. Rev. Phys. Chem.*, vol. 33, no. 4, pp. 447–487, Oct. 2014, doi: 10.1080/0144235X.2014.967951.

[7] T. Fan, “Design of a Novel Microreactor to Study Short Residence Time Combustion.”, 2016

[8] I. C. ANSYS, “13: geometry and mesh generation preprocessor,” *Ansys Inc*, 2012.

[9] L. Zhou, M. D. Boot, B. H. Johansson, and J. J. E. Reijnders, “Performance of lignin derived aromatic oxygenates in a heavy-duty diesel engine,” *Fuel*, vol. 115, pp. 469–478, Jan. 2014, doi: 10.1016/j.fuel.2013.07.047.

[10] M. Tian *et al.*, “Performance of lignin derived compounds as octane boosters,” *Fuel*, vol. 189, pp. 284–292, Feb. 2017, doi: 10.1016/j.fuel.2016.10.084.

[11] Yuan, Wenhao, et al. “Experimental and Kinetic Modeling Investigation on Anisole Pyrolysis: Implications on Phenoxy and Cyclopentadienyl Chemistry.” Combustion and Flame, vol. 201, Mar. 2019, pp. 187–199, https://doi.org/10.1016/j.combustflame.2018.12.028. Accessed 8 Apr. 2023.

[12] A. M. Scheer, C. Mukarakate, D. J. Robichaud, G. B. Ellison, and M. R. Nimlos, “Radical Chemistry in the Thermal Decomposition of Anisole and Deuterated Anisoles: An Investigation of Aromatic Growth,” *J. Phys. Chem. A*, vol. 114, no. 34, pp. 9043–9056, Sep. 2010, doi: 10.1021/jp102046p.

[13] M. Balat, “Mechanisms of Thermochemical Biomass Conversion Processes. Part 1: Reactions of Pyrolysis,” *Energy Sources Part Recovery Util. Environ. Eff.*, vol. 30, no. 7, pp. 620–635, Mar. 2008, doi: 10.1080/15567030600817258.

[14] K. Umeki, G. Häggström, A. Bach-Oller, K. Kirtania, and E. Furusjö, “Reduction of Tar and Soot Formation from Entrained-Flow Gasification of Woody Biomass by Alkali Impregnation,” *Energy Fuels*, vol. 31, no. 5, pp. 5104–5110, May 2017, doi: 10.1021/acs.energyfuels.6b03480.

[15] J. A. Miller and C. F. Melius, “Kinetic and thermodynamic issues in the formation of aromatic compounds in flames of aliphatic fuels,” *Combust. Flame*, vol. 91, no. 1, pp. 21–39, Oct. 1992, doi: 10.1016/0010-2180(92)90124-8.

[16] C.-Y. Lin and M. C. Lin, “Thermal decomposition of methyl phenyl ether in shock waves: the kinetics of phenoxy radical reactions,” *J. Phys. Chem.*, vol. 90, no. 3, pp. 425–431, Jan. 1986, doi: 10.1021/j100275a014.

[17] J. C. Mackie, K. R. Doolan, and P. F. Nelson, “Kinetics of the thermal decomposition of methoxybenzene (anisole),” *J. Phys. Chem.*, vol. 93, no. 2, pp. 664–670, Jan. 1989, doi: 10.1021/j100339a033.

[18] I. W. C. E. Arends, R. Louw, and P. Mulder, “Kinetic study of the thermolysis of anisole in a hydrogen atmosphere,” *J. Phys. Chem.*, vol. 97, no. 30, pp. 7914–7925, Jul. 1993, doi: 10.1021/j100132a020.

[19] M. Pecullan, K. Brezinsky, and I. Glassman, “Pyrolysis and Oxidation of Anisole near 1000 K,” *J. Phys. Chem. A*, vol. 101, no. 18, pp. 3305–3316, May 1997, doi: 10.1021/jp963203b.

[20] M. Nowakowska, O. Herbinet, A. Dufour, and P.-A. Glaude, “Detailed kinetic study of anisole pyrolysis and oxidation to understand tar formation during biomass combustion and gasification,” *Combust. Flame*, vol. 161, no. 6, pp. 1474–1488, Jun. 2014, doi: 10.1016/j.combustflame.2013.11.024.

[21] B. Husson, M. Ferrari, O. Herbinet, S. S. Ahmed, P.-A. Glaude, and F. Battin-Leclerc, “New experimental evidence and modeling study of the ethylbenzene oxidation,” *Proc. Combust. Inst.*, vol. 34, no. 1, pp. 325–333, Jan. 2013, doi: 10.1016/j.proci.2012.06.002.

[22] S. W. Wagnon *et al.*, “Experimental and modeling studies of a biofuel surrogate compound: laminar burning velocities and jet-stirred reactor measurements of anisole,” *Combust. Flame*, vol. 189, pp. 325–336, Mar. 2018, doi: 10.1016/j.combustflame.2017.10.020.

[23] T. Bierkandt, P. Hemberger, P. Oßwald, D. Krüger, M. Köhler, and T. Kasper, “Flame structure of laminar premixed anisole flames investigated by photoionization mass spectrometry and photoelectron spectroscopy,” *Proc. Combust. Inst.*, vol. 37, no. 2, pp. 1579–1587, Jan. 2019, doi: 10.1016/j.proci.2018.07.037.

[24] A. V. Friderichsen, E.-J. Shin, R. J. Evans, M. R. Nimlos, D. C. Dayton, and G. B. Ellison, “The pyrolysis of anisole (C6H5OCH3) using a hyperthermal nozzle,” *Fuel*, vol. 80, no. 12, pp. 1747–1755, Oct. 2001, doi: 10.1016/S0016-2361(01)00059-X.

[25] M. A. Grela, V. T. Amorebieta, and A. J. Colussi, “Very low pressure pyrolysis of furan, 2-methylfuran and 2,5-dimethylfuran. The stability of the furan ring,” *J. Phys. Chem.*, vol. 89, no. 1, pp. 38–41, Jan. 1985, doi: 10.1021/j100247a011.

[26] A. Lifshitz, M. Bidani, and S. Bidani, “Thermal reactions of cyclic ethers at high temperatures. III. Pyrolysis of furan behind reflected shocks,” *J. Phys. Chem.*, vol. 90, no. 21, pp. 5373–5377, Oct. 1986, doi: 10.1021/j100412a096.

[27] P. P. Organ and J. C. Mackie, “Kinetics of pyrolysis of furan,” *J. Chem. Soc. Faraday Trans.*, vol. 87, no. 6, p. 815, 1991, doi: 10.1039/ft9918700815.

[28] D. Fulle, A. Dib, J. H. Kiefer, Q. Zhang, J. Yao, and R. D. Kern, “Pyrolysis of Furan at Low Pressures: Vibrational Relaxation, Unimolecular Dissociation, and Incubation Times,” *J. Phys. Chem. A*, vol. 102, no. 38, pp. 7480–7486, Sep. 1998, doi: 10.1021/jp9823042.

[29] D. Liu *et al.*, “Combustion chemistry and flame structure of furan group biofuels using molecular-beam mass spectrometry and gas chromatography – Part I: Furan,” *Combust. Flame*, vol. 161, no. 3, pp. 748–765, Mar. 2014, doi: 10.1016/j.combustflame.2013.05.028.

[30] Z. Tian *et al.*, “An experimental and kinetic investigation of premixed furan/oxygen/argon flames,” *Combust. Flame*, vol. 158, no. 4, pp. 756–773, Apr. 2011, doi: 10.1016/j.combustflame.2010.12.022.

[31] K. Sendt, G. B. Bacskay, and J. C. Mackie, “Pyrolysis of Furan: Ab Initio Quantum Chemical and Kinetic Modeling Studies,” *J. Phys. Chem. A*, vol. 104, no. 9, pp. 1861–1875, Mar. 2000, doi: 10.1021/jp993537b.

[32] Z. Cheng *et al.*, “Experimental and kinetic modeling studies of low-pressure premixed laminar 2-methylfuran flames,” *Proc. Combust. Inst.*, vol. 36, no. 1, pp. 1295–1302, Jan. 2017, doi: 10.1016/j.proci.2016.07.032.

[33] K. P. Somers *et al.*, “A comprehensive experimental and detailed chemical kinetic modelling study of 2,5-dimethylfuran pyrolysis and oxidation,” *Combust. Flame*, vol. 160, no. 11, pp. 2291–2318, Nov. 2013, doi: 10.1016/j.combustflame.2013.06.007.

[34] K. P. Somers, J. M. Simmie, W. K. Metcalfe, and H. J. Curran, “The pyrolysis of 2-methylfuran: a quantum chemical, statistical rate theory and kinetic modelling study,” *Phys. Chem. Chem. Phys.*, vol. 16, no. 11, pp. 5349–5367, 2014, doi: 10.1039/C3CP54915A.

[35] Z. Cheng *et al.*, “Experimental and Kinetic Modeling Study of 2-Methylfuran Pyrolysis at Low and Atmospheric Pressures,” *Energy Fuels*, vol. 31, no. 1, pp. 896–903, Jan. 2017, doi: 10.1021/acs.energyfuels.6b02399.

[36] Z. Cheng *et al.*, “Experimental and kinetic modeling studies of furan pyrolysis: Fuel decomposition and aromatic ring formation,” *Fuel*, vol. 206, pp. 239–247, Oct. 2017, doi: 10.1016/j.fuel.2017.05.090.

[37] A. Vasiliou, M. R. Nimlos, J. W. Daily, and G. B. Ellison, “Thermal Decomposition of Furan Generates Propargyl Radicals,” *J. Phys. Chem. A*, vol. 113, no. 30, pp. 8540–8547, Jul. 2009, doi: 10.1021/jp903401h.

[38] K. N. Urness *et al.*, “Pyrolysis of furan in a microreactor,” *J. Chem. Phys.*, vol. 139, no. 12, p. 124305, Sep. 2013, doi: 10.1063/1.4821600.

[39] R. Liu, X. Zhou, and L. Zhai, “Theoretical investigation of unimolecular decomposition channels of furan4,” *J. Comput. Chem.*, vol. 19, no. 2, pp. 240–249, 1998, doi: 10.1002/(SICI)1096-987X(19980130)19:2<240::AID-JCC17>3.0.CO;2-L.

[40] W. A. Noyes and P. A. Leighton, *The photochemistry of gases*. New York: Reinhold Pub. Corp., 1941.

[41] H. Gao *et al.*, “High-resolution threshold photoelectron study of the propargyl radical by the vacuum ultraviolet laser velocity-map imaging method,” *J. Chem. Phys.*, vol. 135, no. 22, p. 224304, Dec. 2011, doi: 10.1063/1.3664864.

[42] B. Niu, Y. Bai, and D. A. Shirley, “High resolution photoelectron spectroscopy and femtosecond intramolecular dynamics of H2CCO+ and D2CCO+,” *J. Chem. Phys.*, vol. 99, no. 4, pp. 2520–2532, Aug. 1993, doi: 10.1063/1.465215.

[43] X. Xing, M.-K. Bahng, B. Reed, C. S. Lam, K.-C. Lau, and C. Y. Ng, “Rovibrationally selected and resolved pulsed field ionization-photoelectron study of propyne: Ionization energy and spin-orbit interaction in propyne cation,” *J. Chem. Phys.*, vol. 128, no. 9, p. 094311, Mar. 2008, doi: 10.1063/1.2836429.

Chapter 9: Conclusions and future research directions

9.1 Thesis summary

The identification of renewable and sustainable sources of energy to power mobility and meet global energy demands is an essential research focus. The focus on clean energy will rely on developing accurate chemical kinetic models to predict the behavior and impact of these fuels. Applying a combined experimental and theoretical approach to link the fundamental behavior of these fuel molecules and their structure will be central to developing future fuels. Chapters 2 and 3 outlined the experimental and theoretical approach employed in my work to understand the decomposition behavior and to create chemical kinetic models for the pyrolysis of different organic molecules.

Chapter 4 highlights the application of this combined approach to discern the nuances of the pyrolysis behavior of three methylcyclohexene isomers. The difference in sooting behavior of these isomers is linked to the location of the double bond. The results from the experimental evaluations were used to validate computational models that discovered the competition in decomposition routes for 3-methyl-cyclohexene (3MCHe). The presence of a direct pathway to the formation of benzene via the methyl bond fission, which occurs at similar rates to the retro Diels-Alder decomposition pathway in 3MCHe, was linked to the location of the double bond in this isomer. This has been linked to the increased sooting tendency of 3MCHe in comparison to the other two isomers. The results of these evaluations provide valuable inputs to developing higher accuracy models and automated tools for predicting fuel combustion behavior.

Chapter 5 presented another example of molecular spectroscopy and numerical modeling applied in characterizing the decomposition and abstraction behavior of Poly Oxy Methylene Ether (POM-E) molecules. This effort produced chemical kinetic rates to compare the most likely routes of decomposition and abstraction of polyoxymethylene ether molecules. The primary molecule evaluated was dimethoxymethane (DMM). This was followed by studies on the impact of increasing the chain length by adding $(CH_2\text{-}O)_n$ groups to this baseline molecule. Next, an analysis of experimental spectra and chemical kinetic rates on the effects of altering the end groups by adding longer alkyl chains to the DMM molecule was carried out. These comparisons will aid in identifying likely candidates for molecules that can be used as additives to reduce sooting in diesel fuel.

Chapter 6 presented a detailed examination of the micro-reactor, an integral component in the Photoionization Mass Spectrometry and Matrix Fourier Transform Infra-Red Spectroscopy setups. This resulted in the redesign of the silicon carbide micro-reactor with an internal constriction to produce a more stabilized fluid flow profile within the geometry – a critical requisite for more detailed chemical kinetic examinations. As a part of this effort, it was identified that altering the diameter of the constriction makes it possible to modify the pressure and velocity profile within the micro-reactor. This provides tunability in the micro-reactor design enabling reactions to be evaluated at different pressure levels using the PIMS and FTIR setup. Chapter 7 detailed the creation of a novel digital manufacturing method to produce these redesigned silicon carbide micro-reactors. This novel process can produce ceramic geometries with wall thicknesses of less than 300µm and constrictions as small as 100µm. Initially developed for fabricating silicon carbide micro-reactors with a nozzle, this technique has now been extended to multiple other materials (alumina, YSZ) and other high aspect ratio geometries.

Chapter 8 presents an experimental validation of the three nozzle reactor geometries featuring exit diameters of 0.650 mm, 0.400 mm, and 0.250 mm. Computational Fluid Dynamics (CFD) simulations simulate the fluid flow behavior inside these geometries and highlight the stabilized pressure profile. The performance of these reactors is compared to the results obtained from photoionization mass spectrometry experiments with the Chen reactor. The pressure dependence of unimolecular decomposition reactions is explored by applying these nozzle reactor geometries. The pyrolysis of anisole is studied in these reactor geometries. In particular, the impact of increasing pressure and residence time is evaluated on the bimolecular reaction between methyl radical and cyclopentadienyl radical to form an important soot precursor, methylcyclopentadiene (MCPD). Additionally, the decomposition of furan is evaluated using this suite of micro-reactor geometries. The focus was on understanding the influence of pressure on the likely decomposition pathway, with one pyrolysis route (forming α – carbene) being sensitive to changes in reaction pressure. Results from these evaluations confirm that with an increase in the reactor pressure (or decreasing reactor exit diameter), the ratio of α–carbene to β-carbene increases. These results demonstrate, for the first time, the ability to select reactor pressure by varying the geometry of the micro-reactor used in the experiment. Further, it is possible to estimate pressure, temperature, and fluid residence time values in these reactors, enabling researchers to validate chemical kinetic models through the data extracted from these experiments. Overall, the work presented here advances the experimental capabilities of the mass spectrometry technique by enabling researchers to control and vary the conditions at which combustion chemistry is evaluated. The capabilities of the hybrid manufacturing technique provide a robust method to design and develop tailored devices to meet the requirements of researchers studying future fuels.

9.2 Recommendations for future experiments

9.2.1 Alternate micro-reactor materials and oxidation experiments

Silicon carbide is the current micro-reactor material. The ability to sustain high temperatures, fracture toughness, resistance to corrosion, thermal conductivity, and the capability to withstand thermal shock makes it an ideal material choice for this application. The existing experimental setup harnesses these capabilities to use these micro-reactors as the flow reactor of choice to study short residence time decomposition phenomena. However, the chemical nature of silicon carbide has restricted experiments to only pyrolysis (thermal decomposition in the absence of oxygen). The reactivity of silicon carbide with oxygen has prevented the use of the spectroscopy setup to evaluate oxidation reaction as SiC is unstable in an oxygenated atmosphere at high temperatures. Alternate materials have been identified to extend the experimental setup's capabilities to study reactions involving oxidation. The new micro-reactor material should be chemically inert in an oxidizing atmosphere and structurally sound over a temperature range of 300 to 2000 K. T. Fan[1], in his thesis, identified alternate metal and non-metal candidates that could be used as alternate reactor materials. The creation of a novel manufacturing method described in Chapter 6 has enabled the fabrication of reactor-like geometries with a range of ceramics. Yttria Stabilized Zirconia (YSZ) has been chosen as the most promising candidate. YSZ has been used as an engineering ceramic for a range of applications[2]–[4]. It retains many of the favorable features of silicon carbide, including high-temperature stability, resistance to thermal shock, and high fracture toughness, and it is also resistant to oxidation at high temperatures. Currently, nozzle reactor geometries are being manufactured using this material. Preliminary evaluations of the alternate reactor material (alumina and YSZ) are underway. A novel conductive

heating jacket has been trialed to heat these geometries to a temperature of 1800K. The focus of these efforts has been to understand the impact of reactor material on the pyrolysis reaction. The heating strategy involves encasing the alumina or YSZ reactor geometry in a silicon carbide jacket. The SiC heating jacket is tailor-made using the process developed as part of this work. This jacket is heated using the existing resistive heating strategy employed to flash heat SiC reactors. The interior alumina or YSZ geometry is conductively heated by the exterior SiC jacket. The temperature of the reactants is measured using an infrared thermal camera through the external surface temperature of the silicon carbide jacket. Initial trials have involved studying the decomposition of anisole. The heating jacket assembly is shown in Figure 9.1.

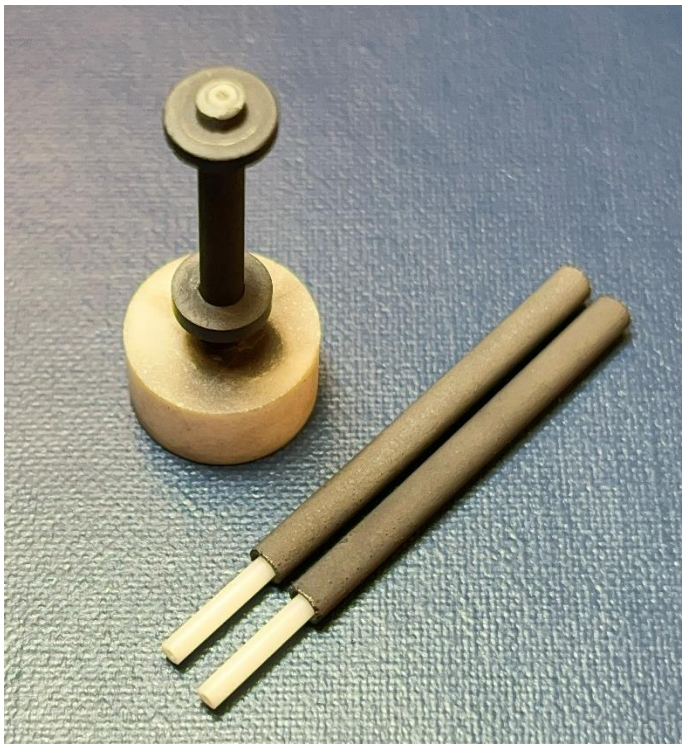

Figure 9.1: Alumina nozzle reactor inside a SiC heating jacket. The upright geometry is shown with two graphite heating disks mounted in a specially designed MACOR collet.

The spectra obtained from the experimental runs are presented in Appendix C9. As part of this effort, it is proposed that a suitable oxidation reaction be identified and evaluated to showcase

the capability of this reactor in simulating reactions of organic molecules with oxygen across a broad temperature range.

9.2.2 X-ray Fluorescence (XRF) Studies

The speed at which highly reactive radicals and intermediates are formed in an engine and the heat released when they continue to react are critical for evaluating the efficiency and viability of any fuel. Capturing this kinetic information means deriving rate constants and gas laws as a function of temperature and pressure. This is only attainable for the micro-reactor if the gas pressure, temperature, flow conditions, and residence times are known. In situ, non-invasive measurements of the micro-reactors internal conditions are difficult for two reasons. First, the micro-reactor being composed of opaque SiC cannot be probed with conventional optical techniques. Second, inserting a probe into the 1 mm in diameter tube would severely disrupt the gas flow dynamics. Typically, as seen in Chapter 2, an inlet and outlet pressure, flow rate, and external wall temperature are reported with experimental data. Using this information, estimates can be made for residence time (of the target molecule inside the heated reactor) and internal gas temperature and pressure. These can only be estimated assuming either laminar or plugged flow. However, this has been shown by Guan et. al.[5] to be an inaccurate assumption – this has been remedied to a certain extent in the nozzle microreactor. As explained in Chapter 5, the addition of the constriction produces a stabilized, high-speed, laminar flow within the reactor, making pressure-based calculations more accurate. In 2017, R. Tranter et al[6] carried-out X-ray fluorescence measurements of flow inside the tube (Chen) reactor. These measurements were among the first to probe fluid flow inside a short residence time flow reactor. The results provide relative gas density that can yield absolute density measurements, which can be correlated to pressure measurements. Figure 9.2 shows the proposed experimental geometry of the X-ray studies

based on the previous work. These experiments will be used to perform non-intrusive XRF measurements conducted through He/Kr flow inside the SiC nozzle micro-reactor at varied wall temperatures. Direct measurements of gas density within the SiC nozzle and the nearly supersonic jet that exits the reactor will be measured with XRF. X-ray absorption measurements will complement the XRF studies and be used to image the internal wall structure of the nozzle geometry. These results will be used in conjunction with other non-invasive measurements, such as the X-ray microscopy and Scanning Electron Microscopy measurements described in Chapter 6. Based on the observations made by Tranter et al. the results from these experiments will be used to improve upon the measurements made previously. The smoother interior walls and thinner wall sections should enable more accurate measurements confirming the applicability of this new geometry for low residence time spectroscopy.

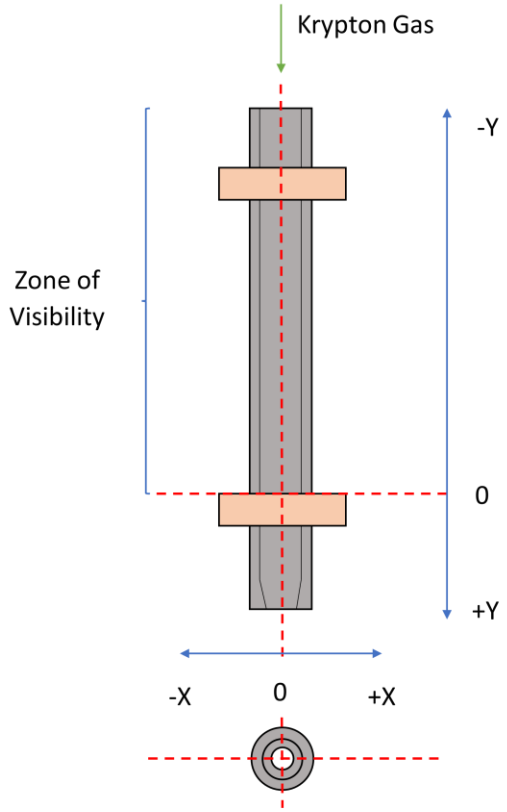

Figure 9.2: The experimental geometry for X-ray studies of Kr fluorescent tags in the nozzle micro-reactor

9.2.3 Building a low temperature and low-pressure oxidation mechanism for aviation fuels

Based on the energetics and results obtained by running experimental evaluations and numerical simulations of Jet A fuel surrogate molecules it is proposed that the reaction rate constants for these molecules be evaluated. The rate data may be used to pinpoint the dominant reaction pathways for jet fuel ignition chemistry and how they may or may be affected by temperature and pressure. Theoretical rate constants for all relevant reactions will be calculated using transition state theory [7]. Tunneling corrections will be obtained from one-dimensional asymmetric Eckart barriers[8], [9]. Rigid rotor harmonic oscillator approximations are assumed to be good except for the treatment of the lowest frequency CH_3 torsional modes that will be treated as hindered rotors. Variational corrections are expected to be significant in these reactions, which are typical for reactions with low barriers. Therefore, where necessary, variable reaction coordinate transition state theory (VRC-TST) will be employed to determine reaction rates using the VaReCoF program from Argonne National Laboratories. [10], [11] Pressure-dependent rate coefficients will be calculated employing master equation calculations performed with the MESS code in the PAPR reaction software suite from Argonne National Laboratories.[12] ANSYS Chemkin-PRO [13] is a computational software package that solves the governing equations for reactive flow systems and is commonly used in the field of combustion to assess the role of chemistry in global combustion phenomena such as ignition timing. Chemkin-Pro required inputs include parameters to define the physics of the problem (adiabaticity, temperature, pressure, volume, flow rate, fuel to air ratio, etc.), a reaction mechanism, and thermodynamic properties file. Thermodynamics parameters for every new molecule from our PES not included in the prior mechanisms will be fit to the NASA 7-parameter polynomial format[14]. Pressure-independent reaction coefficients will be fit to modify Arrhenius-type expressions, while pressure-dependent

reaction coefficients must be fit to Troe 4-parameter reaction expressions. [14] These new rate constants and thermodynamics polynomials will be imported to the prior combustion mechanisms and the Dooley et al. [15], POSF 4658 surrogate model. To judge success, these new models will be used to reproduce prior experimental data sets for ignition, flame speed, and speciation. To determine the effect of pressure and temperature on ignition behavior, a parametric study of ignition delay time predictions in a 0-D constant volume simulation will be conducted with varying pressure, temperature, and equivalence ratio. A combination of reaction path analysis, sensitivity analysis, and kinetic branching analysis will be applied to identify the key reactions for ignition under post-flameout reignition conditions. Through these 3 analyses on the mechanisms produced, correlations between how pressure and temperature influence ignition behavior and the critical reactions that create variation in behavior can be identified.

9.3 Acknowledgment and Funding

I gratefully acknowledge the support from the National Science Foundation (NSF) and the Department of Energy (DOE) for supporting me throughout my Ph.D. Funding and additional acknowledgments for each chapter are listed below.

9.3.1 Methylcyclohexene isomers work (Chapter 4)

I gratefully acknowledge the assistance of G. Barney Ellison, Sadie C. Stutzman, and David E. Couch in this work for their insight and help with the mass spectra analysis. A portion of this research was conducted as part of the Co-Optimization of Fuels & Engines (Co-Optima) project sponsored by the U.S. Department of Energy – Office of Energy Efficiency and Renewable Energy, Bioenergy Technologies, and Vehicle Technologies Offices. Work at the National Renewable Energy Laboratory was performed under Contract No. DE347AC36-99GO10337.

9.3.2 Polyoxymethylene Ether decomposition work (Chapter 5)

Funding for this research is provided by the U.S. Department of Energy's Office of Energy Efficiency and Renewable Energy under the Bioenergy Technologies Office, Co-Optimization of Fuels and Engines Initiative award number DE-EE0008726, with additional financial support from the Colorado Energy Research Collaboratory. This work utilized the RMACC Summit supercomputer, which is supported by the National Science Foundation (awards ACI-1532235 and ACI-1532236), the University of Colorado Boulder, and Colorado State University. The Summit supercomputer is a joint effort of the University of Colorado Boulder and Colorado State University.

9.3.3 Nozzle micro-reactor development and fabrication (Chapter 6, 7 and 8)

This material is based upon work supported by the National Science Foundation under Grant No. 1834656 and 2047259, along with the Office of Basic Energy Sciences under award number DE-SC0018627. I would like to especially acknowledge the support received from Calix Ceramic Solutions in developing and fabricating these devices. Micro-CT imaging was carried out at the MIMIC core facility at the University of Colorado in Boulder (RRID: SCR_0.19307). We would also like to thank the team at Alfred University and Dr. Bill Carty's research group for assisting with the XRD and SEM characterization of these devices and sharing their expertise in ceramics manufacturing.

9.3.4 Aircraft flameout analysis and modeling (Chapter 8 and 9)

CAREER: This material is based upon work supported by the National Science Foundation under Grant No. 2047259. This work utilized the RMACC Summit supercomputer, which is supported by the National Science Foundation (awards ACI-1532235 and ACI-1532236), the

University of Colorado Boulder, and Colorado State University. The Summit supercomputer is a joint effort of the University of Colorado Boulder and Colorado State University.

9.4 References

[1] T. Fan, “Design of a Novel Microreactor to Study Short Residence Time Combustion.”, 2016

[2] R. H. Nielsen, J. H. Schlewitz, H. Nielsen, and U. by Staff, “Zirconium and Zirconium Compounds,” in *Kirk-Othmer Encyclopedia of Chemical Technology*, John Wiley & Sons, Ltd, 2007. doi: 10.1002/0471238961.26091803.a01.pub2.

[3] F. Mohd Foudzi, N. Muhamad, A. Bakar Sulong, and H. Zakaria, “Yttria stabilized zirconia formed by micro ceramic injection molding: Rheological properties and debinding effects on the sintered part,” *Ceram. Int.*, vol. 39, no. 3, pp. 2665–2674, Apr. 2013, doi: 10.1016/j.ceramint.2012.09.033.

[4] R. Maurya, A. Gupta, S. Omar, and K. Balani, “Effect of sintering on mechanical properties of ceria reinforced yttria stabilized zirconia,” *Ceram. Int.*, vol. 42, no. 9, pp. 11393–11403, Jul. 2016, doi: 10.1016/j.ceramint.2016.04.069.

[5] Q. Guan, K. N. Urness, T. K. Ormond, D. E. David, G. Barney Ellison, and J. W. Daily, “The properties of a micro-reactor for the study of the unimolecular decomposition of large molecules,” *Int. Rev. Phys. Chem.*, vol. 33, no. 4, pp. 447–487, Oct. 2014, doi: 10.1080/0144235X.2014.967951.

[6] R. S. Tranter *et al.*, “Measuring flow profiles in heated miniature reactors with X-ray fluorescence spectroscopy,” *Proc. Combust. Inst.*, vol. 36, no. 3, pp. 4603–4610, 2017, doi: 10.1016/j.proci.2016.06.104.

[7] Truhlar, Donald G., et al. “Current Status of Transition-State Theory.” The Journal of Physical Chemistry, vol. 87, no. 15, July 1983, pp. 2664–2682, https://doi.org/10.1021/j100238a003. Accessed 3 Dec. 2021.

[8] C. Eckart, “The Penetration of a Potential Barrier by Electrons,” *Phys. Rev.*, vol. 35, no. 11, pp. 1303–1309, Jun. 1930, doi: 10.1103/PhysRev.35.1303.

[9] B. C. Garrett and D. G. Truhlar, “Semiclassical tunneling calculations,” *J. Phys. Chem.*, vol. 83, no. 22, pp. 2921–2926, Nov. 1979, doi: 10.1021/j100485a023.

[10] L. B. Harding, Y. Georgievskii, and S. J. Klippenstein, “Predictive Theory for Hydrogen Atom−Hydrocarbon Radical Association Kinetics,” *J. Phys. Chem. A*, vol. 109, no. 21, pp. 4646–4656, Jun. 2005, doi: 10.1021/jp0508608.

[11] Argonne National Laboratories. “Home of the PAPR Suite of Chemical Kinetics Codes.” Tcg.cse.anl.gov, 2014, tcg.cse.anl.gov/papr/codes/varecof.html. Accessed 8 Apr. 2023.

[12] Y. Georgievskii, J. A. Miller, M. P. Burke, and S. J. Klippenstein, “Reformulation and solution of the master equation for multiple-well chemical reactions,” *J. Phys. Chem. A*, vol. 117, no. 46, pp. 12146–12154, Nov. 2013, doi: 10.1021/jp4060704.

[13] “ANSYS CHEMKIN-Pro.” [Online]. Available: ANSYS CHEMKIN-PRO 15131, Reaction Design: San Diego, 2013

[14] R. G. Gilbert, K. Luther, and J. Troe, “Theory of Thermal Unimolecular Reactions in the Fall-off Range. II. Weak Collision Rate Constants,” *Berichte Bunsenges. Für Phys. Chem.*, vol. 87, no. 2, pp. 169–177, 1983, doi: 10.1002/bbpc.19830870218.

[15] S. Dooley *et al.*, “A jet fuel surrogate formulated by real fuel properties,” *Combust. Flame*, vol. 157, no. 12, pp. 2333–2339, Dec. 2010, doi: 10.1016/j.combustflame.2010.07.001.

Bibliography

"ANSYS CHEMKIN-Pro." ANSYS CHEMKIN-PRO 15131, Reaction Design: San Diego, 2013

A.B. Burrill and P. M. Johnson, "Torsional analyses of trans-2-butene and propene cations: A comparative investigation of two prototypical ions with different degrees of symmetry," J. Chem. Phys., vol. 115, no. 1, pp. 133–138, Jul. 2001, doi: 10.1063/1.1376634.

A. Bhargava and P. R. Westmoreland, "Measured Flame Structure and Kinetics in a Fuel-Rich Ethylene Flame.," Combust. Flame, vol. 113, no. 3, pp. 333–347, May 1998, doi: 10.1016/S0010-2180(97)00208-3.

A. Cavaliere and M. de Joannon, "Mild Combustion," Prog. Energy Combust. Sci., vol. 30, no. 4, pp. 329–366, Jan. 2004, doi: 10.1016/j.pecs.2004.02.003.

A. Demirbas, "Progress and recent trends in biofuels," Prog. Energy Combust. Sci., vol. 33, no. 1, pp. 1–18, Feb. 2007, doi: 10.1016/j.pecs.2006.06.001.

A. E. Karataş and Ö. L. Gülder, "Soot formation in high pressure laminar diffusion flames," Prog. Energy Combust. Sci., vol. 38, no. 6, pp. 818–845, Dec. 2012, doi: 10.1016/j.pecs.2012.04.003.

A. Ehn, J. Zhu, X. Li, and J. Kiefer, "Advanced Laser-Based Techniques for Gas-Phase Diagnostics in Combustion and Aerospace Engineering," Appl. Spectrosc., vol. 71, no. 3, pp. 341–366, Mar. 2017, doi: 10.1177/0003702817690161.

A. F. Wagner, "The challenges of combustion for chemical theory," Proc. Combust. Inst., vol. 29, no. 1, pp. 1173–1200, Jan. 2002, doi: 10.1016/S1540-7489(02)80148-1.

A. Fleisher et al., "Reaction bonding of silicon carbides by Binder Jet 3D-Printing, phenolic resin binder impregnation and capillary liquid silicon infiltration," Ceram. Int., vol. 45, no. 14, pp. 18023–18029, Oct. 2019, doi: 10.1016/j.ceramint.2019.06.021.

A. H. Kung, J. F. Young, and S. E. Harris, "Erratum: Generation of 1182-Å radiation in phase-matched mixtures of inert gases," p. 2.

A. H. Kung, J. F. Young, and S. E. Harris, "Generation of 1182-Å radiation in phase-matched mixtures of inert gases," Appl. Phys. Lett., vol. 22, no. 6, pp. 301–302, Mar. 1973, doi: 10.1063/1.1654647.

A. K. Agarwal, “Biofuels (alcohols and biodiesel) applications as fuels for internal combustion engines,” Prog. Energy Combust. Sci., vol. 33, no. 3, pp. 233–271, Jun. 2007, doi: 10.1016/j.pecs.2006.08.003.

A. K. Vasiliou et al., “Thermal decomposition of CH3CHO studied by matrix infrared spectroscopy and photoionization mass spectroscopy,” J. Chem. Phys., vol. 137, no. 16, p. 164308, Oct. 2012, doi: 10.1063/1.4759050.

A. Kantrowitz and J. Grey, "A High Intensity Source for the Molecular Beam. Part I. Theoretical," Rev. Sci. Instrum., vol. 22, no. 5, pp. 328–332, May 1951, doi: 10.1063/1.1745921.

A. L. Brown, D. C. Dayton, M. R. Nimlos, and J. W. Daily, “Design and Characterization of an Entrained Flow Reactor for the Study of Biomass Pyrolysis Chemistry at High Heating Rates,” Energy Fuels, vol. 15, no. 5, pp. 1276–1285, Sep. 2001, doi: 10.1021/ef010083k.

A. Lamprecht, B. Atakan, and K. Kohse-Höinghaus, “Fuel-rich flame chemistry in low-pressure cyclopentene flames,” Proc. Combust. Inst., vol. 28, no. 2, pp. 1817–1824, Jan. 2000, doi: 10.1016/S0082-0784(00)80584-6.

A. Lifshitz, M. Bidani, and S. Bidani, “Thermal reactions of cyclic ethers at high temperatures. III. Pyrolysis of furan behind reflected shocks,” J. Phys. Chem., vol. 90, no. 21, pp. 5373–5377, Oct. 1986, doi: 10.1021/j100412a096.

A. M. Scheer, C. Mukarakate, D. J. Robichaud, G. B. Ellison, and M. R. Nimlos, "Radical Chemistry in the Thermal Decomposition of Anisole and Deuterated Anisoles: An Investigation of Aromatic Growth," *J. Phys. Chem. A*, vol. 114, no. 34, pp. 9043–9056, Sep. 2010, doi: 10.1021/jp102046p.

A. M. Scheer, C. Mukarakate, D. J. Robichaud, G. B. Ellison, and M. R. Nimlos, "Radical Chemistry in the Thermal Decomposition of Anisole and Deuterated Anisoles: An Investigation of Aromatic Growth," J. Phys. Chem. A, vol. 114, no. 34, pp. 9043–9056, Sep. 2010, doi: 10.1021/jp102046p.

A. Miyoshi, "Systematic Computational Study on the Unimolecular Reactions of Alkylperoxy (RO2), Hydroperoxyalkyl (QOOH), and Hydroperoxyalkylperoxy (O2QOOH) Radicals," J. Phys. Chem. A, vol. 115, no. 15, pp. 3301–3325, Apr. 2011, doi: 10.1021/jp112152n.

A. Ortona, C. D'Angelo, S. Gianella, and D. Gaia, "Cellular ceramics produced by rapid prototyping and replication," Mater. Lett., vol. 80, pp. 95–98, Aug. 2012, doi: 10.1016/j.matlet.2012.04.050.

A. V. Friderichsen, E.-J. Shin, R. J. Evans, M. R. Nimlos, D. C. Dayton, and G. B. Ellison, “The pyrolysis of anisole (C6H5OCH3) using a hyperthermal nozzle,” Fuel, vol. 80, no. 12, pp. 1747–1755, Oct. 2001, doi: 10.1016/S0016-2361(01)00059-X.

A. Vasiliou, M. R. Nimlos, J. W. Daily, and G. B. Ellison, “Thermal Decomposition of Furan Generates Propargyl Radicals,” J. Phys. Chem. A, vol. 113, no. 30, pp. 8540–8547, Jul. 2009, doi: 10.1021/jp903401h.

A. W. Jasper, K. M. Pelzer, J. A. Miller, E. Kamarchik, L. B. Harding, and S. J. Klippenstein, “Predictive a priori pressure-dependent kinetics,” Science, vol. 346, no. 6214, pp. 1212–1215, Dec. 2014, doi: 10.1126/science.1260856.

Argonne National Laboratories. “Home of the PAPR Suite of Chemical Kinetics Codes.” Tcg.cse.anl.gov, 2014, tcg.cse.anl.gov/papr/codes/varecof.html. Accessed 8 Apr. 2023.

B. A. Williams and T. A. Cool, "Two-photon spectroscopy of Rydberg states of jet-cooled C2H4 and C2D4," J. Chem. Phys., vol. 94, no. 10, pp. 6358–6366, May 1991, doi: 10.1063/1.460314.
B. C. Garrett and D. G. Truhlar, “Semiclassical tunneling calculations,” J. Phys. Chem., vol. 83, no. 22, pp. 2921–2926, Nov. 1979, doi: 10.1021/j100485a023.

B. F. Gray and P. G. Felton, "Low-temperature oxidation in a stirred-flow reactor—I. Propane," Combust. Flame, vol. 23, no. 3, pp. 295–304, Dec. 1974, doi: 10.1016/0010-2180(74)90111-4.

B. Husson, M. Ferrari, O. Herbinet, S. S. Ahmed, P.-A. Glaude, and F. Battin-Leclerc, “New experimental evidence and modeling study of the ethylbenzene oxidation,” Proc. Combust. Inst., vol. 34, no. 1, pp. 325–333, Jan. 2013, doi: 10.1016/j.proci.2012.06.002.

B. Niu, Y. Bai, and D. A. Shirley, “High resolution photoelectron spectroscopy and femtosecond intramolecular dynamics of H2CCO+ and D2CCO+,” J. Chem. Phys., vol. 99, no. 4, pp. 2520–2532, Aug. 1993, doi: 10.1063/1.465215.

Briles, Travis C.,“Production, Deceleration, and Detection of OH Radicals - Thesis.” 2008

C. A. Daly, J. M. Simmie, P. Dagaut, and M. Cathonnet, "Oxidation of dimethoxymethane in a jet-stirred reactor," Combust. Flame, vol. 125, no. 3, pp. 1106–1117, May 2001, doi: 10.1016/S0010-2180(01)00227-9.

C. Barro, M. Parravicini, K. Boulouchos, and A. Liati, "Neat polyoxymethylene dimethyl ether in a diesel engine; part 2: Exhaust emission analysis," fuel, vol. 234, pp. 1414–1421, Dec. 2018, doi: 10.1016/j.fuel.2018.07.108.

C. Boles, Thermodynamics - An Engineering Approach, 8th Edition. McGraw Hill Education, 2019.

C. Eckart, “The Penetration of a Potential Barrier by Electrons,” Phys. Rev., vol. 35, no. 11, pp. 1303–1309, Jun. 1930, doi: 10.1103/PhysRev.35.1303.

C. Gao, G. Liu, and H. Wang, "Experimental Investigations of Drilling Silicon Carbide Using Brazed Diamond Tools," Mater. Perform. Charact., vol. 8, no. 1, pp. 329–343, Jul. 2019, doi: 10.1520/MPC20180190.

C. h. Carter Jr., R. f. Davis, and J. Bentley, "Kinetics and Mechanisms of High-Temperature Creep in Silicon Carbide: I, Reaction-Bonded," J. Am. Ceram. Soc., vol. 67, no. 6, pp. 409–417, 1984, doi: 10.1111/j.1151-2916.1984.tb19726.x.

C. K. Westbrook, “Biofuels Combustion,” Annu. Rev. Phys. Chem., vol. 64, no. 1, pp. 201–219, 2013, doi: 10.1146/annurev-physchem-040412-110009.

C. O. Rogers, K. S. Lockwood, Q. L. D. Nguyen, and N. J. Labbe, “Diol isomer revealed as a source of methyl ketene from propionic acid unimolecular decomposition,” Int. J. Chem. Kinet., vol. 53, no. 12, pp. 1272–1284, 2021, doi: 10.1002/kin.21532.

C. P. Lazzara, J. C. Biordi, and J. F. Papp, "Concentration profiles for radical species in a methane-oxygen-argon flame," Combust. Flame, vol. 21, no. 3, pp. 371–382, Dec. 1973, doi: 10.1016/S0010-2180(73)80060-4.

C. S. McEnally and L. D. Pfefferle, "Improved sooting tendency measurements for aromatic hydrocarbons and their implications for naphthalene formation pathways," Combust. Flame, vol. 148, no. 4, pp. 210–222, Mar. 2007, doi: 10.1016/j.combustflame.2006.11.003.

C. S. McEnally and L. D. Pfefferle, "Sooting Tendencies of Oxygenated Hydrocarbons in Laboratory-Scale Flames," Environ. Sci. Technol., vol. 45, no. 6, pp. 2498–2503, Mar. 2011, doi: 10.1021/es103733q.

C.-J. Sung and H. J. Curran, "Using rapid compression machines for chemical kinetics studies," Prog. Energy Combust. Sci., vol. 44, pp. 1–18, Oct. 2014, doi: 10.1016/j.pecs.2014.04.001.

C.-Y. Lin and M. C. Lin, “Thermal decomposition of methyl phenyl ether in shock waves: the kinetics of phenoxy radical reactions,” J. Phys. Chem., vol. 90, no. 3, pp. 425–431, Jan. 1986, doi: 10.1021/j100275a014.

Carstensen, Hans-Heinrich, and Anthony M. Dean. “Chapter 4 the Kinetics of Pressure-Dependent Reactions.” Modeling of Chemical Reactions, vol. 42, no. 2007, 2007, pp. 101–184, https://doi.org/10.1016/s0069-8040(07)42004-0.

Chaonan Xu, Chong Xu, Feng Han, Feng Zhang, Wei Wei, Zhaoxiang Zhong, Weihong Xing,' Fabrication of high performance macroporous tubular silicon carbide gas filters by extrusion method,' Ceramics International,Volume 44, Issue 15,2018.

Chen, Peter, et al. "Flash pyrolytic production of rotationally cold free radicals in a supersonic jet. Resonant multiphoton spectrum of the 3p2A2". rarw. X2A2" origin band of methyl." The Journal of Physical Chemistry 90.11 (1986): 2319-2321.

Climate Analysis Indicators Tool (CAIT), Climate Data Explorer, World Resources Institute, Washington DC, USA. Data for the Year 2017

Cool, Terrill A., et al. “Photoionization Cross Sections for Reaction Intermediates in Hydrocarbon Combustion.” International Journal of Mass Spectrometry, vol. 247, no. 1-3, Dec. 2005, pp. 18–27, https://doi.org/10.1016/j.ijms.2005.08.018. Accessed 20 Feb. 2021.

D. D. Das, P. C. St. John, C. S. McEnally, S. Kim, and L. D. Pfefferle, "Measuring and predicting sooting tendencies of oxygenates, alkanes, alkenes, cycloalkanes, and aromatics on a unified scale," Combust. Flame, vol. 190, pp. 349–364, Apr. 2018, doi: 10.1016/j.combustflame.2017.12.005.

D. E. Couch et al., "Detection of the keto-enol tautomerization in acetaldehyde, acetone, cyclohexanone, and methyl vinyl ketone with a novel VUV light source," Proc. Combust. Inst., vol. 38, no. 1, pp. 1737–1744, Jan. 2021, doi: 10.1016/j.proci.2020.06.139.

D. E. Couch et al., “Ultrafast 1 MHz vacuum-ultraviolet source via highly cascaded harmonic generation in negative-curvature hollow-core fibers,” Optica, vol. 7, no. 7, p. 832, Jul. 2020, doi: 10.1364/OPTICA.395688.

D. Fulle, A. Dib, J. H. Kiefer, Q. Zhang, J. Yao, and R. D. Kern, “Pyrolysis of Furan at Low Pressures: Vibrational Relaxation, Unimolecular Dissociation, and Incubation Times,” J. Phys. Chem. A, vol. 102, no. 38, pp. 7480–7486, Sep. 1998, doi: 10.1021/jp9823042.

D. Liu et al., “Combustion chemistry and flame structure of furan group biofuels using molecular-beam mass spectrometry and gas chromatography – Part I: Furan,” Combust. Flame, vol. 161, no. 3, pp. 748–765, Mar. 2014, doi: 10.1016/j.combustflame.2013.05.028.

D. T. D. Karimbaev, A. Y. Ezhov, and M. A. Mezentsev, "DEVELOPMENT OF BREAKTHROUGH TECHNOLOGIES FOR CREATING NODES AND DETAILS FROM CERAMIC AND POLYMER COMPOSITE MATERIALS FOR SMALL-SIZED AIRCRAFT ENGINES," p. 10, 2017.

D. W. Kohn, H. Clauberg, and P. Chen, “Flash pyrolysis nozzle for generation of radicals in a supersonic jet expansion,” Rev. Sci. Instrum., vol. 63, no. 8, pp. 4003–4005, Aug. 1992, doi: 10.1063/1.1143254.

Dunoyer, L. "Comptes rendus acad." Sc. Paris 152 (1911): 594.

E. A. Bunt, "Mass analysis of flames and flue gases," Symp. Int. Combust., vol. 7, no. 1, pp. 325–331, Jan. 1958, doi: 10.1016/S0082-0784(58)80060-0.

E. J. Barrientos, J. E. Anderson, M. M. Maricq, and A. L. Boehman, "Particulate matter indices using fuel smoke point for vehicle emissions with gasoline, ethanol blends, and butanol blends," Combust. Flame, vol. 167, pp. 308–319, May 2016, doi: 10.1016/j.combustflame.2016.01.034.

E. L. Petersen, "Interpreting Endwall and Sidewall Measurements in Shock-Tube Ignition Studies," Combust. Sci. Technol., vol. 181, no. 9, pp. 1123–1144, Sep. 2009, doi: 10.1080/00102200902973323.

F. F. Wang and Z. Zhang, "Overview of silicon carbide technology: Device, converter, system, and application," CPSS Trans. Power Electron. Appl., vol. 1, no. 1, pp. 13–32, Dec. 2016, doi: 10.24295/CPSSTPEA.2016.00003.

F. H. Vermeire, H.-H. Carstensen, O. Herbinet, F. Battin-Leclerc, G. B. Marin, and K. M. Van Geem, "Experimental and modeling study of the pyrolysis and combustion of dimethoxymethane," Combust. Flame, vol. 190, pp. 270–283, Apr. 2018, doi: 10.1016/j.combustflame.2017.12.001.
F. Knauer and O. Stern, “Zur Methode der Molekularstrahlen. II,” Z. Fr Phys., vol. 39, no. 10–11, pp. 764–779, Oct. 1926, doi: 10.1007/BF01451747.

F. L. Dryer and M. Chaos, "Ignition of syngas/air and hydrogen/air mixtures at low temperatures and high pressures: Experimental data interpretation and kinetic modeling implications," Combust. Flame, p. 8, 2008.

F. L. Dryer, "High Temperature Oxidation of Carbon Monoxide and Methane in a Turbulent Flow Reactor," PRINCETON UNIV NJ DEPT OF AEROSPACE AND MECHANICAL SCIENCES, Mar. 1972. Accessed: Dec. 26, 2021. [Online]. Available: https://apps.dtic.mil/sti/citations/AD0746284

F. L. Dryer, “Chemical kinetic and combustion characteristics of transportation fuels,” Proceedings of the Combustion Institute, vol. 35, no. 1, pp. 117–144, 2015.

F. Mohd Foudzi, N. Muhamad, A. Bakar Sulong, and H. Zakaria, “Yttria stabilized zirconia formed by micro ceramic injection molding: Rheological properties and debinding effects on the sintered part,” Ceram. Int., vol. 39, no. 3, pp. 2665–2674, Apr. 2013, doi: 10.1016/j.ceramint.2012.09.033.

F. N. Egolfopoulos, N. Hansen, Y. Ju, K. Kohse-Höinghaus, C. K. Law, and F. Qi, "Advances and challenges in laminar flame experiments and implications for combustion chemistry," Prog. Energy Combust. Sci., vol. 43, pp. 36–67, Aug. 2014, doi: 10.1016/j.pecs.2014.04.004.

F. Qi, “Combustion chemistry probed by synchrotron V.U.V. photoionization mass spectrometry,” Proc. Combust. Inst., vol. 34, no. 1, pp. 33–63, Jan. 2013, doi: 10.1016/j.proci.2012.09.002.

F. Qi, “Combustion chemistry probed by synchrotron VUV photoionization mass spectrometry,” Proc. Combust. Inst., vol. 34, no. 1, pp. 33–63, Jan. 2013, doi: 10.1016/j.proci.2012.09.002.
F. Yuchuan, S. Qing, and S. Jianyi, "Synthesis and Reforming of Dimethoxymethane," Chin. J. Catal., vol. 30, no. 8, pp. 791–800, Aug. 2009.

Friderichsen, Anders V., et al. “The Infrared Spectrum of the Matrix-Isolated Phenyl Radical.” Journal of the American Chemical Society, vol. 123, no. 9, 7 Feb. 2001, pp. 1977–1988, https://doi.org/10.1021/ja0024338. Accessed 8 Apr. 2023.

G. B. Bacskay and J. C. Mackie, "The pyrolysis of cyclopentadiene: quantum chemical and kinetic modelling studies of the acetylene plus propyne/allene decomposition channels," Phys. Chem. Chem. Phys., vol. 3, no. 12, pp. 2467–2473, Jan. 2001, doi: 10.1039/B101317N.

G. B. Kistiakowsky and W. P. Slichter, "A High Intensity Source for the Molecular Beam. Part II. Experimental,” Rev. Sci. Instrum., vol. 22, no. 5, pp. 333–337, May 1951, doi: 10.1063/1.1745922.

G. Bieri, F. Burger, E. Heilbronner, and J. P. Maier, "Valence Ionization Energies of Hydrocarbons," Helv. Chim. Acta, vol. 60, no. 7, pp. 2213–2233, 1977, doi: 10.1002/hlca.19770600714.

G. C. Eltenton, "The Study of Reaction Intermediates by Means of a Mass Spectrometer Part I. Apparatus and Method," J. Chem. Phys., vol. 15, no. 7, pp. 455–481, Jul. 1947, doi: 10.1063/1.1746565.

G. da Silva, J. W. Bozzelli, L. Liang, and J. T. Farrell, “Ethanol Oxidation: Kinetics of the α-Hydroxyethyl Radical + O2 Reaction,” The Journal of Physical Chemistry A, vol. 113, no. 31, pp. 8923–8933, Jul. 2009, doi: https://doi.org/10.1021/jp903210a.

G. Ding, R. He, K. Zhang, N. Zhou, and H. Xu, "Stereolithography 3D printing of SiC ceramic with potential for lightweight optical mirror," Ceram. Int., vol. 46, no. 11, pp. 18785–18790, Aug. 2020, doi: 10.1016/j.ceramint.2020.04.196.

G. Freeman and G. B. Haydon, “Emphysema After Low-Level Exposure to NO2,” Arch. Environ. Health Int. J., vol. 8, no. 1, pp. 125–128, Jan. 1964, doi: 10.1080/00039896.1964.10663640.

G. R. Sawyer and T. F. Page, "Microstructural characterization of 'REFEL' (reaction-bonded) silicon carbides," J. Mater. Sci., vol. 13, no. 4, pp. 885–904, Apr. 1978, doi: 10.1007/BF00570528.

G.Mittal, and Chih-Jen Sung. “A Rapid Compression Machine for Chemical Kinetics Studies at Elevated Pressures and Temperatures.” Combustion Science and Technology, vol. 179, no. 3, Mar. 2007, pp. 497–530, https://doi.org/10.1080/00102200600671898.

Gaussian 16, Revision B.01, Frisch, M.J., et al. Gaussian, Inc., Wallingford CT (2016) GaussView 5.0. Wallingford, E.U.A.

H. Chen, X. Su, J. Li, and X. Zhong, “Effects of gasoline and polyoxymethylene dimethyl ethers blending in diesel on the combustion and emission of a common rail diesel engine,” Energy, vol. 171, pp. 981–999, Mar. 2019, doi: https://doi.org/10.1016/j.energy.2019.01.089.

H. Curran, "Developing detailed chemical kinetic mechanisms for fuel combustion," Proc. Combust. Inst., vol. 37, pp. 57–81, Jan. 2019, doi: 10.1016/j.proci.2018.06.054.
H. E. Stokinger, “Ozone Toxicology,” Arch. Environ. Health Int. J., vol. 10, no. 5, pp. 719–731, May 1965, doi: 10.1080/00039896.1965.10664082.

H. Gao et al., “High-resolution threshold photoelectron study of the propargyl radical by the vacuum ultraviolet laser velocity-map imaging method,” J. Chem. Phys., vol. 135, no. 22, p. 224304, Dec. 2011, doi: 10.1063/1.3664864.

H. K. Ciezki and G. Adomeit, "Shock-tube investigation of self-ignition of n-heptane-air mixtures under engine relevant conditions," Combust. Flame, vol. 93, no. 4, pp. 421–433, Jun. 1993, doi: 10.1016/0010-2180(93)90142-P.

H. Petersen, “The Properties of Helium: Density, Specific Heats, Viscosity, and Thermal Conductivity at Pressures from 1 to 100 bar and from Room Temperature to about 1800 K,” p. 46.

H. Zhang, Y. Yang, K. Hu, B. Liu, M. Liu, and Z. Huang, "Stereolithography-based additive manufacturing of lightweight and high-strength C-f/SiC ceramics," Addit. Manuf., vol. 34, p. 101199, Aug. 2020, doi: 10.1016/j.addma.2020.101199.

Han, D. Y., et al. “Influence of Polyoxymethylene Dimethyl Ethers on Diesel Fuel Properties.” Energy Sources, Part A: Recovery, Utilization, and Environmental Effects, vol. 38, no. 18, 16 Sept. 2016, pp. 2687–2692, https://doi.org/10.1080/15567036.2015.1110646. Accessed 8 Apr. 2023.

Haswell, Stephen J., et al. "The application of micro reactors to synthetic chemistry." Chemical Communications 5 (2001): 391-398.

I. A. Khalek, M. G. Blanks, P. M. Merritt, and B. Zielinska, "Regulated and unregulated emissions from modern 2010 emissions-compliant heavy-duty on-highway diesel engines," J. Air Waste Manag. Assoc., vol. 65, no. 8, pp. 987–1001, Aug. 2015, doi: 10.1080/10962247.2015.1051606.

İ. A. Reşitoğlu, K. Altinişik, and A. Keskin, "The pollutant emissions from diesel-engine vehicles and exhaust aftertreatment systems," Clean Technol. Environ. Policy, vol. 17, no. 1, pp. 15–27, Jan. 2015, doi: 10.1007/s10098-014-0793-9.

I. C. ANSYS, “13: geometry and mesh generation preprocessor,” Ansys Inc, 2012.

I. I. Rabi, J. R. Zacharias, S. Millman, and P. Kusch, “A New Method of Measuring Nuclear Magnetic Moment,” Phys. Rev., vol. 53, no. 4, pp. 318–318, Feb. 1938, doi: 10.1103/PhysRev.53.318.

I. Polozov, N. Razumov, D. Masaylo, A. Silin, Y. Lebedeva, and A. Popovich, “Fabrication of Silicon Carbide Fiber-Reinforced Silicon Carbide Matrix Composites Using Binder Jetting Additive Manufacturing from Irregularly-Shaped and Spherical Powders,” Materials, vol. 13, no. 7, p. 1766, Apr. 2020, doi: 10.3390/ma13071766.

I. W. C. E. Arends, R. Louw, and P. Mulder, “Kinetic study of the thermolysis of anisole in a hydrogen atmosphere,” J. Phys. Chem., vol. 97, no. 30, pp. 7914–7925, Jul. 1993, doi: 10.1021/j100132a020.

IEA (2020), Key World Energy Statistics 2020, IEA, Paris https://www.iea.org/reports/key-world-energy-statistics-2020, License: CC BY 4.0

IEA (2022), World Energy Outlook 2022, IEA, Paris https://www.iea.org/reports/world-energy-outlook-2022, License: CC BY 4.0 (report); CC BY NC SA 4.0 (Annex A)

J. A. Cole, J. D. Bittner, J. P. Longwell, and J. B. Howard, “Formation mechanisms of aromatic compounds in aliphatic flames,” Combust. Flame, vol. 56, no. 1, pp. 51–70, Apr. 1984, doi: 10.1016/0010-2180(84)90005-1.

J. A. Miller and C. F. Melius, “Kinetic and thermodynamic issues in the formation of aromatic compounds in flames of aliphatic fuels,” Combust. Flame, vol. 91, no. 1, pp. 21–39, Oct. 1992, doi: 10.1016/0010-2180(92)90124-8.

J. A. Miller and S. J. Klippenstein, "From the Multiple-Well Master Equation to Phenomenological Rate Coefficients: Reactions on a C3H4 Potential Energy Surface," J. Phys. Chem. A, vol. 107, no. 15, pp. 2680–2692, Apr. 2003, doi: 10.1021/jp0221082.

J. A. Miller and S. J. Klippenstein, "The Recombination of Propargyl Radicals and Other Reactions on a C6H6 Potential," J. Phys. Chem. A, vol. 107, no. 39, pp. 7783–7799, Oct. 2003, doi: 10.1021/jp030375h.

J. A. Miller et al., "Combustion chemistry in the twenty-first century: Developing theory-informed chemical kinetics models," Prog. Energy Combust. Sci., vol. 83, p. 100886, Mar. 2021, doi: 10.1016/j.pecs.2020.100886.

J. A. Miller, "Theory and modeling in combustion chemistry," Symp. Int. Combust., vol. 26, no. 1, pp. 461–480, Jan. 1996, doi: 10.1016/S0082-0784(96)80249-9.

J. A. Miller, M. J. Pilling, and J. Troe, "Unravelling combustion mechanisms through a quantitative understanding of elementary reactions," Proc. Combust. Inst., vol. 30, no. 1, pp. 43–88, Jan. 2005, doi: 10.1016/j.proci.2004.08.281.

J. Burger, M. Siegert, E. Ströfer, and H. Hasse, "Poly(oxymethylene) dimethyl ethers as components of tailored diesel fuel: Properties, synthesis and purification concepts," Fuel, vol. 89, no. 11, pp. 3315–3319, Nov. 2010, doi: 10.1016/j.fuel.2010.05.014.

J. C. Biordi, "Molecular beam mass spectrometry for studying the fundamental chemistry of flames,"" Prog. Energy Combust. Sci., vol. 3, no. 3, pp. 151–173, Jan. 1977, doi: 10.1016/0360-1285(77)90002-8.

J. C. Mackie, K. R. Doolan, and P. F. Nelson, “Kinetics of the thermal decomposition of methoxybenzene (anisole),” J. Phys. Chem., vol. 93, no. 2, pp. 664–670, Jan. 1989, doi: 10.1021/j100339a033.

J. E. Dec, "Advanced compression-ignition engines—understanding the in-cylinder processes," Proc. Combust. Inst., vol. 32, no. 2, pp. 2727–2742, Jan. 2009, doi: 10.1016/j.proci.2008.08.008.

J. Herzler, J. A. Manion, and W. Tsang, “1,2-Pentadiene decomposition,” Int. J. Chem. Kinet., vol. 33, no. 11, pp. 755–767, 2001, doi: 10.1002/kin.1072.

J. Holman, Heat Transfer, 10th Edition. McGraw-Hill Education, 2009.

J. L. Garnett, W. D. Johnson, and J. E. Sherwood, "Pyrolysis of 1-methylcyclohexene and methylenecyclohexane," Aust. J. Chem., vol. 29, no. 3, pp. 599–607, 1976, doi: 10.1071/ch9760599.

J. L. Wiza, “Microchannel Plate Detectors,” Nucl Instrum Methods, vol. 162, pp. 60–1, 1979.
J. Lelieveld, K. Klingmüller, A. Pozzer, R. T. Burnett, A. Haines, and V. Ramanathan, "Effects of fossil fuel and total anthropogenic emission removal on public health and climate," Proc. Natl. Acad. Sci., vol. 116, no. 15, pp. 7192–7197, Apr. 2019, doi: 10.1073/pnas.1819989116.

J. Liu, J. Yang, P. Sun, W. Gao, C. Yang, and J. Fang, "Compound combustion and pollutant emissions characteristics of a common-rail engine with ethanol homogeneous charge and polyoxymethylene dimethyl ethers injection," Appl. Energy, vol. 239, pp. 1154–1162, Apr. 2019, doi: 10.1016/j.apenergy.2019.02.036.

J. Luecke, M. J. Rahimi, B. T. Zigler, and R. W. Grout, "Experimental and numerical investigation of the Advanced Fuel Ignition Delay Analyzer (AFIDA) constant-volume combustion chamber as a research platform for fuel chemical kinetic mechanism validation," fuel, vol. 265, p. 116929, Apr. 2020, doi: 10.1016/j.fuel.2019.116929.

J. M. B. Kellogg, I. I. Rabi, N. F. Ramsey, and J. R. Zacharias, “An Electrical Quadrupole Moment of the Deuteron,” Phys. Rev., vol. 55, no. 3, pp. 318–319, Feb. 1939, doi: 10.1103/PhysRev.55.318.

J. M. L. Martin, "Ab initio total atomization energies of small molecules — towards the basis set limit," Chem. Phys. Lett., vol. 259, no. 5, pp. 669–678, Sep. 1996, doi: 10.1016/0009-2614(96)00898-6.

J. P. A. Lockhart, C. F. Goldsmith, J. B. Randazzo, B. Ruscic, and R. S. Tranter, "An Experimental and Theoretical Study of the Thermal Decomposition of C4H6 Isomers," J. Phys. Chem. A, vol. 121, no. 20, pp. 3827–3850, May 2017, doi: 10.1021/acs.jpca.7b01186.

J. P. Porterfield et al., "Thermal Decomposition of Potential Ester Biofuels. Part I: Methyl Acetate and Methyl Butanoate," J. Phys. Chem. A, vol. 121, no. 24, pp. 4658–4677, Jun. 2017, doi: 10.1021/acs.jpca.7b02639.

J. Ramirez et al., “1 MHz Ultrafast High Order Cascaded VUV Generation in Negative Curvature Hollow Fibers,” in Conference on Lasers and Electro-Optics, San Jose, California, 2019, p. JM3E.4. doi: 10.1364/CLEO_AT.2019.JM3E.4.

J. Vandooren, J. Peeters, and P. J. V. Tiggelen, “Rate constant of the elementary reaction of carbon monoxide with hydroxyl radical,” Symp. Int. Combust., vol. 15, no. 1, pp. 745–753, Jan. 1975, doi: 10.1016/S0082-0784(75)80343-2.

J.-H. Eom, Y.-W. Kim, and S. Raju, "Processing and properties of macroporous silicon carbide ceramics: A review," J. Asian Ceram. Soc., vol. 1, no. 3, pp. 220–242, Sep. 2013, doi: 10.1016/j.jascer.2013.07.003.

Jochnowitz, Evan B., et al. “Propargyl Radical: Ab Initio Anharmonic Modes and the Polarized Infrared Absorption Spectra of Matrix-Isolated HCCCH2.” The Journal of Physical Chemistry A, vol. 109, no. 17, 8 Apr. 2005, pp. 3812–3821, https://doi.org/10.1021/jp040719j. Accessed 8 Apr. 2023.

K. Aikawa, T. Sakurai, and J. J. Jetter, "Development of a Predictive Model for Gasoline Vehicle Particulate Matter Emissions," SAE Int. J. Fuels Lubr., vol. 3, no. 2, pp. 610–622, Oct. 2010, doi: 10.4271/2010-01-2115.

K. Alexandrino, Á. Millera, R. Bilbao, and M. U. Alzueta, Gas and soot formed in the dimethoxymethane pyrolysis. Soot characterization," Fuel Process. Technol., vol. 179, pp. 369–377, Oct. 2018, doi: 10.1016/j.fuproc.2018.07.021.

K. Anand, R. D. Reitz, E. Kurtz, and W. Willems, "Modeling Fuel and EGR Effects under Conventional and Low Temperature Combustion Conditions," Energy Fuels, vol. 27, no. 12, pp. 7827–7842, Dec. 2013, doi: 10.1021/ef401989c.

K. Biswas, "Solid State Sintering of SiC-Ceramics," Mater. Sci. Forum, vol. 624, pp. 71–89, 2009, doi: 10.4028/www.scientific.net/MSF.624.71.

K. Cai et al., "Geometrically Complex Silicon Carbide Structures Fabricated by Robocasting," J. Am. Ceram. Soc., vol. 95, no. 8, pp. 2660–2666, 2012, doi: 10.1111/j.1551-2916.2012.05276.x.

K. H. Weber and J. Zhang, "Mechanistic Study of Thermal Decomposition of Isoprene (2-Methyl-1,3-Butadiene) Using Flash Pyrolysis Supersonic Jet VUV Photoionization Mass Spectrometry," J. Phys. Chem. A, vol. 111, no. 45, pp. 11487–11492, Nov. 2007, doi: 10.1021/jp075689+.

K. Hakimov et al., "Ignition delay time and speciation of dibutyl ether at high pressures," Combust. Flame, vol. 223, pp. 98–109, Jan. 2021, doi: 10.1016/j.combustflame.2020.09.028.

K. I. Svensson, M. J. Richards, A. J. Mackrory, and D. R. Tree, "Fuel Composition and Molecular Structure Effects on Soot Formation in Direct-Injection Flames Under Diesel Engine Conditions," SAE Trans., vol. 114, pp. 594–604, 2005.

K. J. Laidler, “The development of the Arrhenius equation,” J. Chem. Educ., vol. 61, no. 6, p. 494, Jun. 1984, doi: 10.1021/ed061p494.

K. Kohse-Höinghaus et al., “Biofuel Combustion Chemistry: From Ethanol to Biodiesel,” Angew. Chem. Int. Ed., vol. 49, no. 21, pp. 3572–3597, 2010, doi: 10.1002/anie.200905335.

K. Kohse-Höinghaus, "Combustion in the future: The importance of chemistry," Proc. Combust. Inst. Int. Symp. Combust., Sep. 2020, doi: 10.1016/j.proci.2020.06.375.

K. Kohse-Höinghaus, Combustion in the future: The importance of chemistry, Proceedings of the Combustion Institute, https://doi.org/10.1016/j.proci.2020.06.375

K. N. Urness et al., “Pyrolysis of furan in a microreactor,” J. Chem. Phys., vol. 139, no. 12, p. 124305, Sep. 2013, doi: 10.1063/1.4821600.

K. N. Urness et al., “Pyrolysis Pathways of the Furanic Ether 2-Methoxyfuran,” J. Phys. Chem. A, vol. 119, no. 39, pp. 9962–9977, Oct. 2015, doi: 10.1021/acs.jpca.5b06779.

K. P. Somers et al., “A comprehensive experimental and detailed chemical kinetic modelling study of 2,5-dimethylfuran pyrolysis and oxidation,” Combust. Flame, vol. 160, no. 11, pp. 2291–2318, Nov. 2013, doi: 10.1016/j.combustflame.2013.06.007.

K. P. Somers, J. M. Simmie, W. K. Metcalfe, and H. J. Curran, “The pyrolysis of 2-methylfuran: a quantum chemical, statistical rate theory and kinetic modelling study,” Phys. Chem. Chem. Phys., vol. 16, no. 11, pp. 5349–5367, 2014, doi: 10.1039/C3CP54915A.

K. Sendt, G. B. Bacskay, and J. C. Mackie, “Pyrolysis of Furan: Ab Initio Quantum Chemical and Kinetic Modeling Studies,” J. Phys. Chem. A, vol. 104, no. 9, pp. 1861–1875, Mar. 2000, doi: 10.1021/jp993537b.

K. Umeki, G. Häggström, A. Bach-Oller, K. Kirtania, and E. Furusjö, “Reduction of Tar and Soot Formation from Entrained-Flow Gasification of Woody Biomass by Alkali Impregnation,” Energy Fuels, vol. 31, no. 5, pp. 5104–5110, May 2017, doi: 10.1021/acs.energyfuels.6b03480.

K. Yamada and M. Mohri, "Properties and Applications of Silicon Carbide Ceramics," in Silicon Carbide Ceramics—1: Fundamental and Solid Reaction, S. Sömiya and Y. Inomata, Eds. Dordrecht: Springer Netherlands, 1991, pp. 13–44. doi: 10.1007/978-94-011-3842-0_2.

Kimura, Katsumi. Handbook of HeI Photoelectron Spectra of Fundamental Organic Molecules. Halsted Press, 1981.

L. B. Harding, Y. Georgievskii, and S. J. Klippenstein, “Predictive Theory for Hydrogen Atom−Hydrocarbon Radical Association Kinetics,” J. Phys. Chem. A, vol. 109, no. 21, pp. 4646–4656, Jun. 2005, doi: 10.1021/jp0508608.

L. Dodge and D. Naegeli, "Combustion Characterization of Methylal in Reciprocating Engines," National Renewable Energy Lab. (NREL), Golden, CO (United States), NREL/TP-425-6345, Jun. 1994. doi: 10.2172/10157045.

L. Golka, D. Gratzfeld, I. Weber, and M. Olzmann, "Temperature- and pressure-dependent kinetics of the competing C–O bond fission reactions of dimethoxymethane," Phys. Chem. Chem. Phys., vol. 22, no. 10, pp. 5523–5530, Feb. 2020, doi: 10.1039/D0CP00136H.

L. Golka, I. Weber, and M. Olzmann, "Pyrolysis of dimethoxymethane and the reaction of dimethoxymethane with H atoms: A shock-tube/ARAS/TOF-MS and modeling study," Proc. Combust. Inst., vol. 37, no. 1, pp. 179–187, Jan. 2019, doi: 10.1016/j.proci.2018.05.036.

L. Lautenschütz, D. Oestreich, P. Seidenspinner, U. Arnold, E. Dinjus, and J. Sauer, "Physico-chemical properties and fuel characteristics of oxymethylene dialkyl ethers," fuel, vol. 173, pp. 129–137, Jun. 2016, doi: 10.1016/j.fuel.2016.01.060.

L. Mangani and C. Bianchini, “HEAT TRANSFER APPLICATIONS IN TURBOMACHINERY,” p. 12, 2007.

L. Marrodán, E. Royo, Á. Millera, R. Bilbao, and M. U. Alzueta, "High Pressure Oxidation of Dimethoxymethane," Energy Fuels, vol. 29, no. 5, pp. 3507–3517, May 2015, doi: 10.1021/acs.energyfuels.5b00459.

L. Marrodán, F. Monge, Á. Millera, R. Bilbao, and M. U. Alzueta, "Dimethoxymethane Oxidation in a Flow Reactor," Combust. Sci. Technol., vol. 188, no. 4–5, pp. 719–729, May 2016, doi: 10.1080/00102202.2016.1138826.

L. P. Lautenschütz, "Neue Erkenntnisse in der Syntheseoptimierung oligomerer Oxymethylendimethylether aus Dimethoxymethan und Trioxan," 2015. https://archiv.ub.uni-heidelberg.de/volltextserver/19210/ (accessed Feb. 02, 2022).

L. Wright, B. Boundy, B. Perlack, S. Davis, and B. Saulsbury, "Biomass Energy Data Book, Volume 1," p. 189.

L. Zhou, M. D. Boot, B. H. Johansson, and J. J. E. Reijnders, "Performance of lignin derived aromatic oxygenates in a heavy-duty diesel engine," Fuel, vol. 115, pp. 469–478, Jan. 2014, doi: 10.1016/j.fuel.2013.07.047.

Labbe, N. J.; Sivaramakrishnan, R.; Klippenstein, S. J. The Role of Radical+fuel-Radical Well-Skipping Reactions in Ethanol and Methylformate Low-Pressure Flames. Proceedings of the Combustion Institute 2015, 35 (1), 447–455. https://doi.org/10.1016/j.proci.2014.05.107.

Laidler, K. J., and M. T. H. Liu. "The Mechanism of the Acetaldehyde Pyrolysis." Proceedings of the Royal Society of London. Series A. Mathematical and Physical Sciences, vol. 297, no. 1450, 7 Mar. 1967, pp. 365–375, https://doi.org/10.1098/rspa.1967.0073.

Li, Yuyang, and Fei Qi. "Recent Applications of Synchrotron VUV Photoionization Mass Spectrometry: Insight into Combustion Chemistry." Accounts of Chemical Research, vol. 43, no. 1, 25 Aug. 2009, pp. 68–78, https://doi.org/10.1021/ar900130b. Accessed 14 May 2022.

Luo, Z.H., et al. "Preparation of Reaction-Bonded Silicon Carbide with Well Controlled Structure by Tape Casting Method." Ceramics International, vol. 38, no. 3, Apr. 2012, pp. 2125–2128, https://doi.org/10.1016/j.ceramint.2011.10.053. Accessed 30 Nov. 2021.

M. A. Bolshov, Yu. A. Kuritsyn, and Yu. V. Romanovskii, "Tunable diode laser spectroscopy as a technique for combustion diagnostics," Spectrochim. Acta Part B At. Spectrosc., vol. 106, pp. 45–66, Apr. 2015, doi: 10.1016/j.sab.2015.01.010.

M. A. Grela, V. T. Amorebieta, and A. J. Colussi, "Very low pressure pyrolysis of furan, 2-methylfuran and 2,5-dimethylfuran. The stability of the furan ring," J. Phys. Chem., vol. 89, no. 1, pp. 38–41, Jan. 1985, doi: 10.1021/j100247a011.

M. B. Toftegaard, J. Brix, P. A. Jensen, P. Glarborg, and A. D. Jensen, "Oxy-fuel combustion of solid fuels," Prog. Energy Combust. Sci., vol. 36, no. 5, pp. 581–625, Oct. 2010, doi: 10.1016/j.pecs.2010.02.001.

M. Balat, “Mechanisms of Thermochemical Biomass Conversion Processes. Part 1: Reactions of Pyrolysis,” Energy Sources Part Recovery Util. Environ. Eff., vol. 30, no. 7, pp. 620–635, Mar. 2008, doi: 10.1080/15567030600817258.

M. Härtl, K. Gaukel, D. Pélerin, and G. Wachtmeister, “Oxymethylenether als potenziell CO2-neutraler Kraftstoff für saubere Dieselmotoren Teil 1: Motorenuntersuchungen,” MTZ - Mot. Z., vol. 78, no. 2, pp. 52–59, Feb. 2017, doi: 10.1007/s35146-016-0170-9.

M. Härtl, P. Seidenspinner, E. Jacob, and G. Wachtmeister, "Oxygenate screening on a heavy-duty diesel engine and emission characteristics of highly oxygenated oxymethylene ether fuel OME1," fuel, vol. 153, pp. 328–335, Aug. 2015, doi: 10.1016/j.fuel.2015.03.012.

M. Iqbal, M. Konneh, A. Y. B. M. Said, and A. F. B. M. Zaini, "Surface Quality of High Speed Milling of Silicon Carbide by Using Diamond Coated Tool," in Advanced Research in Material Science and Mechanical Engineering, Pts 1 and 2, Durnten-Zurich, 2014, vol. 446–447, pp. 275-+. doi: 10.4028/www.scientific.net/AMM.446-447.275.

M. J. Frisch, Wallingford CT: Gaussian, Inc., 2016. Accessed: Nov. 13, 2019. [Online]. Available: https://gaussian.com/citation/

M. Noguchi, Y. Tanaka, T. Tanaka, and Y. Takeuchi, “A Study on Gasoline Engine Combustion by Observation of Intermediate Reactive Products during Combustion,” S.A.E. Trans., vol. 88, pp. 2816–2828, 1979.

M. Nowakowska, O. Herbinet, A. Dufour, and P.-A. Glaude, “Detailed kinetic study of anisole pyrolysis and oxidation to understand tar formation during biomass combustion and gasification,” Combust. Flame, vol. 161, no. 6, pp. 1474–1488, Jun. 2014, doi: 10.1016/j.combustflame.2013.11.024.

M. Pecullan, K. Brezinsky, and I. Glassman, “Pyrolysis and Oxidation of Anisole near 1000 K,” J. Phys. Chem. A, vol. 101, no. 18, pp. 3305–3316, May 1997, doi: 10.1021/jp963203b.
M. Tian et al., “Performance of lignin derived compounds as octane boosters,” Fuel, vol. 189, pp. 284–292, Feb. 2017, doi: 10.1016/j.fuel.2016.10.084.

M. Uchiyama, T. Tomioka, and A. Amano, "Thermal Decomposition of Cyclohexene," J. Phys. Chem., vol. 68, no. 7, pp. 1878–1881, Jul. 1964, doi: 10.1021/j100789a036.

M. W. Jarvis et al., “Direct Detection of Products from the Pyrolysis of 2-Phenethyl Phenyl Ether,” J. Phys. Chem. A, vol. 115, no. 4, pp. 428–438, Feb. 2011, doi: 10.1021/jp1076356.
M. Willander, M. Friesel, Q. Wahab, and B. Straumal, "Silicon carbide and diamond for high temperature device applications," J. Mater. Sci. Mater. Electron., vol. 17, no. 1, p. 1, Jan. 2006, doi: 10.1007/s10854-005-5137-4.

N. Hansen, T. A. Cool, P. R. Westmoreland, and K. Kohse-Höinghaus, "Recent contributions of flame-sampling molecular-beam mass spectrometry to a fundamental understanding of combustion chemistry," Prog. Energy Combust. Sci., vol. 35, no. 2, pp. 168–191, Apr. 2009, doi: 10.1016/j.pecs.2008.10.001.

N. Schmitz, J. Burger, E. Ströfer, and H. Hasse, "From methanol to the oxygenated diesel fuel poly(oxymethylene) dimethyl ether: An assessment of the production costs," fuel, vol. 185, pp. 67–72, Dec. 2016, doi: 10.1016/j.fuel.2016.07.085.

O. Stern, “Zur Methode der Molekularstrahlen. I,” Z. Fr Phys., vol. 39, no. 10–11, pp. 751–779, Oct. 1926, doi: 10.1007/BF01451747.

O. US EPA, “Evolution of the Clean Air Act,” May 29, 2015. https://www.epa.gov/clean-air-act-overview/evolution-clean-air-act (accessed Dec. 26, 2021).

O. US EPA, “Regulations for Greenhouse Gas Emissions from Passenger Cars and Trucks,” Sep. 09, 2016. https://www.epa.gov/regulations-emissions-vehicles-and-engines/regulations-greenhouse-gas-emissions-passenger-cars-and (accessed Dec. 26, 2021).

Ormond, Thomas K., et al. “Pyrolysis of Cyclopentadienone: Mechanistic Insights from a Direct Measurement of Product Branching Ratios.” The Journal of Physical Chemistry A, vol. 119, no. 28, 17 Feb. 2015, pp. 7222–7234, https://doi.org/10.1021/jp511390f. Accessed 8 Apr. 2023.

P. C. St. John, P. Kairys, D. D. Das, C. S. McEnally, L. D. Pfefferle, D. J. Robichaud, M. R. Nimlos, B. T. Zigler, R. L. McCormick, T. D. Foust, Y. J. Bomble, and S. Kim, “A quantitative model for the prediction of sooting tendency from molecular structure,” Energy & Fuels, vol. 31, no. 9, pp. 9983–9990, 2017.

P. C. St. John, Y. Guan, Y. Kim, S. Kim, and R. S. Paton, "Prediction of organic homolytic bond dissociation enthalpies at near chemical accuracy with sub-second computational cost," Nat. Commun., vol. 11, no. 1, Art. no. 1, May 2020, doi: 10.1038/s41467-020-16201-z.

P. Chen, J. B. Pallix, W. A. Chupka, and S. D. Colson, “Resonant multiphoton ionization spectrum and electronic structure of CH radical. New states and assignments above 50 000 cm − 1,” J. Chem. Phys., vol. 86, no. 2, pp. 516–520, Jan. 1987, doi: 10.1063/1.452303.

P. Chen, S. D. Colson, W. A. Chupka, and J. A. Berson, “Flash pyrolytic production of rotationally cold free radicals in a supersonic jet. Resonant multiphoton spectrum of the 3p2A2" .rarw. X2A2" origin band of methyl,” J. Phys. Chem., vol. 90, no. 11, pp. 2319–2321, May 1986, doi: 10.1021/j100402a014.

P. Dagaut et al., "A jet-stirred reactor for kinetic studies of homogeneous gas-phase reactions at pressures up to ten atmospheres ($\approx$1 MPa)," J. Phys. [E], vol. 19, no. 3, pp. 207–209, Mar. 1986, doi: 10.1088/0022-3735/19/3/009.

P. Kumar and S. Singh Sandhu, "Impact analysis of partially premixed combustion strategy on the emissions of a compression ignition engine fueled with higher octane number fuels: A review," Mater. Today Proc., vol. 45, pp. 5772–5777, Jan. 2021, doi: 10.1016/j.matpr.2021.02.621.

P. P. Organ and J. C. Mackie, “Kinetics of pyrolysis of furan,” J. Chem. Soc. Faraday Trans., vol. 87, no. 6, p. 815, 1991, doi: 10.1039/ft9918700815.

P. Pal, A. Mansfield, P. Arias, M. Wooldridge, and H. Im, "A computational study of syngas auto-ignition characteristics at high-pressure and low-temperature conditions with thermal inhomogeneities," Combust. Theory Model., vol. 19, pp. 587–601, Jul. 2015, doi: 10.1080/13647830.2015.1068373.

P. Pal, Y. Wu, T. Lu, S. Som, Y. C. See, and A. Le Moine, "Multidimensional Numerical Simulations of Knocking Combustion in a Cooperative Fuel Research Engine," J. Energy Resour. Technol., vol. 140, no. 10, May 2018, doi: 10.1115/1.4040063.

P. Weilmünster, A. Keller, and K.-H. Homann, "Large molecules, radicals, ions, and small soot particles in fuel-rich hydrocarbon flames: Part I: positive ions of polycyclic aromatic hydrocarbons(PAH) in low-pressure premixed flames of acetylene and oxygen,” Combust. Flame, vol. 116, no. 1, pp. 62–83, Jan. 1999, doi: 10.1016/S0010-2180(98)00049-2.

P. Zhang, J. Liang, L. Yin, and S. Guo, "The synthesis of micro-sized silicon carbide whiskers and the application for heat transfer enhancement," Sci. China Technol. Sci., vol. 57, no. 12, pp. 2371–2378, Dec. 2014, doi: 10.1007/s11431-014-5704-0.

Q. An, J. Chen, W. Ming, and M. Chen, "Machining of SiC ceramic matrix composites: A review," Chin. J. Aeronaut., vol. 34, no. 4, pp. 540–567, Apr. 2021, doi: 10.1016/j.cja.2020.08.001.

Q. Guan, K. N. Urness, T. K. Ormond, D. E. David, G. Barney Ellison, and J. W. Daily, “The properties of a micro-reactor for the study of the unimolecular decomposition of large molecules,” Int. Rev. Phys. Chem., vol. 33, no. 4, pp. 447–487, Oct. 2014, doi: 10.1080/0144235X.2014.967951.

R. A. Alliegro, L. B. Coffin, and J. R. Tinklepaugh, "Pressure-Sintered Silicon Carbide," J. Am. Ceram. Soc., vol. 39, no. 11, pp. 386–389, 1956, doi: 10.1111/j.1151-2916.1956.tb15609.x.

R. Beelen et al., "Effects of long-term exposure to air pollution on natural-cause mortality: an analysis of 22 European cohorts within the multicentre ESCAPE project," The Lancet, vol. 383, no. 9919, pp. 785–795, Mar. 2014, doi: 10.1016/S0140-6736(13)62158-3.

R. Burnett et al., "Global estimates of mortality associated with long-term exposure to outdoor fine particulate matter," Proc. Natl. Acad. Sci., vol. 115, no. 38, pp. 9592–9597, Sep. 2018, doi: 10.1073/pnas.1803222115.

R. D. Reitz and G. Duraisamy, "Review of high efficiency and clean reactivity controlled compression ignition (RCCI) combustion in internal combustion engines," Prog. Energy Combust. Sci., vol. 46, pp. 12–71, Feb. 2015, doi: 10.1016/j.pecs.2014.05.003.

R. D. Reitz, "Directions in internal combustion engine research," Combust. Flame, vol. 160, no. 1, pp. 1–8, Jan. 2013, doi: 10.1016/j.combustflame.2012.11.002.

R. E. Winters and J. H. Collins, "Mass spectrometric studies of structural isomers. I. Mono- and bicyclic C7H12 molecules," J. Am. Chem. Soc., vol. 90, no. 5, pp. 1235–1239, Feb. 1968, doi: 10.1021/ja01007a022.

R. Friedman and J. A. Cyphers, "Flame Structure Studies. III. Gas Sampling in a Low-Pressure Propane-Air Flame," J. Chem. Phys., vol. 23, no. 10, pp. 1875–1880, Oct. 1955, doi: 10.1063/1.1740596.

R. G. Gilbert, K. Luther, and J. Troe, “Theory of Thermal Unimolecular Reactions in the Fall-off Range. II. Weak Collision Rate Constants,” Berichte Bunsenges. Für Phys. Chem., vol. 87, no. 2, pp. 169–177, 1983, doi: 10.1002/bbpc.19830870218.

R. Gutierrez, T. Frauenheim, T. Köhler, and G. Seifert, "Stability of silicon carbide structures: from clusters to solid surfaces," J. Mater. Chem., vol. 6, no. 10, pp. 1657–1663, Jan. 1996, doi: 10.1039/JM9960601657.

R. H. Nielsen, J. H. Schlewitz, H. Nielsen, and U. by Staff, “Zirconium and Zirconium Compounds,” in Kirk-Othmer Encyclopedia of Chemical Technology, John Wiley & Sons, Ltd, 2007. doi: 10.1002/0471238961.26091803.a01.pub2.

R. He et al., "Progress and challenges towards additive manufacturing of SiC ceramic," J. Adv. Ceram., vol. 10, no. 4, pp. 637–674, Aug. 2021, doi: 10.1007/s40145-021-0484-z.

R. J. Tancin, G. C. Mathews, and C. S. Goldenstein, "Design and application of a high-pressure combustion chamber for studying propellant flames with laser diagnostics," Rev. Sci. Instrum., vol. 90, no. 4, p. 045111, Apr. 2019, doi: 10.1063/1.5081671.

R. K. Hanson, "Applications of quantitative laser sensors to kinetics, propulsion and practical energy systems," Proc. Combust. Inst., vol. 33, no. 1, pp. 1–40, Jan. 2011, doi: 10.1016/j.proci.2010.09.007.

R. Liu, X. Zhou, and L. Zhai, “Theoretical investigation of unimolecular decomposition channels of furan4,” J. Comput. Chem., vol. 19, no. 2, pp. 240–249, 1998, doi: 10.1002/(SICI)1096-987X(19980130)19:2<240::AID-JCC17>3.0.CO;2-L.

R. Luque et al., “Biofuels: a technological perspective,” Energy Environ. Sci., vol. 1, no. 5, p. 542, 2008, doi: 10.1039/b807094f.

R. M. Fristrom, "The structure of laminar flames," Symp. Int. Combust., vol. 6, no. 1, pp. 96–110, Jan. 1957, doi: 10.1016/S0082-0784(57)80016-2.

R. Maurya, A. Gupta, S. Omar, and K. Balani, “Effect of sintering on mechanical properties of ceria reinforced yttria stabilized zirconia,” Ceram. Int., vol. 42, no. 9, pp. 11393–11403, Jul. 2016, doi: 10.1016/j.ceramint.2016.04.069.

R. Moene, M. Makkee, and J. A. Moulijn, "High surface area silicon carbide as catalyst support characterization and stability," Appl. Catal. Gen., vol. 167, no. 2, pp. 321–330, Feb. 1998, doi: 10.1016/S0926-860X(97)00326-8.

R. R. Baker, R. R. Baldwin, C. J. Everett, and R. W. Walker, "The addition of neopentane to slowly reacting mixtures of hydrogen and oxygen at 480°C—I: Formation of primary products from neopentane," Combust. Flame, vol. 25, pp. 285–300, Aug. 1975, doi: 10.1016/0010-2180(75)90100-5.

R. R. Baldwin and R. F. Simmons, "Inhibition of the First Limit of the Hydrogen–Oxygen Reaction by Ethane," Nature, vol. 175, no. 4451, pp. 346–347, Feb. 1955, doi: 10.1038/175346b0.

R. S. Evans, D. L. Bourell, J. J. Beaman, and M. I. Campbell, "Rapid manufacturing of silicon carbide composites," Rapid Prototype. J., vol. 11, no. 1, pp. 37–40, Jan. 2005, doi: 10.1108/13552540510573374.

R. S. Tranter et al., “Measuring flow profiles in heated miniature reactors with X-ray fluorescence spectroscopy,” Proc. Combust. Inst., vol. 36, no. 3, pp. 4603–4610, 2017, doi: 10.1016/j.proci.2016.06.104.

R. Van de Vijver and J. Zádor, "KinBot: Automated stationary point search on potential energy surfaces," Comput. Phys. Commun., vol. 248, p. 106947, Mar. 2020, doi: 10.1016/j.cpc.2019.106947.

R.-J. Huang et al., "High secondary aerosol contribution to particulate pollution during haze events in China," Nature, vol. 514, no. 7521, Art. no. 7521, Oct. 2014, doi: 10.1038/nature13774.

Roberge, Dominique M., et al. "Micro-reactor technology: a revolution for the fine chemical and pharmaceutical industries?" Chemical engineering & technology 28.3 (2005): 318-323.

S. D. Chambreau, J. Lemieux, L. Wang, and J. Zhang, "Mechanistic studies of the pyrolysis of 1,3-butadiene, 1,3-butadiene-1,1,4,4-d4, 1,2-butadiene, and 2-butyne by supersonic jet/photoionization mass spectrometry," J. Phys. Chem. A, vol. 109, no. 10, pp. 2190–2196, Mar. 2005, doi: 10.1021/jp045010r.

S. de Persis, A. Dollet, and F. Teyssandier, “Pressure Dependence of Gas-Phase Reaction Rates,” J. Chem. Educ., vol. 81, no. 6, p. 832, Jun. 2004, doi: 10.1021/ed081p832.

S. Deutz et al., "Cleaner production of cleaner fuels: wind-to-wheel – environmental assessment of CO 2 -based oxymethylene ether as a drop-in fuel," Energy Environ. Sci., vol. 11, no. 2, pp. 331–343, 2018, doi: 10.1039/C7EE01657C.

S. Ding, Y.-P. Zeng, and D. Jiang, "Thermal shock resistance of in situ reaction bonded porous silicon carbide ceramics," Mater. Sci. Eng. A, vol. 425, no. 1, pp. 326–329, Jun. 2006, doi: 10.1016/j.msea.2006.03.075.

S. Dooley et al., “A jet fuel surrogate formulated by real fuel properties,” Combust. Flame, vol. 157, no. 12, pp. 2333–2339, Dec. 2010, doi: 10.1016/j.combustflame.2010.07.001.

S. Fuzzi et al., "Particulate matter, air quality and climate: lessons learned and future needs," Atmospheric Chem. Phys., vol. 15, no. 14, pp. 8217–8299, Jul. 2015, doi: 10.5194/acp-15-8217-2015.

S. H. Chung, “Several applications of laser diagnostics for visualization of combustion phenomena,” J. Vis., vol. 6, no. 2, pp. 95–106, Jun. 2003, doi: 10.1007/BF03181614.

S. H. Gardiner, M. L. Lipciuc, and C. Vallance, "Gas-Phase Retro-Diels-Alder Reactions of Cyclohexene, 1-Methylcyclohexene, and 4-Methylcyclohexene following Photoexcitation at 193 nm: A Velocity-Map Imaging Study," J. Phys. Chem. A, vol. 119, no. 50, pp. 12218–12223, Dec. 2015, doi: 10.1021/acs.jpca.5b06185.

S. J. Klippenstein, "From theoretical reaction dynamics to chemical modeling of combustion," Proc. Combust. Inst., vol. 36, no. 1, pp. 77–111, Jan. 2017, doi: 10.1016/j.proci.2016.07.100.

S. Jacobs et al., "A Comprehensive Experimental and Kinetic Modeling Study of the Combustion Chemistry of Diethoxymethane," Energy Fuels, vol. 35, no. 19, pp. 16086–16100, Oct. 2021, doi: 10.1021/acs.energyfuels.1c01988.

S. Kim et al., "Experimental and theoretical insight into the soot tendencies of the methylcyclohexene isomers," Proc. Combust. Inst., vol. 37, no. 1, pp. 1083–1090, Jan. 2019, doi: 10.1016/j.proci.2018.06.095.

S. Meyers, L. De Leersnijder, J. Vleugels, and J.-P. Kruth, "Direct laser sintering of reaction bonded silicon carbide with low residual silicon content," J. Eur. Ceram. Soc., vol. 38, no. 11, pp. 3709–3717, Sep. 2018, doi: 10.1016/j.jeurceramsoc.2018.04.055.

S. N, P. A. Arnold, B. K. Carpenter, M. R. Nimlos, D. C. Dayton, and G. B. Ellison, “Polarized Infrared Absorption Spectra of Matrix-Isolated Allyl Radicals.” 2001.

S. N. Foner and R. L. Hudson, "The Detection of Atoms and Free Radicals in Flames by Mass Spectrometric Techniques," J. Chem. Phys., vol. 21, no. 8, pp. 1374–1382, Aug. 1953, doi: 10.1063/1.1699226.

S. Onishi, S. H. Jo, K. Shoda, P. D. Jo, and S. Kato, “Active Thermo-Atmosphere Combustion (ATAC) — A New Combustion Process for Internal Combustion Engines,” S.A.E. Trans., vol. 88, pp. 1851–1860, 1979.

S. R. Logan, “The origin and status of the Arrhenius equation,” J. Chem. Educ., vol. 59, no. 4, p. 279, Apr. 1982, doi: 10.1021/ed059p279.

S. S. Penner, C. P. Wang, and M. Y. Bahadori, “Laser diagnostics applied to combustion systems,” Symp. Int. Combust., vol. 20, no. 1, pp. 1149–1176, Jan. 1985, doi: 10.1016/S0082-0784(85)80605-6.

S. Suyama, T. Kameda, and Y. Itoh, "Development of high-strength reaction-sintered silicon carbide," Diam. Relat. Mater., vol. 12, no. 3, pp. 1201–1204, Mar. 2003, doi: 10.1016/S0925-9635(03)00066-9.

S. T. Pratt, P. M. Dehmer, and J. L. Dehmer, "Zero-kinetic-energy photoelectron spectroscopy from the Ã 1Au state of acetylene: Renner–Teller interactions in the trans-bending vibration of C2H+2 X̃ 2Πu," J. Chem. Phys., vol. 99, no. 9, pp. 6233–6244, Nov. 1993, doi: 10.1063/1.465888.

S. W. Wagnon et al., "Experimental and modeling studies of a biofuel surrogate compound: laminar burning velocities and jet-stirred reactor measurements of anisole," Combust. Flame, vol. 189, pp. 325–336, Mar. 2018, doi: 10.1016/j.combustflame.2017.10.020.

Sivaramakrishnan, R., et al. "Shock Tube and Theoretical Studies on the Thermal Decomposition of Propane: Evidence for a Roaming Radical Channel." The Journal of Physical Chemistry A, vol. 115, no. 15, 29 Mar. 2011, pp. 3366–3379, https://doi.org/10.1021/jp2006205. Accessed 27 Feb. 2023.

T. A. Cool et al., "Photoionization mass spectrometer for studies of flame chemistry with a synchrotron light source," Rev. Sci. Instrum., vol. 76, no. 9, p. 094102, Sep. 2005, doi: 10.1063/1.2010307.

T. A. Cool et al., "Selective detection of isomers with photoionization mass spectrometry for studies of hydrocarbon flame chemistry," J. Chem. Phys., vol. 119, no. 16, pp. 8356–8365, Oct. 2003, doi: 10.1063/1.1611173.

T. B. Hunter, H. Wang, T. A. Litzinger, and M. Frenklach, "The oxidation of methane at elevated pressures: Experiments and modeling," Combust. Flame, vol. 97, no. 2, pp. 201–224, May 1994, doi: 10.1016/0010-2180(94)90005-1.

T. Bierkandt, P. Hemberger, P. Oßwald, D. Krüger, M. Köhler, and T. Kasper, "Flame structure of laminar premixed anisole flames investigated by photoionization mass spectrometry and photoelectron spectroscopy," Proc. Combust. Inst., vol. 37, no. 2, pp. 1579–1587, Jan. 2019, doi: 10.1016/j.proci.2018.07.037.

T. D. Gordon et al., "Secondary organic aerosol production from diesel vehicle exhaust: impact of aftertreatment, fuel chemistry and driving cycle," Atmospheric Chem. Phys., vol. 14, no. 9, pp. 4643–4659, May 2014, doi: 10.5194/acp-14-4643-2014.

T. Fan, "Design of a Novel Microreactor to Study Short Residence Time Combustion.", 2016

T. G. Leone et al., "The Effect of Compression Ratio, Fuel Octane Rating, and Ethanol Content on Spark-Ignition Engine Efficiency," Environ. Sci. Technol., vol. 49, no. 18, pp. 10778–10789, Sep. 2015, doi: 10.1021/acs.est.5b01420.

T. S. Kasper, P. Oßwald, M. Kamphus, and K. Kohse-Höinghaus, “Ethanol flame structure investigated by molecular beam mass spectrometry,” Combust. Flame, vol. 150, no. 3, pp. 220–231, Aug. 2007, doi: 10.1016/j.combustflame.2006.12.022.

T. W. Chan, E. Meloche, J. Kubsh, and R. Brezny, "Black Carbon Emissions in Gasoline Exhaust and a Reduction Alternative with a Gasoline Particulate Filter," Environ. Sci. Technol., vol. 48, no. 10, pp. 6027–6034, May 2014, doi: 10.1021/es501791b.

T. Whalen, W. Trela, and J. Baer, "Injection-Molding of Silicon-Carbide - Statistical Design of Experiments," Int. J. Powder Metall., vol. 27, no. 2, pp. 155–158, Apr. 1991.

T. Yu, X. Wu, X. Zhou, A. Bodi, and P. Hemberger, "Hydrogen migration as a potential driving force in the thermal decomposition of dimethoxymethane: New insights from pyrolysis imaging photoelectron photoion coincidence spectroscopy and computations," Combust. Flame, vol. 222, pp. 123–132, Sep. 2020, doi: 10.1016/j.combustflame.2020.08.040.

Tang, Zhu Xing, Xia Zhao, Hui Hui Tan, and He Zhang. "Technology Research of Silicon Carbide by Extruding." Advanced Materials Research. Trans Tech Publications, Ltd., September 2011. https://doi.org/10.4028/www.scientific.net/amr.335-336.717.

Th. Ackermann, "S. W. Benson: Thermochemical Kinetics. Methods for the Estimation of Thermochemical Data and Rate Parameters. John Wiley & Sons, Inc., New York, 1968. XII und 223 Seiten, 4 Abbildungen. Preis: 94 s,” Berichte Bunsenges. Für Phys. Chem., vol. 73, no. 2, pp. 241–241, 1969, doi: 10.1002/bbpc.19690730226.

Truhlar, Donald G., et al. “Current Status of Transition-State Theory.” The Journal of Physical Chemistry, vol. 87, no. 15, July 1983, pp. 2664–2682, https://doi.org/10.1021/j100238a003. Accessed 3 Dec. 2021.

Tsang et al,’Unimolecular Rate Expression for Cyclohexene Decomposition and Its Use in Chemical Thermometry under Shock Tube Conditions’, 2015

U. Bonne, K. H. Homann, and H. Gg. Wagner, ""Carbon formation in premixed flames," Symp. Int. Combust., vol. 10, no. 1, pp. 503–512, Jan. 1965, doi: 10.1016/S0082-0784(65)80197-7.

U. Paik, H.-C. Park, S.-C. Choi, C.-G. Ha, J.-W. Kim, and Y.-G. Jung, "Effect of particle dispersion on microstructure and strength of reaction-bonded silicon carbide," Mater. Sci. Eng. A, vol. 334, no. 1, pp. 267–274, Sep. 2002, doi: 10.1016/S0921-5093(01)01897-4.

Uchiyama et al,' Thermal Decomposition of Cyclohexene', 1964

V. A. Izhevskyi, L. A. Genova, J. C. Bressiani, and A. H. A. Bressiani, "Review article: silicon carbide. Structure, properties and processing," Cerâmica, vol. 46, pp. 4–13, Mar. 2000, doi: 10.1590/S0366-69132000000100002.

V. D. Knyazev, “Energy Dependence of .ltbbrac..DELTA.E.rtbbrac.down and the Shape of Falloff Curves: Implications for Modeling of Experimental Data,” J. Phys. Chem., vol. 99, no. 40, pp. 14738–14741, Oct. 1995, doi: 10.1021/j100040a023.

V. Detilleux and J. Vandooren, “Molecular Beam Mass Spectrometry Analysis of Pah Production Pathways in C 6 H 6 /O 2 /Ar and C 6 H 6 /C 2 H 2 /O 2 /Ar Flames,” Combust. Sci. Technol., vol. 180, no. 7, pp. 1347–1369, May 2008, doi: 10.1080/00102200802043284.

V. Dias and C. Renard, "Modeling of Rich Premixed C2H4/O2/Ar and C2H4/Dimethoxymethane/O2/Ar Flames".

V. Sick, “High Speed Imaging in Fundamental and Applied Combustion Research.” Proceedings of the Combustion Institute, vol. 34, no. 2, Jan. 2013, pp. 3509–3530, https://doi.org/10.1016/j.proci.2012.08.012. Accessed 15 Feb. 2023.

Vasiliou, A., et al. “Thermal Decomposition of Furan Generates Propargyl Radicals.” The Journal of Applied Physical Chemistry, vol. 113, no. 30, 6 July 2009, pp. 8540–8547, https://doi.org/10.1021/jp903401h. Accessed 8 Apr. 2023.

Vasiliou, A.; Nimlos, M. R.; Daily, J. W.; Ellison, G. B. "Thermal Decomposition of Furan Generates Propargyl Radicals"

Vasiliou, AnGayle, et al. “The Products of the Thermal Decomposition of CH3CHO.” The Journal of Chemical Physics, vol. 135, no. 1, 7 July 2011, p. 014306, https://doi.org/10.1063/1.3604005. Accessed 8 Apr. 2023.

W. A. Kopp et al., "Detailed kinetic modeling of dimethoxymethane. Part I: Ab initio thermochemistry and kinetics predictions for key reactions," Combust. Flame, vol. 189, pp. 433–442, Mar. 2018, doi: 10.1016/j.combustflame.2017.07.037.

W. A. Noyes and P. A. Leighton, The photochemistry of gases. New York: Reinhold Pub. Corp., 1941.

W. Cai and C. F. Kaminski, "Tomographic absorption spectroscopy for the study of gas dynamics and reactive flows," Prog. Energy Combust. Sci., vol. 59, pp. 1–31, Mar. 2017, doi: 10.1016/j.pecs.2016.11.002.

W. G. Mallard, J. H. Miller, and K. C. Smyth, "The ns Rydberg series of 1,3-trans-butadiene observed using multiphoton ionization," J. Chem. Phys., vol. 79, no. 12, pp. 5900–5905, Dec. 1983, doi: 10.1063/1.445770.

W. H. Green et al., "Computer Construction of Detailed Chemical Kinetic Models for Gas-Phase Reactors," Ind. Eng. Chem. Res., vol. 40, no. 23, pp. 5362–5370, Nov. 2001, doi: 10.1021/ie001088s.

W. Sun, T. Tao, M. Lailliau, N. Hansen, B. Yang, and P. Dagaut, "Exploration of the oxidation chemistry of dimethoxymethane: Jet-stirred reactor experiments and kinetic modeling," Combust. Flame, vol. 193, pp. 491–501, Jul. 2018, doi: 10.1016/j.combustflame.2018.04.008.

W. Wesch, "Silicon carbide: synthesis and processing," Nucl. Instrum. Methods Phys. Res. Sect. B Beam Interact. Mater. At., vol. 116, no. 1, pp. 305–321, Aug. 1996, doi: 10.1016/0168-583X(96)00065-1.

X. Li, K. Zhang, H. Konietzky, Y. Wang, and X. Li, "Experimental study on the dynamic mechanical behaviors of silicon carbide ceramic after thermal shock," Nucl. Mater. Energy, vol. 24, p. 100774, Aug. 2020, doi: 10.1016/j.nme.2020.100774.

X. She, A. Q. Huang, Ó. Lucía, and B. Ozpineci, "Review of Silicon Carbide Power Devices and Their Applications," IEEE Trans. Ind. Electron., vol. 64, no. 10, pp. 8193–8205, Oct. 2017, doi: 10.1109/TIE.2017.2652401.

X. Xing, M.-K. Bahng, B. Reed, C. S. Lam, K.-C. Lau, and C. Y. Ng, “Rovibrationally selected and resolved pulsed field ionization-photoelectron study of propyne: Ionization energy and spin-orbit interaction in propyne cation,” J. Chem. Phys., vol. 128, no. 9, p. 094311, Mar. 2008, doi: 10.1063/1.2836429.

X. Zhang et al., “Intense, hyperthermal source of organic radicals for matrix-isolation spectroscopy,” Rev. Sci. Instrum., vol. 74, no. 6, pp. 3077–3086, Jun. 2003, doi: 10.1063/1.1574397.

Y. Chen, B. Deng, M. Chen, and K. Hou, "An approach to estimate CCV (cycle-to-cycle variation) of effective energy output of thermal engine: A case study on a high speed gasoline engine," Case Stud. Therm. Eng., vol. 28, p. 101624, Dec. 2021, doi: 10.1016/j.csite.2021.101624.

Y. Georgievskii, J. A. Miller, M. P. Burke, and S. J. Klippenstein, "Reformulation and solution of the master equation for multiple-well chemical reactions," J. Phys. Chem. A, vol. 117, no. 46, pp. 12146–12154, Nov. 2013, doi: 10.1021/jp4060704.

Y. Georgievskii, J. A. Miller, M. P. Burke, and S. J. Klippenstein, "Reformulation and solution of the master equation for multiple-well chemical reactions," J. Phys. Chem. A, vol. 117, no. 46, pp. 12146–12154, Nov. 2013, doi: 10.1021/jp4060704.

Y. Hidaka, T. Higashihara, N. Ninomiya, H. Masaoka, T. Nakamura, and H. Kawano, "Shock tube and modeling study of 1,3-butadiene pyrolysis," Int. J. Chem. Kinet., vol. 28, no. 2, pp. 137–151, 1996, doi: 10.1002/(SICI)1097-4601(1996)28:2<137::AID-KIN9>3.0.CO;2-W.

Y. Yang, A. L. Boehman, and R. J. Santoro, "A study of jet fuel sooting tendency using the threshold sooting index (TSI) model," Combust. Flame, vol. 149, no. 1, pp. 191–205, Apr. 2007, doi: 10.1016/j.combustflame.2006.11.007.

Yuan, Wenhao, et al. “Experimental and Kinetic Modeling Investigation on Anisole Pyrolysis: Implications on Phenoxy and Cyclopentadienyl Chemistry.” Combustion and Flame, vol. 201, Mar. 2019, pp. 187–199, https://doi.org/10.1016/j.combustflame.2018.12.028. Accessed 8 Apr. 2023.

Z. Chen et al., "3D printing of ceramics: A review," J. Eur. Ceram. Soc., vol. 39, no. 4, pp. 661–687, Apr. 2019, doi: 10.1016/j.jeurceramsoc.2018.11.013.

Z. Cheng et al., “Experimental and kinetic modeling studies of furan pyrolysis: Fuel decomposition and aromatic ring formation,” Fuel, vol. 206, pp. 239–247, Oct. 2017, doi: 10.1016/j.fuel.2017.05.090.

Z. Cheng et al., “Experimental and kinetic modeling studies of low-pressure premixed laminar 2-methylfuran flames,” Proc. Combust. Inst., vol. 36, no. 1, pp. 1295–1302, Jan. 2017, doi: 10.1016/j.proci.2016.07.032.

Z. Cheng et al., “Experimental and Kinetic Modeling Study of 2-Methylfuran Pyrolysis at Low and Atmospheric Pressures,” Energy Fuels, vol. 31, no. 1, pp. 896–903, Jan. 2017, doi: 10.1021/acs.energyfuels.6b02399.

Z. Tian et al., “An experimental and kinetic investigation of premixed furan/oxygen/argon flames,” Combust. Flame, vol. 158, no. 4, pp. 756–773, Apr. 2011, doi: 10.1016/j.combustflame.2010.12.022.

Z. Tian, S. Zhu, J. Li, and Y. Yan, "Decomposition of 3-methylcyclohexene radicals: Beginning of its mechanism development," Fuel, vol. 271, p. 117591, Jul. 2020, doi: 10.1016/j.fuel.2020.117591.

Z. Wang, H. Liu, X. Ma, J. Wang, S. Shuai, and R. D. Reitz, "Homogeneous charge compression ignition (HCCI) combustion of polyoxymethylene dimethyl ethers (PODE)," Fuel, vol. 183, pp. 206–213, Nov. 2016, doi: 10.1016/j.fuel.2016.06.033.

Z. Yong, H. Xinbo, X. Qu, and Z. Zhen, "Research on ceramic injection molding of silicon carbide," RARE Met. Mater. Eng., vol. 36, pp. 326–329, Aug. 2007.

Z. Z. Yang, L. S. Wang, Y. T. Lee, D. A. Shirley, S. Y. Huang, and W. A. Lester, "Molecular Beam Photoelectron Spectroscopy of Allene," Aug. 1989, Accessed: Sep. 29, 2021. [Online]. Available: https://escholarship.org/uc/item/5xp6476b

Z. Zhang et al., "Influence of Carbon Content on Ceramic Injection Molding of Reaction-Bonded Silicon Carbide," Int. J. Appl. Ceram. Technol., vol. 13, no. 5, pp. 838–843, 2016, doi: 10.1111/ijac.12570.

Z. Zhang, W. Yan, Q. Chen, N. Zhou, and Y. Xu, “The relationship between exposure to particulate matter and breast cancer incidence and mortality,” Medicine (Baltimore), vol. 98, no. 50, p. e18349, Dec. 2019, doi: 10.1097/MD.0000000000018349.

Zhang, Taichang, et al. “Pyrolysis of Methyl Tert-Butyl Ether (MTBE). 1. Experimental Study with Molecular-Beam Mass Spectrometry and Tunable Synchrotron VUV Photoionization.” The Journal of Physical Chemistry A, vol. 112, no. 42, 30 Sept. 2008, pp. 10487–10494, https://doi.org/10.1021/jp803622w. Accessed 14 May 2022.

Zhang, Xu, et al. “Unimolecular Thermal Fragmentation Of ortho-Benzyne.” The Journal of Chemical Physics, vol. 126, no. 4, 28 Jan. 2007, p. 044312, https://doi.org/10.1063/1.2409927. Accessed 5 Nov. 2019.

Appendix

C4: Experimental and theoretical evaluation of the links between structural details and the sooting tendency of methylcyclohexene isomers

Photoionization Mass Spectra

This section contains photoionization mass spectra results for each isomer at all three wavelengths used in this study: 9.6 eV, 10.8 eV, and 10.487 eV (using Nd:YAg laser). Additionally, the line-plots showing the percentage (%) of the total maximum peak signal height as a function of temperature for relevant masses from the 9.6 and 10.8 eV wavelengths are presented.

A4.1A) 1MCHe experimental temperature sweeps

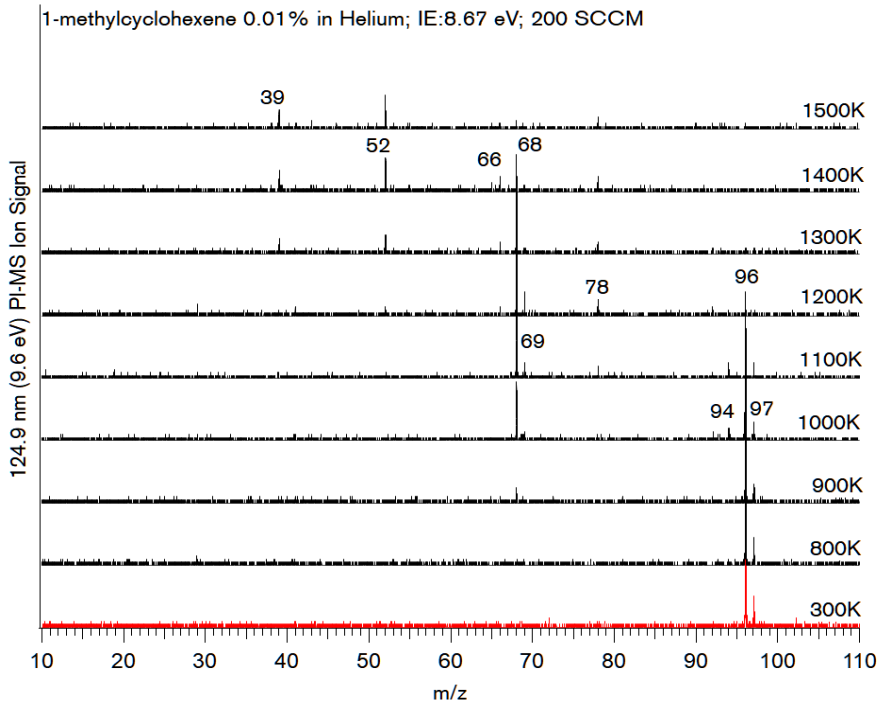

Figure A4C1: PIMS of 0.01% 1-methylcyclohexene in He in the microreactor at 200 SCCM heated between 300K and 1500K and ionized by 124.9 nm (9.6 eV) photons.

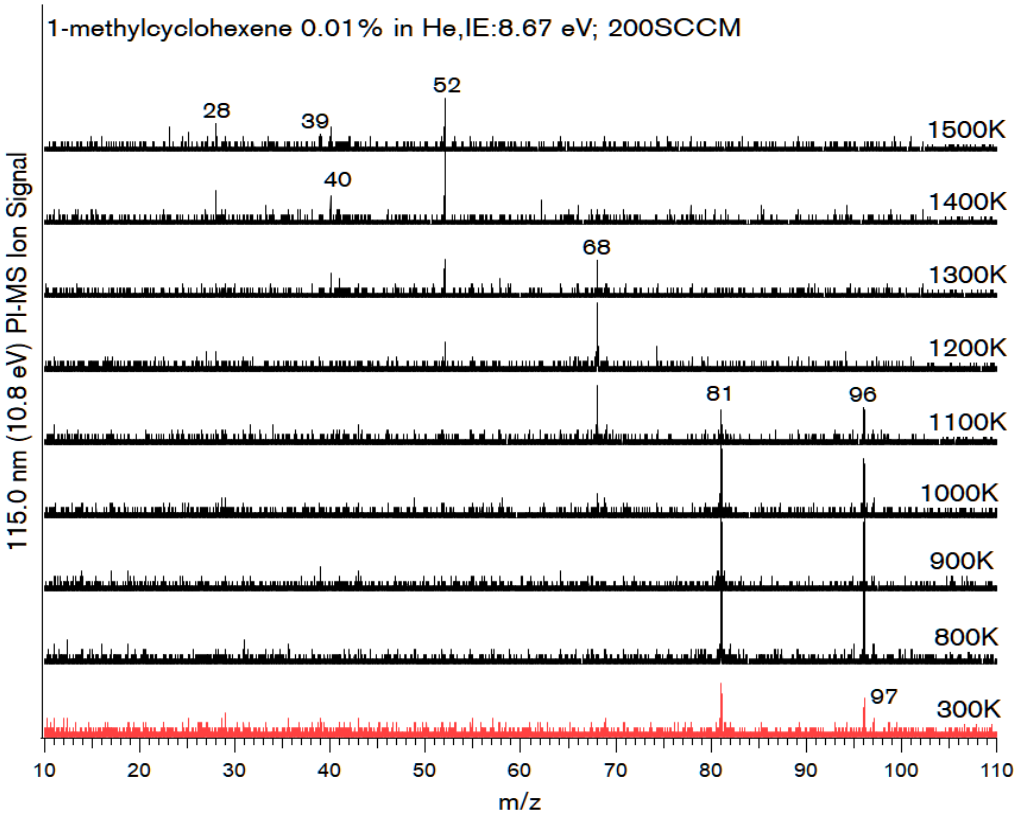

Figure A4C2: PIMS of 0.01% 1-methylcyclohexene in He in the microreactor at 200 SCCM heated between 300K and 1500K and ionized by 115.0 nm (10.8eV) photons.

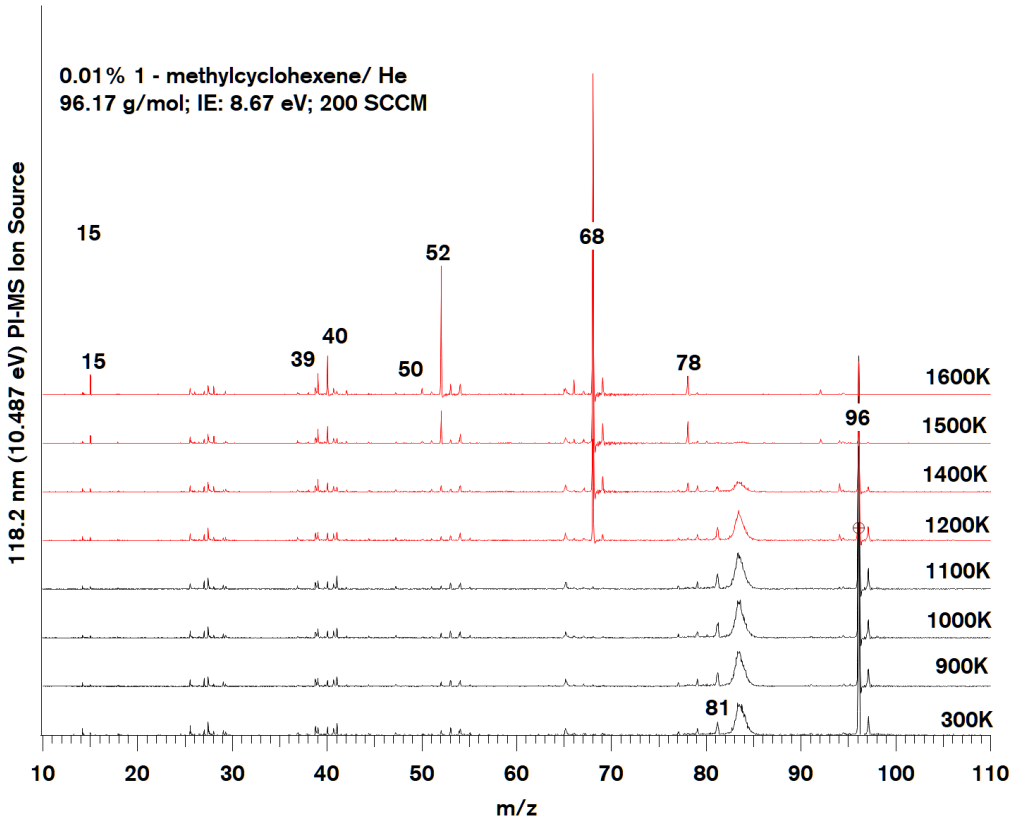

Figure A4C3: PIMS of 0.01% 1-methylcyclohexene in He in the microreactor at 200 SCCM heated between 300K and 1600K and ionized by 118.2 nm (10.487 eV) photons.

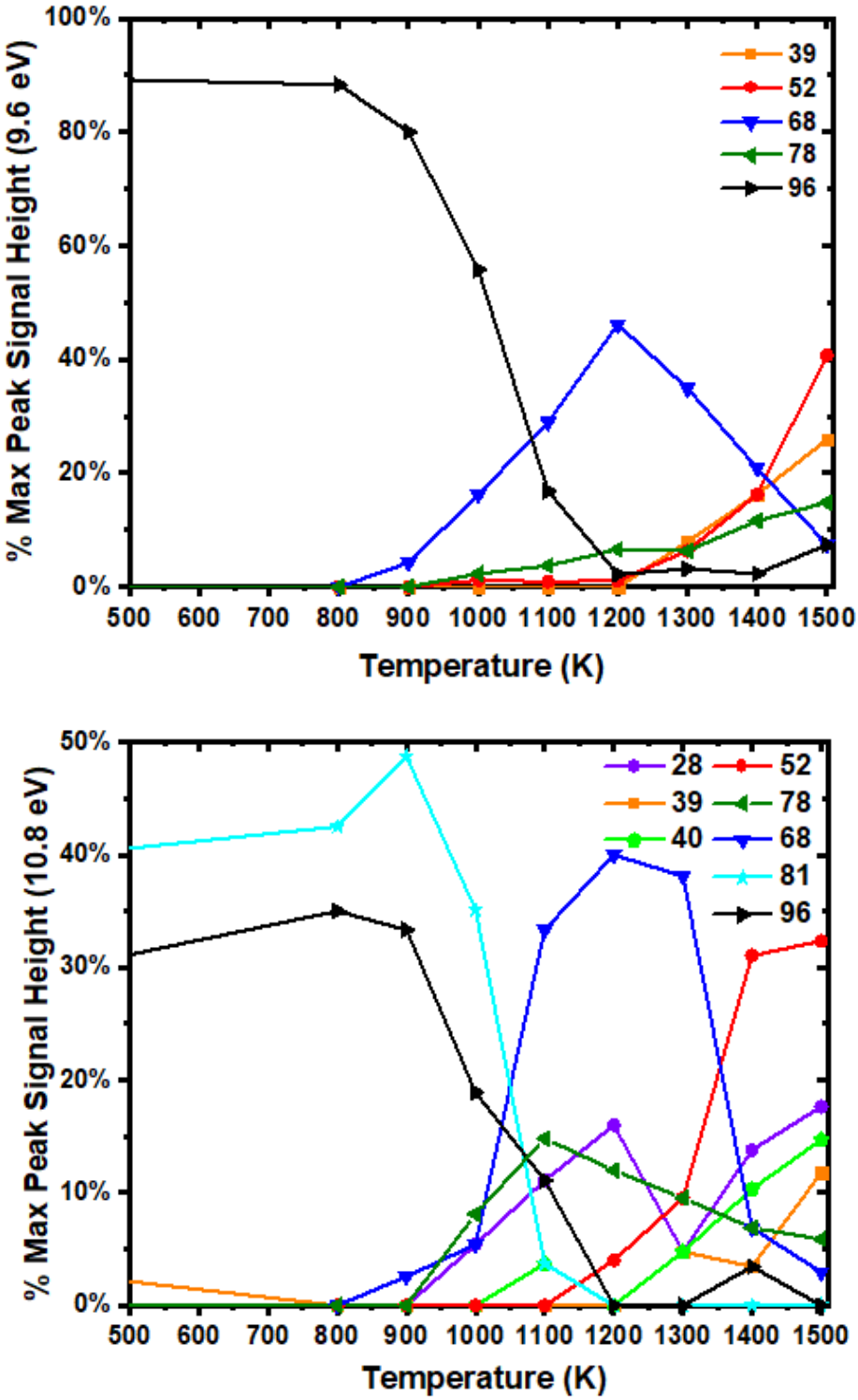

Figure A4C4: Percentage (%) of the total maximum peak signal height as a function of temperature are shown for significant mass values from 1MCHe spectra (IE= 8.67 ± 0.02 eV [35]). Top: 9.6 eV. Bottom: 10.8 eV. The presence **of dissociative** ionization is detected in the 10.8 eV plot by the presence of m/z 81 at room temperature.

A4.1B) 4MCHe experimental temperature sweeps

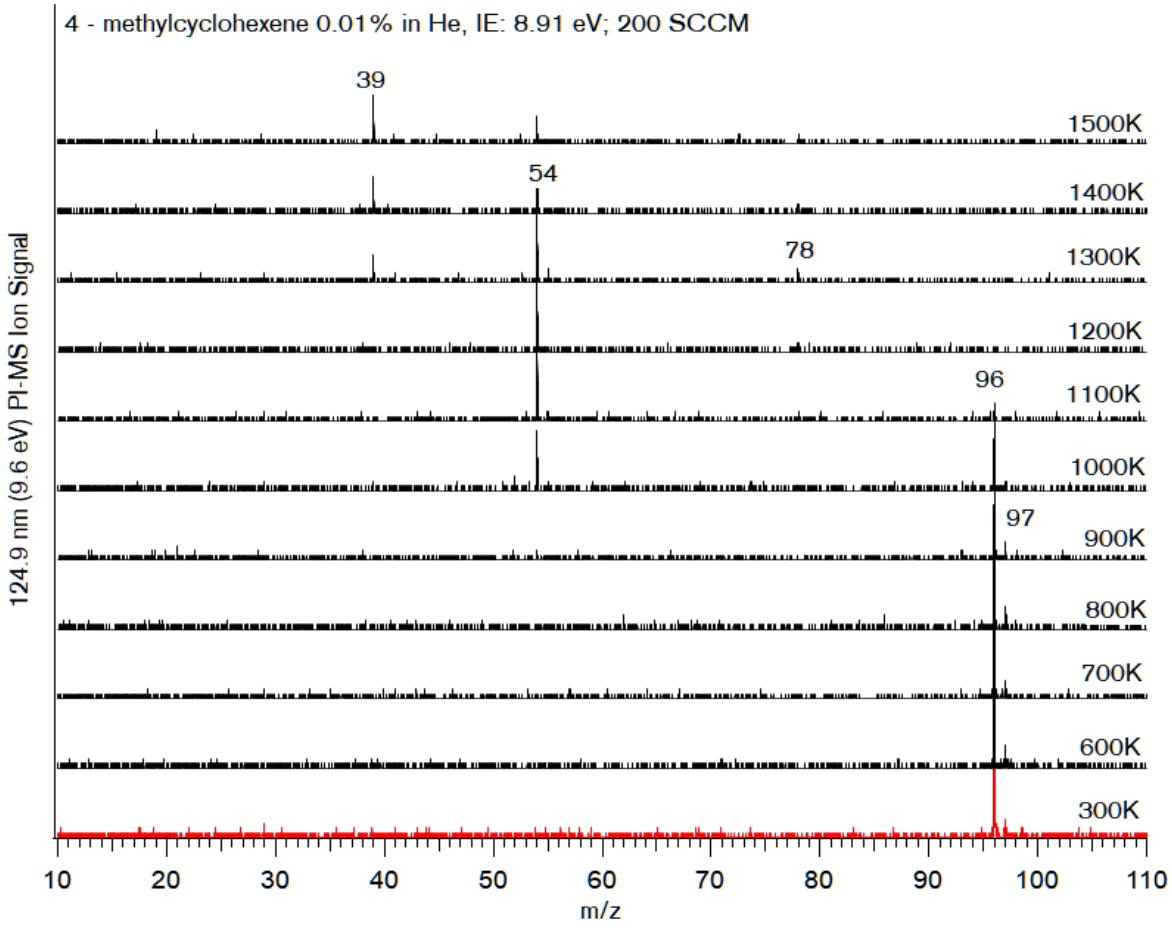

Figure A4C5: PIMS of 0.01% 4-methylcyclohexene in He in the microreactor at 200 SCCM heated between 300K and 1500K and ionized by 124.9 nm (9.6 eV) photons.

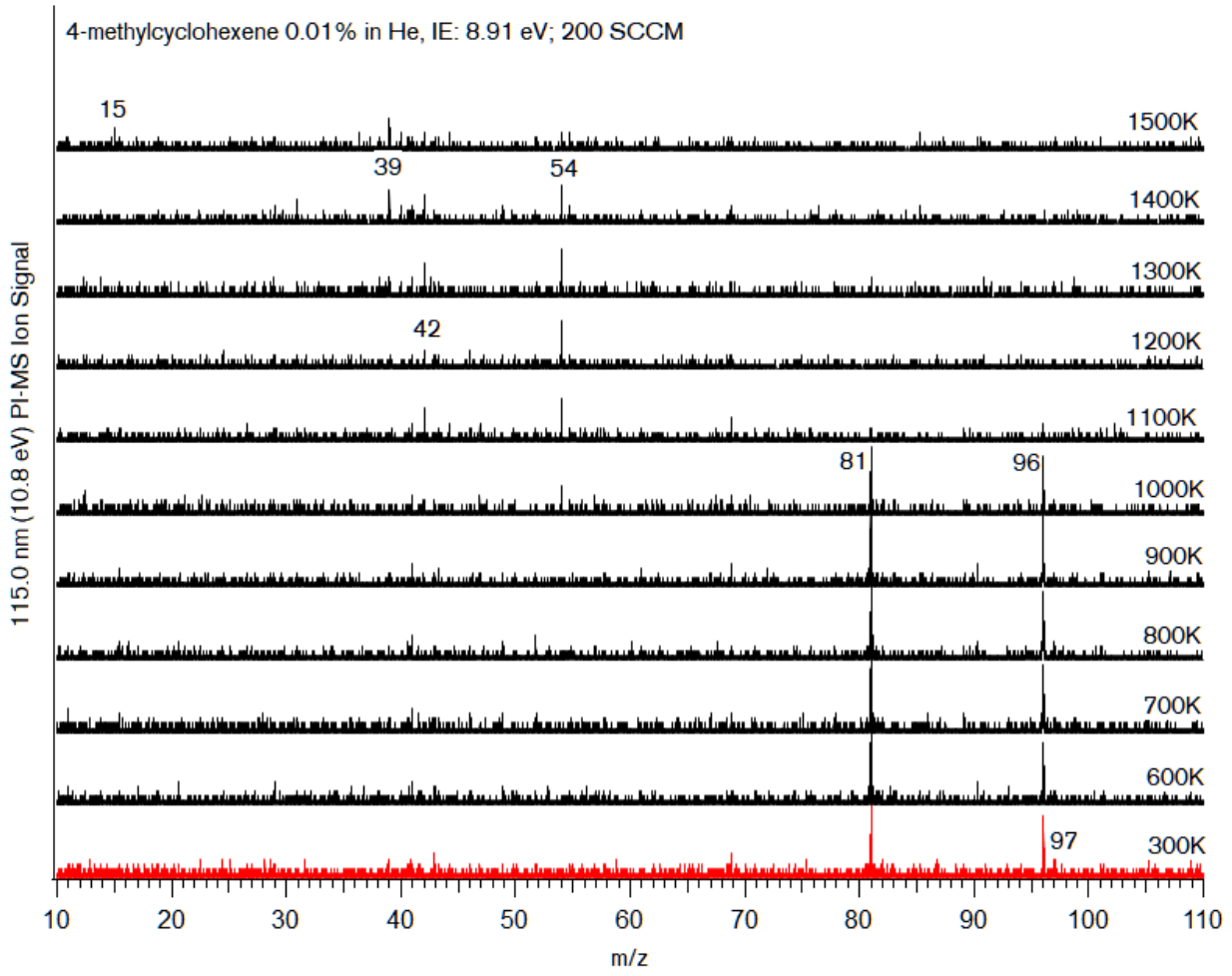

Figure A4C6: PIMS of 0.01% 4-methylcyclohexene in He in the microreactor at 200 SCCM heated between 300K and 1500K and ionized by 115.0 nm (10.8 eV) photons.

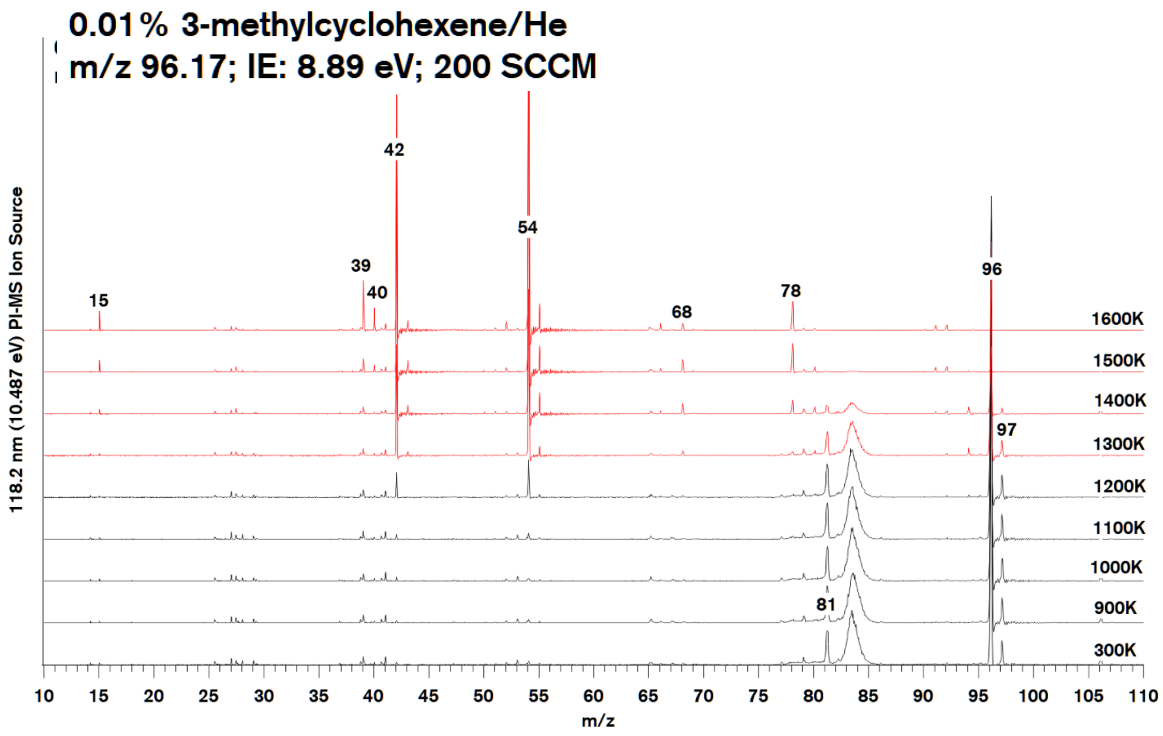

Figure A4C7: PIMS of 0.01% 4-methylcyclohexene in He in the microreactor at 200 SCCM heated between 300K and 1500K and ionized by 118.2 nm (10.487 eV) photons.

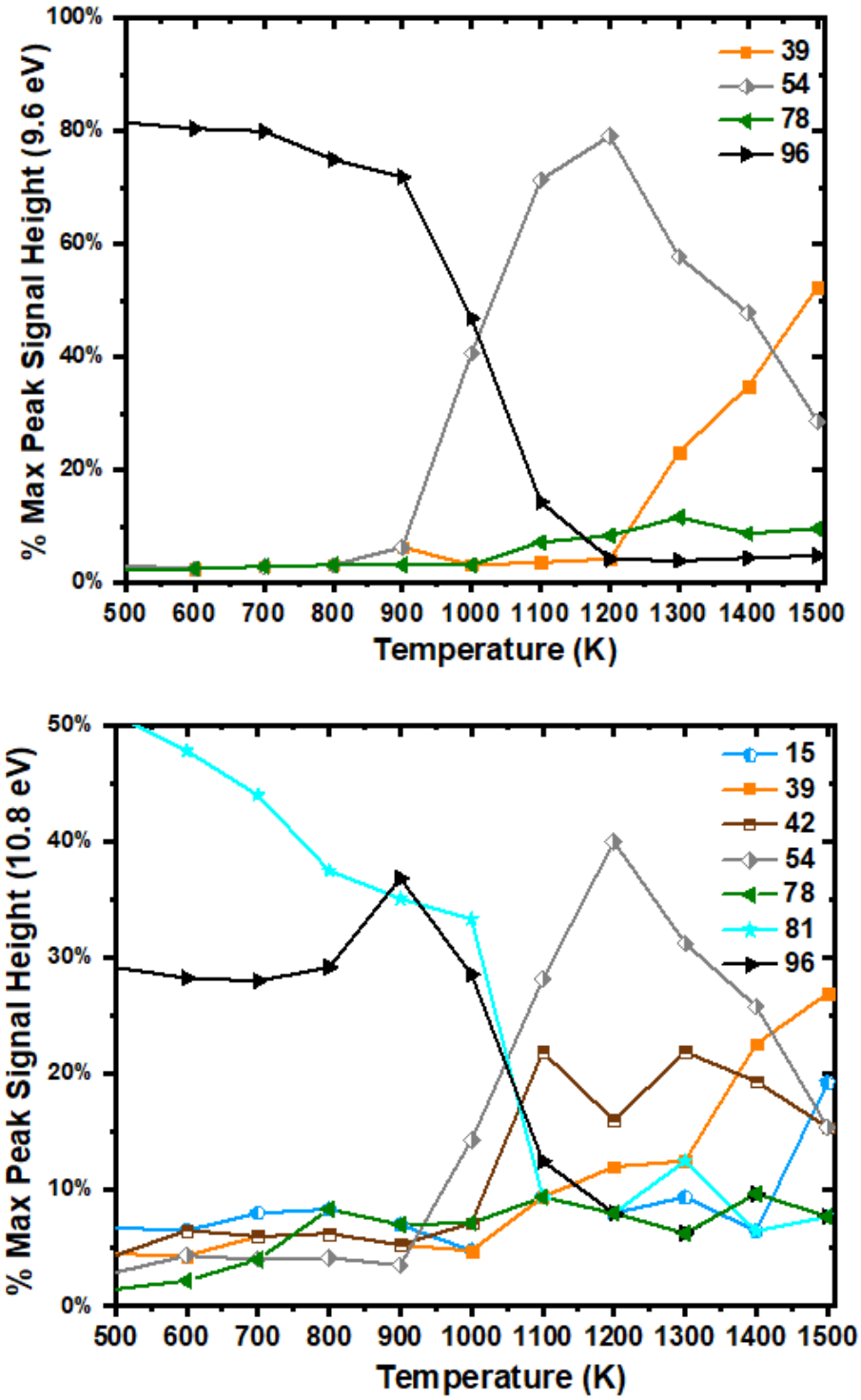

Figure A4C8: Percentage (%) of the total maximum peak signal height as a function of temperature are shown for significant mass values from 4MCHe spectra (IE= 8.91 ± 0.01 eV [35]). Top: 9.6 eV. Bottom: 10.8 eV. The presence of dissociative ionization is detected in the 10.8 eV plot by the presence of m/z 81 at room temperature.

A4.1C) 3MCHe experimental temperature sweeps

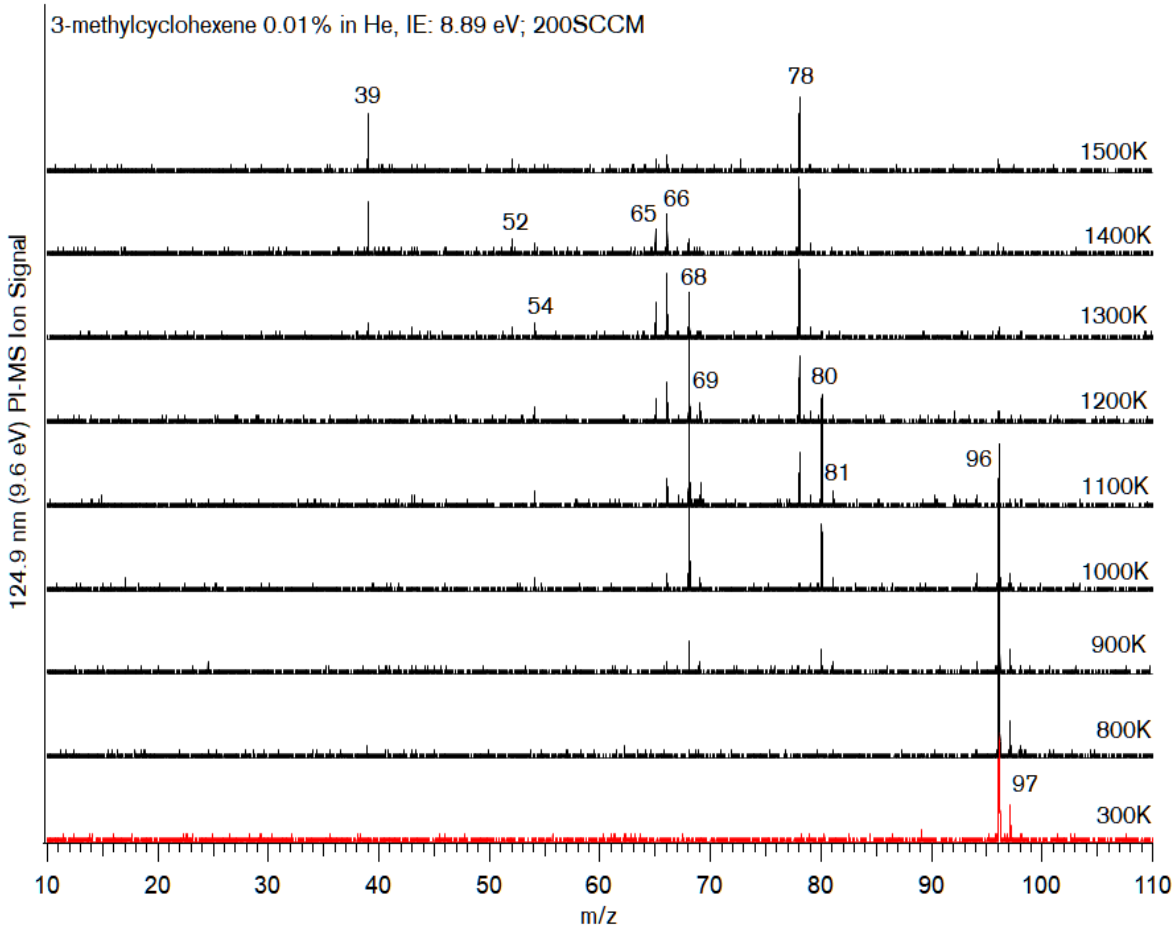

Figure A4C9: PIMS of 0.01% 3-methylcyclohexene in He in the microreactor at 200 SCCM heated between 300K and 1500K and ionized by 124.9 nm (9.6 eV) photons.

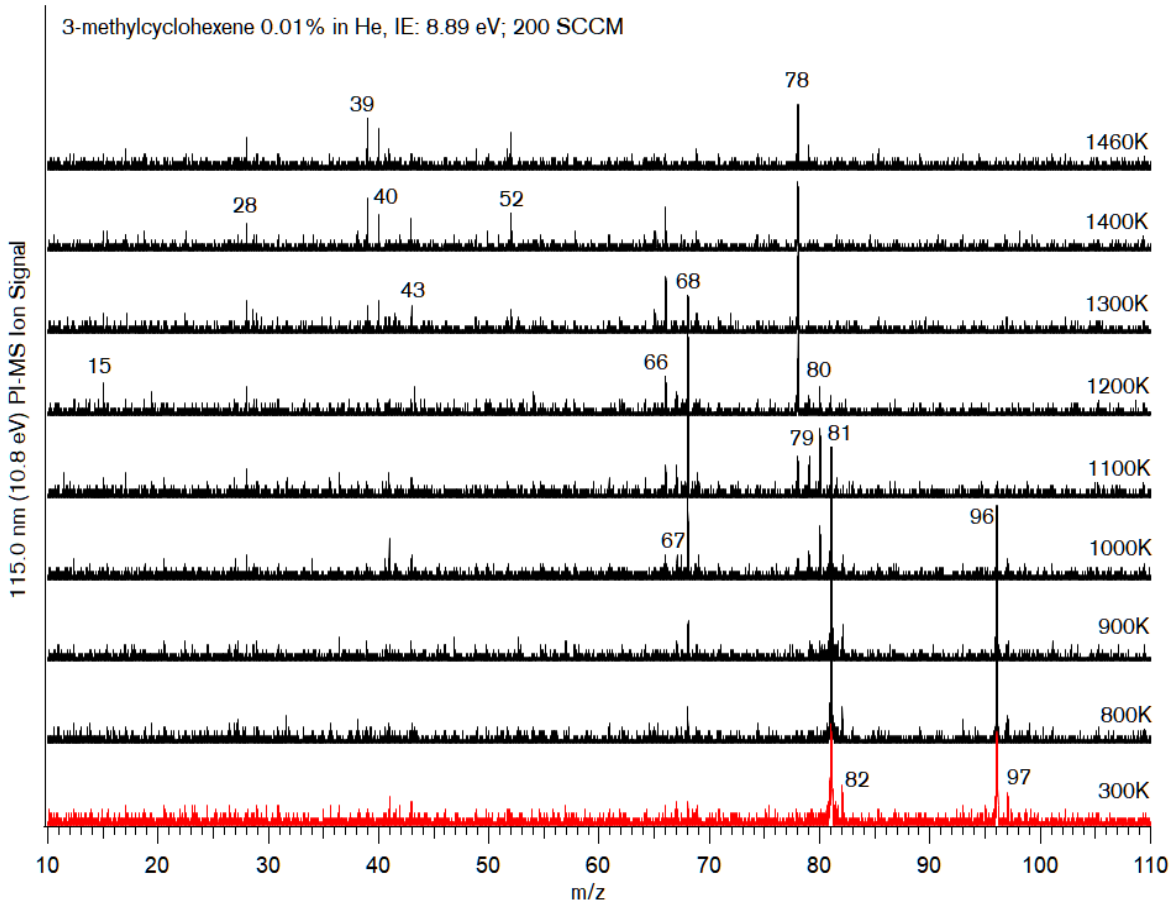

Figure A4C10: PIMS of 0.01% 3-methylcyclohexene in He in the microreactor at 200 SCCM heated between 300K and 1460K and ionized by 115.0 nm (10.8 eV) photons.

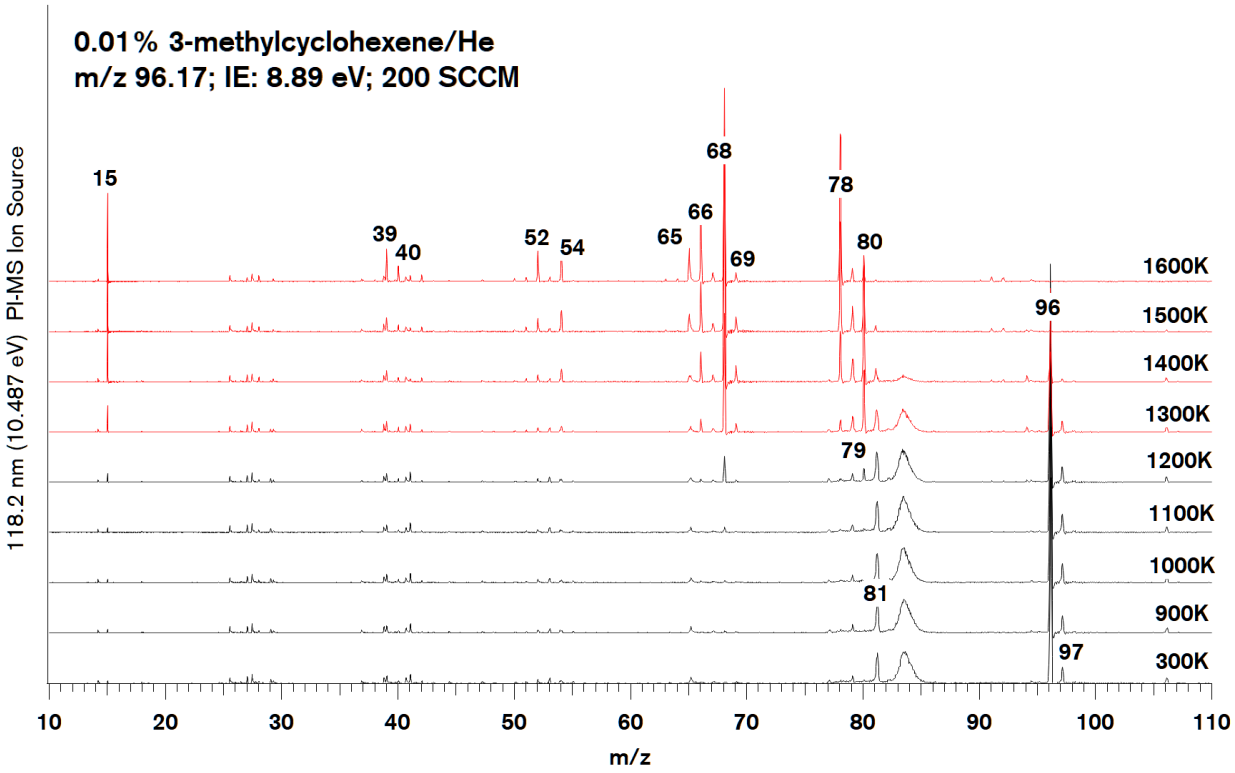

Figure A4C11: PIMS of 0.01% 3-methylcyclohexene in He in the microreactor at 200 SCCM heated between 300K and 1460K and ionized by (8.89 eV) photons.

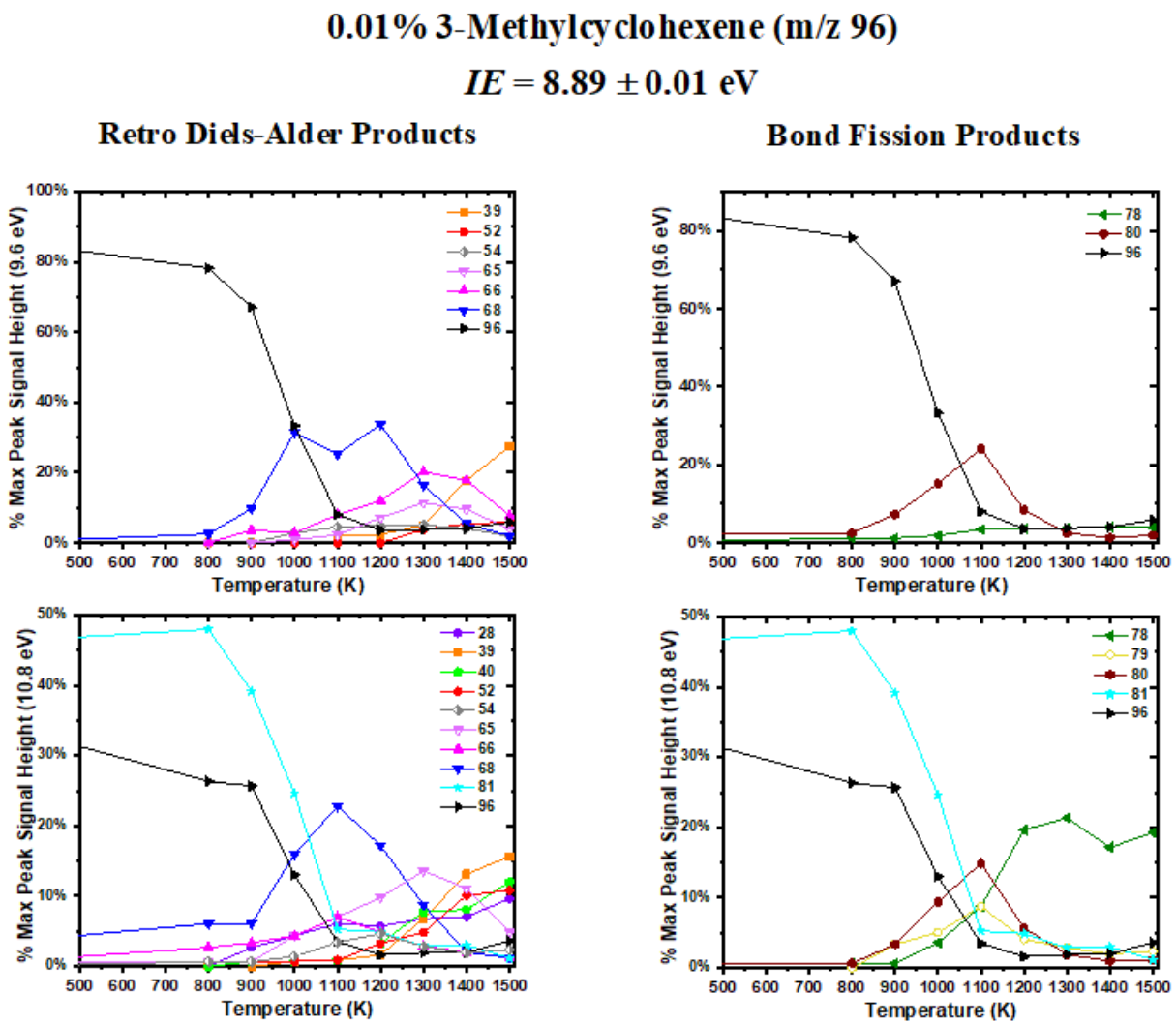

Figure A4C12: Percentage (%) of the total maximum peak signal height as a function of temperature are shown for significant mass values from 1MCHe spectra (IE= 8.89 ± 0.01 eV [35]). Top: 9.6 eV. Bottom: 10.8 eV. Left: Masses from the retro-Diels-Alder pathway. Right: Masses resulting from bond fission routes. The presence of dissociative ionization is detected in the 10.8 eV plot by the presence of m/z 81 at room temperature.

A4.2A) Potential energy surfaces (PES) of relevant MCHe isomer radicals

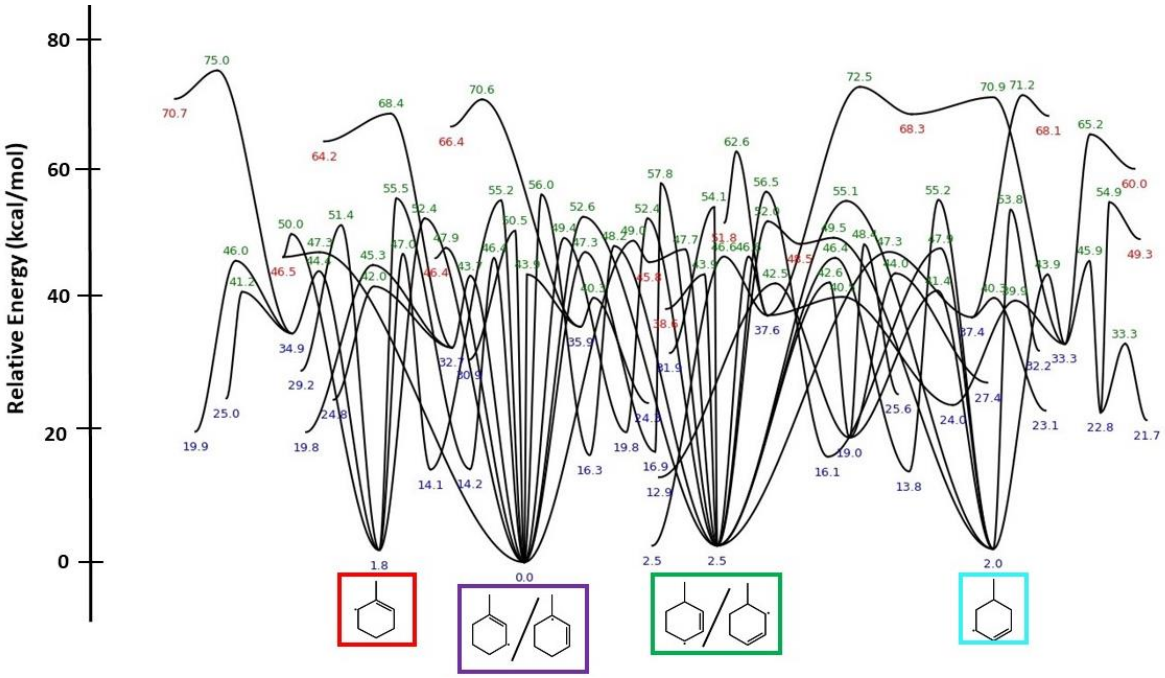

Figure A4C13: Full PES showing the interconnectedness between the MCHe isomer radicals. Due to the complexity of the PES, many of the drawn structures are not included. More detailed PESs of the 4 main radicals are presented subsequently. Energies are calculated at the m06-2X/CC-pVTZ level of theory with zero point correction.

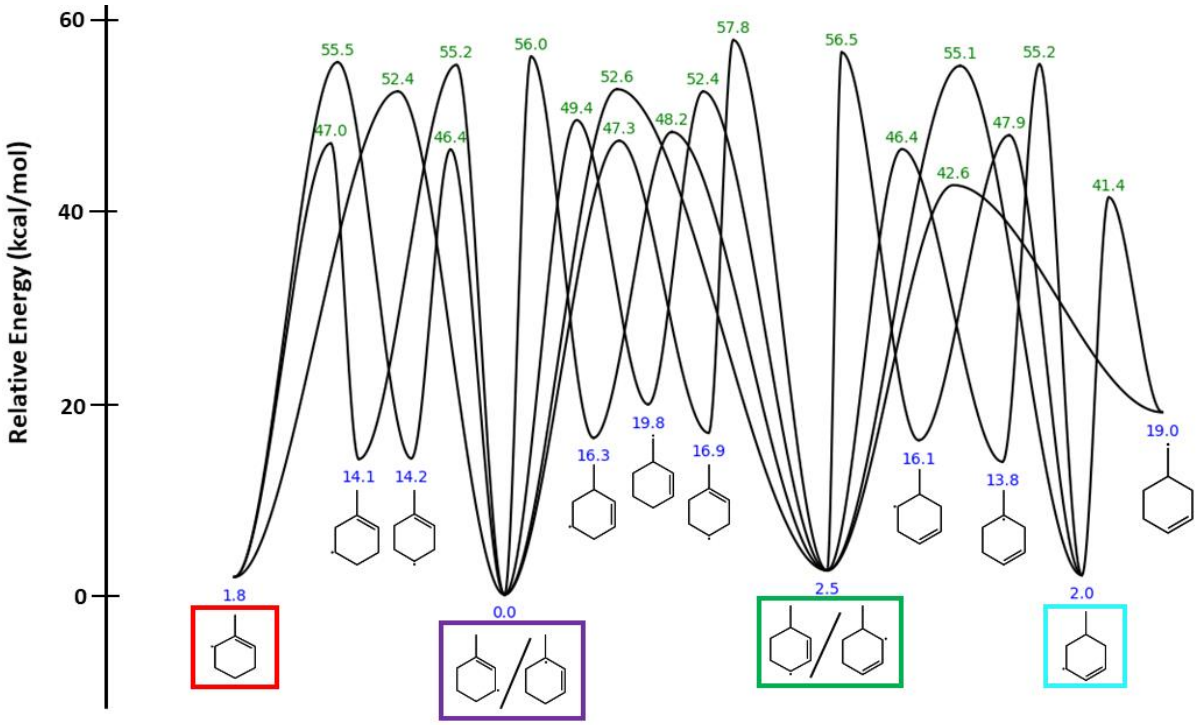

Figure A4C14: PES of the isomerizations between the different MCHe isomer radicals. Energies are calculated at the m06-2X/CC-pVTZ level of theory with zero point correction.

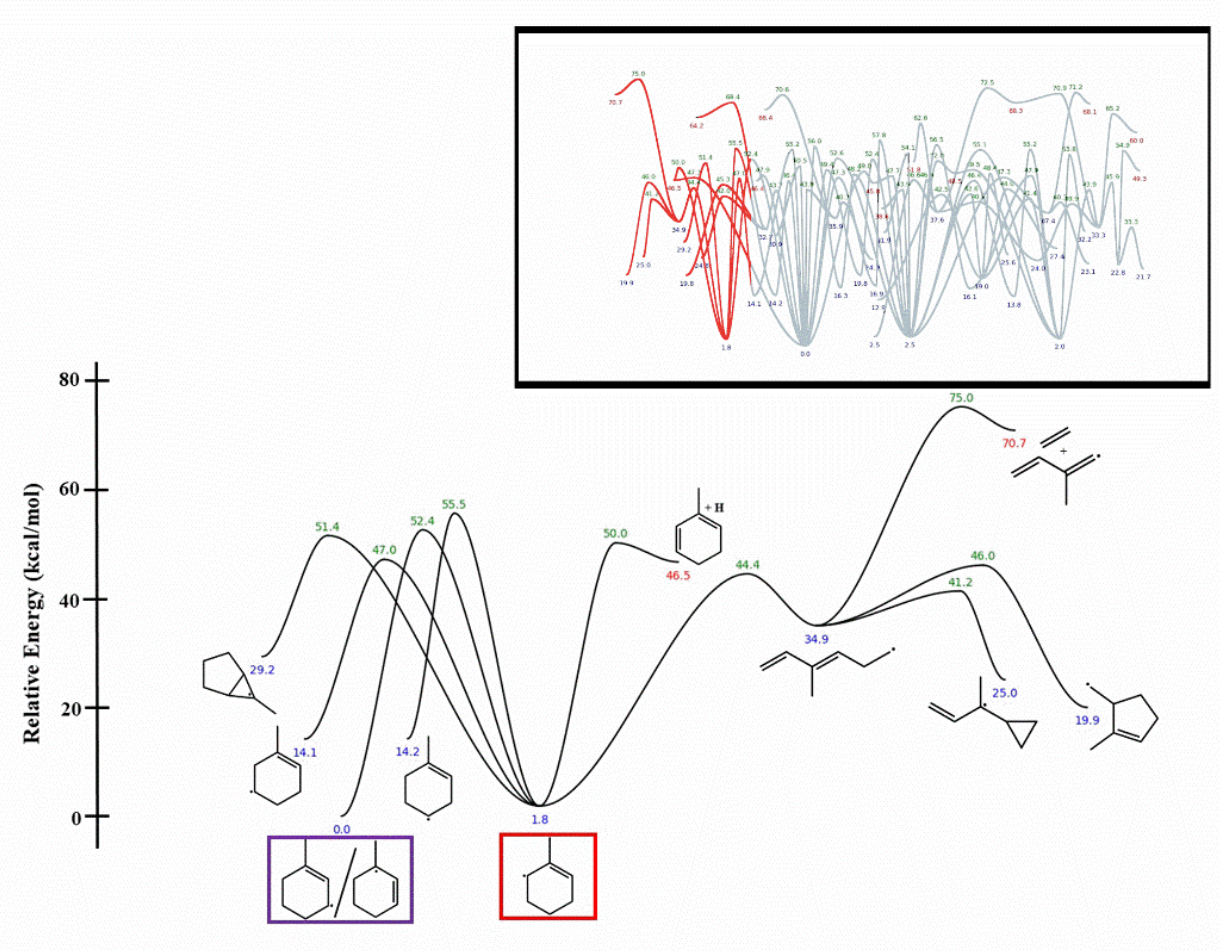

Figure A4C15: PES of the 1MCHe-R6 formed during the 2nd lowest bond fission of 1MCHe. Energies are calculated at the m06-2X/CC-pVTZ level of theory with zero point correction.

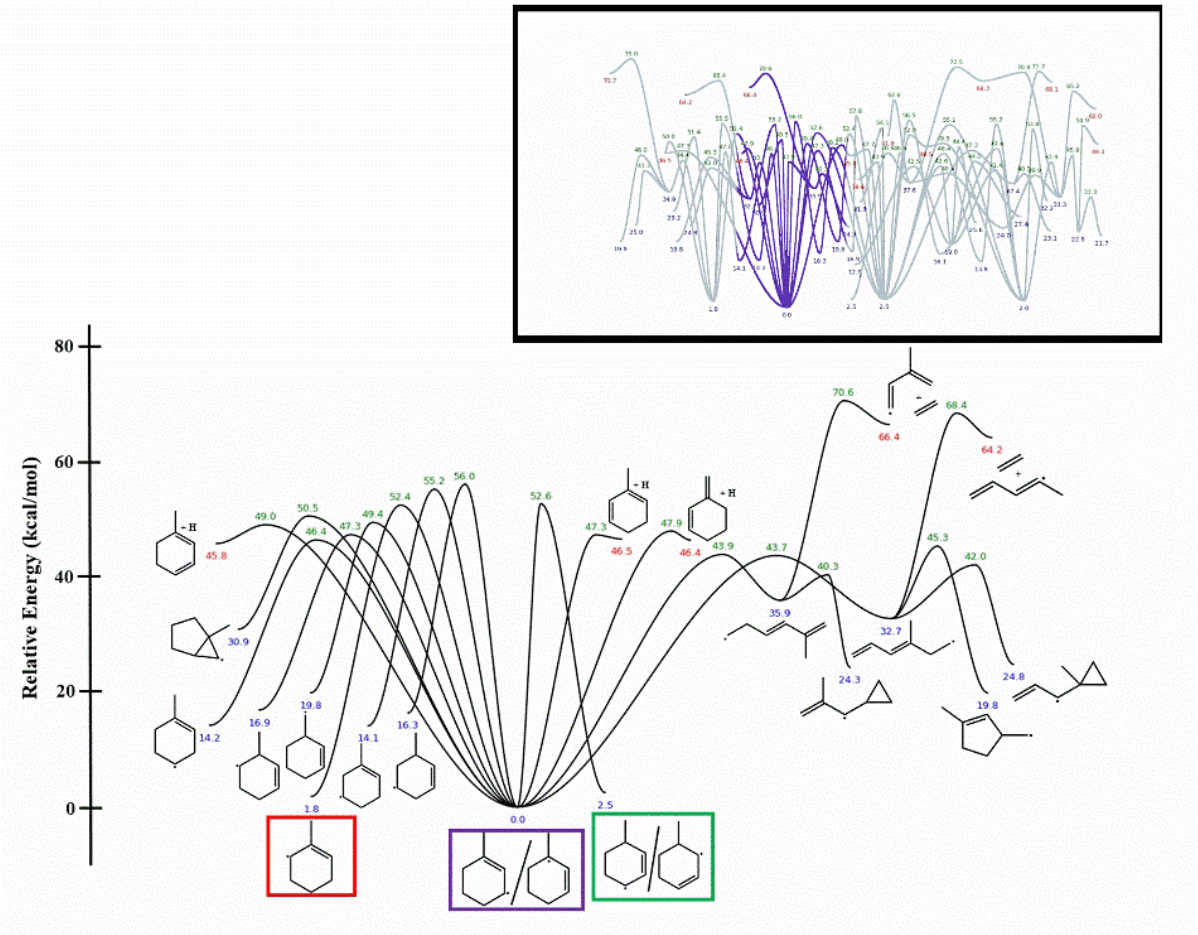

Figure A4C16: PES of the 1MCHe-R3/3MCHe-R1 resonantly stabilized allylic radical formed during the lowest bond fission of 1MCHe and 2nd lowest bond fission of 3MCHe. Energies are calculated at the m06-2X/CC-pVTZ level of theory with zero point correction.

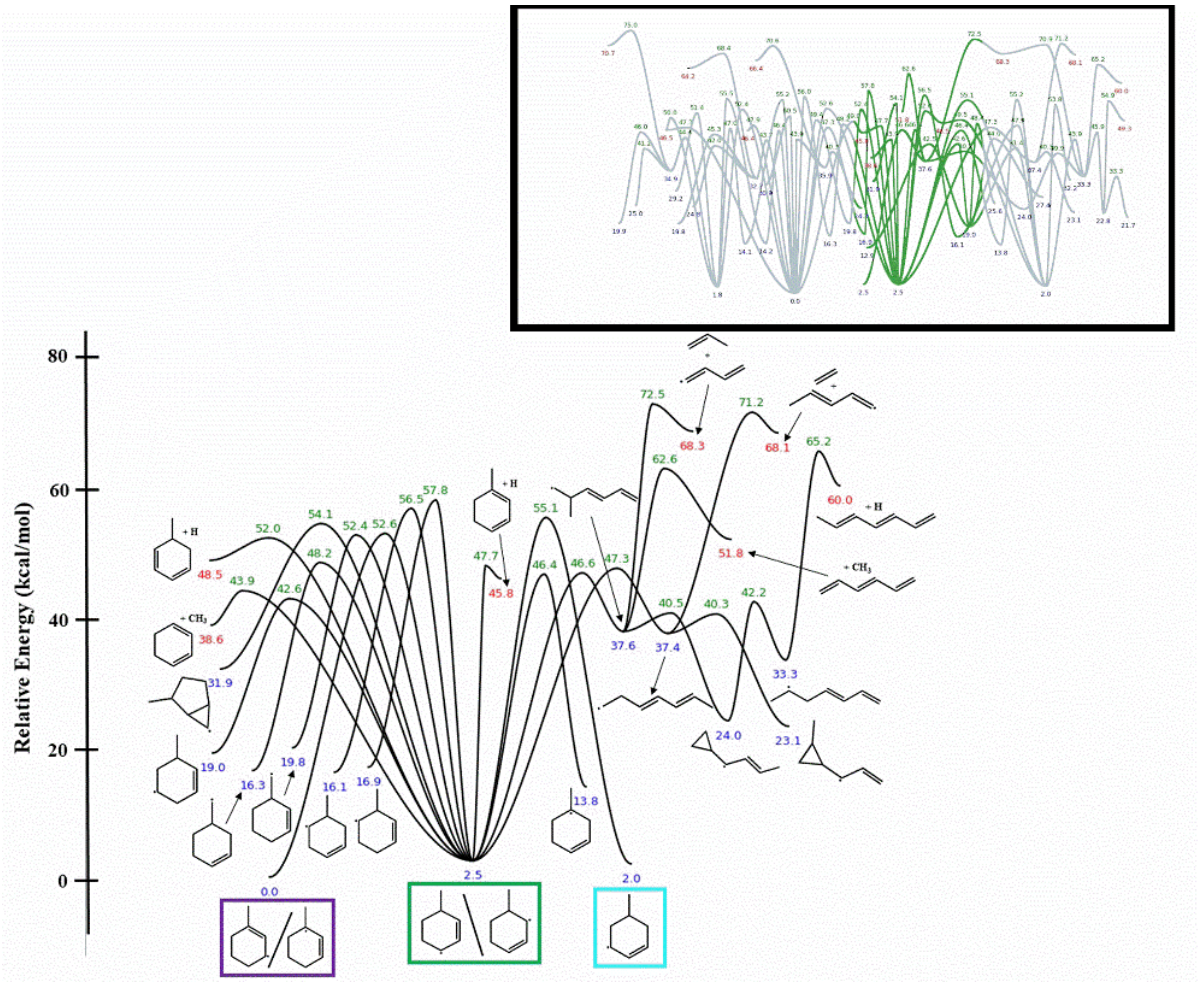

Figure A4C17: PES of the 3MCHe-R4/4MCHe-R2 resonantly stabilized allylic radical formed during the 3rd lowest bond fission of 3MCHe and 2nd lowest bond fission of 4MCHe. Energies are calculated at the m06-2X/CC-pVTZ level of theory with zero point correction.

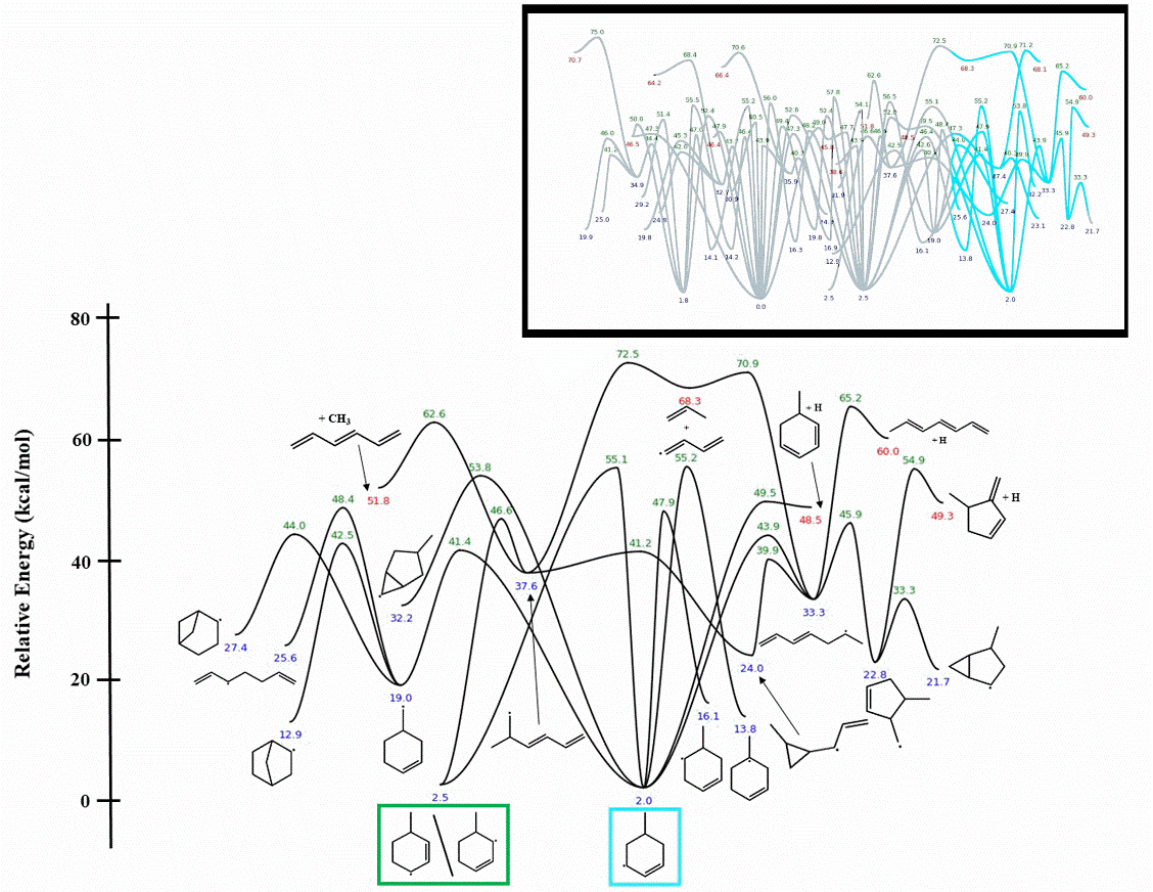

Figure A4C18: PES of the 4MCHe-R5 allylic radical formed during the lowest bond fission of 4MCHe. Energies are calculated at the m06-2X/CC-pVTZ level of theory with zero point correction.

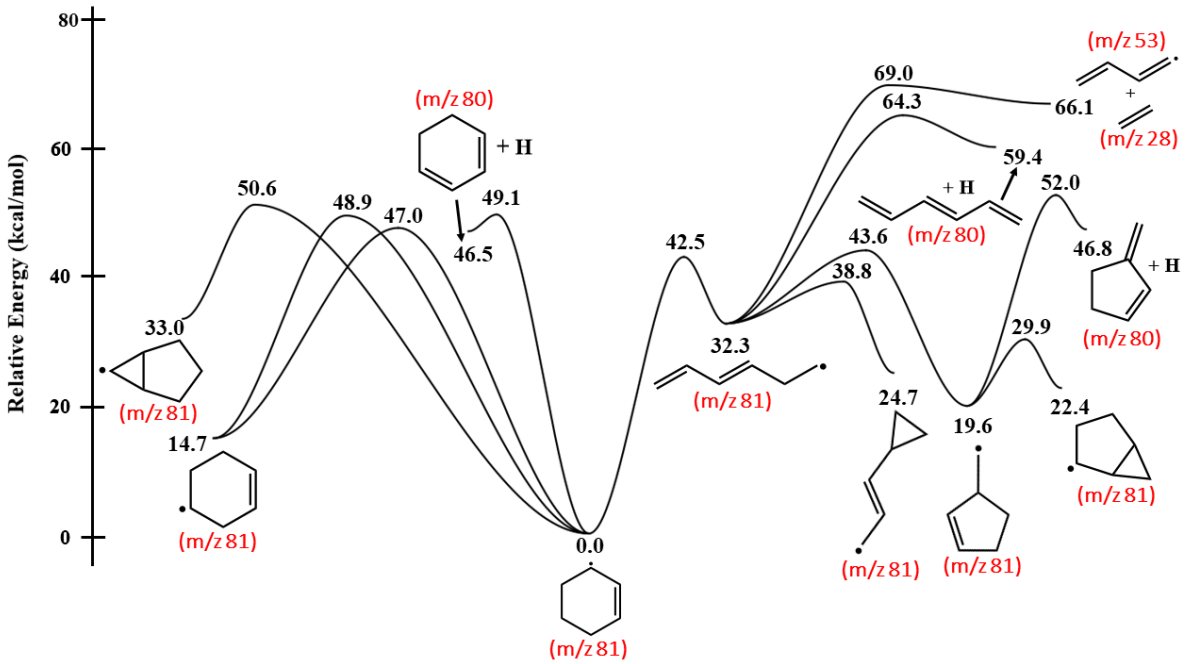

Figure A4C19: PES of the 2-cyclohexenyl radical formed from the lowest bond fission of 3MCHe. Energies are calculated at the CCSD(T)/cc-pV∞Z//M06-2X/cc-pVTZ level of theory. Only isomerization pathways of 1,3-hexadiene radical (32.3 kcal/mol) below the lowest b-scission the 2-cyclohexenyl radical (49.1 kcal/mol) are included for clarity. The masses (m/z) of each species are listed to help compare with the experimental data.

C5: Probing the pyrolysis of Polyoxymethylene Ethers (POM-E)

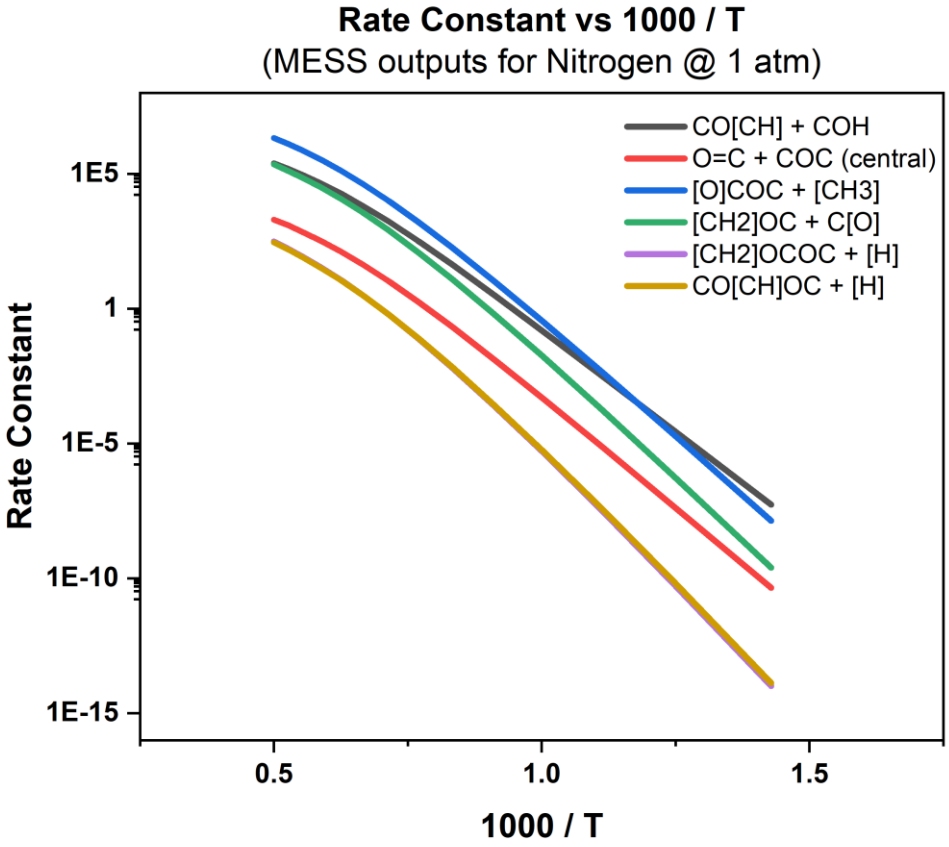

Figure A5C1: Rate constant as a function of temperature for the thermal decomposition of DMM (dimethoxymethane), with nitrogen at a pressure of 1 atm.

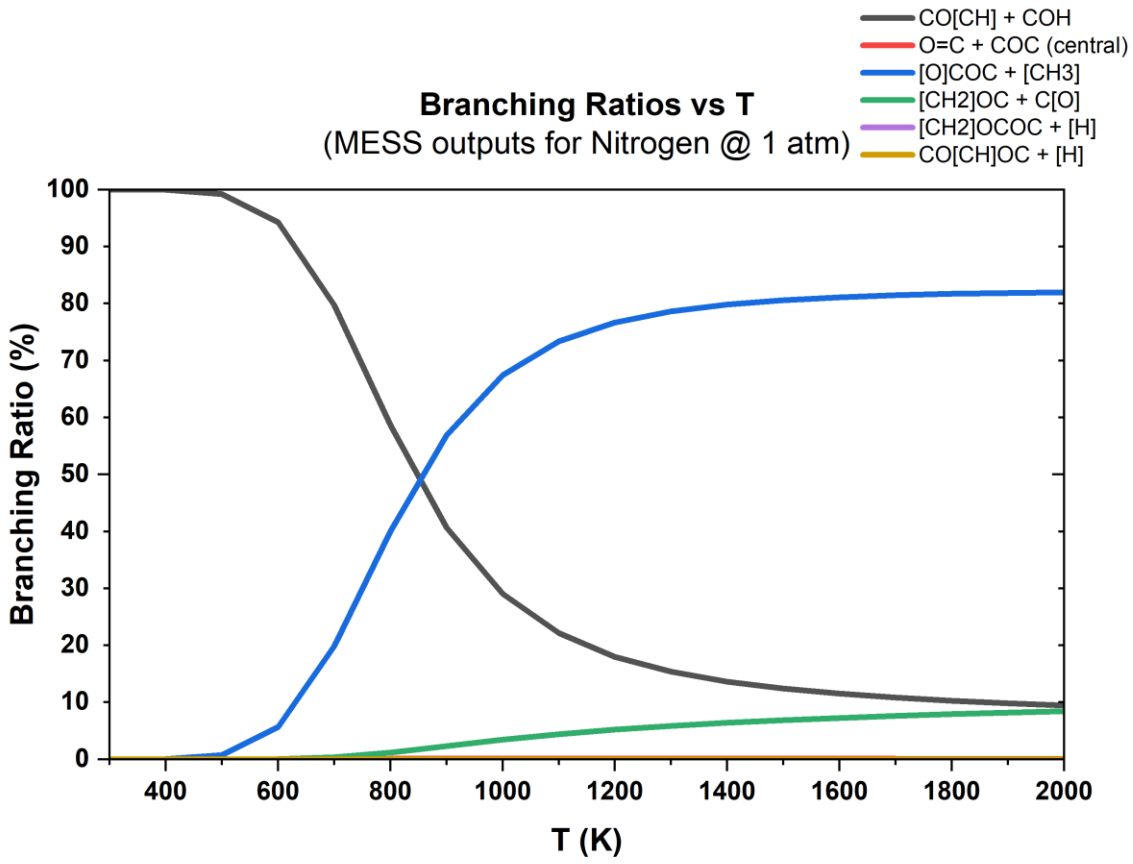

Figure A5C2: Branching ratios for the primary decomposition reactions of DMM (dimethoxymethane) as a function of temperature, with nitrogen at a pressure of 1 atm.

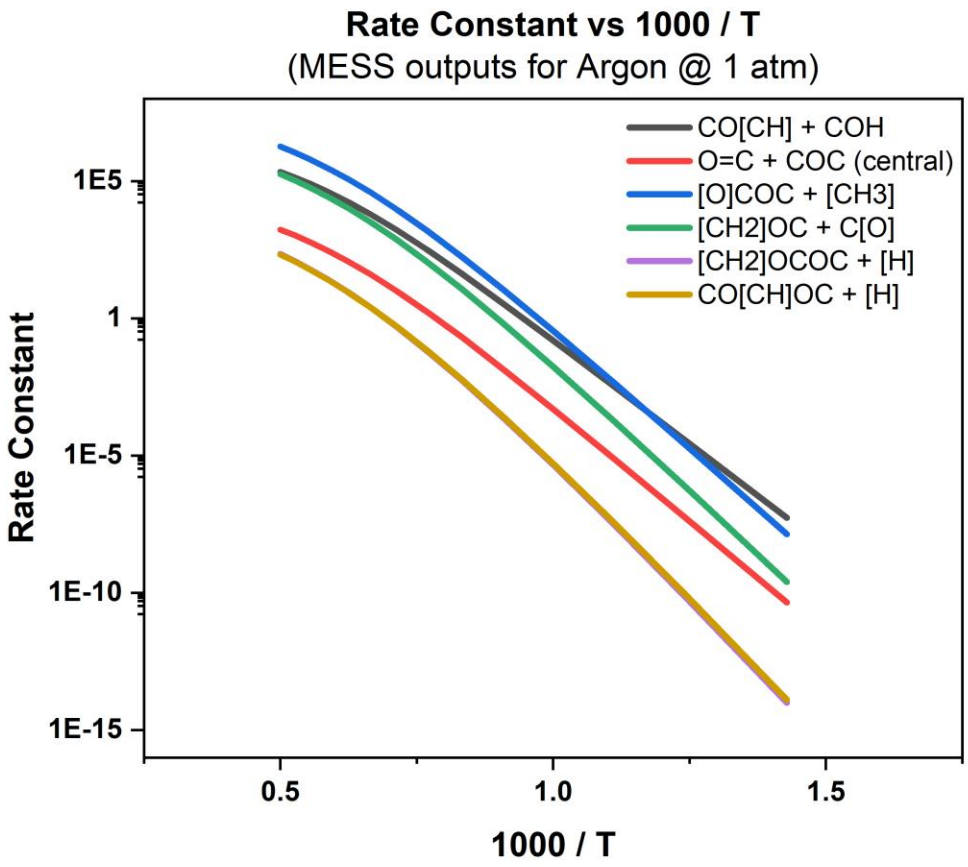

Figure A5C3: Rate constant as a function of temperature for the thermal decomposition of DMM (dimethoxymethane), with argon at a pressure of 1 atm.

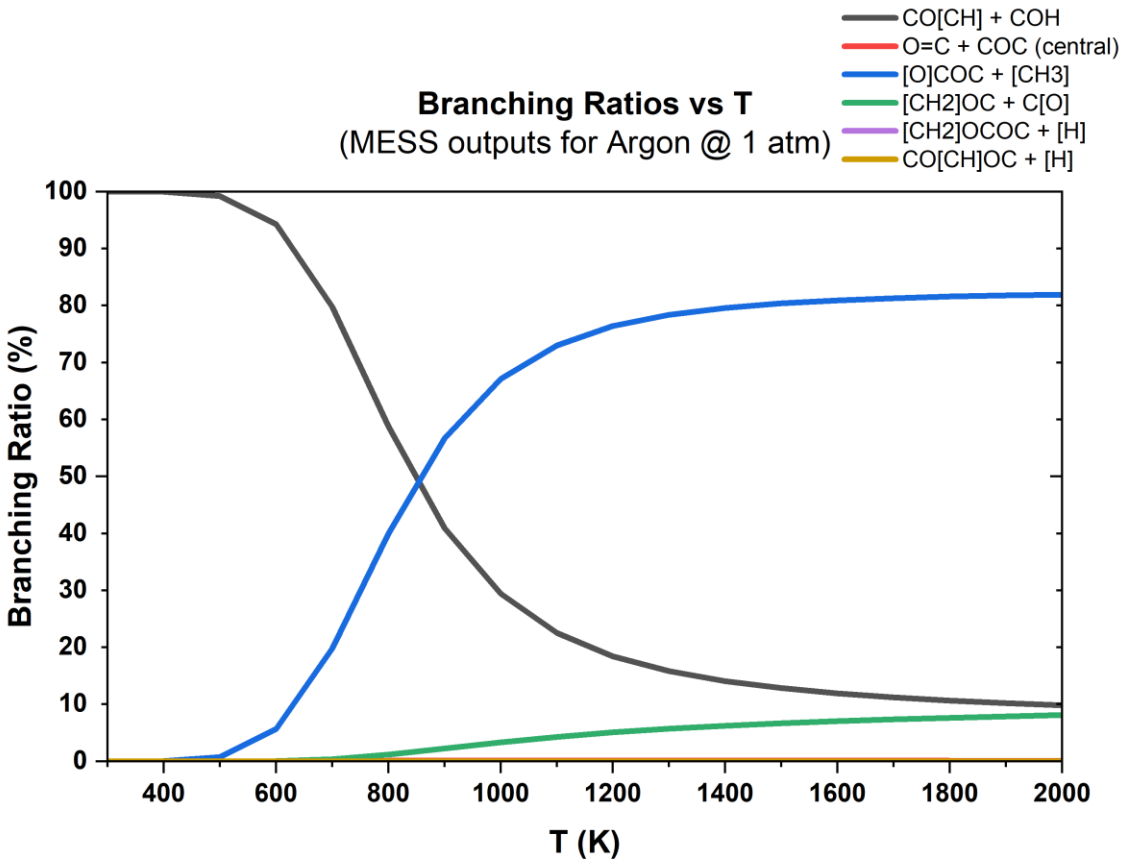

Figure A5C4: Branching ratios for the primary decomposition reactions of DMM (dimethoxymethane) as a function of temperature, with argon at a pressure of 1 atm.

C7: Fabrication of the novel micro-reactor geometry

Table C7.1: Chemical and physical properties of the Calix High Strength 2 ready-to-press (RTP) powder.

Properties	**Calix Ceramic High Strength 2**
Specific surface area (m^2/g)	14–16
Tap density (g/cm^3)	0.97
Granule size (μm)	<125
Particle size distribution *d*90 (μm)	1.0
*d*50 (μm)	0.5
*d*10 (μm)	0.25
Oxygen (wt%)	<1.0
Boron (wt%)	0.5-1.0
Carbon (wt%)	3-7
Organic binder (wt%)	3-10

C9: Conclusions and future research directions

C9.1 Photoionization mass spectra of anisole using alumina micro-reactor

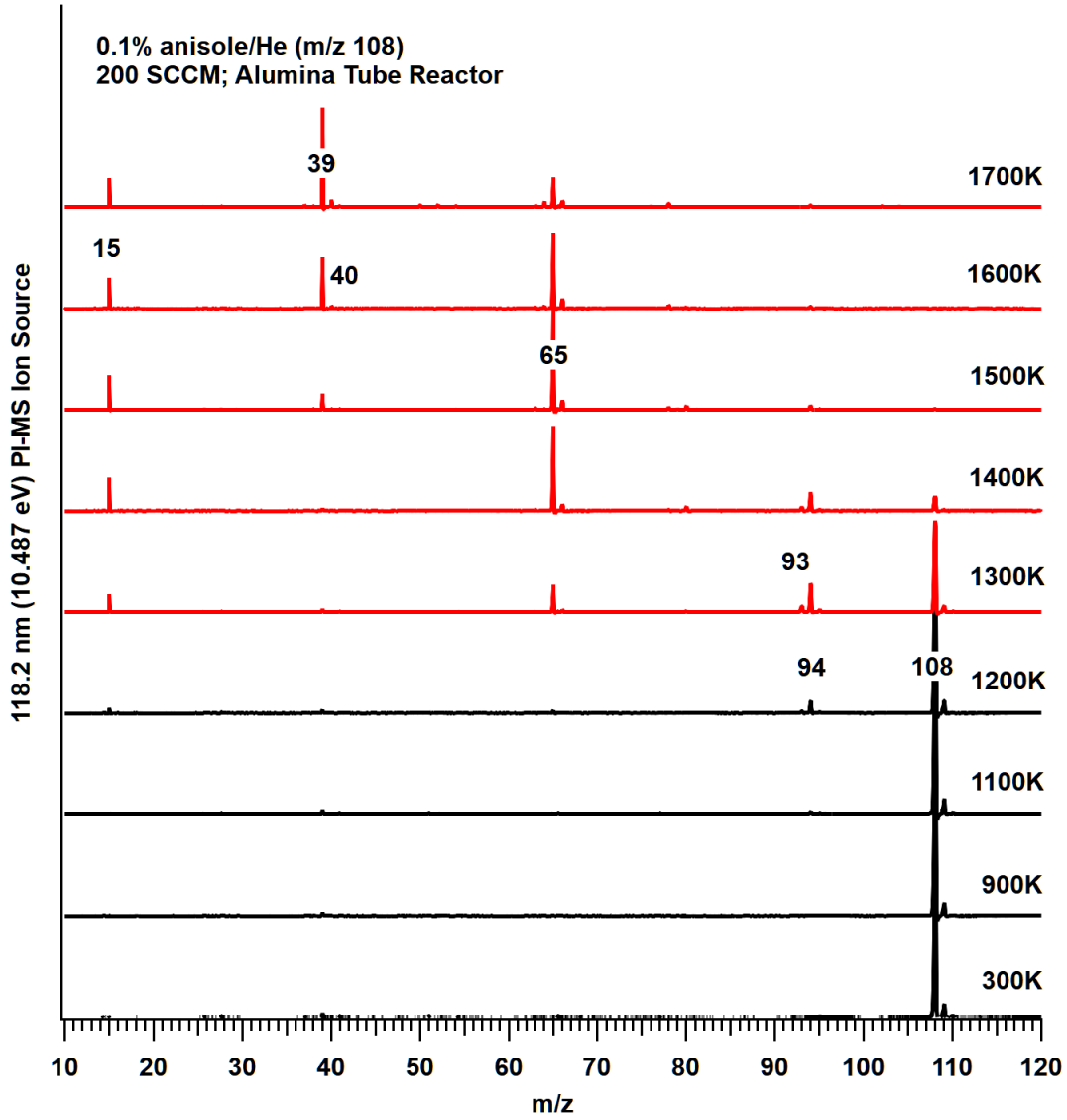

Figure A9C1: PIMS of 0.1% anisole in He in an Alumina tube micro-reactor at 200 SCCM heated between 300K and 1700K and ionized by 118.0 nm (10.5 eV) photons.

C9.2 Photoionization mass spectra of anisole using alumina micro-reactor

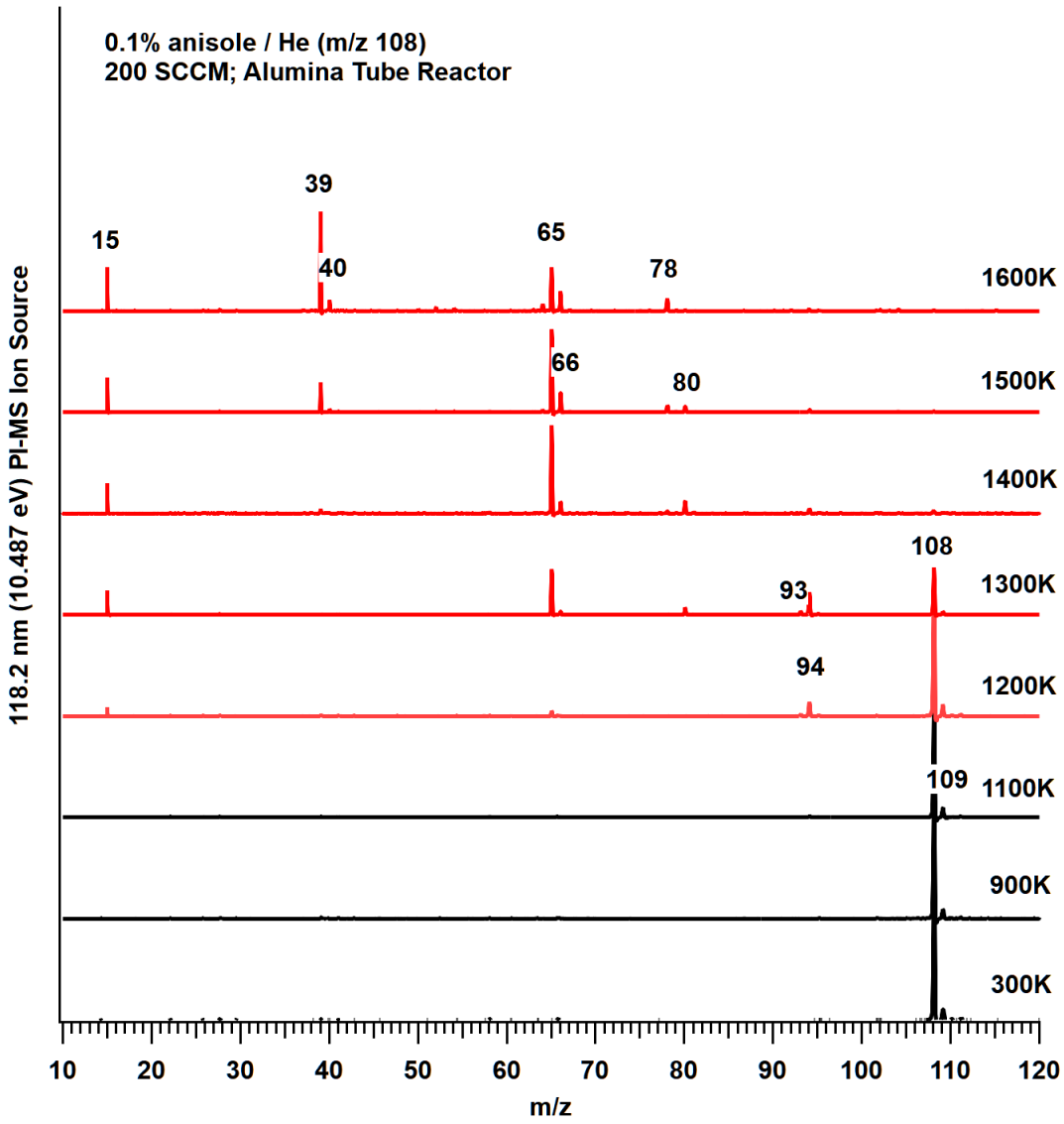

Figure A9C2: PIMS of 0.1% anisole in He in an Alumina tube micro-reactor at 200 SCCM heated between 300K and 1700K and ionized by 118.0 nm (10.5 eV) photons.